Detections of seven faint g-ray pulsars and constraints on neutron star moments of inertia with the Fermi–LAT

Xian Hou

Numéro d'ordre: 5003

THÈSE

présentée à

L'UNIVERSITÉ BORDEAUX I

ÉCOLE DOCTORALE DES SCIENCES PHYSIQUES ET DE L'INGÉNIEUR

par Xian Hou
(侯賢)

POUR OBTENIR LE GRADE DE

DOCTEUR

SPÉCIALITÉ ASTROPHYSIQUE, PLASMAS ET CORPUSCULES

Detections of seven faint γ-ray pulsars and constraints on neutron star moments of inertia with the *Fermi*–LAT

Soutenue le 18 décembre 2013

Après avis de :

Mme N. Webb	Astronome-adjoint	IRAP, Toulouse, France	**Rapporteurs**
M. G. Theureau	Astronome	LPC2E, Orléans, France	

Devant la commission d'examen formée de :

M. G. Theureau	Astronome	LPC2E, Orléans, France	**Président du jury**
M. D. A. Smith	Directeur de recherche	CENBG Bordeaux-Gradignan, France	**Directeur de thèse**
Mme N. Webb	Astronome-adjoint	IRAP, Toulouse, France	**Rapporteur**
M. G. Theureau	Astronome	LPC2E, Orléans, France	**Rapporteur**
Mme N. Brouillet	Astronome-adjoint	LAB, Floirac, France	**Examinatrice**
M. K. J. Lee (李柯伽)	Professeur	MPI für Radioastronomie, Bonn, Germany, Kavli Institute for Astronomy and Astrophysics, Peking University, Beijing, China	**Invité**

To Fang Yang (楊芳), my family, my friends

Life is not easy for any of us. But what of that? We must have perseverance and above all confidence in ourselves. We must believe that we are gifted for something and that this thing must be attained.

MARIE SKLODOWSKA-CURIE
(1867 - 1934)

Acknowledgements

My dream of accomplishing a thesis work in Physics, precisely in Astrophysics, has finally become true. This is a milestone in my life, even though there is still definitely a long way to go in the ultimate pursuit of science. I owe my deep acknowledgements to all who have made me who I am today.

First of all, I'm extremely grateful to David Smith, my thesis supervisor, for having accepted me to be a graduate student working on *Fermi* gamma-ray pulsars in the Astroparticle group in CENBG, and for having accompanied me in these three years with his fruitful instructive guidance in my work. I appreciate also his American humor and his optimistic attitude for the life, which have brought me happiness and courage in the sometimes no so easy western world. Special thanks are addressed to his great support on my family's visit tour in France. Thank you for all that you have done for me, David!

Many thanks to Bernard Hass and Philippe Moretto, former and current director of CENBG, for their authorization and support on my doctoral work in the last three years. Thanks also our colleagues in administration department for their great support: Nathalie, Nadine, Sylvie, Aziz and others.

Moreover, sincere thanks are owed to the marvellous members of our Astroparticle group in CENBG: Denis Dumora, Thierry Reposeur, Marianne Lemoine-Goumard, Benot Lott for very useful discussions on the scientific work and also for many interesting topics and funny jokes on the daily life during the lunch time. I appreciate definitely on the other hand Romain Rousseau (we have known each other for 5 years, wow! You know, you have always made jokes on me, I will never forget that!), Lise Escande, excellent graduate students, Matthew Dalton, Hélène Laffon and Jérémie Méhaut, great posdocs in our group, for their help in my work (especially thanks Romain) and the happy time enjoyed together. Thanks also Marie-Hélène Grondin for her encouragement each time when she visited CENBG. I wish all of them a prosperous future and a wonderful life.

I thank Gilles Theureau and Natalie Webb for having accepted to be referees of my thesis and for their constructive comments and suggestions which have helped me to improve greatly my manuscript. Thanks equally Nathalie Brouillet and Kejia Lee (李柯伽) to be members of the advisory committee of my defense and for their comments on my manuscript. It has taken Kejia hours of hours of train to come to Bordeaux from Bonn. Thanks equally for his advice and help on my future career plan. He is now the father of a very cute daughter, what a happiness! Thanks Nathalie also for her organization of my defense in the Laboratoire d'Astrophysique de Bordeaux (LAB) given that there were no rooms available in CENBG.

I wish absolutely to address my acknowledgements to the *Fermi* collaboration in which I have been able to achieve my thesis work and to enjoy the visit in Stanford University, San Francesco and Venice during the collaboration meetings. Particularly, sincere thanks to Damien Parent, Lucas Guillemot, two former graduate students in the Astroparticle group, for their extreme patience and efficient help whenever I need. Many thanks also to Ismaël Cognard, Matthew Kerr, Tyrel Johnson, Pierre Jean, Toby Burnett, Pablo Saz Parkinson and the rest of the collaboration. Pierre, you have been always in great support on me since my

Master study in Toulouse, thank you! Tyrel has been so nice to encourage me and support me in the last year of my thesis and in my job hunting, though we haven't really chatted much in the real world, incredible! I will not forget to express my appreciation to the Pulsar Timing Consortium which has generously provided radio ephemerides for pulsars without which my detections of gamma-ray pulsars would have not been possible.

And great gratitude to my dear friends. Fang Yang (楊芳), even though we haven't kept in touch all the time, you are always in my heart. I'll never forget what has made us best friends and decide to choose an un-ordinary and maybe very hard life when we were still little girls: physics, right? Now you are ahead of me, but I'm catching up! Xingheng Lu (陸幸恒), you have become my best friend since we arrived in France to pursue our dreams. It's more than thanks to say for your absolute support, encouragement and certainly the happiness you brought to me. Meng Su (蘇萌), we became good friends thanks to *Fermi*, thanks to Astrophysics and thanks to Rome. Your achievements in Astrophysics have embraved me to be more firm to my dream. Kuo Liu (劉闊), even though we haven't met much, I do appreciate your kindness and encouragement in my last doctoral year. Meng Hock Koh (明福), we have spent only five months together in CENBG, but it has been a very pleasant memory. Your encouragement and your lovely personal characters have made this last year less harder. Many thanks also to Xuetong Li (李雪桐), Bin Yang (楊斌) ... for the wonderful time we spent together in Bordeaux.

Finally, I am deeply indebted to my family, my parents and my brother for their full support and the freedom they give to me each time when I made a choice in my life since I was very young. Owing to this, I have been able to achieve my thesis abroad, far far away from them. It's regretful that my grandparents who loved me so much have not been able to witness this great moment in my life. I have nothing else to recompense my family than to accomplish more and to live a happy life.

Surely, there is also my high school physics professor, and all the others who have accompanied me from my primary shcool to Master study, both in China and in France...

登鸛雀樓
唐 王之渙

白日依山盡，黃河入海流.
欲窮千裏目，更上一層樓.

HOU Xian (侯賢)

Résumé

Ma thèse concerne l'étude des pulsars à l'aide de l'analyse des données prises par le Large Area Telescope (LAT) à bord du satellite *Fermi*.

Une cinquantaine d'années se sont écoulées depuis la découverte du premier pulsar par J. Bell et A. Hewish à Cambridge en 1967. Le catalogue de pulsars ATNF compte désormais plus de 2000 pulsars. La majorité émet des ondes électromagnétiques à des longueurs d'ondes radio, tandis que certains sont également détectés à des longueurs d'onde optiques, en rayons X et en rayons γ. Mais, que sont les pulsars? Pourquoi sont-ils intéressants? Les pulsars sont des étoiles à neutrons fortement magnétisées en rotation rapide nées dans l'effondrement gravitationnel d'étoiles massives terminant leurs vies en supernova violente. L'émission des pulsars est observée périodiquement sur Terre quand elle traverse la ligne de visée, d'où leur nom "Pulsating Source of Radio". La découverte des pulsars a offert la possibilité d'étudier la physique dans des conditions extrêmes inaccessibles sur la Terre : une forte densité de matière et des champs magnétiques élevés. Cela a ouvert la porte pour tester la relativité générale dans des conditions de champ gravitationnel intense. Les pulsars sont également utilisés pour cartographier la structure à grande échelle du champ magnétique galactique et pour sonder le milieu interstellaire.

Alors que les pulsars radio dominent en nombre, le ciel en pulsars γ est beaucoup plus lumineux, même avec seulement dix détections avec EGRET à bord du Compton Gamma Ray Observatory, avant le lancement du *Fermi*, compte tenu de la luminosité γ beaucoup plus élevée que celle en radio. Dédié à l'astronomie γ, *Fermi* a été lancé en Juin 2008. Il s'agit d'une collaboration internationale entre les états-Unis, l'Italie, la Suède, la France, l'Allemagne et le Japon. Le LAT, l'instrument principal du *Fermi*, est sensible aux rayons γ de 20 MeV à plus de 300 GeV. Son champ de vue, sa surface efficace, sa résolution temporelle et sa PSF (résolution angulaire) sont meilleurs que ceux de EGRET. C'est avec *Fermi* que les pulsars γ ont finalement retiré leur voile mystérieux et embrassé leur printemps.

Ma thèse est organisée en trois parties décrivant la physique des étoiles à neutrons/pulsars, le fonctionnement et les méthodes d'analyse des données du *Fermi*-LAT, et les nouveaux résultats issus de cette thèse.

Dans la première partie, j'introduis d'abord la formation des étoiles à neutrons/pulsars et leur propriétés générales, leur catégorie (pulsars jeunes ou "normaux", pulsars millisecondes) avec une attention particulière portée aux différentes méthodes d'estimation des distances. La distance est critique pour l'interprétation correcte des observations γ qu'on verra dans les Chapiters 6, 7.

Ensuite, dans le Chapitre 2, je présente les aspects théoriques et d'observation de pulsars γ en décrivant brièvement les différents modèles d'émission γ en termes de distribution spectrale et de courbes de lumière (histogramme du nombre de photons par intervalle de phase rotationnelle du pulsar) et un résumé des caractéristiques des pulsars γ basé sur le deuxième catalogue du *Fermi*-LAT (2PC). 148 pulsars γ (décembre 2013) ont été découverts avec le *Fermi*-LAT, dont 117 ont été présentés dans 2PC. Les pulsars constituent la plus grande classe de sources au GeV dans la Voie Lactée. Les pulsars millisecondes ont été pour la première fois établis en tant qu'émetteurs de rayons γ et représentent un tiers de la population actuelle observée

par *Fermi*. Actuellement, tous sont aussi détectés en radio (radio-loud). Le reste est des pulsars jeunes (ou "normaux") qui sont en plus regroupés selon qu'ils sont détectés en radio (radio-loud) ou pas (radio-quiet).

Le nombre croissant de pulsars γ détectés avec *Fermi* offre une excellente occasion de réaliser des études statistiques de leurs mécanismes d'émission et de leur géométrie. Les caractérisations du profil de pulsation et l'analyse spectrale de l'échantillon actuel favorisent l'émission γ venant de la magnétosphère externe de l'étoile à neutrons, par exemple le modèle "Cavité Externe" (Outer Gap), par opposition à l'émission près du pôle magnétique d'où proviennent l'emission en radio et l'emission thermique en rayons X, par exemple le modèle "Calotte Polaire" (Polar Cap). Cependant, aucun des modèles d'émission actuels est capable de reproduire toutes les propriétés observées.

La deuxième partie est consacrée à l'instrument qui a rendu possibles les observations actuelles. Après avoir présenté le principe de détection, les composantes principales et les performances du *Fermi*-LAT dans le Chapitre 3, j'introduis la chronométrie de pulsars et les techniques employés pour chercher les pulsations γ (Chapitre 4): soit "empiler" les photons γ avec les éphémérides radio en utilisant le plugin **fermi** de Tempo2 (l'outil pour traiter les données radio), soit chercher "à l'aveugle" dans les données du *Fermi*-LAT, ou bien chercher en radio pour des sources *Fermi* non-identifiées qui présentent des caractéristiques de pulsars. Un test statistique (H-test pondéré) est utilisé pour évaluer la significativité d'un signal pulsé dans les données γ. La pondération, soit la probabilité qu'un photon vienne du pulsar plutôt que d'autres sources, est obtenue à partir de la convolution du spectre avec la PSF.

En particulier, la correction de l'effet Doppler sur la dérivée de la période $\dot{P}$ de pulsar est présentée en détail et constitue ma contribution au 2PC. Cette correction est une combinaison de l'effet Shklovskii dû au mouvement propre du pulsar par rapport au soleil et à sa distance, et l'effet d'accélération dû à la rotation de notre Galaxie. La correction sur $\dot{P}$ est ensuite propagagée aux grandeurs dérivées telles que $\dot{E}$ (le taux de perte d'énergie rotationnelle), l'âge du pulsar et le champ magnétique à sa surface. Pour cela, j'ai compilé une bibliothèque pour 242 pulsars avec les mesures de mouvement propre dans la littérature. J'ai obtenu les meilleures valeurs disponibles pour la distance et le mouvement propre des pulsars millisecondes pour lesquels l'effet Doppler est important. Ce travail se reflète dans 2PC: Section 4.3, 6.3, Tableau 6 et Figure 11.

Le Chapitre 5 décrit les outils et les méthodes d'analyse des données de *Fermi*-LAT. L'analyse spectrale est basée sur la méthode du maximum de vraisemblance (l'outil *gtlike* des Science Tools, logiciels standards dévelopés par la collaboration *Fermi*). Les modélisations spectrales et spatiales de différentes sources et de l'émission diffuse à partir desquelles on extrait leurs contributions ainsi que les propriétés spectrales du pulsar d'intérêt sont présentées. Les paramètres de la courbe de lumière, tels que le nombre de pics, le décalage en phase entre les pics radio et γ (δ) et la séparation entre les pics γ (Δ) sont estimés via le fit du profil en employant différentes formes mathématiques.

La troisième partie présente les résultats de ce manuscrit. Dans le Chapitre 6, une étude multi-longueurs d'onde (radio, X et γ) de sept nouveaux pulsars faibles, dont quatre jeunes et trois millisecondes, détectés à l'aide des éphémerides radio et avec le H-test pondéré est présentée en détail. Ces pulsars sont faibles, voire juste à la limite de la sensibilité du LAT par rapport à la population de 2PC du fait de raisons diverses: (1) la luminosité $L_\gamma = 4\pi d^2 f_\Omega G_{100}$ (d est la distance du pulsar, G_{100} est le flux en énergie γ, et f_Ω est le facteur de beaming qui décrit la géométrie du rayonnement dans le ciel. $f_\Omega = 1$ dans 2PC) baisse avec $\dot{E} = 4\pi^2 I\dot{P}/P^3$ (I est le moment d'inertie du pulsar, P est la période de rotation). Quelques pulsars sont près de la "ligne de l'extinction" ("deathline") γ empirique $\dot{E} \approx 3 \times 10^{33}$ erg s^{-1}. (2) ces pulsars se trouvent à grande distance, ce qui limite fortement le flux observé sur la Terre. (3) s'ils sont baignés dans des régions caractérisées par une forte émission diffuse, par exemple dans le plan galactique, leur flux sera faible devant le grand bruit

de fond. (4) lié à f_Ω, l'émission peut être ratée sur certaines lignes de visée, ou bien l'intensité d'émission est trop petite pour être détectée par le LAT.

La faiblesse de ces pulsars rend l'analyse difficile et moins précise. Dans notre échantillon, seuls les quatre pulsars jeunes sont ajustés avec une loi de puissance avec une coupure exponentielle, forme spectrale généralement utilisée pour les pulsars. Les trois pulsars millisecondes sont ajustés avec une loi de puissance simple, la coupure étant impossible à mesurer (Figure 6.3). Du côté des courbes de lumière, certains pulsars montrent des pics très larges et un peu compliqués, ce qui est rarement prédit par les modèles et rend la caractérisation du profile plus délicate (Figure 6.7, 6.10−6.16, Tableau 6.7). J'ai discuté la luminosité, "la ligne de l'extinction", la géométrie et la détectabilité impliquées par ces pulsars. Un bilan de mon analyse est présenté dans le Tableau 6.3. Mes nouvelles détections ont enrichi la population de 2PC et confirmé certaines propriétés observées. Par exemple, δ et Δ sont anti-corrélés (Figure 6.8), en gros L_γ est proportionnelle à $\sqrt{\dot{E}}$ (Figure 6.9), et le modèle "Cavité Externe" est généralement favorisé, etc. Tous mes résultats sont résumés dans un papier dédié.

Le Chapitre 7 est consacré à un échantillon de pulsars γ dans 2PC avec des efficacités $\eta = L_\gamma/\dot{E}$ peu plausibles (par exemple $\eta > 100\%$). Une telle grande efficacité peut indiquer que la distance d et/ou f_Ω sont surestimés, notons que G_{100} venant de l'analyse spectral est plutôt robuste. Une autre solution pour résoudre ce paradoxe est d'imaginer un plus grand moment d'inertie $I = KMR^2$ (M est la masse et R le rayon du pulsar). En étudiant ces paramètres qui influencent l'efficacité, un par un, en particulier en estimant la distance par différentes méthodes, par exemple l'émission en radio/rayon X d'hydrogène neutre (Figure 7.5−7.9), parallaxe (Figure 7.3), etc, j'ai identifié quelques pulsars comme candidats à un grand moment d'inertie. Une nouveauté dans notre approche est que le mouvement propre du pulsar, s'il est connu, fournit d'autres contraintes sur la distance, par la correction Doppler sur $\dot{P}$ et la vitesse spatiale du pulsar (Figure 7.4). Les mesures de grandes masses d'étoile à neutrons dans la littérature impliquent des plus grands moments d'inertie et favorisent les équations d'Etat (EOS) théoriques "rigides" des étoiles à neutrons. Mon étude suggère que les observations de *Fermi* en rayons γ pourraient apporter des contraintes indépendantes sur le moment d'inertie et donc sur les EOS des étoiles à neutrons.

En conclusion, d'une part, mes nouvelles détections de pulsars γ marquent la transition de la première phase (pulsars brillants) à la seconde phase (pulsars faibles) d'opération de *Fermi*. Elles permettent d'étendre la population actuelle de pulsars γ et de remplir les parties peu peuplées dans l'espace des paramètres, ainsi que de tester la "ligne de l'extinction". D'autre part, mon étude sur un échantillon de pulsars γ qui manifestent une grande efficacité montre que les observations de *Fermi* pourraient contraindre indépendament le moment d'inertie et les EOS des étoiles à neutrons, afin de comprendre la nature de la matière extrêmement dense.

En perspective, *Fermi* entre dans la deuxième moitié de sa mission de dix ans, les nouveaux pulsars à venir seront faibles, comme ceux étudiés dans cette thèse. Néanmoins, l'ensemble des données de *Fermi*-LAT sur cinq ans sera bientôt retraité avec *pass 8*, avec une meilleure surface efficace inférieur à 100 MeV, améliorant notre capacité à détecter des pulsars avec les coupures spectrales d'énergie faibles, comme c'est déjà le cas pour B1509−58 avec un grand champ magnétique. En outre, il faudra réévaluer les critères de détection (actuellement $> 5\sigma$ avec H-test) et la possibilité d'employer d'autres tests/stratégies statistiques afin d'obtenir l'échantillon de pulsars γ le plus complet possible. Une telle population est importante pour un recensement complet de la population d'étoiles à neutrons galactique. En plus, les pulsars non résolus contribuent à l'émission diffuse γ. Un échantillon de pulsar γ plus grand et plus complet permettra de clarifier la nature de la "bosse au GeV " récemment observée dans le centre de la Voie Lactée: de la matière noire ou des pulsars ?

Contents

INTRODUCTION

About fifty years have passed since the discovery of the first pulsar by J. Bell and A. Hewish in Cambridge in 1967. The ATNF[1] pulsar catalog tallies now more than 2000 pulsars. The majority emit electromagnetic waves at radio wavelengths, while some are also detected at optical wavelengths, X rays and γ rays. But, what are pulsars? Why are they interesting? Pulsars are rapidly rotating neutron stars born in the gravitational core collapse of massive stars ending their lives by a violent supernova explosion. The emission of pulsars is observed on Earth periodically when it crosses our line of sight, from which comes the name "Pulsating Source of Radio". The discovery of pulsars has offered the possibility to study physics in extreme conditions unattainable in any terrestrial laboratory: high matter density and high magnetic fields. This has opened the door to test general relativity in conditions of an intense gravitational field. Pulsars are also used to map the large-scale structure of the Galactic magnetic field and to probe the interstellar medium.

While radio pulsars dominate in numbers, the γ-ray pulsar sky is much brighter even with only ten detected in γ rays with EGRET aboard the Compton Gamma Ray Observatory before the launch of the *Fermi* satellite, given the much higher luminosity in γ rays than at radio wavelengths. Dedicated to γ-ray astronomy, *Fermi* was launched in June 2008. It is an international collaboration between the United States, Italy, Sweden, France, Germany and Japan. The Large Area Telescope (LAT), *Fermi*'s main instrument, is sensitive to γ rays from 20 MeV to over 300 GeV. Its field of view, effective area, temporal resolution and PSF (angular resolution) are better than those of EGRET. It is with *Fermi* that γ-ray pulsars have finally taken off their mysterious veil and embrace their Spring.

γ-ray pulsations from 148 (December 2013) pulsars have been discovered with the *Fermi*-LAT, 117 of which were presented in the second *Fermi*-LAT pulsar catalog. Pulsars are by far the largest GeV source class in the Milky Way. Pulsars with millisecond rotation periods have been for the first time established as γ-ray emitters and constitute one-third of the current *Fermi* pulsar sample. Currently all are radio-loud. The rest are young or normal pulsars which are further evenly divided into young radio-loud and young radio-quiet pulsars, the latter being discovered directly in *Fermi*-LAT data, in contrast to radio-loud ones for which radio ephemerides allowed the detections. The increasing number of γ-ray pulsars detected with *Fermi* offers an excellent opportunity to perform statistical studies of pulsar emission mechanisms and pulsar geometry. Pulse profile characterization and spectral analysis for the current sample favor γ-ray emission from the neutron star's outer magnetosphere, as opposed to emission from near the magnetic pole where radio and thermal X-ray signals originate. However, none of the current theoretical emission models are able to reproduce all the observed properties.

My thesis concerns data analysis for pulsars with the *Fermi*-LAT. But what is left for me when the bright pulsars have already been discovered in the first three years of observations? As we can imagine, new pulsars to come will be less bright, implying that the profile and spectral characterization will be more difficult and less precise. However, such faint pulsars will be valuable because they will probe under-sampled parts of parameter space. My thesis is therefore devoted to the study of faint pulsars with the *Fermi*-LAT. Parameters affecting pulsar detectability include the intrinsic γ-ray luminosity, which translates to the observed flux, depending partly on pulsar distance and sky location, the pulsar geometry represented by the beaming factor, and the pulse profile shape. The newly discovered pulsars in this thesis have a lower signal-to-noise ratio which may be due to various reasons: they have low spin-down power with which the γ-ray luminosity decreases; they are farther which makes the observed flux weak; they are in regions characterized by strong diffuse emission, their flux is small compared to the large background noise; and possibly the geometry configuration makes the emission intensity be too low to be detected earlier in the *Fermi* mission. We will be able to, for example, from the study of pulsars with low spin-down power, test the predictions of different models for the "deathline", the minimum power required to generate γ-ray emissions. Unbiased popu-

[1] A list of acronyms and abbreviations is included on the last page of this manuscript.

lation syntheses will benefit from more detections of such faint pulsars in the future. The more complete pulsar sample with such faint pulsars added may be able to provide strong constraints on theoretical models.

In the first part of this manuscript, I first introduce some general properties of neutron stars/pulsars, their formation, category, etc. Then I present theoretical and observational aspects of γ-ray pulsars by describing briefly different γ-ray emission models and a summary of the *Fermi* γ-ray pulsar characteristics based on the second *Fermi*-LAT pulsar catalog.

The second part is dedicated to the instrument which has made the current observations possible. After presenting the detection principle, main components and the performance of the *Fermi*-LAT, I introduce the pulsar timing and γ-ray pulsar searching techniques employed in this thesis. *Fermi*-LAT data analysis tools and methods follow naturally leading to the last part of this manuscript, the results.

Two main works constitute the results. The first focuses on detections of seven faint γ-ray pulsars after the second *Fermi*-LAT pulsar catalog. Detailed spectral analysis and light curve characterizations will be presented and compared to the catalog population. The second one concerns possible constraints on the moment of inertia of neutron stars by studying a sample of γ-ray pulsars in the second *Fermi*-LAT pulsar catalog which exhibit implausible γ-ray efficiency.

Publications

- X. Hou *et al.*, *Six Faint Gamma-ray Pulsars Seen with the Fermi Large Area Telescope: Towards a Sample Blending into the Background*, A&A, 2014, submitted.
- X. Hou *et al.*, *Beyond the 2nd Fermi Pulsar Catalog*, Astron. Nachr. /AN 335, No. 3, 334, 2014, arXiv:1310.5481.
- A. A. Abdo, *et al.* (*Fermi*-LAT Collaboration), *The Second Fermi Large Area Telescope Catalog of Gamma-ray Pulsars*, ApJS, 208, 17, 2013.
- C. M. Espinoza, L. Guillemot, ..., X. Hou, ... *et al.*, *Six millisecond pulsars detected by the Fermi Large Area Telescope and the radio/Gamma-ray connection of millisecond pulsars*, MNRAS 430, 571-587, 2013.
- T. J. Johnson, C. Venter, ... X. Hou, ... *et al.*, *Light Curve Modeling of Gamma-ray Millisecond Pulsars from the Second LAT Pulsar Catalog*, ApJ, 2013, submitted.
- X. Hou *et al.*, *Tracking Down the Highest Spindown Power Gamma-ray Pulsars*, in proceedings of 2011 Fermi Symposium, Rome, Italy. arXiv:1110.1210.

Other publications

- A. Allafort *et al.* (*Fermi*-LAT Collaboration), *PSR J2021+4026 in the Gamma Cygni Region: The First Variable γ-ray Pulsar Seen by the Fermi-LAT*, ApJ, 777L, 2, 2013.
- F. Acero. *et al.* (*Fermi*-LAT Collaboration), *Constraints on the Galactic Population of TeV Pulsar Wind Nebulae Using Fermi Large Area Telescope Observations*, ApJ, 773, 77, 2013.
- M. Ackermann *et al.* (*Fermi*-LAT Collaboration), *Search for Gamma-ray spectral lines with the Fermi Large Area Telescope and dark matter implications*, PhRvD, 88h2002, 2013.

- M. Ackermann *et al.* (*Fermi*-LAT Collaboration), *The Fermi All-sky Variability Analysis: A List of Flaring Gamma-ray Sources and the Search for Transients in Our Galaxy*, ApJ, 771, 57, 2013.
- M. Ackermann *et al.* (*Fermi*-LAT Collaboration), *Determination of the Point-spread Function for the Fermi Large Area Telescope from On-orbit Data and Limits on Pair Halos of Active Galactic Nuclei*, ApJ, 765, 54, 2013.
- M. Ackermann *et al.* (*Fermi*-LAT Collaboration), *Fermi Large Area Telescope Study of Cosmic-Rays and the Interstellar Medium in Nearby Molecular Clouds*, ApJ, 778, 82, 2013.
- M. Ackermann *et al.* (*Fermi*-LAT Collaboration), *The First Fermi-LAT Gamma-ray Burst Catalog*, ApJS, 209, 11, 2013.
- H. J. Pletsch *et al.* (*Fermi*-LAT Collaboration), *Binary Millisecond Pulsar Discovery via Gamma-ray Pulsations*, Science, 338,1314, 2012.
- M. Ackermann *et al.* (*Fermi*-LAT Collaboration), *The Fermi Large Area Telescope on Orbit: Event Classification, Instrument Response Functions, and Calibration*, ApJS, 203, 4, 2012.
- A. A. Abdo, *et al.* (*Fermi*-LAT Collaboration), *Fermi Observations of γ-ray Emission from the Moon*, ApJ, 758,140, 2012.
- M. Ackermann *et al.* (*Fermi*-LAT Collaboration), *Gamma-ray Observations of the Orion Molecular Clouds with the Fermi Large Area Telescope*, ApJ, 756, 4, 2012.
- M. Ackermann *et al.* (*Fermi*-LAT Collaboration), *A Statistical Approach to Recognizing Source Classes for Unassociated Sources in the First Fermi-LAT Catalog*, ApJ, 753, 83, 2012.
- M. Ackermann *et al.* (*Fermi*-LAT Collaboration), *Fermi-LAT Observations of the Diffuse γ-ray Emission: Implications for Cosmic Rays and the Interstellar Medium*, ApJ, 750, 3, 2012.
- M. Ackermann *et al.* (*Fermi*-LAT Collaboration), *Anisotropies in the diffuse Gamma-ray background measured by the Fermi LAT*, PhRvD, 85h3007, 2012.
- P. L. Nolan *et al.* (*Fermi*-LAT Collaboration), *Fermi Large Area Telescope Second Source Catalog*, ApJS, 199, 31, 2012.
- M. Ackermann *et al.* (*Fermi*-LAT Collaboration), *Search for Dark Matter Satellites Using Fermi-LAT*, ApJ, 747, 121, 2012.
- M. Ackermann *et al.* (*Fermi*-LAT Collaboration), *The Second Catalog of Active Galactic Nuclei Detected by the Fermi Large Area Telescope*, ApJ, 743, 171, 2011.

PART I

AN OVERVIEW OF THE PULSARS

CHAPTER 1

From neutron stars to pulsars

Contents

1.1 Discovery

Pulsars were one of the most remarkable discoveries in astronomy in the 1960. Although the observational techniques in radio astronomy underwent great improvements before the 1960s leading to various unexpected discoveries, it wasn't until 1967 that the first pulsar, named PSR B1919+21 or PSR J1921+2153[1], was detected by Antony Hewish and his student Jocelyn Bell in Cambridge (Hewish *et al.* 1968). Just as some discoveries in the history, this pulsar was discovered by chance when they were initially studying interplanetary scintillation[2] using a telescope sensitive to weak discrete radio sources. Jocelyn Bell first noticed the unusual periodic signal and rechecked with Antony Hewish using a recorder with an even faster response time. In November, the "little green man" (a play name for extraterrestrial intelligent beings they called it at first) was finally confirmed as a new celestial source which emitted such signals with an extremely stable period of 1.337 seconds (Hewish *et al.* 1968).

It's now well known that pulsars are highly magnetized, rotating neutron stars (Section 1.2, 1.3). Interestingly, more than 30 years before, the existence of neutrons stars had already been proposed by Walter Baade and Fritz Zwicky in 1934 (Baade & Zwicky 1934), just two years after the discovery of neutrons. A

[1]PSR denotes "Pulsating Source of Radio". B and J correspond respectively to the equatorial coordinate systems (B1950 and J2000), with 1919 (or 1921) and +21 (or +2153) coordinates of the pulsar (right ascension of 19h19' and declination of $+21^\circ$).

[2]Variation of radio signal strength due to the refraction in the terrestrial ionosphere, in the ionised interplanetary gas in the Solar system and in the ionised interstellar gas of the galaxy.

few years later, predictions of the physical conditions inside a neutron star were also made by Oppenheimer & Volkoff (1939). Unfortunately, these theoretical works were almost ignored by radio astronomers who didn't expect to detect radio emissions from such sorts of strange objects.

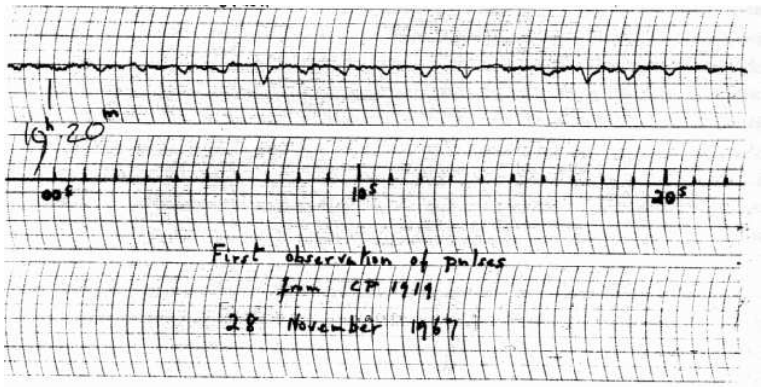

Figure 1.1: This first record of pulsation of the first pulsar PSR B1919+21 discovered in November 28, 1967 (Hewish *et al.* 1968).

The firm identification of the 1.337 second pulsar as a neutron star was not established until the end of 1968. The reason is that theories of white dwarfs could explain pulsars with periods of about 1 second (Meltzer & Thorne 1966), even though Pacini had shown before the discovery of PSR B1919+21 that a rapidly rotating neutron star with a strong magnetic field could be the source of energy for radiation from the Crab nebula (Pacini 1967). Independently and shortly after the discovery of the pulsar, Gold (1968) also clearly proposed the concept of pulsars as neutron stars. The discovery of the Vela pulsar with a period of 89 ms in the Vela supernova remnant (Large *et al.* 1968) and the 33 ms Crab pulsar in the Crab nebula (Staelin & Reifenstein 1968) then finally cleared of the confusion and provided a dramatic verification of the Baade-Zwicky prediction.

1.2 Neutron Stars

1.2.1 Formation and structure

Neutron stars are stellar remnants that can be understood in the context of stellar evolution. After a star was formed from collapsing clouds of gas and dust, it enters the *main sequence* in the Hertzsprung-Russell diagrams (Russell 1921) if its mass is higher than ~ 0.08 of the solar mass $M_\odot$. The nuclear fusion of hydrogen into helium begins in the core of the star. The stability of the star is maintained by a hydrostatic equilibrium, where the radiation pressure exerted by the released energy in the core balances the star's gravity. When the core exhausts its hydrogen, the star evolves off the *main sequence* and the core contracts due to insufficient outward pressure to counteract the gravity.

Further evolution depends upon the star's mass. For massive stars ($M > 8\ M_\odot$), if the temperature of the core is high enough, the nuclear fusion of heavier elements occur successively: ${}^{1}_{1}\mathrm{H} \rightarrow {}^{4}_{2}\mathrm{He} \rightarrow {}^{12}_{6}\mathrm{C} \rightarrow {}^{20}_{10}\mathrm{Ne} \rightarrow {}^{16}_{8}\mathrm{O} \rightarrow {}^{31}_{14}\mathrm{Si}$, releasing energy to sustain the hydrostatic equilibrium (Woosley *et al.* 2002). The star contracts progressively due to less and less energy produced by such fusion of heavier and heavier elements and the core becomes denser and denser (Burbidge *et al.* 1957). When the temperature attains $\sim 3 \times 10^9$ K, silicon fuses to form iron ${}^{56}\mathrm{Fe}$. Since the fusion of iron is endothermic, the hydrostatic equilibrium can't be maintained any more, and the star is mainly composed of a high density iron core and free electrons (Giacobbe 2003). These electrons obeying the *Pauli exclusion principle* are forced to occupy higher and

higher quantum states as the density increases, yielding the electron degeneracy pressure which resists the collapse of the star (see e.g. Kothari & Singh 1938).

The combustion of other lighter elements around the core increases the density and brings free electrons to higher and higher quantum states continuously. When the density reaches $\rho \sim 10^7$ g cm^{-3}, the *neutronisation* occurs through the inverse β decay (or electron capture: $p^+ + e^- \rightarrow n + \nu_e$) which converts protons to neutrons and emits neutrinos (Bisnovatyi-Kogan & Seidov 1970). This reduces dramatically the electron degeneracy pressure which is now insufficient to resist the gravity. The star collapses if the mass of the core exceeds the Chandrasekhar limit[3] (~ 1.4 M$_\odot$, Chandrasekhar 1935). The gravitational collapse creates a shock expelling the outer layers of the star in the interstellar medium, which is known as Type II supernova (Baade & Zwicky 1934; Cappellaro & Turatto 2001) explosions. At $\rho \sim 4 \times 10^{11}$ g cm^{-3}, neutrons are ejected from nucleus creating the *neutron drip* (Pethick *et al.* 1995). These neutrons are free and stable, the degeneracy pressure of which resists further collapse by the *Pauli exclusion principle*, similar to but stronger than that of electrons. A neutron star is formed. With a birth rate of $\sim$1 Type II supernova per century (see e.g. Cappellaro *et al.* 1999; van den Bergh & Tammann 1991; Strom 1994), there are $\sim 10^8$ neutron stars in the Milky Way.

An alternate scenario to explain the neutron star formation proposes that a white dwarf[4] in a binary system accretes matter from its companion (van den Heuvel *et al.* 1992), and when the mass exceeds the Chandrasekhar limit, a neutron star is created from the supernova Type Ia (Cappellaro & Turatto 2001) explosion of the white dwarf.

In general, a neutron star consists of five major regions (Figure 1.2, Lattimer & Prakash 2004): the inner and outer cores, the crust, the envelope and the atmosphere. The mass contained in the last two regions is negligible. The crust, with a thickness of about $1-2$ km, is rich in ion nuclei ($56 \leq Z \leq 200$) which varies with density. The density in the outer crust is $\sim 10^6$ g cm^{-3} and increases with depth. The interface of the outer-inner crust is characterized by the *neutron drip* point, which results in a neutron superfluid in the inner crust. 99% of the mass of the star comes from the core. A soup of neutron superfluid, proton superconductor, electrons and muons forms in the outer core. For the inner core, some models predict the existence of exotic particles in the form of hyperons/Bose condensate (pions or kaons), or deconfined quark matter (Glendenning 1992). The latter forms the hypothetical "strange quark matter" (SQM) stars[5] (Alcock & Olinto 1988) as distinguished from the "normal neutron stars".

With a mass of the order of 1.4 M$_\odot$, a radius of ~ 12 km, and a central density $\rho \sim 4 \times 10^{15}$ g cm^{-3}, neutron stars are the most compact objects known in our Universe, just after black holes[6]. They serve as an ideal laboratory with extreme physical conditions unachievable on Earth for dense matter physics.

1.2.2 Mass, radius and equations of state

The global properties of neutron stars, such as the mass-radius relation, are determined by the equation of state (EOS), i.e. the pressure-density $P-\rho$ relation in hydrostatic equilibrium. By solving the Einstein equations in the context of General Relativity (GR), we have the TOV (Tolman-Oppenheimer-Volkov)

[3]Named after the Indian-American astrophysicist Subrahmanyan Chandrasekhar, the Chandrasekhar limit represents the mass above which the electron degeneracy pressure in the core is insufficient to balance the star's gravitational self-attraction.

[4]A stellar remnant which is formed when the star has exhausted its fuel of hydrogen and helium through nuclear fusion, but the core is not heavy enough to become a neutron star. The stability of the white dwarf is maintained by the electron degeneracy pressure which balances the gravity. The maximum mass of a white dwarf is the Chandrasekhar limit.

[5]SQM stars have either a bare quark matter surface composed of up, down and strange quarks, or a tiny layer of nucleons. Such stars are self-bound unlike normal stars which are gravitationally bound.

[6]When the stellar remnant mass is higher than $\sim 2-3$ M$_\odot$, the neutron degeneracy pressure is insufficient to prevent the gravitational collapse below the Schwarzschild radius to form a black hole. Schwarzschild radius specifies the radius of a sphere that, with all the mass of an object within it, the escape speed from the surface of the sphere would equal the speed of light. Light and matters cannot escape and flow from the interior of a black hole and the object is no longer visible.

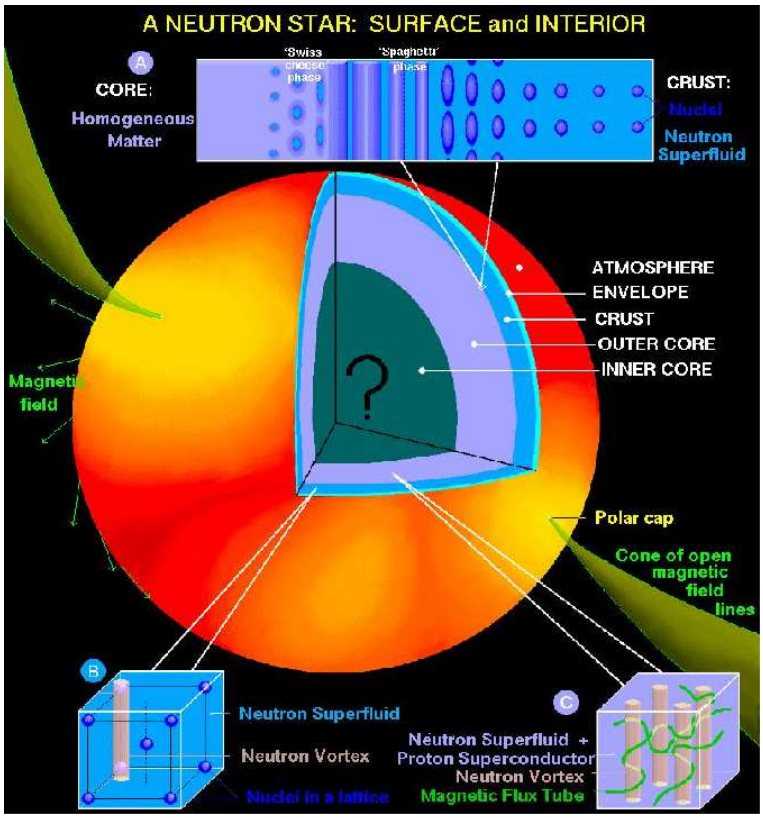

Figure 1.2: Representation of neutron star surface and interior structure (Lattimer & Prakash 2004, from courtesy D. Page).

equations (Tolman 1934; Oppenheimer & Volkoff 1939):

$$\frac{dP}{dr} = -\frac{G(m(r)+4\pi r^3 P/c^2)(\rho+P/c^2)}{r(r-2Gm(r)/c^2)}$$

$$\frac{dm(r)}{dr} = 4\pi\rho r^2 \tag{1.1}$$

with $G = 6.67384\times10^{-11}$ m^{3}kg^{-1}s^{-1} Newton's gravitational constant and $m(r)$ the gravitational mass contained within a radius r. Figure 1.3 (A) shows the Mass-Radius diagram for different type of EOS. Blue curves are for nucleons; pink for nucleons plus exotic particles; green for strange quark matter. The upper dark region is excluded by the Schwarzschild condition $R \geq 2GM/c^2$ in GR. The first gray region followed is ruled out by the condition that the central pressure $p < \infty$ ($R \geq 2.25GM/c^2$). The second gray region is excluded by causality $R \geq 3GM/c^2$ (Lattimer *et al.* 1990), i.e. the speed of sound in the dense matter is smaller than the speed of light. Another constraint on the EOS follows from the rotation of neutron stars (lower gray region). The Keplerian, or mass-shedding, rotational limit is obtained when the equatorial surface velocity equals that of a particle orbiting just above the surface. The minimum rotation period has the same scaling $P_{\rm min} \propto \sqrt{R^3/M}$ in both Newtonian and GR cases. For a star of an arbitrary mass $M_{\rm sph}$ and a nonrotating radius $R_{\rm sph}$, an empirical formula (Lattimer *et al.* 1990) is:

$$P_{\rm min} \simeq (0.96\pm0.03)\left(\frac{M_\odot}{M_{\rm sph}}\right)^{1/2}\left(\frac{R_{\rm sph}}{10\,{\rm km}}\right)^{3/2}\ {\rm ms} \tag{1.2}$$

which is useful to constrain the mass and radius of observed neutron stars:

$$R_{\rm sph} < 10.4 \left(\frac{1000\,{\rm Hz}}{\nu}\right)^{2/3} \left(\frac{M_{\rm sph}}{{\rm M}_\odot}\right)^{1/3} {\rm km} \tag{1.3}$$

Taking the most rapidly known rotating pulsar PSR J1748−2446ad[7] (Hessels *et al.* 2006) with a spin rate ν of 716 Hz, it follows that the non-rotating radius $R_{\rm sph} < 14.3$ km for a 1.4 $M_\odot$ star (lower gray region in Figure 1.3 (A)).

For normal neutron stars ("rigid" EOS with higher density, blue curves), the radius has relatively little dependence on the mass in the range of about 0.5 to 2 $M_\odot$ unless the maximum mass is small (e.g. MS1, FSU, PAL6). In the case of normal stars with exotic particles, the EOS (e.g. GS1, GM3) have considerable softening and relatively small radius and maximum mass. SQM stars are almost incompressible for small masses. Raising the maximum mass could eliminate whole families of EOS, especially the ones with exotic particles and substantial softening. The mass measurement thus plays a key role. Lattimer & Prakash (2001) established an empirical relation between radius and pressure (Equation 5 in the article) which might provide constraints on the EOS from a single measurement of a neutron star's radius, rather than requiring a simultaneous measurement of mass-radius as proposed by Lindblom (1992).

The most accurate method of mass measurement is from radio timing (Section 4.1) of binary pulsars (Section 1.4), which may include pulsars orbiting around another neutron star, a white dwarf, or a main sequence star. In some cases, the detection of relativistic effects, such as the Shapiro delay (Shapiro 1964, Section 4.1), is possible. For highly inclined (nearly edge-on) binary pulsar systems, this allows the measurement of both masses in the binary to high precision (Verbiest *et al.* 2008; Demorest *et al.* 2010). Another method to estimate masses is from X-ray binaries in which the pulsar is accreting matter from its stellar companion, but this approach usually comes with bigger error bars. Masses can also be estimated from spectroscopy/photometry if the companion star is visible at optical wavelengths (see e.g. van Kerkwijk *et al.* 2011; Romani *et al.* 2012).

It's more and more evident that neutron star masses in binaries with white dwarf companions have a broader range than in other binaries, suggesting that neutron stars may be heavier than the canonical 1.4 $M_\odot$. Table 1.1 lists some high mass neutron stars, indicating also whether they are γ-ray pulsars. The maximum mass (above which the neutron star collapses to a black hole) allowed for neutron stars is $3M_\odot$, coming from causality (Rhoades & Ruffini 1974), while the lower limit of the maximum mass is the highest and most accurate measurements in the literature for J0348+0432 (Antoniadis *et al.* 2013) and J1614−2230 (Demorest *et al.* 2010) of ~ 2 $M_\odot$. Shown as the red horizontal band in Figure 1.3 (A), the precise mass measurement of J1614−2230 seems to favor "normal matter" hadronic EOS. The strange quark matter EOS are highly constrained, but not totally excluded. Some authors explored the possibility of exotic and strange quark matter EOS through the fine tuning of model parameters (see e.g. Lai & Xu 2011; Bednarek *et al.* 2012; Weissenborn *et al.* 2012). The radius is limited to be in the range of $11 - 15$ km. This measurement implies the existence of more massive neutron stars with more confidence.

Note that the mass distribution depends slightly on the type of neutron stars (recycled, young or non-recycled, binaries with double neutron stars, or with white dwarf, Section 1.4), but the mean mass lies in a narrow range of ~ 1.2 $M_\odot$ to ~ 1.5 $M_\odot$ (Özel *et al.* 2012b). For a relatively full list of mass measurements of neutron stars, refer to e.g. Lattimer & Prakash (2007), Özel *et al.* (2012b). The existence of high mass neutron stars would imply larger moments of inertia (Section 1.2.3), for which independent constraints may be obtained from *Fermi* γ-ray observations of pulsars that will be detailed in Chapter 7.

Upper limits on the radius come from GR, causality and rotation as described previously. Significant progress in constraints on the radius has been made available only recently through observations of the X-ray thermal emission from neutron stars. This involves three major approaches. One is the spectroscopic

[7]Letters at the end of the pulsar name mean it is either in a double pulsar system, or in a globular cluster where they have the same coordinates. The letters begin from A to Z, and after Z, from aa to az, then from ba to bz, etc.

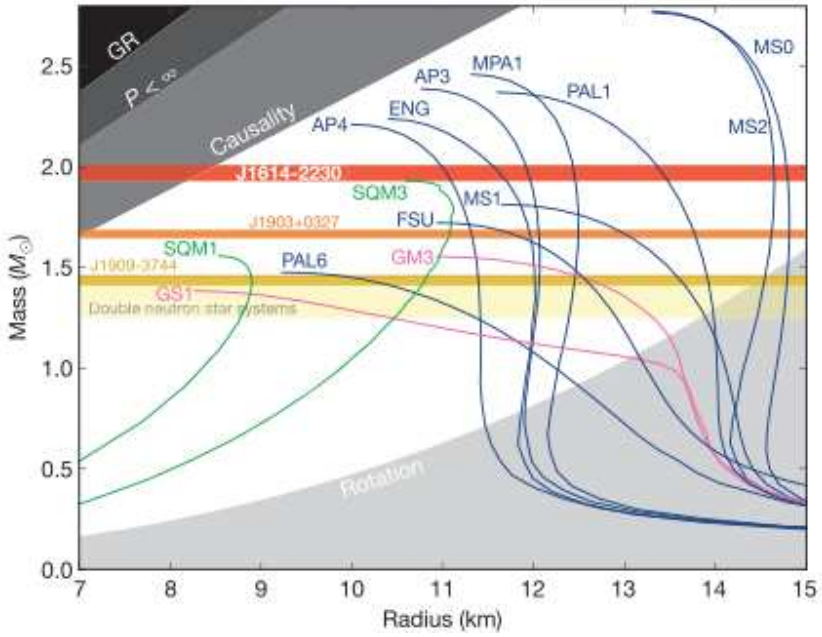

(A) Mass−Radius diagram for typical EOSs

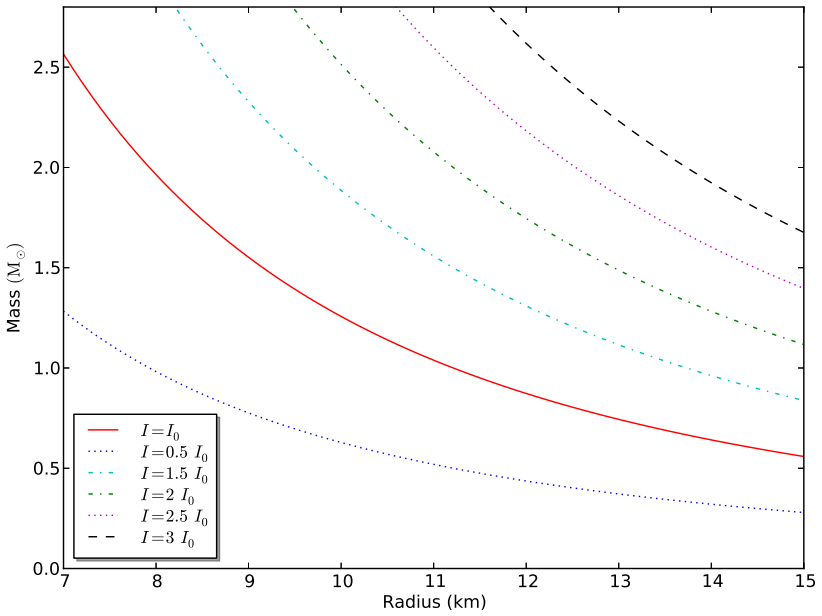

(B) Mass−Radius relation for different moments of inertia

Figure 1.3: (A) : Mass−Radius relation for different EOS (Demorest *et al.* 2010; Lattimer & Prakash 2007). Blue, nucleons; pink, nucleons plus exotic particles; green, strange quark matter. The grey regions are ruled out by theoretical or observational constraints (see text). (B) : Curves representing $I = 0.4MR^2$, for different values of the moment of inertia I around $I_0 = 10^{45}$ g cm^2. Adapted from Guillemot (2009).

Pulsar	M_1 ($M_\odot$)	M_2 ($M_\odot$)	Method	γ–ray?	Ref.
J0348+0432	2.01 ± 0.04	0.172 ± 0.003 (WD)	SP/PH/RT	No	Antoniadis *et al.* (2013)
J0437−4715	1.76 ± 0.20	$0.25(WD)$	RT	Yes	Verbiest *et al.* (2008)
J0621+1002	$1.70^{+0.32}_{-0.29}$	$0.97^{+0.27}_{-0.15}$(WD)	RT	No	Splaver *et al.* (2002)
J0751−1807	2.1 ± 0.2	0.19 ± 0.02(WD)	RT	Yes	Nice *et al.* (2005)
J1311−3430	>2.1	0.01(BD)	SP/PH	Yes	Romani *et al.* (2012)
J1614−2230	1.97 ± 0.04	0.5(WD)	RT	Yes	Demorest *et al.* (2010)
J1903+0327	1.67 ± 0.02	~ 1(MS)	RT	No	Freire *et al.* (2011b)
J1959+2048	2.40 ± 0.12	0.01(WD)	SP/PH	Yes	van Kerkwijk *et al.* (2011)

Table 1.1: Some high mass neutron stars. WD: white dwarf; BD: brown dwarf; MS: main sequence star; RT: radio timing; SP/PH: spectroscopy/photometry.

modelling of quiescent low-mass X-ray binaries[8] in globular clusters (Rutledge *et al.* 2001; Heinke *et al.* 2006; Webb & Barret 2007; Guillot *et al.* 2011, 2013). The second concerns the spectroscopic observations on the thermonuclear X-ray bursts[9] (Özel *et al.* 2009, 2012a; Zamfir *et al.* 2012; Güver *et al.* 2012a,b; Güver & Özel 2013). These work put the radius to be in the range of $8-12$ km, which is consistent with low radius "normal matter" EOS (e.g. AP3, AP4, ENG in Figure 1.3 (A)), but also with "strange quark matter" EOS (SQM3 in Figure 1.3 (A)). Systematic uncertainties on the spectroscopic determination of neutron star radius are less than 10% as demonstrated by Güver *et al.* (2012a,b) based on a population study of thermonuclear X-ray bursts. The last approach combines the X-ray spectroscopic and timing observations for pulsed emission from neutron stars, as was done for the pulsar J0030+0451 (Bogdanov & Grindlay 2009) and J0437−4715 (Bogdanov 2013). These studies placed constraints on the neutron star radius of $R > 10.7$ km and $R > 11.1$ km respectively, favoring the "rigid" EOS.

1.2.3 Moment of inertia

The moment of inertia, defined as $I = kMR^2$, is another observable variable of neutron stars. Figure 1.4 displays the moment of inertia in units of MR^2 (i.e. k) as a function of M/R for different families of EOS. The value of the moment of inertia generally used is $I_0 = 10^{45}$ g cm^2, for the case of a sphere of uniform density, $k = 0.4$ and assuming $M = 1.4$ M$_\odot$ and $R = 10$ km. The ~ 2 M$_\odot$ PSR J1614−2230 in Section 1.2.2 limits the radius to be in the range of $11-15$ km. This mass and radius can be translated to a M/R between 0.13 and 0.18. On the other hand, since all the EOS involving exotic particles (e.g. GS1, GM3) and some "rigid" ones (e.g. MS1, PAL6) are ruled out by this mass measurement, one can read from Figure 1.4 that $k \sim 0.45-0.48$ for $R = 11$ km and $k \sim 0.38-0.48$ for $R = 15$ km. Taking $M = 1.4$ M$_\odot$, the moment of inertia is then 1.4 to $2.7I_0$. The possibility of larger moments of inertia is thus favoured by the mass measurement of PSR J1614−2230. In Chapter 7, we will explore whether γ-ray observations support this. Figure 1.3 (B) shows the mass-radius relation for different values of moment of inertia $I = 0.4MR^2$ around I_0.

[8]Instead of having persistent X-ray luminosity, they show alternate period of high luminosity state (outbursts) and low luminosity state (quiescent) which last, respectively, weeks or months and years. This is proposed to be caused by the oscillation of accreting disk between a cold neutral state (quiescent) and a hot ionized state (outbursts) (Lasota 2001).

[9]When the matter accreted onto the neutron star surface from its companion is sufficiently thick, the nuclear fusion starts. The helium ignition gives rise to an increase in the temperature and a sudden rise in the X-ray flux, creating a thermonuclear X-ray bursts. See Lewin *et al.* (1993) for a review.

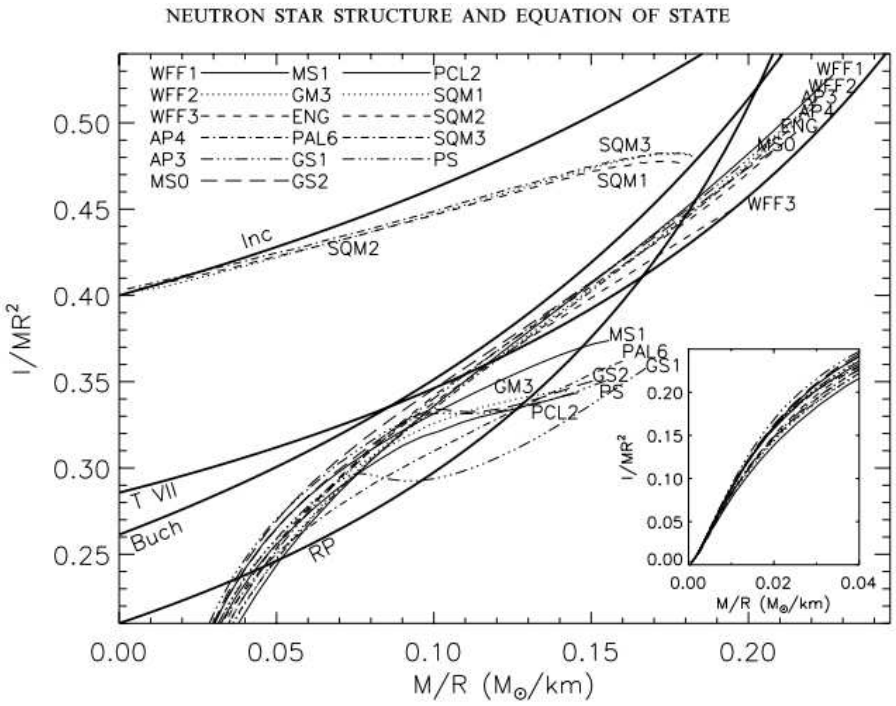

Figure 1.4: Neutron star moment of inertia I, in units of MR^2 for different EOS (Lattimer & Prakash 2001).

1.3 General properties of pulsars

1.3.1 Rotation and spin-down

Pulsars are highly magnetized rotating neutron stars. The angular momentum $I\Omega$ with $\Omega = 2\pi/P$ (rotational angular velocity, P is the rotation period and I is the moment of inertia) and the magnetic flux $\phi \propto BR^2$ of the parent massive star are assumed to be conserved during the gravitational core collapse. Assuming an initial period $P_0 \sim 10^6$ s (as for the Sun) and an initial magnetic field $B_0 = 100$ Gauss (10^{-2} Tesla), the resulting rotation period is of order of 10 ms and the magnetic field B of order of 10^{12} Gauss.

Pulsars are observed to slow down with time, loosing their rotational kinetic energy $E = \frac{1}{2}I\Omega^2$, considering the pulsar as a solid rotator with moment of inertia I. The rate of loss of E, called "*spin-down power*" is:

$$\dot{E} \equiv -\frac{dE}{dt} = -I\Omega\dot{\Omega} = 4\pi^2 I\dot{P}P^{-3} \simeq 3.95 \times 10^{31}\,\mathrm{erg\ s^{-1}} \left(\frac{P}{\mathrm{s}}\right)^{-3} \left(\frac{\dot{P}}{10^{-15}}\right) \tag{1.4}$$

with $\dot{P} = dP/dt$ the "*spin-down rate*" and by adopting the canonical moment of inertia $I_0 = 10^{45}$ g cm^2.

The rotational energy is mostly converted to the magnetic dipole radiation and an outflow of charged particles (mostly electrons, with some protons) forming a relativistic wind, as will be discussed in Section 1.3.2.

1.3.2 Dipole model

In the basic dipole model, pulsars are viewed as magnetized rotating superconducting spheres emitting dipole radiation in a vacuum (Deutsch 1955). However, Goldreich & Julian (1969) demonstrated that in the case of a neutron star with aligned rotation and magnetic axes (inclination $\alpha = 0$, Figure 1.7), the vacuum

condition could not be maintained. For a perfect conductor, the magnetic dipole $\vec{B}$ rotating with angular velocity $\vec{\Omega}$ induces an electric field $\left(\vec{\Omega}\times\vec{r}\right)\times\vec{B}$ which will be balanced by the distribution of charges within the sphere at any distance $\vec{r}$:

$$\vec{E}_{\rm int}+\frac{1}{c}\left(\vec{\Omega}\times\vec{r}\right)\times\vec{B}_{\rm int}=0 \tag{1.5}$$

with $\vec{B}_{\rm int}$ the internal magnetic field without rotation and $\vec{r}$ the vector at a given position inside the star. A force-free state ($\vec{E}\cdot\vec{B}=0$ following Equation 1.5) is maintained inside the star. However, in the surface charge layer, this is not true if the pulsar is surrounded by a vacuum. If it is in a vacuum, an electric potential field will appear at the surface and in consequence the appearance of an electric field parallel to the magnetic field given by:

$$E_{\parallel}=\frac{\vec{E}\cdot\vec{B}}{B}|_{r=R}=-\frac{\Omega B_0 R}{c}\cos^3\theta \tag{1.6}$$

where (r,θ) are polar coordinates in a coordinate system centred on the star, R is the neutron star radius and B_0 is the magnetic field at the pole. The resulting electric force $F=qE_{\parallel}$ at the stellar surface is so intense (≥ 10 times gravity) that the charged particles are extracted from the surface and a magnetosphere of plasma is created. The star is then not in a vacuum. The charge distribution in the magnetosphere given by:

$$\rho(r,\theta)=\frac{1}{4\pi}\vec{\bigtriangledown}\cdot\vec{E}=-\frac{\vec{\Omega}\cdot\vec{B}}{2\pi c}=-\frac{\Omega B_0 R^3}{4\pi c r^3}(3\cos^2\theta-1)\equiv\rho_{\rm GJ} \tag{1.7}$$

will screen the parallel electric field $E_{\parallel}$ and therefore the force-free state of Equation 1.5 is also reached outside the star. The net number density at the magnetic pole ($r=R,\theta=0$), known as the *Goldreich-Julian* density represents a maximum value in this basic picture:

$$n_{\rm GJ}=\frac{\rho_{\rm GJ}}{e}\simeq 7\times10^{10}{\rm cm}^{-3}\left(\frac{P}{\rm s}\right)^{-1/2}\left(\frac{\dot{P}}{10^{-15}}\right)^{1/2} \tag{1.8}$$

The plasma co-rotates with the neutron star out to the imaginary "*light cylinder*" surface at a distance of $r_c=cP/(2\pi)$ where the co-rotation speed reaches the speed of light c. As shown in Figure 1.5, the magnetic field lines confined in the light cylinder are closed, while others are "obliged" to extend out of the light cylinder creating the open field line region. Goldreich & Julian (1969) noted that the above charge density is only applicable to the co-rotating part of the magnetosphere which is bounded by the last open field lines. In the open filed line region, charged particles are accelerated to relativistic velocity and can escape, along the open field lines, from the star pole, emitting photons and forming a narrow beam centred on the magnetic axis, which can be observed in a periodic way when pointing toward the Earth. This accounts for the basic observation of radio emission first detected. High energy emission of pulsars requires more complicated geometry modelling and will be addressed in Section 2.1.

As shown above, Goldreich & Julian (1969) demonstrated that the surrounding of a pulsar is not a vacuum by studying the special case of an aligned rotator. Although not realistic, it provides some basic concepts that are helpful to understand pulsars. The more general and realistic case where inclination $\alpha\neq0$ is on the other hand solved numerically (see e.g. the MHD[10] approach of Spitkovsky 2006).

Assuming that the pulsar spin down purely due to the dipole radiation, i.e. a rotating magnetic dipole radiates at its rotation frequency *in the vacuum*, we have (Jackson 1999):

$$\dot{E}=-I\Omega\dot{\Omega}=\frac{2}{3c^3}\vec{\mu}^2\Omega^4\sin^2\alpha=\dot{E}_{\rm dipole} \tag{1.9}$$

[10]MHD: Magnetohydrodynamics, is the study of the dynamics of electrically conducting fluids, like plasmas, etc. The basic idea is that the magnetic field induces currents in the conductive fluid, which in turn creates forces on the fluid and also changes the magnetic field itself.

with $\vec{\mu}$ the dipole moment of the pulsar and α the inclination ($\alpha \neq 0$, otherwise no radiation). This results in:

$$\dot{\Omega} = -\left(\frac{2\vec{\mu}^2 \sin^2 \alpha}{3Ic^3}\right)\Omega^3 \tag{1.10}$$

As described above, the existence of a magnetosphere (i.e. *not in the vacuum*) can lead to spin down too, even for an aligned rotator $\alpha = 0$. This indicates that other mechanisms, like an outflowing charged particle wind, is also responsible for the rotational kinetic energy loss. In fact, we can generalize Equation 1.10 as:

$$\dot{\Omega} = -K\Omega^n \tag{1.11}$$

with n the *braking index* and K a constant. n can in principle be determined by measuring Ω, $\dot{\Omega}$ and $\ddot{\Omega}$ with pulsar timing (Section 4.1). However, in practice, $\ddot{\Omega}$ due to dipole braking is smaller compared to other long-term effects, and n is measured for few pulsars. The current pulsar observations show a wide range of n from 1.4 to 2.9 (see e.g. Kaspi & Helfand 2002) providing evidence that $n \neq 3$, i.e. non pure dipole braking.

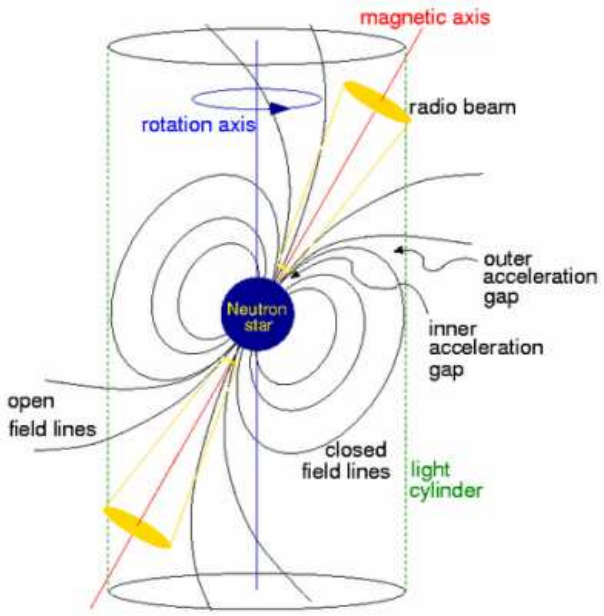

Figure 1.5: Simplified illustration of the magnetosphere of pulsars (Lorimer & Kramer 2004).

Nevertheless, some useful pulsar quantities are derived under the assumption of pure dipole radiation. The first quantity is the pulsar age. Integrating Equation 1.11 in terms of spin period P and assuming $n \neq 1$ gives the age as:

$$T = \frac{P}{(n-1)\dot{P}}\left[1 - \left(\frac{P_0}{P}\right)^{n-1}\right] \tag{1.12}$$

with P_0 the period at birth and P, $\dot{P}$ the current values of the period and the spin-down rate. Further assuming $P_0 \ll P$ and $n = 3$, we have the "*characteristic age*":

$$\tau \equiv \frac{P}{2\dot{P}} \simeq 15.8\,\mathrm{Myr}\left(\frac{P}{\mathrm{s}}\right)\left(\frac{\dot{P}}{10^{-15}}\right)^{-1} \tag{1.13}$$

Note that this age doesn't suit millisecond pulsars which have much larger ages than young pulsars (Section 1.4). Similarly, the magnetic field at the star surface, the "*characteristic magnetic field*", can be estimated as:

$$B_{\rm S} \equiv B(r=R) = \sqrt{\frac{3Ic^3}{8\pi^2 R^6 \sin^2\alpha} P\dot{P}} \simeq 3.2\times10^{19}\sqrt{P\dot{P}} \text{ Gauss} \tag{1.14}$$

for $I_0 = 10^{45}$ g cm^2, $R = 10$ km and $\alpha = 90^\circ$ (orthogonal rotator). The magnetic field at the light cylinder is:

$$B_{\rm LC} \equiv B(r=r_c) = B_S\left(\frac{2\pi R}{cP}\right)^3 \tag{1.15}$$

In reality, the rotation and magnetic axes of pulsars being in any configuration, the moment of inertia and radius being not perfectly understood, the above quantities only serve as an estimate of the pulsar properties. The pulsar geometry involving the inclination α and the viewing angle β which determines the observed pulsar emissions will be discussed in 1.3.3 and 2.1.

1.3.3 Radio profile and Rotating-Vector Model

Pulsars being very weak radio sources, it is generally necessary to add a sequence of some hundreds of individual pulses to obtain an integrated radio pulse profile. This process is known as "folding". The integrated profile is usually very stable for a given pulsar while it varies from pulsar to pulsar. In general, according to the number of pulse components contained, three classes of radio profiles are observed: single, double and multiple. Most pulsars have a single narrow pulse with a width of $\sim 10^\circ$; some pulsars possess an "interpulse" (J1705−1906 in Figure 1.6[11]) separated from the "main pulse" by 180°. This is usually interpreted as two beams from the two magnetic poles of an orthogonal rotator (inclination $\alpha = 90^\circ$). Other interpretations such as the bidirectional model are also proposed, according to which the "interpulse" comes from the same single pole as the "main pulse", but directs oppositely (Weltevrede *et al.* 2007). Other wide pulses which occupy almost all the rotation period, are considered to be from a nearly aligned rotator ($\alpha = 0^\circ$). One notes the profile evolution with frequency.

The pulse profile depends on the geometry of the emission beam. In the widely used cone-shaped model (Radhakrishnan & Cooke 1969), photons are emitted by the interaction of charged particles with the magnetic field. The emission region being defined by the last open field lines, the half-opening angle ρ of the beam depends in consequence on the width of the open field line region at the emission height r_{em}. The observed profile on the other hand depends on how the beam intersects the observer's line of sight. Figure 1.7 illustrates the emission geometry. Besides the half-opening angle ρ and the inclination α, the "*impact parameter*" β represents the closest approach of the line of sight to the magnetic axis. Obviously, $|\beta| \leq \rho$, otherwise the emission cone would be missed. The "*fiducial plane*" is defined as the plane containing the rotation and the magnetic axes at which the longitude $\phi = 0$. In pulsar timing (Section 4.1), the reference point, "*fiducial point*"", can be defined at any point of the pulse profile, depending on the method used for the profile template fit. For example, it can be the midpoint of a peak or can correspond to the "*fiducial plane*".

The measured pulse width[12] W in units of rotational longitude is related to the half-opening angle ρ as (Gil *et al.* 1984):

$$\cos\rho = \cos\alpha\cos(\alpha+\beta) + \sin\alpha\sin(\alpha+\beta)\cos\left(\frac{W}{2}\right) \tag{1.16}$$

[11] Available at http://www.atnf.csiro.au/people/joh414/ppdata/index.html

[12] Available at http://www.atnf.csiro.au/research/pulsar/psrcat/

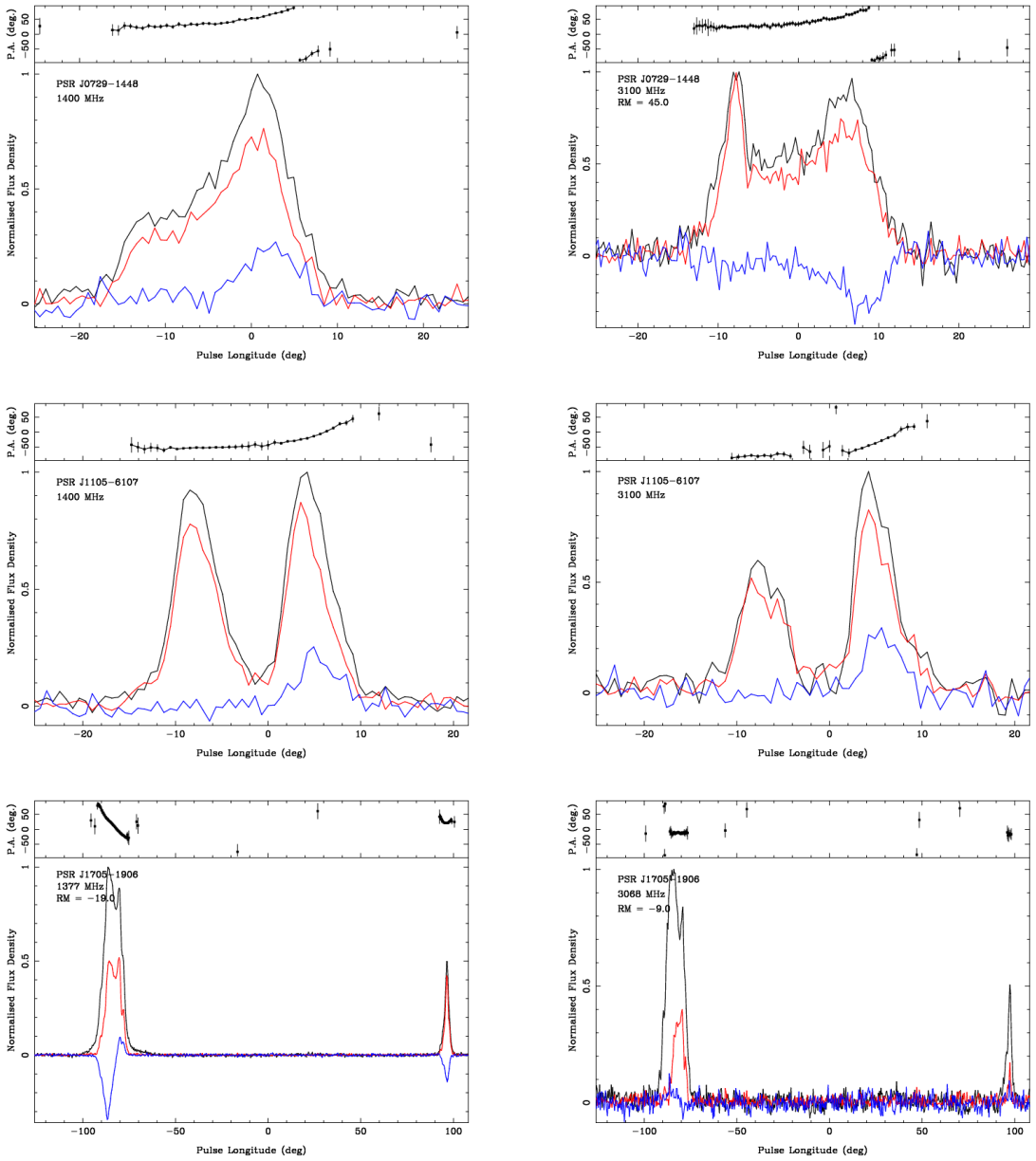

Figure 1.6: Examples of integrated radio profiles for observation frequencies of 1.4 GHz (left) and 3.1 GHz (right). For the lower panel of each plot, black: total intensity; red: linear polarization intensity; blue: circular polarization intensity. For the top panel of each plot: position angle PPA variation as a function of pulse longitude. Figures are from http://www.atnf.csiro.au/people/joh414/ppdata/.

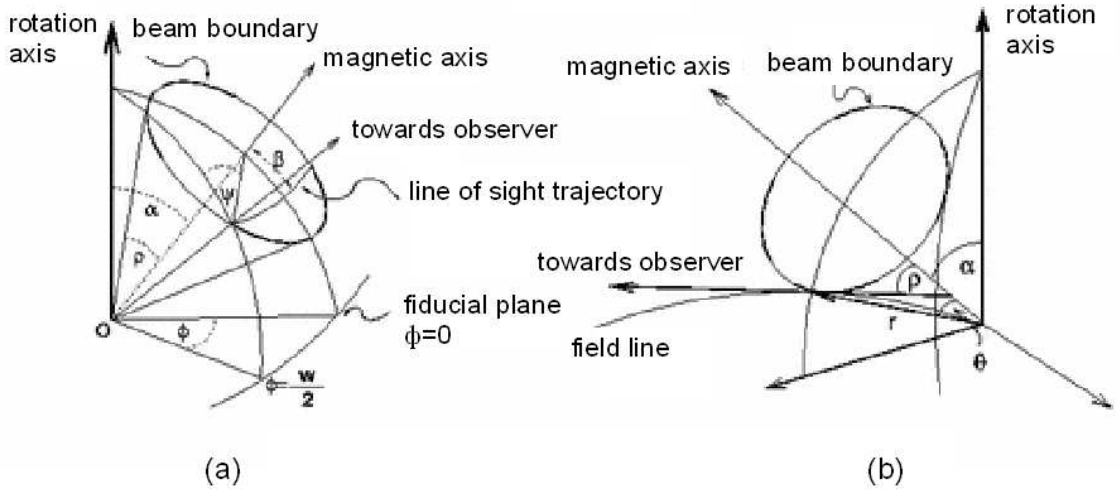

Figure 1.7: The geometry of the pulsar beam. (a): The inclination angle between the rotation and megnetic axes is α; the half-opening angle of the emission cone is ρ; the "*impact parameter*" β is the closest approach of the line of sight to the magnetic axis. The position angle Ψ of linear polarization is measured respective to the projected direction of the magnetic axis. The "*fiducial plane*" is defined as the plane containing the rotation and magnetic axes with rotational longitude $\phi = 0$. The pulse width W is measured in rotational longitude. (b): The relation between the polar coordinates (r, θ) and the half-opening angle ρ (Lorimer & Kramer 2004).

In the case of the emission region close to the magnetic axis (i.e. $\theta \lesssim 20^\circ$ and $\rho \lesssim 30^\circ$), ρ can be approximated as (e.g. Gangadhara & Gupta 2001):

$$\rho \approx \frac{3}{2}\theta_{em} \approx \sqrt{\frac{9\pi r_{em}}{2cP}} \text{ radians} = 1.24^\circ \left(\frac{r_{em}}{10\,\text{km}}\right)^{1/2} \left(\frac{P}{\text{s}}\right)^{-1/2} \tag{1.17}$$

with (r_{em}, θ_{em}) the coordinates of the emission point.

Radhakrishnan & Cooke (1969) established a Rotating-Vector Model (RVM, Figure 1.8) to estimate α and β using radio polarization information from the pulsar profile, assuming that the linear polarization vector is locked to the dipole magnetic field. In this model, the position angle (PPA) of the linear polarization defined as[13] $\Psi = \frac{1}{2}\tan^{-1}(U/Q)$ varies smoothly and regularly throughout the pulse and is measured with respect to the projected direction of the magnetic axis. Ψ is predicted as:

$$\tan(\Psi - \Psi_0) = \frac{\sin\alpha \sin(\phi - \phi_0)}{\sin(\alpha+\beta)\cos\alpha - \cos(\alpha+\beta)\sin\alpha\cos(\phi-\phi_0)} \tag{1.18}$$

with ϕ_0 the pulse longitude at the "*fiducial point*" and Ψ_0 the corresponding position angle. While a typical variation of Ψ is S-shaped (Figure 1.8a, bottom), this is not the case for all the pulsars.

Examples of profile morphology and RVM modelling can be found in e.g. Johnston & Weisberg (2006) and Weltevrede & Johnston (2008a). A method of combining the RVM with γ-ray profile modelling in the context of different γ-ray emission models (Section 2.1) has been recently developed to better constrain the pulsar emission zone and the magnetosphere structure (see e.g. Romani & Watters 2010; Theureau *et al.* 2011).

[13] Stokes parameters for polarized wave: I, Q, U, M with total intensity $I = \sqrt{Q^2+U^2+V^2}$, linearly polarized intensity $L = \sqrt{Q^2+U^2}$ and V circularly polarized intensity.

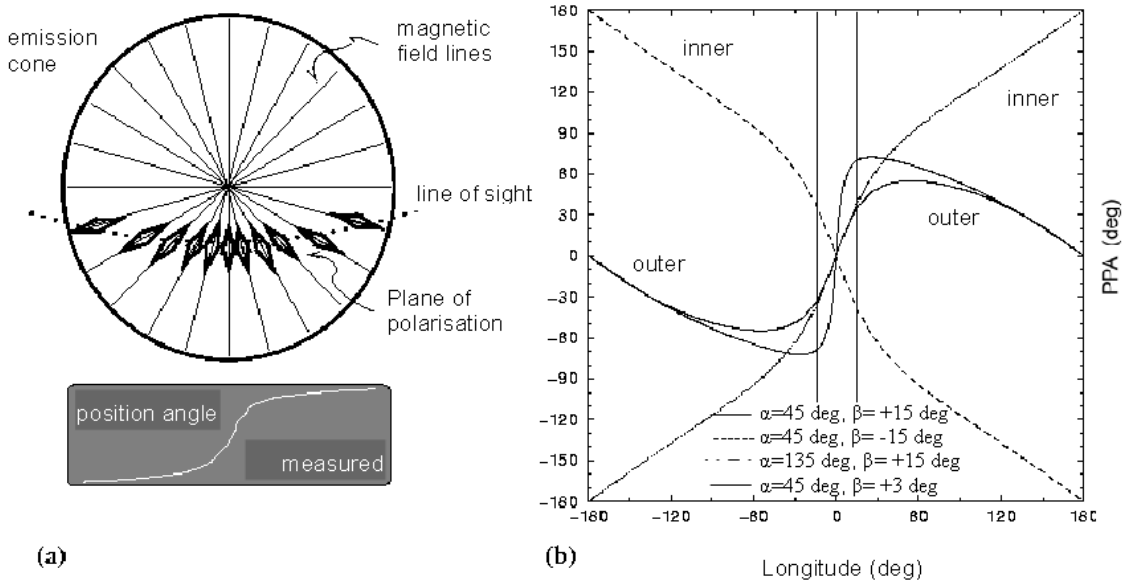

Figure 1.8: Rotating-Vector Model of Radhakrishnan & Cooke (1969). (a) Illustration of the "S-shaped" position angle Ψ variation throughout the pulse from a pole-on view of the magnetic axis. (b) Position angle Ψ as a function of pulse longitude for some configurations of inclination α and impact parameter β. Vertical lines indicate the mean pulse width of 30° (Lorimer & Kramer 2004).

1.4 Pulsar category and distribution

As presented in Section 1.3, pulsars spin down due to the loss of rotational kinetic energy. The $P-\dot{P}$ diagram (Figure 1.9) shows the spin-down rate $\dot{P}$ versus spin period P for >2000 known rotation-powered pulsars mostly from the ATNF pulsar catalog[14] (Manchester *et al.* 2005). 132 public γ-ray pulsars with 117 included in The Second *Fermi*-LAT γ-ray Pulsar Catalog (2PC, Abdo *et al.* 2013) are indicated by filled color markers. Six new detections after the 2PC sample was frozen are indicated with arrows and names and will be presented in detail in Chapter 6. Also shown are constant characteristic age τ lines, surface magnetic field B_S lines and spin-down power $\dot{E}$ lines. We distinguish clearly two different pulsar groups: the *normal pulsars* (upper right, with P of ~ 0.1 s to several seconds, $\dot{P}$ of $\sim 10^{-17}$ to 10^{-13}) and the *millisecond pulsars* (MSP, lower left, with $P \leq 30$ ms and $\dot{P} \leq 10^{-17}$). The *normal pulsars* are relatively young (10^7 yr) and highly magnetized (10^{12} G), while MSPs have larger ages (10^9 yr) and lower magnetic field (10^8 G). The spin-down powers $\dot{E}$ are highest for young pulsars and MSPs. The *normal pulsars* constitute 90% of the pulsars observed, while MSPs 10%.

It is natural to imagine that the *normal pulsars* were born with a small spin period in the upper left of the $P-\dot{P}$ diagram and spin down towards the currently occupied region with a time scale of 10^{5-7} yr. After 10^7 yr, their flux may become too weak to be detectable on Earth. Such an evolution scenario is not applicable to MSPs which have characteristic ages τ of 10^9-10^{11} yr that are even older than the Universe. In fact, for MSPs, the characteristic ages are not their true ages.

More than 80% of MSPs are in binary systems, while only less than 1% of all normal pulsars. According to the current stellar evolution theory, the formation of MSPs can be explained in the context of binary systems (see e.g. Bhattacharya & van den Heuvel 1991; van den Heuvel 2011). We start with a binary system composed of two main-sequence stars. The more massive star evolves faster and ends its life with

[14] http://www.atnf.csiro.au/research/pulsar/psrcat

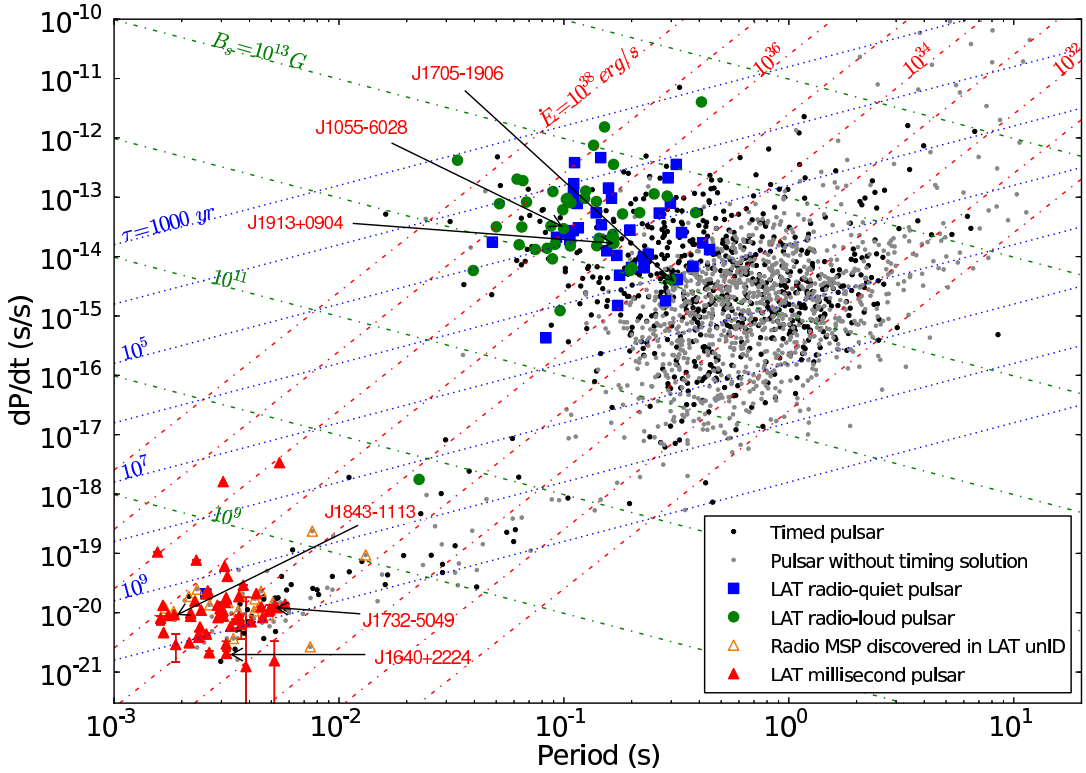

Figure 1.9: Pulsar spin-down rate $\dot{P}$ versus spin period P for $>$ 2000 known rotation-powered pulsars mostly from the ATNF pulsar catalog. 132 public γ-ray pulsars with 117 included in 2PC are indicated by filled color markers. Orange open triangles indicate radio MSPs discovered at the positions of previously unassociated LAT sources for which γ-ray pulsations have not been seen. Doppler corrections to $\dot{P}$ have been applied to all pulsars with proper motion measurements (Section 4.1.2, 7.1). For visibility, error bars are only shown for γ-ray MSPs for which the correction is important. Six new detections after 2PC are highlighted with arrows and names and will be presented in detail in Chapter 6.

a supernova explosion, perhaps creating a neutron star. In 90% of the cases, such an explosion will disrupt the binary system explaining that only a few normal pulsars are in binary systems (see e.g. Radhakrishnan & Shukre 1985). In the other 10% of the cases, the neutron star remains bound gravitationally to its companion. If the orbital parameters permit, the high gravitational force of the neutron star will accrete matter from the companion and the system becomes detectable in X-rays due to thermal X-ray emissions from the accretion, such as the binary system B1259−63 (Johnston *et al.* 1992). Such accretion transfers angular momentum to the neutron star and thereby accelerates it to very short spin periods and significantly reduces its magnetic field (Bisnovatyi-Kogan & Komberg 1974; Shibazaki *et al.* 1989). After reaching equilibrium between the magnetic pressure and the infalling matter pressure, a period limit is reached and the neutron star begins to spin down slowly (Bhattacharya & van den Heuvel 1991; Arzoumanian *et al.* 1999). MSPs are therefore also referred to as *recycled pulsars*. Such a scenario seems to be confirmed with the discovery of a MSP for which an accretion disk has existed in the past several hundred years (Archibald *et al.* 2009).

Depending on the mass of the companion, X-ray binaries fall into two classes: high mass X-ray binaries

(HMXBs) and low mass X-ray binaries (LMXBs). In the case of HMXBs, the companion may also undergo a supernova explosion and become a second neutron star. If the system survives the explosion, a double neutron star system will be formed, e.g. the double-pulsar binary J0737-3039 (Lyne *et al.* 2004; Guillemot *et al.* 2013). In general, accretion may be interrupted by the explosion, forming *mildly recycled* pulsars (region between normal pulsars and MSPs in the $P - \dot{P}$ diagram). In the case of LMXBs, the companion being not massive enough to explode as a supernova, the mass transfer will last longer. When the companion finally exhausts its outer layer, the resulting system is a MSP with a white dwarf. The origin of isolated MSPs is still not clear. In globular clusters with a high density of stars, interactions among stars can disrupt the binary system leaving an isolated MSP. In the Milky Way, one possible explanation is that the companion may have been evaporated by the strong particle wind from the MSP during the X-ray phase (Ruderman *et al.* 1989).

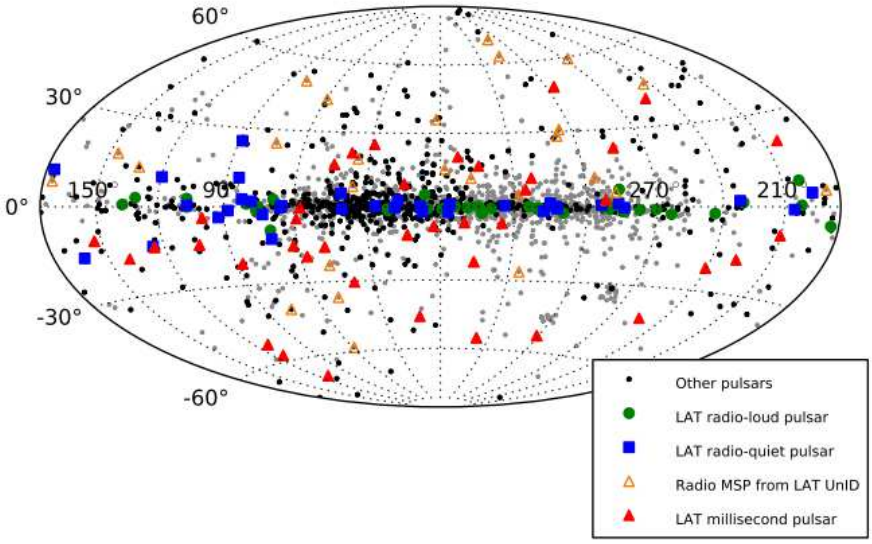

Figure 1.10: Pulsar sky distribution in Galactic coordinates. The markers are the same as in Figure 1.9.

Figure 1.10 shows the sky distribution of the same pulsar population as in Figure 1.9, in Galactic coordinates. Pulsars, especially normal pulsars, are concentrated in the Galactic plane, as are massive O and B stars. This observation is consistent with the standard hypothesis that neutron stars are born in gravitational core collapse of massive stars in supernova explosion. The violent explosion may give pulsars a "birth kick" due to the asymmetry in the explosion resulting in a birth velocity of several hundreds km s^{-1} (Lyne & Lorimer 1994). Proper motion measurements (Section 4.1.2) confirm such high space velocities. This picture may explain the fact that there are pulsars detected far from the Galactic plane, which is more evident for MSPs. This observation may due to: 1) MSPs are generally less bright than normal pulsars, so they are usually detected at small distances ($\lesssim 3$ kpc for non globular cluster MSPs), which implies possible detections at higher Galactic latitudes than normal pulsars. 2) They are relatively older than normal pulsars, and have migrated to higher latitudes from their birth places in the Galactic plane.

It's worth noting that pulsars are mostly detected in the neighbourhood of the Sun ($0.2 < d \lesssim 5$ kpc) due to their intrinsic weakness at radio wavelengths and the radio signal distortion when passing through the interstellar medium. On the other hand, radio observations have been mostly carried out in the Galactic plane introducing strong observational bias. The current pulsar sample represents therefore only a small fraction of a total population of about $10^5 - 10^6$ active pulsars in the Milky Way. More information on the neutron star formation and stellar evolution can be found in e.g. van den Heuvel (2011).

1.5 Pulsar distances

The distance of the pulsar is an important piece of information for various studies, such as modelling the Galactic pulsar distribution, probing the Galactic electron distribution through dispersion measurements (Section 1.5.4) and estimating the magnetic field along the line of sight by Faraday rotation of the radio polarization (Han *et al.* 2006). Distance is essential to Doppler correct MSPs' spin-down rate (Section 4.1.2, 7.1) and to then deduce the pulsar's γ-ray efficiency which helps to constrain the emission models (Chapter 2).

Below sections present different distance measurement methods. γ-ray pulsar distances in 2PC determined by any of the following methods are shown in Appendix B.

1.5.1 Parallax distance

For nearby pulsars (within 1 kpc of the Sun), the distance can be obtained from the measurement of their annual parallax due to the Earth's motion around the Sun from pulsar timing (Section 4.1). This is the most direct and precise method so far, but is limited by the pulsar's position in the Galaxy as we can see from Equation 4.5. This method is applicable to MSPs close to the ecliptic plane (see e.g. Hotan *et al.* 2006), because only MSPs provide accurate enough timing measurements to detect the parallax induced time delay. Comparing the amplitude of such delay to the pulsar timing residual would give a lower limit on the pulsar distance, and inversely, how possible it would be to obtain a parallax measurement assuming the pulsar distance determined in other ways is right. Examples of such study are illustrated in Chapter 6 and 7.

The VLBI (very long baseline interferometry) technique gives higher precision on the parallax and other astrometric parameters of pulsars (Deller *et al.* 2008). About 60 parallax measurements have been obtained to date. One bias, known as Lutz-Kelker bias, concerning the systematic overestimate of the parallax due to the larger volume sampling at small parallax values, should be corrected before converting the parallax to distance (Lutz & Kelker 1973). Such bias corrected parallax distances have been adopted in 2PC based on the work of Verbiest *et al.* (2010) and Verbiest *et al.* (2012).

1.5.2 Kinematic distance

Hydrogen is the most abundant element in the Interstellar Medium (ISM), in forms of neutral hydrogen atom (H_0 or HI), molecular hydrogen (H_2), hydrogen ions (HII) and other molecules (H_2O...). The ISM is full of gas and clouds composed of these different hydrogen forms visible at radio and infra-red wavelengths through observations of different transition lines.

Kinematic distances can be derived from the 21 cm (1.42 GHz) line of neutral hydrogen atoms[15] in combination with a Galactic rotation model (Appendix A) for pulsars at low galactic latitudes. The basic idea is that the pulsar's continuum emission will be absorbed at the wavelength of 21 cm if there are clouds (like in the spiral arms in the Galaxy) rich in neutral hydrogen located between the pulsar and the observer. This line being Doppler shifted (Section 4.1.2) from its rest-frame value by relative motion between the source and the observer, the frequency shift can be transferred to a radial velocity via Equation 4.10, while the latter can be converted to distances using a Galactic rotation model, e.g. Fich *et al.* (1989). The relationship between the pulsar distance d and the radial velocity $v_{\rm R}$, for a flat rotation curve, is:

$$d = \frac{R_0 \cos l \pm \sqrt{R^2 - R_0^2 \sin^2 l}}{\cos b} \tag{1.19}$$

[15]The neutral hydrogen line, 21 cm line or HI line refers to the hyperfine transition created when spins of the proton and the electron change from a parallel to an anti-parallel configuration, resulting in a lower energy state of the hydrogen atom. While this line is highly forbidden in Earth-based laboratories with an extremely small rate of $2.9 \times 10^{-15}\,{\rm s}^{-1}$, it is often observed at radio wavelengths due to the very large amount of neutral hydrogen atoms in the interstellar medium.

where

$$R = R_0 \left(\frac{v_0 \sin l \cos b}{v_R + v_0 \sin l \cos b} \right) \tag{1.20}$$

with R_0, R the galactocentric radius of the Local Standard of Rest (LSR[16]) defined at the solar neighbourhood and of the pulsar respectively; l, b are the Galactic longitude and latitude of the pulsar; v_0 denotes the Galactic rotation velocity of the LSR at R_0.

This method gives usually only the lower or upper limit of the pulsar distance. A reliable determination of the pulsar distance requires both the absorption and the emission spectrum. As shown in Figure 1.11, clouds in front of the pulsar will show spectral features in both the absorption and emission spectra, and a lower limit can be obtained from the highest velocity (the farthest) of the deepest absorption (the highest intensity) feature in the absorption spectrum. An absence of absorption features at velocity with strong HI emission sets an upper limit on the pulsar distance indicating that the hydrogen cloud is behind the pulsar.

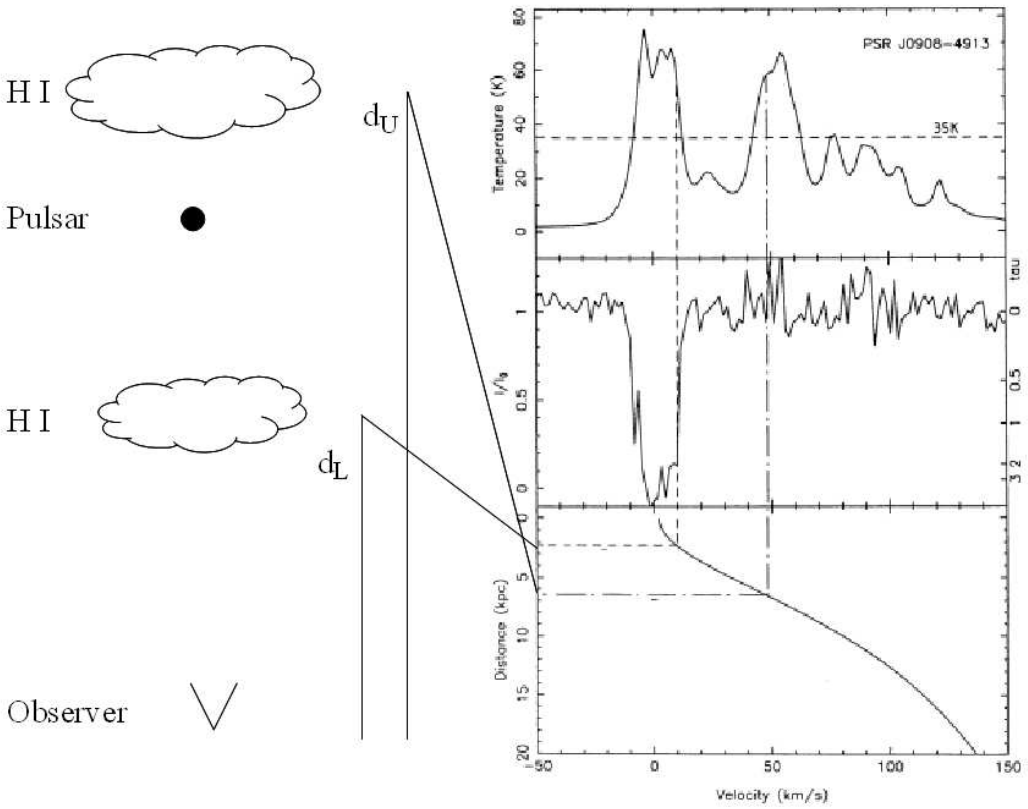

Figure 1.11: Left: basic geometry showing a pulsar with HI clouds in front of and behind it. Right: upper (d_U) and lower (d_L) distance limits derived from the HI emission (top) and absorption (middle) spectra using a Galactic rotation model (bottom, Fich *et al.* 1989) along the line of sight of PSR J0908−4913 (Koribalski *et al.* 1995). I/I_0 represents the HI absorption by the cloud in front of the pulsar which is the intensity difference between the on-pulse and off-pulse normalized to the pulsar continuum.

[16]LSR is a point in space that is moving on a perfect circular orbit at R_0 around the Galaxy center with a velocity v_0 equal to the average velocity of stars in the solar neighbourhood, including the Sun. All velocities of stars are measured relative to this point LSR resulting in the radial velocity v_R.

One notes that the accuracy of the kinematic distance estimate is limited by for example the non-circular motions of the pulsar and the ambiguity in the inner Galaxy where the distance is double-valued for a given radial velocity (Green 1984; Burton 1988). Combining the HI emission/absorption and CO emission[17] spectra may help to solve the double distance ambiguity as demonstrated by Leahy & Tian (2010). In this case, there will be no absorption in the HI spectrum for a CO cloud behind the pulsar, and if the CO velocity is greater than the farthest HI absorption velocity, the pulsar should be in the nearer distance of the farthest HI absorption velocity.

1.5.3 Optical, X-ray or association distance

In some rare cases, pulsar distances may be inferred from its optical identification or of its companion star for pulsars in binaries if the absolute magnitude of the star can be estimated. On the other hand, measuring the X-ray absorption in an X-ray energy spectrum gives the hydrogen column density $N_{\rm H}$. This can be compared to $N_{\rm H}^{\rm radio}$ obtained from HI and CO surveys to obtain a rough estimate of the distance (Chapter 7). The association of the pulsar with a Supernova Remnant (SNR) or a Pulsar Wind Nebula (PWN)[18] can provide good distance measurements of the pulsar given the distance of SNR or PWN determined with e.g. the kinematic method described previously.

1.5.4 Dispersion measures

As introduced in Section 1.5.2, gas and clouds rich in hydrogen element fill our Galaxy. HII regions are often created around very hot O and B type stars which are responsible for the ionisation. The ISM is full of free electrons and plasma mostly concentrated in the Galactic plane where hot stars reside. The propagation velocity (group velocity $v_{\rm g}$) of the electromagnetic wave in the plasma is less than the speed of light c due to the frequency-dependent refraction. The consequence is that the arrival time of the radio waves to the observer will be delayed compared to a signal of speed c by a amount of:

$$t = \left(\int_0^d \frac{{\rm d}l}{v_{\rm g}} \right) - \frac{d}{c} = \frac{\rm DM}{k \times f^2} \tag{1.21}$$

(Figure 4.1) with the *dispersion measure* (DM, free electron column density):

$$\rm DM = \int_0^d n_e \, {\rm d}l \tag{1.22}$$

in units of pc cm^{-3} and the *dispersion constant* $k = 2.41 \times 10^{-4}$ MHz^{-2} pc cm^{-3} s^{-1} (Manchester & Taylor 1977). $n_{\rm e}$ is the free electron number density in cm^{-3}. DM is determined by measuring the pulse time delay at two or more different frequencies:

$$\Delta t = \frac{\rm DM}{k} \left(\frac{1}{f_1^2} - \frac{1}{f_2^2} \right) \tag{1.23}$$

The distance can be inferred from the measured DM from the free electron density $n_{\rm e}$ for a given line of sight. This serves as the basic idea for DM distance estimate. Systematically modelling the Galactic electron distribution was first performed by Taylor & Cordes (1993) and improved by Cordes & Lazio (2002), known as the "NE2001" model (Figure 1.12). In this model, the electron density distribution is modelled by three large scale components (spiral arms, thick and thin disk), one local ISM component (including a local hot bubble (LHB), a local superbubble (LSB), a low density region (LDR) and the Loop I component), one

[17] The rotational transition line of CO molecule from the quantum energy state 1 to 0 at 115 GHz (2.6 mm) by loosing its angular momentum induced by collisions of CO with H_2 molecules.

[18] Created by the interaction of the charged particle outflow from the pulsar magnetosphere with the interstellar medium.

Galactic Center component, contributions of individual regions of intense density ("Clumps", e.g. the Gum nebula and the Vela SNR) and of low density ("Voids"). The model is "tuned" to give the measured DM for a small number of line of sight where the pulsar distance is obtained independently. In addition, "Clumps" and "Voids" are not systematically modelled, yielding sometimes completely wrong distances. Uncertainties on DM distances are estimated by varying the DM by $\pm 20\%$ as recommended by the "NE2001" authors.

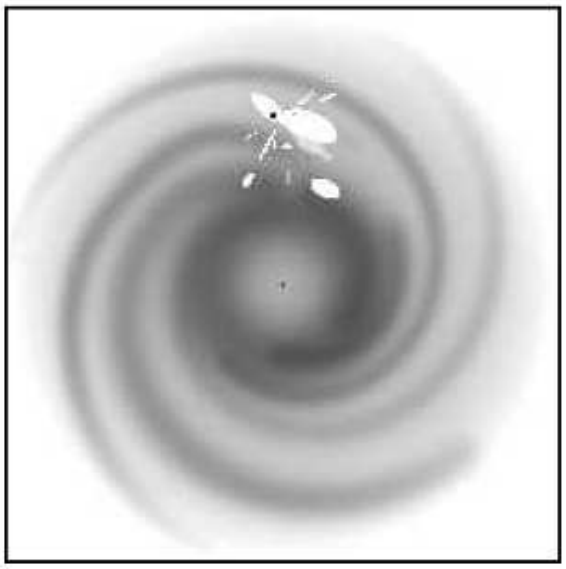

Figure 1.12: The NE2001 Galactic electron density distribution model plotted in logarithmic scale on a 30×30 kpc $x-y$ plane at $z = 0$ and centered on the Galactic center. The large scale structure is represented by spiral arms and a disk. The Galactic center component is shown by a small dot. The local ISM component near the sun is represented by the small scale, lighter structure on upper part of the figure. The black dot in one of the ellipsoidal regions corresponds to the Gum Nebula and Vela supernova remnant (Cordes & Lazio 2002).

CHAPTER 2

γ-ray pulsars

Contents

2.1 Theoretical models

Pulsars are seen to emit from radio to γ-ray wavelengths suggesting that pulsars are charged particle accelerators. While nearly 50 years passed since the discovery of the first pulsar in 1967 and more than 145 γ-ray pulsars have been detected with *Fermi* (Section 2.2), the understanding of the pulsar γ-ray emission and acceleration mechanisms is still far from perfect.

The current existing emission models can be grouped into two major categories. The first (Figure 2.1) assumes that the acceleration occurs in the open field line region where the force-free condition ($\vec{E}\cdot\vec{B}=0$, Section 1.3.2) breaks down and the re-arrangement of charges leads to a parallel electric field $E_{\parallel}$ responsible for the particle acceleration. The γ-ray emission is initiated by the curvature radiation of accelerated charged particles (e.g. electrons e^- and positrons e^+) along the open field lines. In the closed field line region, the force-free state is maintained and thus no particle acceleration is possible. The spectrum of the curvature radiation is often characterized by the critical energy above which the emission will fall off significantly:

$$\varepsilon_{cr} = \frac{3}{2}\hbar c\frac{\gamma^3}{\rho_{\rm cr}} \quad \text{eV} \tag{2.1}$$

where c is the speed of light, $\gamma=(1-\beta^2)^{-1/2}$ is the Lorentz factor of the particle ($\beta=v/c$, v is the velocity of the charged particle), $\rho_{\rm cr}$ is the curvature radius of the magnetic field lines and $\hbar=h/2\pi$ is the reduced Planck constant (see e.g. Jackson 1999). In the radiation-reaction regime[1], the acceleration of charged

[1] According to Newton's third law of motion, for every action there is an equal and opposite reaction. Applying to the charged particles, they experience a change of momentum therefore a reaction force by emitting photons. That means, the accelerating force will not only accelerate the particle, but also counter the reaction force which scales as the emitted photon energy. The balance is reached when all the accelerating force is for countering the reaction force. The particle can't be accelerated any more, the emitted photons attain the maximum energy possible.

particles saturates at (Venter & De Jager 2010):

$$\gamma = \left(\frac{3}{2}\frac{\rho_{\rm cr}^2}{e}E_{\parallel}\right)^{1/4} \tag{2.2}$$

with e the charge of e^+ and e^-. This results in:

$$\varepsilon_{\rm cr} = \left(\frac{3}{2}\right)^{7/4}\hbar c\rho_{\rm cr}^{1/2}\left(\frac{E_{\parallel}}{e}\right)^{3/4} \tag{2.3}$$

This is the origin of the energy cutoff observed in γ-ray pulsar spectra without considering the photon attenuation which modifies the detailed cutoff in different models. It's obvious that greater $\rho_{\rm cr}$ leads to higher ε_{cr}.

With the curvature radiation in common, the first category of models differ on the location of the acceleration site in the open field line region and can be grouped into two sub-categories: low altitude models with acceleration just above the magnetic surface (Polar Cap) and higher altitude models (Slot Gap, Two-pole Caustic and Outer Gap) with acceleration extending to the light cylinder. The second major category argues that the emission is due to synchrotron radiation[2] from particles located in the stripe of the pulsar wind (Striped Wind model). We describe these models individually in the following sections.

2.1.1 Polar Cap model

The Polar Cap (PC) model was first proposed by Sturrock (1971) and then investigated by different authors (see e.g. Ruderman & Sutherland 1975; Harding 1981; Daugherty & Harding 1982, 1994, 1996). In the standard PC model (Daugherty & Harding 1994, 1996; Harding 2009), the acceleration takes place over an extended region from just above the neutron star surface to a few stellar radii in the open field line region. The γ-ray emission is initiated by the curvature radiation of primary electrons injected from the neutron star surface and accelerated along the field lines. Photons with energies $\gtrsim 2m_ec^2$ will interact with the intense magnetic field via one photon pair production ($\gamma + B \rightarrow e^+ + e^-$). Pairs in turn emit photons by synchrotron radiation and curvature radiation, leading to the pair-photon cascade. Electrons and positrons are accelerated in opposite directions according to their charge sign, establishing an electric field which opposes and eventually cancels out the accelerating field, forming the so-called Pair Formation Front (PFF). Pairs accelerated downward hit the star surface to create thermal X-ray emission. These X-ray photons interact with the pairs via Inverse Compton Scattering (ICS)[3] to emit high energy photons. The observed γ-ray emission is thought to come from primaries and secondaries above the acceleration region at high altitude.

2.1.2 Outer Gap model

The Outer Gap (OG) model (see e.g. Cheng *et al.* 1986; Romani 1996; Zhang & Cheng 1997; Cheng *et al.* 2000; Zhang *et al.* 2007; Takata *et al.* 2008; Wang & Hirotani 2011) is based on the assumption that the *Goldreich-Julian* charge density (Section 1.3.2) is valid everywhere in the magnetosphere, not just in the co-rotating region (bounded by the last open field lines). An OG is located between the "null charge surface" (NCS, $\vec{\Omega}\cdot\vec{B} = 0$, Section 1.3.2), the light cylinder and the last open field lines. Since the magnetic field is relatively weak in the outer magnetosphere, pairs are mainly created by photon-photon interaction

[2]Synchrotron radiation can be considered as a specific case of curvature radiation when an electron gyrates around a magnetic field line with an angle χ which is the angle between the direction of the magnetic field and that of the particle velocity. Details can be found in e.g. Rybicki & Lightman (1979), Jackson (1999)

[3]Inverse Compton Scattering occurs when a relativistic electron with energy γm_ec^2 interacts with a low energy photon. The electron transfers part of its kinematic energy to the photon.

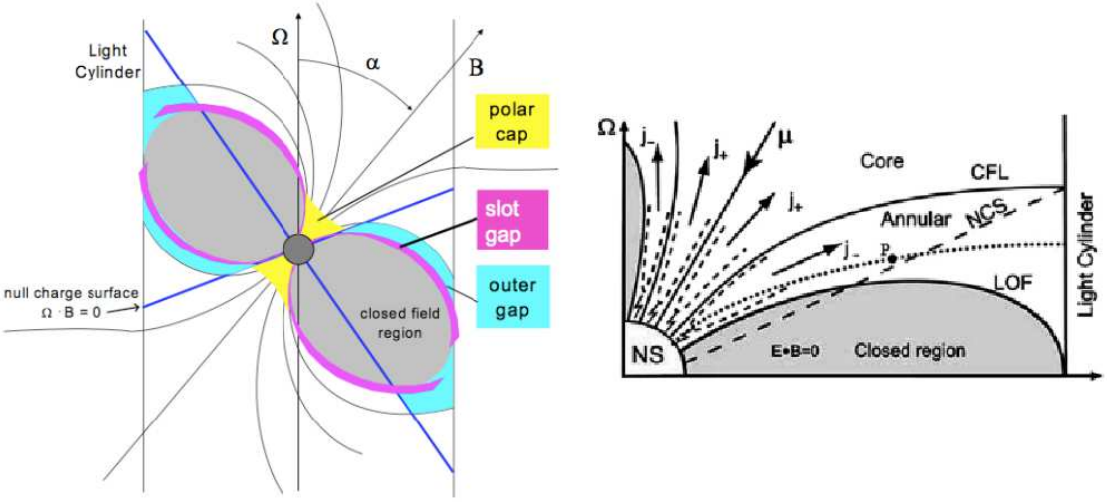

Figure 2.1: Left: pulsar magnetosphere and acceleration regions of different emission models. right: Annular Gap model with two acceleration regions: annular gap and core gap. CFL stands for critical magnetic field lines crossing the intersection of the NCS and the light cylinder. LOF stands for the last open field lines (Du *et al.* 2011).

($\gamma + \gamma \rightarrow e^+ + e^-$). The resulting photon-pair cascade limits the gap size and screens the accelerating electric field. It is argued that the observed γ rays are not from the primary photons emitted by accelerated electrons in the gap, but from secondary photons emitted by secondary pairs which are themselves produced by primary photons interacting with thermal X-rays from the neutron star surface (Cheng *et al.* 1986).

Recent developments of 3-dimensional OG models include for example Hirotani (2011) and Wang *et al.* (2011) which take into account a full treatment of the radiation spectrum and its variation through the magnetosphere, rather than a simple geometry approach only.

2.1.3 Slot Gap and Two-pole Caustic models

The Slot Gap (SG) model (Arons 1983; Muslimov & Harding 2003, 2004a) is a natural extension of the PC model, in which the primary electrons are accelerated at the PC rim extending to very high altitudes bounded by the surface of the last open field lines before pair conversion occurs. Emission can therefore occur over a large fraction of the boundary of the open field line region. Muslimov & Harding (2004a) also noted the possibility of the formation of caustic emission on trailing field lines due to the relativistic aberration and time delay, effects that are important at high altitudes.

The Two-Pole Caustic (TPC) model (Dyks & Rudak 2003) is a geometric realization of the SG model. In this model, the acceleration gap, extending from each polar cap to the light cylinder, is thin and confined by the last open field lines.

2.1.4 Pair-starved Polar Cap model and Annular Gap model

First proposed by Muslimov & Harding (2004b), the PSPC model serves as a possible solution for γ-ray emission from pulsars lying below the pair-production death line of the curvature radiation. Accelerating primary electrons at low altitudes above the PC can't produce enough pairs to screen the accelerating electric field $E_{\parallel}$, and thereby continue to be accelerated up to high altitudes near the light cylinder (Harding & Muslimov 2002). The authors showed that the ICS pair-production is only efficient for high magnetic field pulsars to screen $E_{\parallel}$. The PSPC model was previously believed to explain the high energy emission from

MSPs (with low magnetic field), but recent light curve (Section 2.1.6) modellings for *Fermi* γ-ray MSPs shows that most of them can be best fit by the TPC and OG models, suggesting a narrow acceleration gap in the outer magnetosphere where copious pairs are produced even for MSPs: they are no longer pair-starved (Venter *et al.* 2009).

The Annular Gap model combines advantages of the OG and TPC models as originally suggested by Qiao *et al.* (2004, 2007) and further developed by Du *et al.* (2010, 2011, 2012, 2013). In this model, two acceleration sites are defined: the *annular gap* between the critical field lines (CFL) and the last open field lines; the *core gap* between the CFL and the magnetic axis. The CFL are magnetic field lines which cross the intersection of the null charge surface and the light cylinder. The Annular Gap model is a self-consistent model for both young pulsars and MSPs, and can reproduce the radio and γ-ray emissions simultaneously (Du *et al.* 2013).

2.1.5 Striped Wind model

The Striped Wind model, as the second major category of pulsar emission models, differs significantly from all the previously described gap models in the following aspects (Pétri 2012): (1) pairs are created in the magnetosphere but quickly cool down before reaching the striped pulsar wind zone; (2) the pulsar's spin-down power $\dot{E}$ is not the unique energy source and the magnetic field in the striped pulsar wind serves as an alternate energy reservoir; (3) pulsar emission is due to synchrotron radiation from particles in the striped wind, thus well outside the magnetosphere, but not curvature radiation in the open field line region; (4) the observed luminosity could exceed the spin-down power. In chapter 7, we will explore a sample of high efficiency (conversion fraction of $\dot{E}$ to the luminosity) pulsars.

This model has been successfully applied to the optical observation of the Crab pulsar (Pétri & Kirk 2005). The recent work of Pétri (2012) extended it to higher energies by applying it to The First *Fermi*-LAT γ-ray Pulsar Catalog (1PC, Abdo *et al.* 2010b) and found that the striped wind model is able to reproduce the ensemble of *Fermi* data with reasonable accuracy, such as spectral index and luminosity, while individual pulsars deserve further investigation.

2.1.6 Model predictions: spectrum and geometry

Light curves (or profiles) and spectra are two pulsar observables. Comparing model predictions with observations is a natural way to discriminate between and eventually constrain different models.

Spectrum

All the gap models for pulsar emission predict a spectrum with an energy cutoff at a few GeV due to 1-photon ($\gamma + B \rightarrow e^+ + e^-$) or photon-photon ($\gamma + \gamma \rightarrow e^+ + e^-$) attenuation. The spectrum in terms of the expected photon number N as a function of the photon energy E can be expressed as (PLEC hereafter):

$$\frac{dN}{dE} = N_0 \left(\frac{E}{E_0}\right)^{-\Gamma} \exp\left(-\left(\frac{E}{E_c}\right)^b\right) \tag{2.4}$$

with N_0 the prefactor, E_0 the energy scale, E_c the cutoff energy, Γ the spectral index and b the cutoff index.

The spectrum of the PC model is relatively hard ($\Gamma \backsim 1.5 - 2.0$), with a super-exponential cutoff ($b \sim 2$) principally due to the significant attenuation from 1-photon attenuation in the intense magnetic field near the polar cap. For outer magnetosphere models (SG, OG, TPC, PSPC, Annular Gap), the spectrum is expected to cut off only exponentially (PLEC1, $b = 1$) since the magnetic field at high altitudes is not strong enough to significantly attenuate the γ-ray photons. LAT observations are expected to be able to discriminate between e.g. the simple or super exponential cutoff. The latest results will be presented in Section 2.2.3.

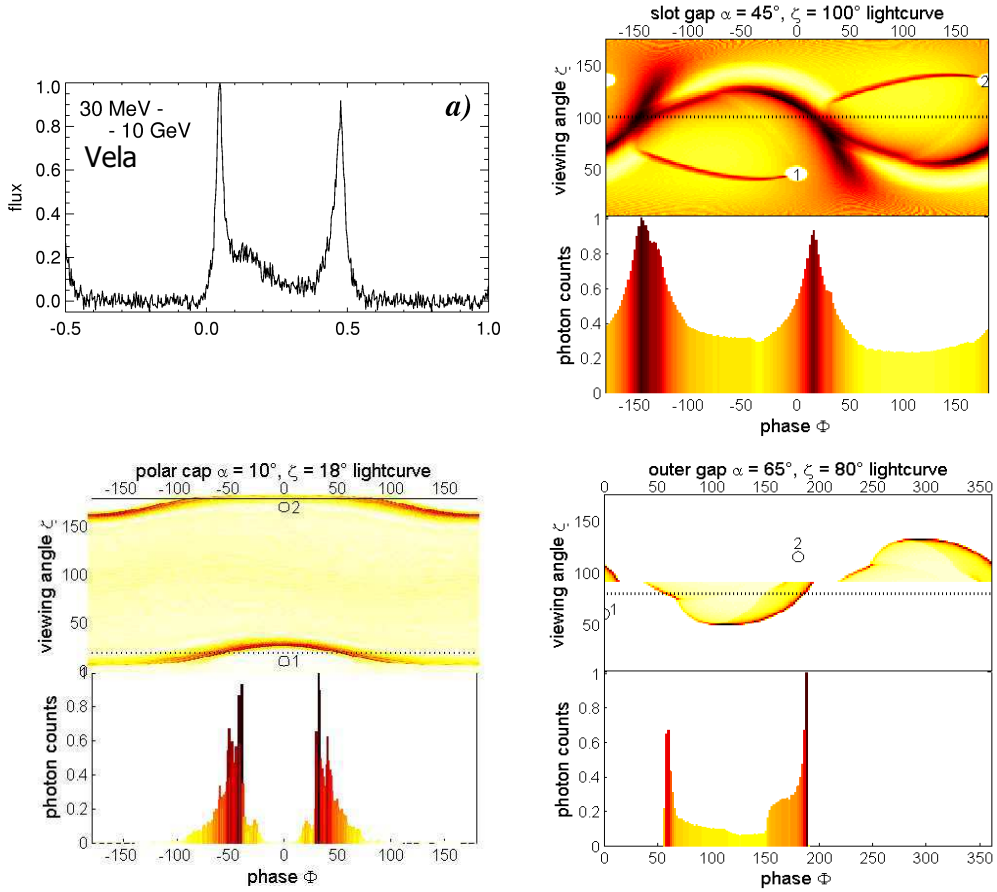

Figure 2.2: *Upper left:* γ-ray light curves of Vela pulsar seen with the EGRET telescope in the energy band of 30 MeV−10 GeV. *Others:* Light curve simulations with different emission models (*Polar Cap*, *Slot Gap* et *Outer Gap*) and for different geometric configurations (α, ζ). α is the inclination angle between the magnetic axis and the rotation axis, ζ is the line of sight with respect to the rotation axis. For each model, the upper panel represents the γ-ray emission as a function of the rotational phase Φ (from $-180°$ to $180°$ or $0°$ - $360°$) and the line of sight ζ. For a given ζ (dashed line) and α, the lower panel shows the corresponding observed light curves. Adapted from Harding (2007).

Light curves and geometry

The observed light curves depend on the pulsar geometry: for a given magnetic inclination α, observers with different lines of sight ζ with respect to the pulsar rotation axis will observe different pulse profiles or even no pulsation can be detected. This can be clearly inferred from Figure 2.2. The OG and SG models predict less symmetric profiles than the PC model since the emission is produced to higher altitudes. Note that recent work of e.g. Du *et al.* (2011) and Wang *et al.* (2011) have been able to successfully explain the third peak evolution of Vela pulsar in the context of a full treatment of magnetospheric radiation spectrum.

The observed pulsar emission does not represent its total all-sky emission. This leads to a beaming factor f_Ω which corrects the observed flux to obtain the all-sky flux (Watters *et al.* 2009):

$$f_\Omega(\alpha,\zeta) = \frac{\int\int F_\gamma(\alpha,\zeta,\phi)\sin\zeta\, d\zeta\, d\phi}{2\int F_\gamma(\alpha,\zeta,\phi)\, d\phi} \tag{2.5}$$

with $F_\gamma(\alpha, \zeta, \phi)$ the predicted flux along the line of sight at ζ for a pulsar with magnetic inclination α and over pulse phase ϕ. f_Ω is certainly model dependent. Light curve simulations for different models give possible configurations of (α, ζ), thus f_Ω, which in turn help to discriminate between models by comparing them with the observed profiles.

2.2 γ-ray observations

2.2.1 γ-ray pulsars before *Fermi*

The first pulsars detected in γ rays were Vela and the Crab by the *Small Astronomy Satellite* (SAS-2, Fichtel *et al.* 1975) and *COsmic ray Satellite (option B)* (COS-B, Swanenburg *et al.* 1981) in the 1970s, marking the start of the γ-ray astronomy. Before the launch of *Fermi*, only seven γ-ray pulsars (Figure 2.3), including Vela, the Crab and Geminga (Blgnami & Caraveo 1992) had been detected with high confidence by the *Energetic Gamma Ray Experiment* (EGRET) and *COMPton TELescope* (COMPTEL) aboard the *Compton Gamma Ray Observatory* (CGRO) operated in the 1990s (Thompson *et al.* 1993). Geminga is undetected at radio wavelengths. There were two new detections (J2021+3651, J2229+6114) by the *Astrorivelatore Gamma and Immagini LEggero* (AGILE, Tavani *et al.* 2009) just a few months after *Fermi* started observations in Aug 2008. These pulsars are amongst the most energetic ones with high spin-down power ($\dot{E}$) and are relatively close to the Earth (the distance of J2021+3651 is controversial, Section 7.2.1). They are certainly confirmed later by *Fermi*.

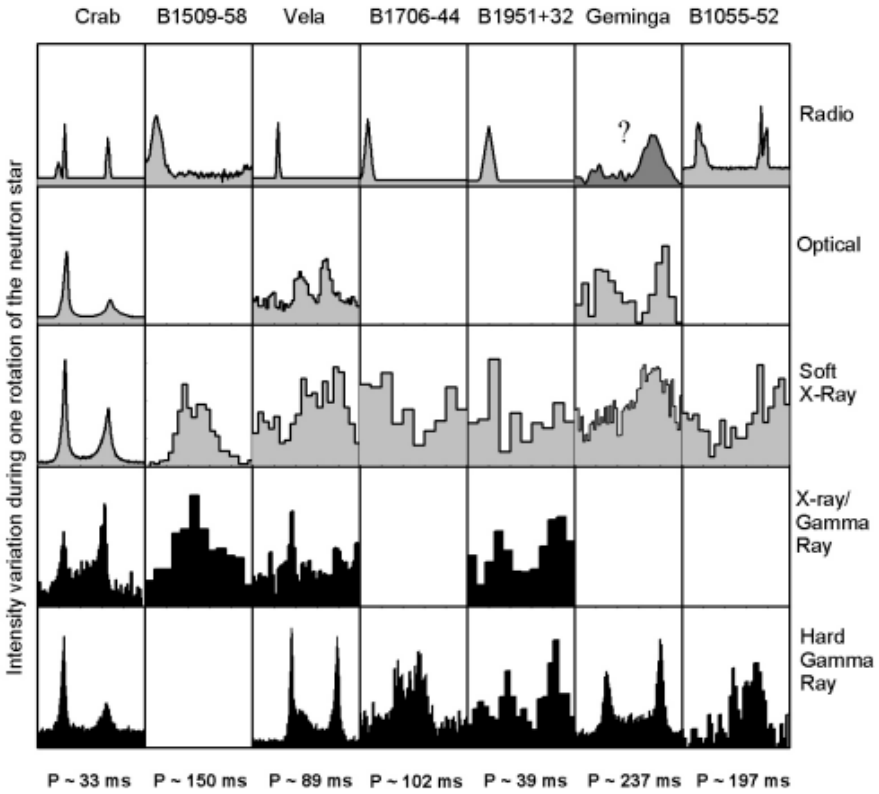

Figure 2.3: Multi-wavelength light curves of seven γ-ray pulsars detected by EGRET/COMPTEL aboard CGRO (Thompson 2008).

2.2.2 γ-ray pulsar candidates for *Fermi*

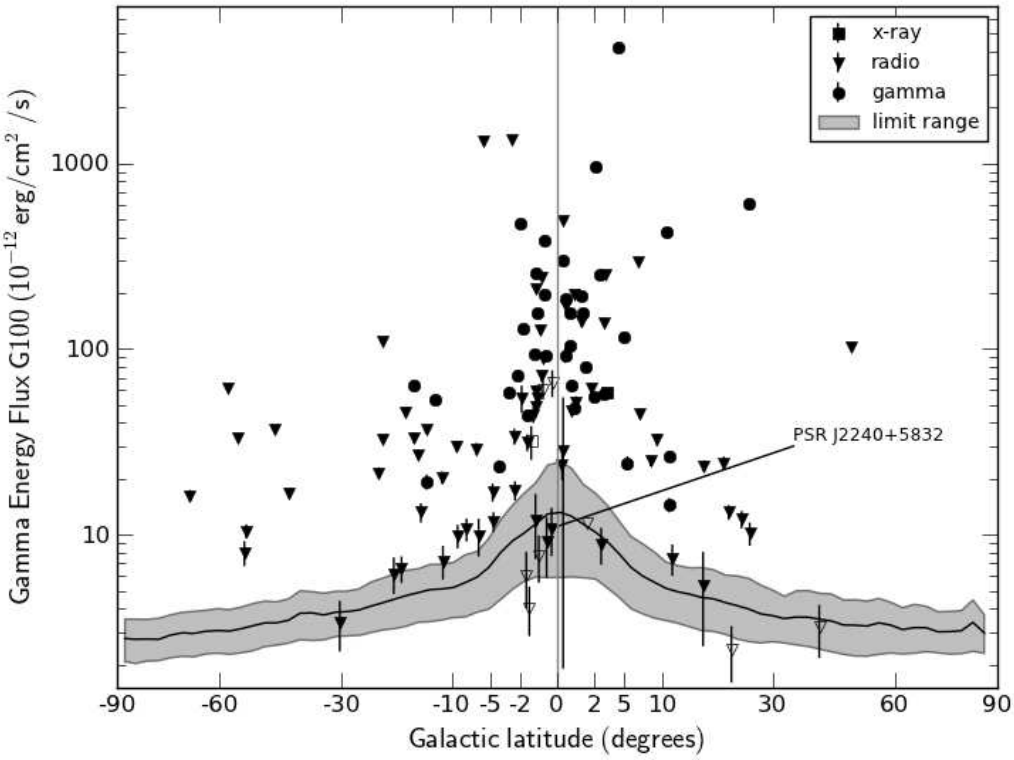

Figure 2.4: Integral energy flux from 0.1 to 100 GeV, G_{100} vs. Galactic latitude b (scaled as $b^{0.65}$ for clarity). Circles indicate gamma-selected pulsars discovered in blind period searches (Section 4.2), while triangles and squares indicate previously known pulsars discovered in gamma rays by phase-folding with rotation ephemerides (Section 4.1) obtained from radio or X-ray data. Open symbols indicate TS < 25 (Section 5.2.4). The gray band shows the 10% to 90% percentile range of the three-year mean sensitivity for point-source detection averaged over longitude. Adapted from 2PC (Abdo *et al.* 2013).

The EGRET pulsars all have $\dot{E} \gtrsim 3 \times 10^{34}$ ergs s^{-1} (Thompson *et al.* 1999). Taking into account the uncertainty caused by the unclear emission geometry and the not well-known relation between $\dot{E}$ and the observed γ-ray flux, a list of γ-ray candidates for *Fermi* was established from the ATNF pulsar catalog with a criterion of $\dot{E} \geq 10^{34}$ ergs s^{-1}. This resulted in 218 pulsars excluding some in globular clusters which have unphysical $\dot{E}$ due to the acceleration in the gravitational potential field. This is the list of pulsars for which regular timing has been organized since 2007, prior to the launch of *Fermi* (Chapter 4, Smith *et al.* 2008). To quantify the detectability, we introduce the γ-ray luminosity:

$$L_\gamma = 4\pi d^2 f_\Omega G_{100} \tag{2.6}$$

with d the pulsar distance, f_Ω the beaming factor (Equation 2.5) and G_{100} the observed γ-ray energy flux above 100 MeV. Assuming a linear dependence of L_γ on the open field line voltage $V \simeq 3.18 \times 10^{-3}\sqrt{\dot{E}}$ volts, above some threshold of which e^+e^- cascades occur (Arons 1996), gives $L_\gamma \propto \sqrt{\dot{E}}$. The γ-ray efficiency is:

$$\eta = \frac{L_\gamma}{\dot{E}} \tag{2.7}$$

We obtain $\eta \propto 1/\sqrt{\dot{E}}$. A figure-of-merit for the detectability is then defined as:

$$F_{\rm eff} = \eta \frac{\dot{E}}{d^2} = \frac{\sqrt{\dot{E}}}{d^2} \tag{2.8}$$

This is proportional to the effective flux observed on Earth which is the spin-down flux $\dot{E}/d^2$ scaled with the γ-ray efficiency. This quantity gives us an idea about the most promising candidates in the 218 pulsars selected. For pulsars with similar $\dot{E}$, the closer ones will be easier to detect. Nevertheless, one should bear in mind that this quantity doesn't take into account the pulsar emission geometry and the local background level. As is shown in Figure 2.4, the detectable flux is very Galactic latitude dependent, the worst case is in the Galactic plane ($b = 0$) where a higher energy flux is needed to be detectable. In addition, the distance is usually not well-constrained. Therefore the implied uncertainty may result in the non-detection of pulsars in γ rays with high $\sqrt{\dot{E}}/d^2$. In fact, according to this ranking, the six EGRET pulsars are classified among the first 20, while there are some pulsars non-detected by EGRET in the first 10.

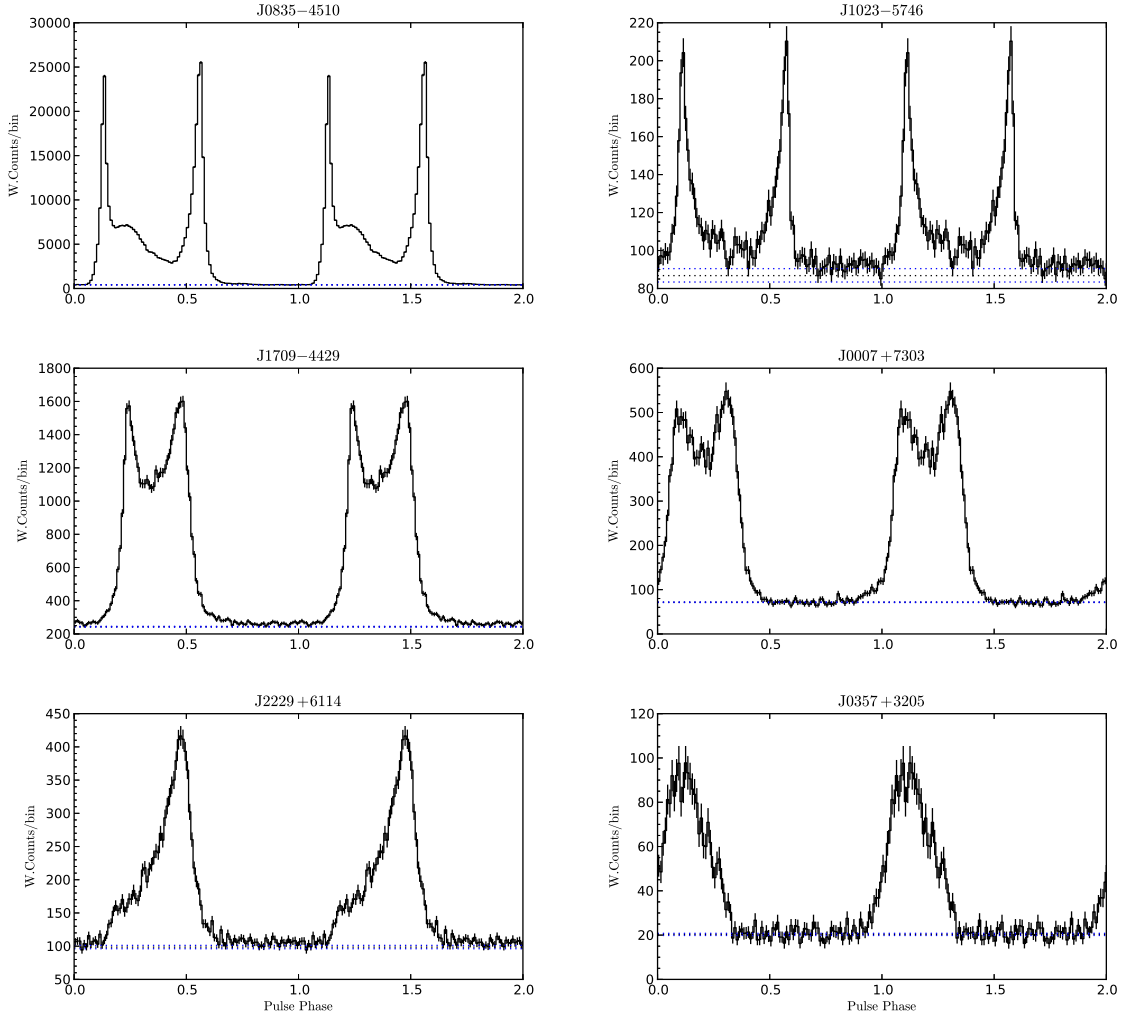

Figure 2.5: Examples of *Fermi* γ-ray pulsar light curves above 100 MeV. Left: radio-loud pulsars; Right: radio-quiet pulsars. Adapted from 2PC (Abdo *et al.* 2013).

2.2.3 *Fermi* γ-ray pulsars

1PC established pulsars as the dominant GeV γ-ray source class in the Milky Way (Abdo *et al.* 2010b). MSPs were identified as γ-ray emitters for the first time and constitute a subclass of γ-ray pulsars (see e.g. Abdo *et al.* 2009d). 2PC included 117 γ-ray pulsars which can be evenly divided into three categories: 42 LAT young radio-loud pulsars (defined as S1400 $> 30\mu$Jy with S1400 the radio flux density at 1.4 GHz), 35 LAT young radio-quiet pulsars and 40 LAT radio-loud MSPs.

Figure 2.5 shows some examples of *Fermi* γ-ray pulsar light curves in 2PC. As observed in 1PC, MSPs and young pulsars have similar light curves, but MSPs exhibit a certain complexity. The majority of the pulsars have two peaks with sharp outer edges suggesting caustic emissions from a hollow cone. Another feature is that for pulsars with two peaks, the ratio of P1/P2 increases with energy. A few pulsars have evidence for a third peak, like Vela (J0835−4510), which is not expected from a simple caustic origin. Full radiation modelling is needed besides the geometrical approximation in order to explain this structure. Most young pulsars have an anti-correlation between the radio lag δ and the γ-ray peak separation Δ ($\Delta \propto -\delta$) in terms of rotational phase, which is a general property of outer magnetosphere models with caustic profiles (Romani & Yadigaroglu 1995). MSPs have less correlation and larger δ and Δ than young pulsars.

Figure 2.6 shows examples of *Fermi* γ-ray pulsar spectra modeled with a power law + simple exponential cutoff (PLEC1, $b = 1$ in Equation 2.4) which is predicted by outer magnetosphere models. *Fermi* observations favor PLEC1. Evidence of correlation between the spectral index Γ and $\dot{E}$: higher $\dot{E}$, softer spectrum (larger Γ), has been observed separately for young pulsars and MSPs, with MSPs having a steeper slope. By contrast, no such correlation is observed between the cutoff energy $E_{\rm cut}$ and $\dot{E}$.

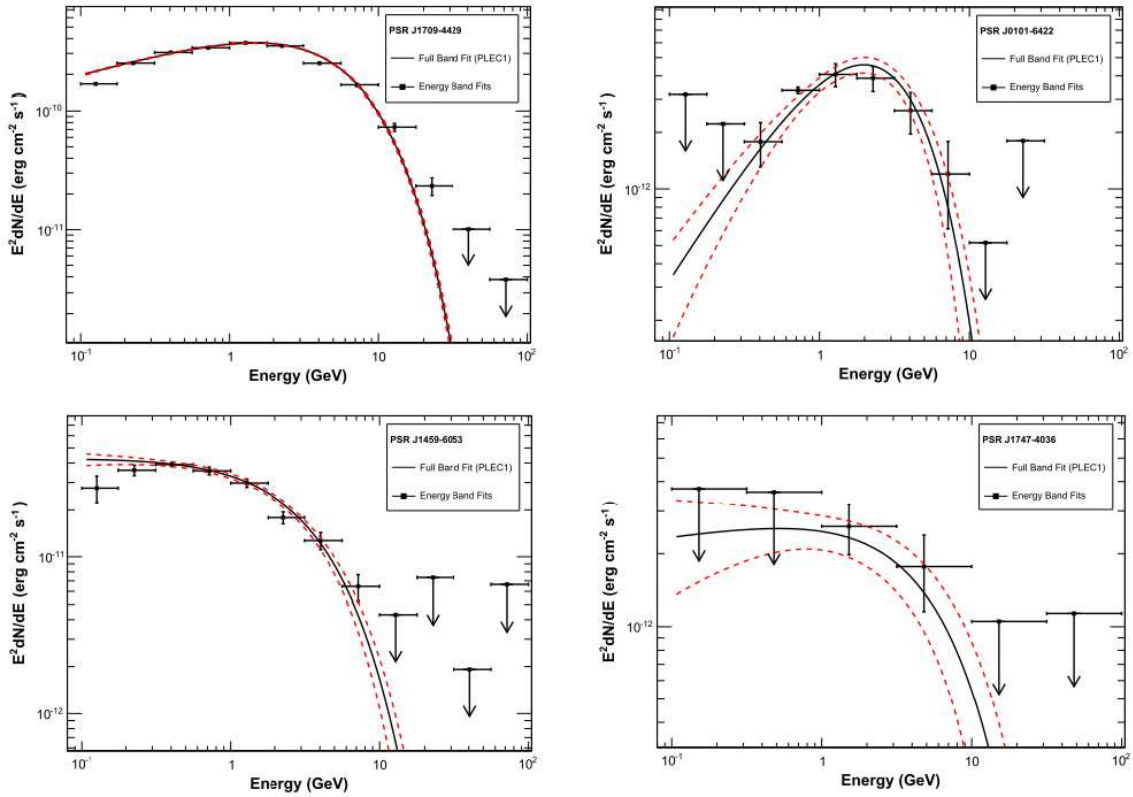

Figure 2.6: Examples of *Fermi* γ-ray pulsar spectra modeled with a power law + simple exponential cutoff (PLEC1) in the energy band of 100 MeV−100 GeV. Adapted from 2PC (Abdo *et al.* 2013).

The increasing number of γ-ray pulsars detected by *Fermi* offers an excellent opportunity to perform a statistical study of pulsar emission mechanisms and regions. Examples[4] of simulations can be found in e.g. Venter *et al.* (2009), Watters *et al.* (2009), Romani & Watters (2010), Du *et al.* (2013), Pierbattista *et al.* (2013) and Johnson *et al.* (2013). These works favor the outer magnetosphere models and a $f_\Omega \backsim 1$ almost valid for all of them. In general, γ-ray emission is suggested to be distributed in a narrow gap bordering the closed field line boundary, favoring the outer magnetosphere model, but no single model can best fit all the observed light curves.

Beyond the 117 γ-ray pulsars included in 2PC, more and more fainter pulsars are being discovered. In Chapter 6, I will present some new detections in detail, which further enrich the current *Fermi* pulsar sample.

[4]The Striped Wind model is not included in these works.

PART II

INSTRUMENT

CHAPTER 3

The *Fermi* Large Area Telescope (LAT)

Contents

3.1 The *Fermi* satellite

Launched on 2008 June 11, the *Fermi Gamma-ray Space Telescope (Fermi)* of the National Aeronautics and Space Administration (NASA), formerly the *Gamma-ray Large Area Space Telescope (GLAST)*, is a satellite dedicated to the high energy study of astrophysical sources (Figure 3.1). It was developed within an international collaboration between the United States, France, Italy, Sweden, Germany and Japan. The operation duration of *Fermi* has been extended to 2016 by NASA compared to 2013 at the beginning of the project.

Objectives

With much improved performance (field of view, angular resolution, energy resolution..., Table 3.1, Section 3.3) compared to its precedent instrument EGRET on board of CGRO (Thompson *et al.* 1993) and an energy band of 8 keV to $>$ 300 GeV, *Fermi* offers an excellent opportunity to study various astrophysical sources and also permits the multi-wavelength observations in collaboration with other telescopes.

Among the scientific objectives addressed by *Fermi*, we find: (1) determining the nature of the unidentified sources and the origin of the diffuse emission revealed by EGRET; (2) understanding the particle acceleration mechanisms in celestial sources, particularly in active galactic nuclei (AGNs), pulsars, PWNs and SNRs; (3) understanding the high-energy behavior of γ-ray bursts (GRBs) and transients; (4) using γ-ray observations as a probe of dark matter and the early universe.

Composition

Fermi has two instruments (Figure 3.2):

- Large Area Telescope (LAT): the main instrument of *Fermi*. It's designed to measure the directions and arrival times of photons in the energy range of 20 MeV to $>$ 300 GeV while rejecting charged particles (Atwood *et al.* 2009). It is composed of three detectors: the Converter-tracker, the calorimeter and the anti-coincidence detectors. Details will be presented in Section 3.2.

- Gamma-ray Burst Monitor (GBM): dedicated to the study of GRBs in the energy range of 10 keV−30 MeV. It is composed of 12 NaI scintillator detectors and 2 bismuth germinate (BGO) scintillation detectors. More information can be found in Meegan *et al.* (2009).

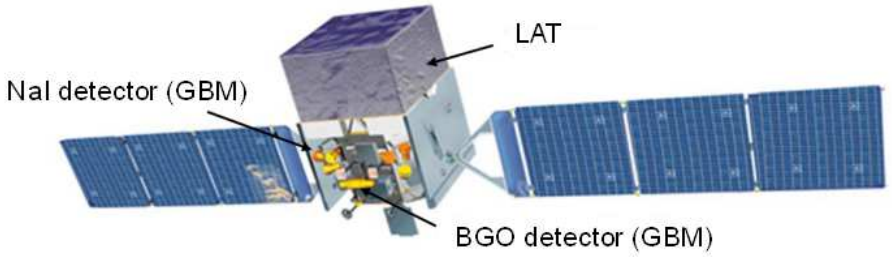

Figure 3.1: The *Fermi Gamma-ray Space Telescope*

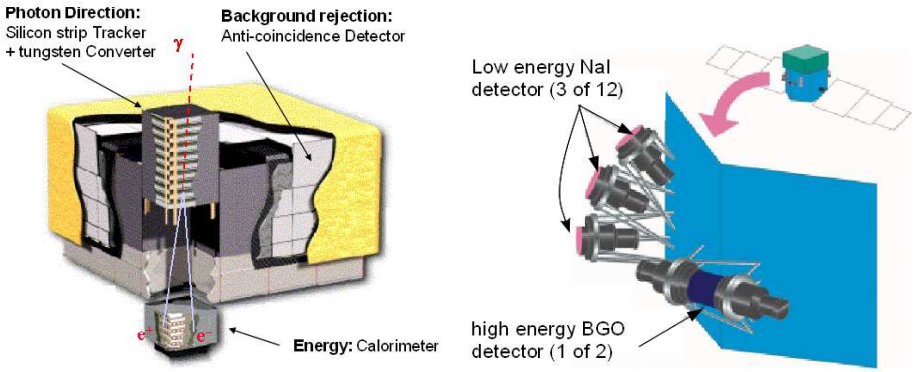

(A) LAT (B) GBM

Figure 3.2: The Large Area Telescope (LAT) and the Gamma-ray Burst Monitor (GBM)

Operation

Fermi orbits the Earth quasi-circularly at an altitude of ∼565 km and an inclination of 25.5 ° with a period of 95 minutes (Atwood *et al.* 2009). It is operated essentially in "Survey" mode to take advantage of the LAT's large field of view (FoV, 2.4 steradian, 20% of the sky at any moment): the LAT is oriented with a *rocking angle* of ±50° (angle between the instrument z axis and the zenith, towards the pole of the orbit) for each alternate orbit. This permits observing the sky continually and uniformly. The whole sky is observed every 2 orbits (about 3 hours) which gives uniform sky exposure. *Fermi* can change to "Pointing" mode when there is a particular interesting target detected, e.g. GRB, sun flare, etc. In this case, the LAT points to the target for several hours in order to accumulate more photons.

3.2 LAT subsystems

3.2.1 Principle of detection

At high energy ($>$ 5 MeV), the light-matter interaction is dominated by the e^+e^- pair production of γ rays when interacting with the electric field of the material. The LAT is thereby a pair-conversion tele-

scope. Information on the incident photon or charged particles (cosmic rays) is recorded by three detector subsystems of the LAT: (1) the Converter-Tracker (TRK) enables the pair-conversion and records the path of the photon or particles; (2) the Calorimeter (CAL) measures the energy deposition of e^+e^- in the electromagnetic shower and images the shower profile for the purpose of background rejection; (3) the Anti-Coincidence Detector (ACD), covering the tracker, distinguishes photons from charged particles and rejects the latter. Together with a trigger and Data Acquisition System (DAQ), the most-likely γ-ray events are recorded and transmitted to the ground for scientific use.

3.2.2 Converter-Tracker

The TRK has 16 modules assembled in a 4×4 grid (Figure 3.3 (A)). Each module consists of 18 parallel $x-y$ planes and each plane has 2 layers (x and y) of single-sided Silicon-Strip Detectors (SSDs) oriented perpendicular to each other. The z axis is the normal to the instrument's detection surface. The paths of the incident photons or charged particles are therefore traced in three dimensions. Each SSD layer has an area of 8.95×8.95 cm^2 and a thickness of 400 μm. Two adjacent layers are separated by 228 μm. Interleaved between the 18 tracking planes are the high-Z (atomic number) tungsten foils in which γ rays are converted into e^+e^- pairs.

The conversion probability depends on the radiation length X_0, hence the thickness of the material. The thicker the material, the more pair conversions. Thicker converters are thus preferred to maximize the effective area ($\propto$ conversion probability, Section 3.3.2) at high energy. On the other hand, the angular resolution (PSF, $\sim$ 1/E, Section 3.3.2) concerning the reconstructed directions of incident photons prefers a thinner material to decrease the multiple scattering of e^+e^- at low energy. The configuration of tungsten foils is thereby arranged (Figure 3.3 (B)) to balance these two contradictory needs : the first top 12 planes have thin tungsten converters with 0.03 X_0 to assure good angular resolution at low energy (front region), while the next 4 planes with converters of 0.18 X_0 maximize the effective area and sacrifice a factor of 2 in angular resolution (back region). The last 2 planes have no tungsten foils since the TRK trigger requires hits[1] in three adjacent $x-y$ planes. According to the region where the conversion has happened, photons are identified as two different classes: FRONT and BACK. The converter-tracker is maintained by 19 composite trays, supported by carbon-composite side walls.

The direction of the incident photon which converts to e^+e^- in one of the tungsten foils is reconstructed by measuring the trajectory of the pair with their (x,y,z) coordinates traced by the SSDs of each tracker module that are hit by the pair.

3.2.3 Calorimeter

Like the TRK, the CAL is also a 4×4 grid of 16 modules. Each module consists of 8 layers of 12 CsI (TI) crystals with a size of 2.7 cm × 2.0 cm × 32.6 cm. The crystals are optically isolated from each other and are arranged horizontally in each layer. Each layer is perpendicular to its adjacent one along the x and y directions (Figure 3.4). There are 2 photodiodes at each end of the crystal with different sizes to measure the scintillation light of the crystal. The bigger photodiode is for the low energy range (2 MeV$-$1.6 GeV), while the smaller one is for the high energy range (100 MeV$-$70 GeV). Each photodiode is connected to an electronic system to amplify the signal. The entire calorimeter module is supported by a carbon composite.

The thickness of the CAL (= 8.6 X_0) permits the development of an electromagnetic shower created by the incident photons in the TRK. The CAL measures the energy deposition of the e^+e^- pair and, by imaging the shower developing profile, to localize the position of the energy deposition. The energy is estimated by measuring the scintillation light by the photodiodes created when particles go through the crystals. The position of the energy deposition is measured with the (x,y,z) coordinates of the crystals in the array, similar

[1] "hit" refers to the detection of the path of a photon or a charged particle through a silicon strip and the recording of the strip localization.

to the principle of the TRK, but with less precision. By reconstructing the shower trajectories combining the total energy of particles, the energy of the incident photon which has first triggered the electromagnetic shower in the TRK is determined. The imaging capacity of the CAL also plays an important role in the rejection of cosmic ray induced electromagnetic showers.

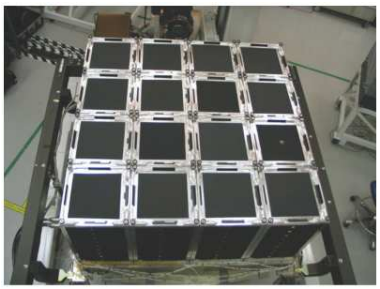

(A) Tracker grid

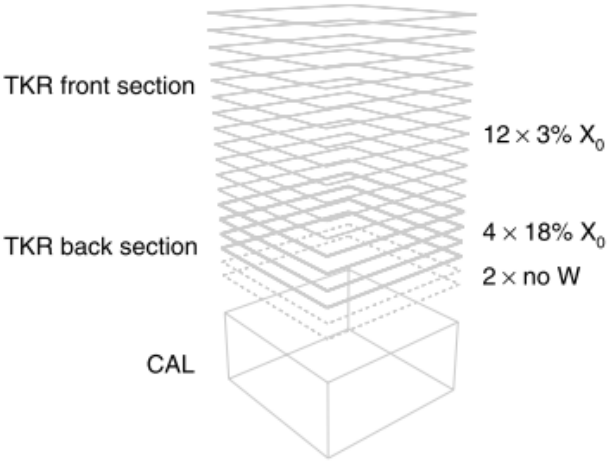

(B) LAT tower (TRK+CAL)

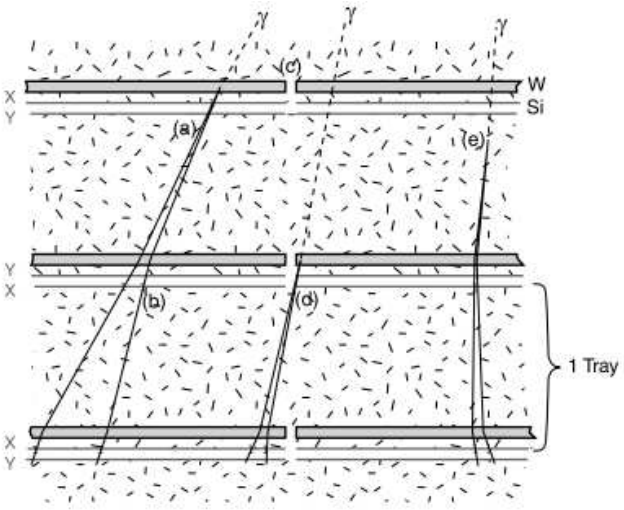

(C) Pair production

Figure 3.3: (A) The assembly of the TRK of the LAT (Atwood *et al.* 2009). (B) Illustration of a LAT tower including a TRK and a CAL module (Ackermann *et al.* 2012a). (C) Pair production in the TRK with dashed lines representing the γ-ray photon trajectories and solid lines those of the $e^+ e^-$ pair (Atwood *et al.* 2009).

3.2.4 Anti-Coincidence Detector

The ACD is a critical subsystem of the LAT with the purpose of rejecting cosmic rays coming from every direction. The ratio of cosmic ray particles (mostly protons) to γ rays being $\sim 10^4$, the ACD is required to have a high detection efficiency of at least 99.97% for charged particles entering the FoV of the LAT. The principle is: γ rays interact little with the ACD. A coincident signal detected by the ACD and the

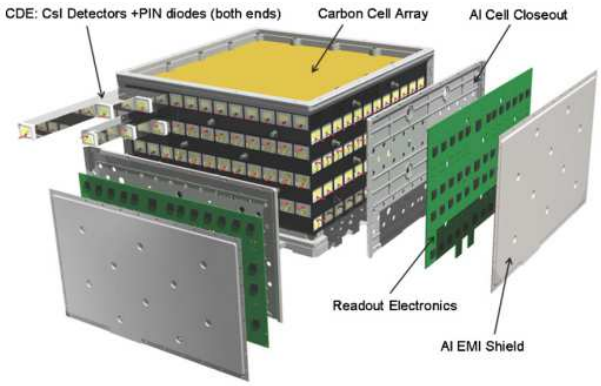

Figure 3.4: The LAT calorimeter module. The 96 CsI (TI) crystal detectors are arranged in 8 layers with each one rotating 90° relative to its neighbor (Atwood *et al.* 2009).

TRK corresponds to a charged particle, while a signal in the TRK not detected by the ACD represents a γ-ray photon.

The ACD consists of 89 scintillating plastic tiles and 8 scintillating fiber ribbons to cover the gaps. The scintillation light in each tile created by the charged particles is retrieved by the wavelength shifting fibers (WLS) and is transmitted to two photomultiplier tubes (PMTs) for redundancy (Figure 3.5).

The high mass of the CAL ($\sim$ 1800 kg) creates a "backsplash" effect (Figure 3.5 (B)): the electromagnetic shower initialized by incident high energy photons can create low energy photons ($10-1000$ keV) which may enter the ACD and interact with electrons by Compton scattering creating thereby a false veto signal with the scattered electrons. This "self-veto" effect limits the photon detection and has resulted in an efficiency above 10 GeV two times lower than at 1 GeV for EGRET. The fact that the ACD is segmented permits the reduction of this effect by comparing the triggered ACD segments to the incident direction measured by the TRK: signals far from this direction are considered as "backsplash" and ignored, no veto is sent. The design requirement is that no more than 20% of incident photons are rejected at 300 GeV due to the "backsplash" effect.

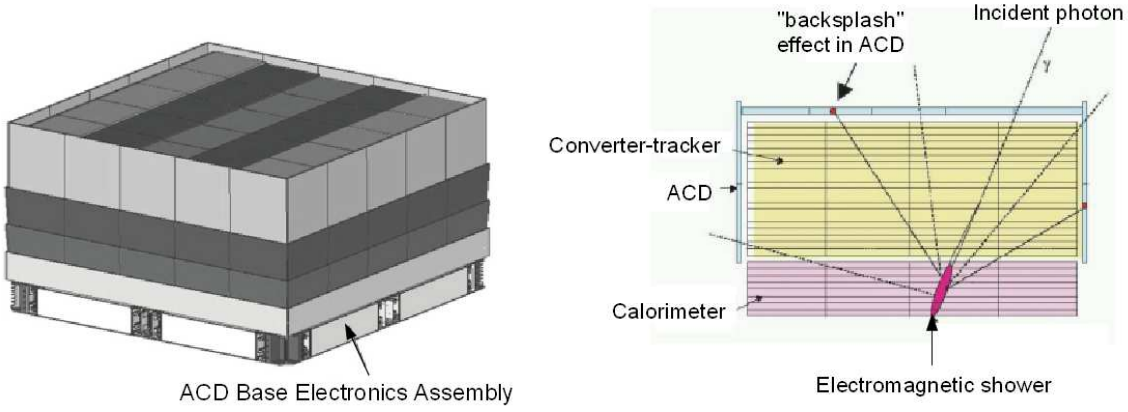

(A) ACD (B) "backsplash" effect

Figure 3.5: (A) The LAT ACD design (Atwood *et al.* 2009). (B) Illustration of the "backsplash" effect in the LAT ACD.

Parameter	Value
Dimensions	$1.8 \times 1.8 \times 0.72$ m^3
Total mass	2789 kg
Energy band	20 MeV – $>$ 300 GeV
Maximum effective area (normal incidence)	$\sim$8000 cm^2
Field of view (foV)	2.4 sr
Event readout time (dead time)	26.5 μs
Time precision	$< 1\mu$s
Energy resolution (normal incidence, 1σ Gaussian) :	
100 MeV – 1 GeV	9% – 15%
1 GeV – 10 GeV	8% – 9%
$\geq$ 10 GeV	8.5% – 18%
Angular resolution (normal incidence, 68% PSF) :	
100 MeV	3.5°
1 GeV	0.6°
$>$ 10 GeV	$\leq$ 0.15°

Table 3.1: LAT instrument parameters and estimated performances (Atwood *et al.* 2009), except the time precision which is achieved (Abdo *et al.* 2009a).

3.2.5 Data Acquisition System and trigger

The DAQ on board the LAT collects the trigger primitives (or trigger requests) from the combination of the above three subsystems and issues a global trigger (or trigger accept) if these primitives satisfy some specified conditions. The event is then read out and passed to the on-board filter. Due to the limited telemetry bandwidth, the filter reduces the event rate from $2-4$ kHz to $\sim$ 400 Hz by rejecting the charged particle background while maximizing the rate of γ-ray photons within the 400 Hz. This resulted dataset is then transmitted to the ground for further reconstruction and analysis as will be discussed in 3.3.

3.3 LAT performance

The performance of the LAT is determined by the instrument characteristics, the event reconstruction algorithms (the accuracy and efficiency of determining the event direction and energy) and the event selection algorithms (the efficiency of identifying well reconstructed γ rays). The development of the algorithms and the resulted performance rely on Monte Carlo simulations of γ-ray interactions with the LAT. Along with the *Fermi* mission, real data has served as the best source of calibration data to account for on-orbit effects and thereby to improve the LAT performance. Table 3.1 summarizes the LAT instrument parameters and estimated performance. Details can be found in Abdo *et al.* (2010a), Nolan *et al.* (2012), Ackermann *et al.* (2012a,b), Bregeon *et al.* (2013).

3.3.1 Event reconstruction and classification

The raw data downlinked to the ground undergoes more analysis before becoming finally usable by the end user as high quality γ-ray data (Figure 3.6, Ackermann *et al.* 2012a). The first step involves the event reconstruction which estimates the possible tracks and energies of each event ranked by the probability of being charged particles which will be rejected later in the event-level analysis stage. In this event-level

analysis stage, a set of "Figure-of-merit" quantities are extracted from the reconstruction output. By applying a Classification Tree (CT) method, best estimates of track and energy are assigned to each event. The Charged Particles in the FoV (CPF) analysis distinguishes γ rays from particle background and removes more than 95% of the latter while sacrificing 10% of the γ rays. Since e^+ and e^- (can come from the electromagnetic shower of incident photons or from cosmic rays) produce electromagnetic showers that look extremely similar to incident γ-ray photon interactions with the material, the unidentified cosmic ray backgrounds in the CPF stage are now identified based on the topology (e.g. shape, density, and smoothness). A final CT analysis is applied making use of the output of previous analysis to define the standard γ-ray event classes.

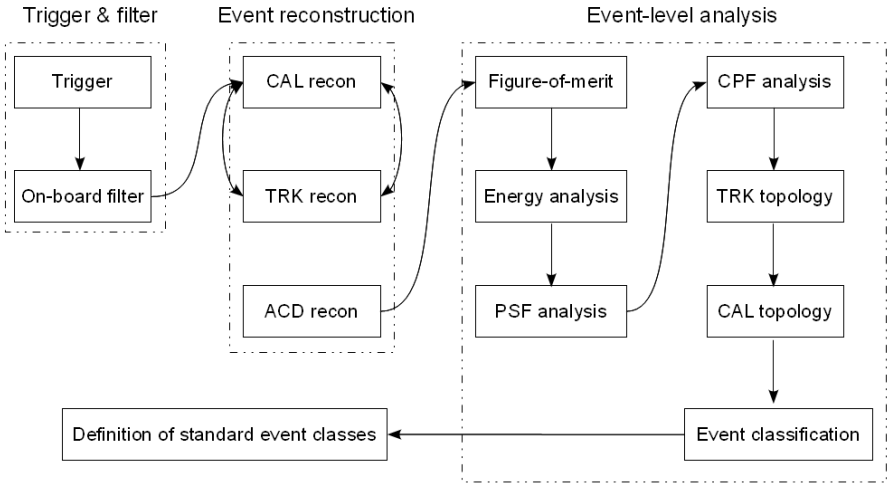

Figure 3.6: Structure of the analysis steps for event classification (Ackermann *et al.* 2012a).

The broad range of LAT observations and analysis leads to different event selection criteria and different background residuals corresponding to different event classes. On the other hand, improved event analysis algorithms using real LAT events accumulated in the past years have yielded the re-optimized data set *Pass 7* since 2011 August over *Pass 6* (Atwood *et al.* 2009; Rando & for the Fermi LAT Collaboration 2009) whose analysis scheme was defined prior to the launch of *Fermi*. The resulted *Pass 7* includes four event classes (Ackermann *et al.* 2012a):

- P7TRANSIENT, suitable for transient sources (e.g. GRB, Sun flare), has the most relaxed background rejection cuts since the short time window and the small region of interest in the sky limit the amount of background. The background residual is of a few Hz while maintaining a high γ-ray efficiency.
- P7SOURCE, designed for point source analysis, is a subclass of P7TRANSIENT class. More strict cuts on the same quantities as for P7TRANSIENT are applied to ensure a high enough signal-to-noise ratio which is essential for point source localization and characterization. The remaining background is less than ~ 1 Hz.
- P7CLEAN, intended for Galactic diffuse γ-ray emission, is a subclass of P7SOURCE class. Additional cuts are applied to reduce the contamination level to ~ 0.1 Hz, being below the extragalactic γ-ray background at all energies.
- P7ULTRACLEAN, defined for the extragalactic diffuse γ-ray emission, is a subclass of P7CLEAN class. The contamination is reduced to be even further below the extragalactic γ-ray background, for example, be 40% lower than the P7CLEAN class at around 100 MeV.

The residual background presented in the final event classes is integrated to the isotropic diffuse emission template (Section 5.2.1) to be accounted for in the spectral analysis of astrophysical sources.

A number of calibration constants is required to enable the *Fermi*-LAT data acquisition system to work properly (Abdo *et al.* 2009a) and is tracked by the LAT team. Most of them are stable. The main shift happens for the scintillation light yield of the CAL CsI (Tl) crystals. A $\sim 1\%$ per year decrease due to the on-orbit radiation damage after three years operation has been observed. The full LAT data has therefore been reprocessed (P7REP[2]) with new calibration accounting for the shift. The major effects of the P7REP data against *Pass 7* are a slight increase in the LAT energies of the events and more accurate direction reconstructions at energies greater than $\sim$3 GeV. This leads to the optimized P7REP IRFs (Section 3.3.2) and new diffuse models to accurately reflect the improved performance of the P7REP data. In this thesis, the P7REP_SOURCE_V15 IRFs [3] and the corresponding reprocessed diffuse models have been used for the analysis of some recently detected pulsars (Chapter 6).

3.3.2 Instrument response functions

Due to different selections used in the event reconstruction and analysis procedure, each event class has its associated Instrument Response Functions (IRFs) which can be formulated in general as:

$$\mathrm{IRF}(\theta^{'},E^{'};\theta,E) = \mathrm{A_{eff}}(\theta,E) \times \mathrm{PSF}(\theta^{'};\theta,E) \times P_E(E^{'};\theta,E) \tag{3.1}$$

with

- $\mathrm{A_{eff}}(\theta,E)$ Effective Area of the LAT which is the ratio of the number of photons detected and accepted by the analysis, and the incident flux of a γ-ray source during a period of time.

- $PSF(\theta^{'};\theta,E)$ *Point Spread Function*, i.e. the probability density of reconstructing a direction $\theta^{'}$ for an incident photon of angle θ and energy E.

- $P_E(E^{'};\theta,E)$ Energy dispersion, i.e. the probability density of reconstructing an energy $E^{'}$ for an incident photon of angle θ and energy E.

As mentioned in Section 3.2, FRONT and BACK events are treated separately, which leads to separated IRFs accordingly.

Effective area

The upper left panel of Figure 3.7 shows the on-axis (normal incident angle $\theta = 0^{\circ}$) evolution of the effective area with energy. For Total (FRONT+BACK) events, the effective area is ~ 7000 cm^2 at 1 GeV, increasing with energy and reaching ~ 8000 cm^2 at 10 GeV. The upper right panel shows the θ dependence of the effective area at 10 GeV, averaged over the azimuthal angle ϕ. It decreases with θ.

PSF

The PSF can be translated in general as the angular resolution, or the angular deviation for an incident photon. At low energy, it's determined by the multiple scattering. The middle left panel of Figure 3.7 shows the energy dependence of the PSF at normal incidence. The 68% containment for Total events is $\sim 5^{\circ}$ at 100 MeV and $\sim 0.8^{\circ}$ at 1 GeV, decreasing to less than 0.2° at 100 GeV. The middle right panel shows the θ dependence of the PSF for $\phi = 0^{\circ}$.

[2] http://fermi.gsfc.nasa.gov/ssc/data/analysis/documentation/Pass7REP_usage.html

[3] http://www.slac.stanford.edu/exp/glast/groups/canda/lat_Performance_files/

Energy resolution

The energy resolution is usually a figure-of-merit to express the energy dispersion. It's defined as $\Delta E/E$ with ΔE the half width of the 68% energy containment and E the most probable value or the peak of the energy dispersion. The lower left panel of Figure 3.7 shows the on-axis energy resolution as a function of energy. It is maximized in the broad range of $1-10$ GeV, decreasing at lower energies due to the energy deposit in the TRK, and at higher energies due to the leakage of the electromagnetic shower in the CAL. For a given energy of 10 GeV, the energy resolution increases with the incident angle (lower right panel) since a bigger θ implies a longer path in the CAL, thus less energy leakage. The FRONT events with $\theta \geq 55^\circ$ tend to leave the sides of the CAL and result in worse energy resolution.

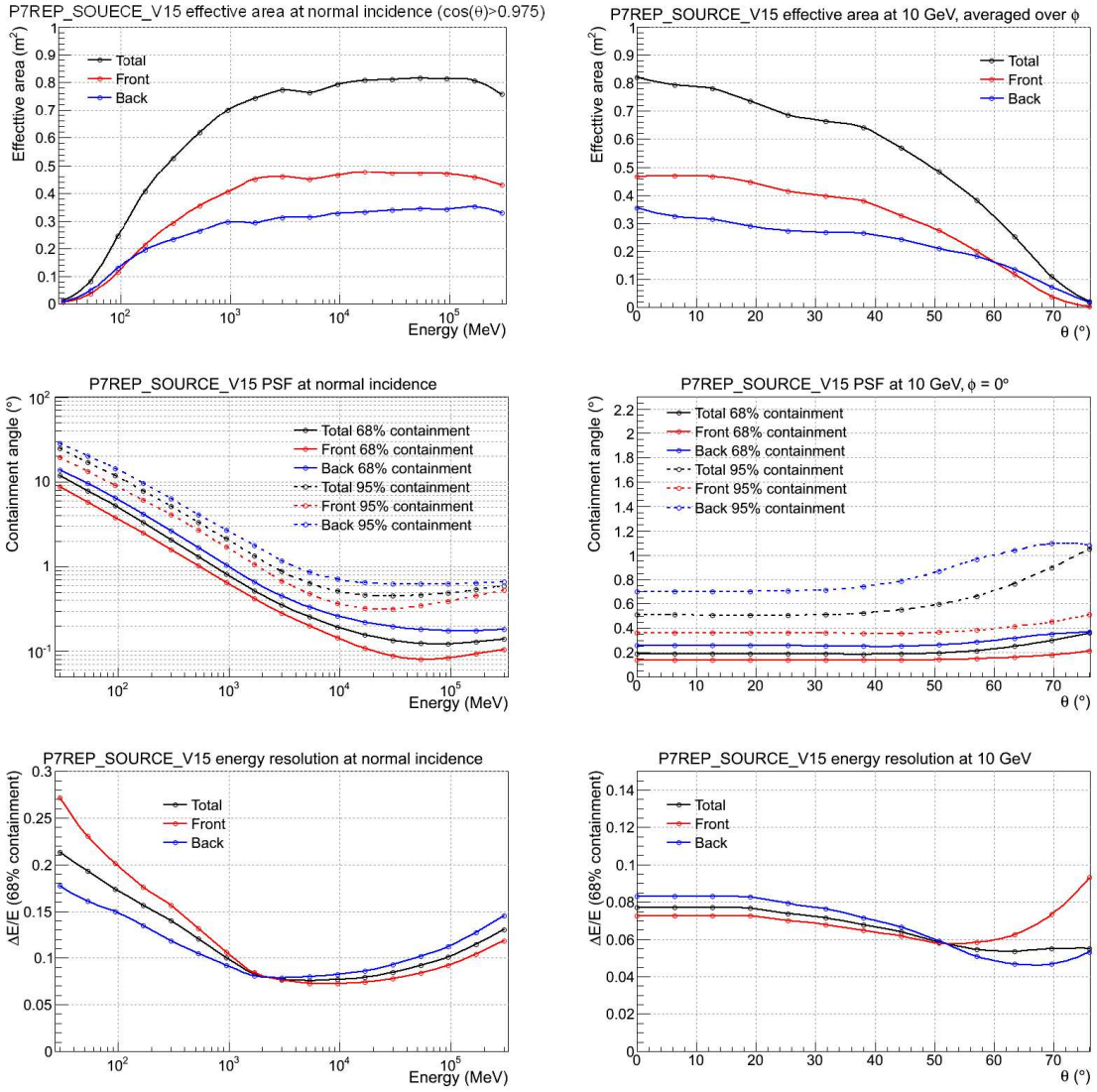

Figure 3.7: LAT P7REP_SOURCE_V15 IRFs. Top: Effective area; middle: PSF; bottom: Energy resolution.

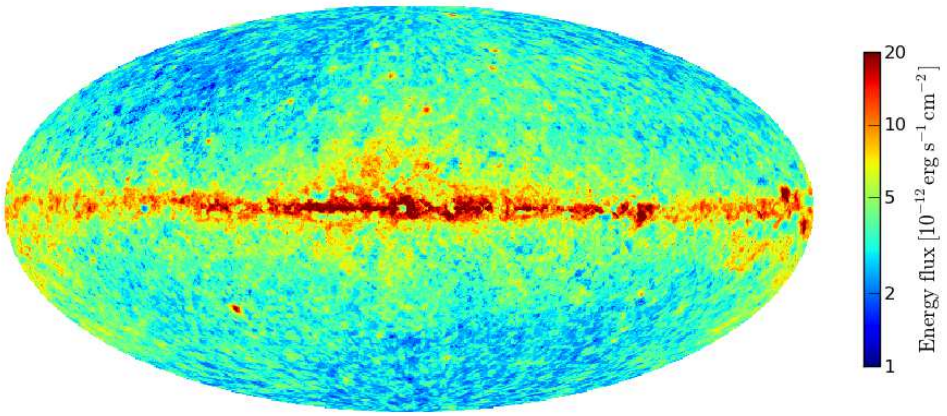

Figure 3.8: *Fermi*-LAT sensitivity map above 100 MeV with three-year exposure for the P7SOURCE_V6 event class for a point source with pulsar-like exponentially cutoff power law energy spectrum (adapted from 2PC Abdo *et al.* 2013).

3.3.3 Sensitivity, localization and variability

The high level event analysis and IRFs result in the global performance of the LAT: point-source sensitivity, point-source localization and source variability.

The sensitivity of the LAT is defined as the minimal flux required for a point source to be detected at the 5σ level with at least 10 γ rays collected. It depends on the spectrum and the position of the source in the sky due to the anisotropic Galactic diffuse emission. Figure 3.8 shows the LAT three-year sensitivity map above 100 MeV assuming a pulsar-like exponentially cutoff power law energy spectrum. The sensitivity is uniform far from the Galactic plane, while in the plane, the uncertainty on the diffuse emission can affect the source detection significance. Sources in the Galactic plane are less easy to detect than those with same flux at higher latitude.

The point-source localization depends also on the source flux, the spectral index and the background level. In the *Fermi* Large Area Telescope Second Source Catalog (2FGL, Nolan *et al.* 2012), the 95% localization radius for an isolated point source detected at the 5σ significance at high Galactic latitudes varies from $\sim 0.1^\circ$ for a hard spectral index ($\Gamma = 1.5$) to $\sim 0.3^\circ$ for a soft spectral index ($\Gamma = 3.0$). Due to the intense diffuse emission in the Galactic plane, for a given Γ, more flux is needed to reach the 5σ detection threshold. This results in a smaller localization region in the Galactic plane. The localization improvement with time is of order of 10% from a 3-year to 5-year observation. No systematic increase of localization shift with respect to that determined by the associated multi-wavelength counterparts is observed in the Galactic plane despite the big uncertainty on the Galactic diffuse emission.

The variability measurement of the LAT depends both on the characteristics of the source under study and the background emission, similar to the sensitivity and the localization. AGNs are more subject to vary with time, while pulsars are generally steady sources[4]. In general, the variability level induced by the time varying uncertainties on the A_{eff} and PSF is small ($< 5\%$) for all time scales between 12 hours and 2 years (Ackermann *et al.* 2012a).

[4]The pulsar J2021+4026 has been observed once to have flux and spin-down rate change simultaneously (Allafort *et al.* 2013).

CHAPTER 4

Pulsar timing and γ-ray pulsar discovery

Contents

4.1 Pulsar timing

4.1.1 Principle of pulsar timing

Pulsars are astronomical clocks with their emission beam sweeping the Earth at extremely precise periodic times. Most applications of pulsars benefit from this through the powerful technique of "pulsar timing", i.e., the measurement of the *time of arrival* (TOA) of photons emitted by the pulsar. Each TOA represents a time at which the pulsar is at a specific rotation state. The knowledge of TOAs allows the construction of the ephemeris which describes the pulsar's rotation on a longer time scale.

TOA recording

As the integrated pulse is very stable compared to individual pulses, TOAs can be obtained through the cross-correlation of the observed profile to an "ideal" template. This template can be obtained by analytical functions, e.g. a sum of Gaussian components (Kramer *et al.* 1994), or by using a high sensitivity (high signal-to-noise) profile constructed by the addition of many earlier observations. The observed profile $\mathscr{P}(t)$ can be expressed as (Taylor 1992):

$$\mathscr{P}(t) = a + b\mathscr{T}(t-\tau) + \mathscr{N}(t) \tag{4.1}$$

with $\mathscr{T}(t)$ the template, $\mathscr{N}(t)$ the noise, a an arbitrary offset and b a scaling factor. The TOA is then determined by τ, the time shift between the profile and the template, relative to the fiducial point of the template and the start time of the observation.

TOA corrections

TOAs are measured at the local time (topocentric time) at the observatory. It is necessary to convert the topocentric TOAs to the Solar System Barycenter (SSB, the mass center of the solar system) on the scale of Barycentric Dynamical Time (TDB), since the SSB is, to a very good approximation, an inertial frame. The transformation from the topocentric time $t_{\rm topo}$ to the barycentric time $t_{\rm SSB}$ is called *barycentrisation* (Edwards *et al.* 2006):

$$t_{\rm SSB} = t_{\rm topo} + t_{\rm clock} - \Delta_{\rm D} + \Delta_{\rm R\odot} + \Delta_{\rm S\odot} + \Delta_{\rm E\odot} + \Delta_{\rm B} \tag{4.2}$$

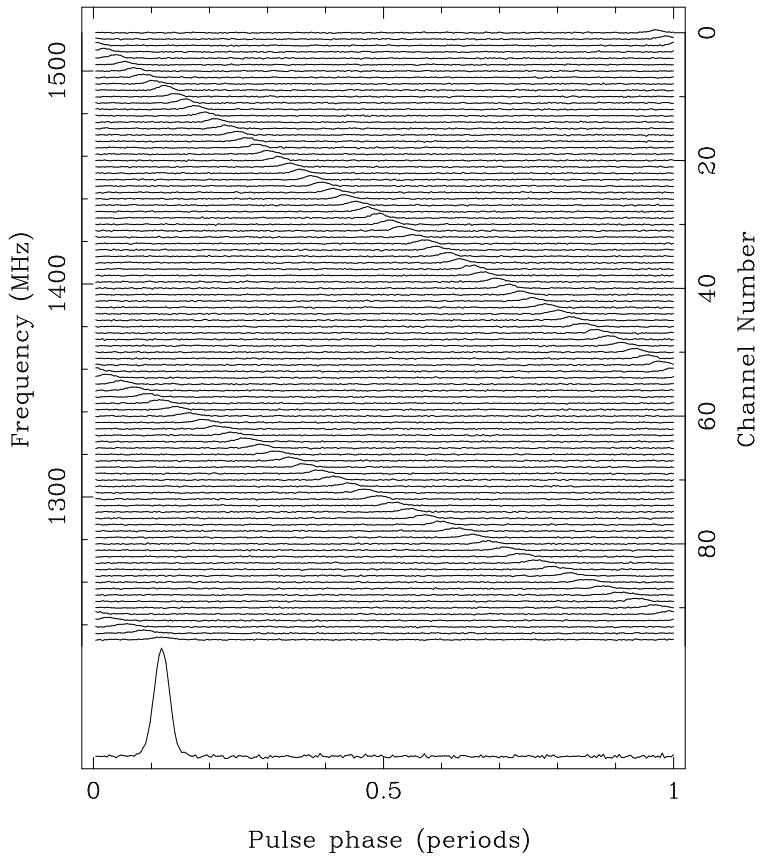

Figure 4.1: Interstellar effect on the arrival times of radio pulses. The band of observation is 288 MHz centred at 1380 MHz (Lorimer & Kramer 2004).

- $t_{\rm clock}$ includes various clock corrections[1].

- $\Delta_{\rm D}$ is the correction due to the dispersion measure (Section 1.5.4):

$$\Delta_{\rm D} = \frac{\rm DM}{k \times f^2} \tag{4.3}$$

with f (in GHz) the observing frequency in the SSB and $\mathrm{k} = 2.41 \times 10^{-4}\,\mathrm{MHz^{-2}\,pc\,cm^{-3}\,s^{-1}}$ (Manchester & Taylor 1977). Photons of different frequencies will arrive at different times after crossing the interstellar medium, as illustrated in Figure 4.1. This dispersion effect is removed by extrapolation to an infinitely high frequency. DM may change with time due to the motions of the pulsar, the Earth and the interstellar clouds which can change the electron column density distribution responsible for DM. High precision timing requires thereby taking into account the variation of DM such as $\dot{\rm DM}$, etc.

- $\Delta_{\rm R\odot}$ is the *Römer delay* which represents the light travel time between the observatory and the SSB:

$$\Delta_{\rm R\odot} = -\frac{(\vec{r_{SE}} + \vec{r_{EO}}) \cdot \vec{r_{SP}}}{c} \tag{4.4}$$

[1]The topocentric time is typically defined by a hydrogen maser clock and is measured on the scale of Coordinated Universal Time (UTC). UTC is related to the International Atomic Time (TAI) by TAI=UTC+$\Delta_{\rm T}$ with $\Delta_{\rm T}$ the leap seconds added to follow the solar year. TAI is an average of the atomic clocks in the world and is related to the Terrestrial Time (TT) by TT=TAI+32.184 s, in units of SI seconds. $t_{\rm topo} + t_{\rm clock}$ gives the time in TT.

with $\vec{r_{SE}}$ the vector pointing from the SSB to the Earth, $\vec{r_{EO}}$ the vector pointing from the Earth to the observatory and $\vec{r_{SP}}$ the vector pointing from the SSB to the pulsar. These vectors are calculated based on the knowledge of the positions of the main bodies in the solar system using a *Solar System Ephemeris* such as "DE200" (Standish 1990) or "DE405" (Standish 1998) published by the *Jet Propulsion Laboratory*[2].
As will be discussed in 4.1.2, the proper motion, i.e. the angular motion of the pulsar relative to the SSB in the sky (which can be transferred to a transverse velocity by Equation 4.13), will modify the vector from the SSB to the pulsar, leading to an extra time-dependant term in Equation 4.2. Such effect can be recognized in the timing residuals as a gradually amplified sinusoidal line with time (Figure 4.2). The radial velocity along the line of sight (Equation 4.11) which contributes a non-linear term is usually too small to measure. It takes usually many years with precise timing observations to measure a significant radial velocity effect, while the radial velocity can otherwise be determined more easily at optical wavelengths or from neutral hydrogen line observations (Section 1.5.2) due to the Doppler effect (Section 4.1.2).
The annual timing parallax due to the variation of the curvature of the wavefront of pulsar emission as the Earth orbits the Sun has a contribution to the pulse arrival time with an amplitude of

$$dT = (1\,\mathrm{AU})^2 \cos\beta/(2cd) = 1.25\cos\beta/d \tag{4.5}$$

with 1 AU the Earth-Sun distance, β the ecliptic latitude[3] of the pulsar, d the pulsar distance to the SSB and c the speed of light. Taking the maximum $\cos\beta = 1$ and for a pulsar at 1 kpc, this time delay is only 1.25 μs. So this effect is only measurable for MSPs away from the Ecliptic poles and at close distances.

- $\Delta_{S\odot}$, the *Shapiro delay*, is a relativistic correction which accounts for the time delay due to the curved space-time caused by massive bodies in the solar system (Shapiro 1964). This delay is typically of order of 100 μs close to the Sun while Jupiter can contribute about 200 ns.

- $\Delta_{E\odot}$, the *Einstein delay*, represents the combined relativistic time dilation due to the Earth's motion in the gravitational field of the solar system and the gravitational redshift caused by other bodies in the solar system (Backer & Hellings 1986).

- Δ_B is the correction for pulsars in binary systems. The orbital movement introduces the corresponding orbital *Römer delay*, *Shapiro delay* and *Einstein delay* analogue to those in the case of the solar system described as above. These new items involve the classical Keplerian parameters: orbital period P_b, projected semi-major orbital axis x, orbital eccentricity e, longitude of periastron ω, and epoch of periastron passage T_0, as well as the "post-Keplerian" parameters if relativistic effects can't be ignored (see e.g. Lorimer & Kramer 2004). One notes that the measurement of *Shapiro delay* for edge-on (inclination $i = 90°$) binary systems leads to the mass determination for both the pulsar and the companion, as is the case for J1614−2230 (Demorest *et al.* 2010).

Construction of ephemerides

The direct aim of pulsar timing is to reproduce precisely the pulsar rotation in a reference frame co-moving with the pulsar (an inertial frame such as the SSB) to construct the pulse profile, i.e. histogram of the pulse phase (the rotational state of the pulsar at a given time). In this frame, one way to describe the pulsar's rotation is through the "pulsar spin equation":

$$f(t) = f_0 + \dot{f}_0(t - T_0) + \frac{\ddot{f}_0}{2}(t - T_0)^2 + \ldots \tag{4.6}$$

[2]http://www.jpl.nasa.gov

[3]Ecliptic coordinate system is a celestial coordinate system with origin at the Earth center and l, β the ecliptic longitude and ecliptic latitude, respectively. Its reference plane is the Earth's orbit around the Sun.

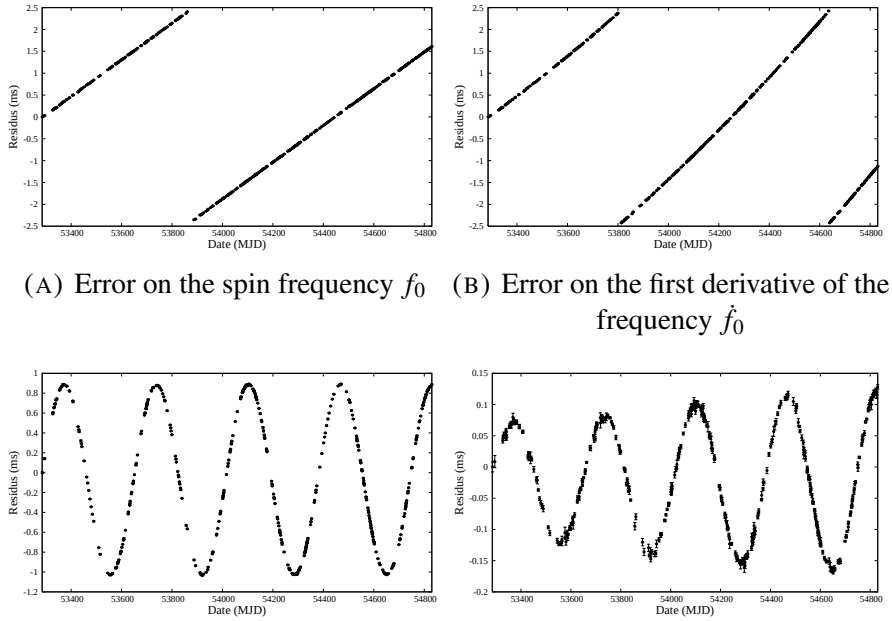

(A) Error on the spin frequency f_0

(B) Error on the first derivative of the frequency $\dot{f}_0$

(C) Bad position of pulsar

(D) Proper motion of the pulsar not taken into account

Figure 4.2: Examples of residuals with incorrect or incomplete parameters for the pulsar J0030+0451 observed at Nançay (Guillemot 2009).

with f_0, $\dot{f}_0$ and $\ddot{f}_0$ the spin frequency and its first and second derivatives at T_0, an arbitrary starting time. The integral of Equation 4.6 yields the pulse phase:

$$\Phi(t) = \Phi_0 + f_0(t-T_0) + \frac{\dot{f}_0}{2}(t-T_0)^2 + \frac{\ddot{f}_0}{6}(t-T_0)^3 + \ldots \tag{4.7}$$

The integer part of $\Phi(t)$ gives the rotation number between T_0 and t, while the fractional part represents the state of the rotation for one turn. Φ_0 is the pulse phase at T_0 and is determined at the *fiducial time* TZRMJD (Table 4.1) for which the phase is 0:

$$\Phi_0 = -f_0(TZRMJD - T_0) - \frac{\dot{f}_0}{2}(TZRMJD - T_0)^2 - \frac{\ddot{f}_0}{6}(TZRMJD - T_0)^3 - \ldots \tag{4.8}$$

An ephemeris (timing solution) consists of three kinds of parameters of the pulsar: (a) spin parameters ($f_0, \dot{f}_0, \ddot{f}_0$...); (b) astrometric parameters (right ascension α, declination δ, proper motion μ_α, μ_δ, parallaxe π); (c) binary parameters. An example is shown in Table 4.1. To construct an ephemeris, we start with a minimal set of parameters and transform the observed N TOAs to the barycentric time T_i using Equation 4.2. A phase $\Phi(T_i)$ is then calculated for each T_i using the model 4.7. To minimize the residual, a least squares fit is applied:

$$\chi^2 = \sum_{i=1}^{N} \left(\frac{\Phi(T_i) - n_i}{\sigma(T_i)} \right)^2 \tag{4.9}$$

with n_i the nearest integer to $\Phi(T_i)$ and $\sigma(T_i)$ the uncertainty on TOA.

Parameters are adjusted by iteration to improve the ephemeris. An optimal residual has a Gaussian distribution with mean=0 and RMS of the residual is comparable to the TOA uncertainties. Larger data

Name	J1614−2230
Right Ascension α (J2000)	16h14m36.5064507s
Declination δ (J2000)	$-22°30'31.19000''$
Frequency f_0 (s^{-1})	317.378937123607(6)
First derivative of frequency f_1 (s^{-2})	$-9.692182(3)^{-16}$
Dispersion measure DM (pc cm^{-3})	34.4878
Proper motion in Right Ascension μ_α (mas yr^{-1})	2.48
Proper motion in Declination μ_δ (mas yr^{-1})	−37.51
Reference epoch T_0 (MJD)	52334.8
Observation interval (MJD)	54155.3 − 55789.8
Zero phase epoch TZRMJD (MJD)	54965.0
Observing frequency TZRFRQ (MHz)	1398
Residual (μs)	3.310
Solar system ephemeris	DE405
Number of TOAs	123

Table 4.1: Example of ephemeris for PSR J1614−2230. Numbers in parentheses are 1 σ uncertainties on the last decimal number. MJD: Modified Julian Date.

sets and different observing frequencies help to improve the ephemeris gradually. Incorrect or missing parameters in the timing solution can lead to characteristic structures in the residual as are shown in Figure 4.2.

Young pulsars exhibit more *timing noise* and *glitches* than MSPs, most of which are extremely stable. *Timing noise* is the random change of rotational parameters on time scales of months to years. It's usually identified by looking at timing residuals. *Glitches* refer to a sudden increase in the spin frequency. While the exact cause of glitches is unknown, they are considered to be provoked by the angular momentum transfer from the interior superfluid to the crust of the neutron star (Anderson & Itoh 1975) by expelling vortices for which the "pinning" (be strongly attached) to the crust ions (Alpar 1977; Link 2003) can't be maintained any more due to large enough spindown lags of the superfluid with respect to the crust. This mechanism can successfully explain the glitches observed in Vela and other pulsars (Pizzochero 2011; Haskell *et al.* 2012; Seveso *et al.* 2012) and the population studies of glitch sizes and time scales (Melatos *et al.* 2008; Melatos & Warszawski 2009). The recovery periods of pulsars from *glitches* have been observed to last from days to years.

Recently, an *anti-glitch* (sudden decrease in the spin frequency) was reported for the first time for the magnetar 1E 2259+586 (Archibald *et al.* 2013), challenging the traditional glitch theories described above. Different scenarios have been proposed since then to explain this observation, among which are the wind braking scenario (Tong 2013), collision of a solid body with the magnetar (Huang & Geng 2013) or sudden accretion of retrograde matte (Katz 2013). See also Hu *et al.* (2013) for a statistical modelling approach.

Timing noise and *glitches* disturb the timing precision. To remove the *timing noise*, one way is to include higher derivatives of the spin frequency in the timing solution; another way models the *timing noise* as a sum of sine waves and extract it from the timing residual before performing further analysis. For *glitches*, it's necessary to increase the value of some pre-*glitch* parameters to follow the new rotation, e.g. the spin frequency and its derivatives.

For a given pulsar, different observatories have different instrumentation and they use different reference pulses ("templates"). This requires "jumps" from one observation to another when building a combined timing model benefiting of different observations.

The above procedure and functionalities of pulsar timing have been integrated to a publicly available

software package TEMPO2[4] (Hobbs *et al.* 2006). One of the main techniques used to search γ-ray pulsars with *Fermi* is using the ephemerides of known radio/X-ray pulsars to "phase-fold" the γ-ray photons (Section 4.2).

4.1.2 Doppler effect

Theoretical formulas and methods of calculation

The relative motion between the pulsar and the solar system barycenter SSB in the Milky Way, i.e. the space motion of the pulsar, results in a shift of the observed period P from the intrinsic value $P^{\rm int}$, characterized by the Doppler factor (first order, Damour & Taylor 1991):

$$D = 1 + \frac{v_{\rm R}}{c} = \frac{P}{P^{\rm int}} \tag{4.10}$$

with

$$v_{\rm R} = \vec{n}_{10} \cdot (\vec{v}_1 - \vec{v}_0) \tag{4.11}$$

the radial velocity of the pulsar relative to the SSB. $\vec{v}_1$ and $\vec{v}_0$ denote the SSB velocity and the pulsar velocity, respectively, in the Milky Way. $\vec{n}_{10}$ is the unit vector directed from the SSB to the pulsar (Figure 4.3 (A)). Illustrated in Figure 4.3 (B) is the pulsar's space motion in the galactocentric coordinate system in the absence of vertical velocity and for Galactic latitude $b = 0$ (assuming the pulsar and the SSB are in the Galactic plane). In this system, the pulsar's velocity is denoted as $(\Pi, \Theta, Z)_{\rm pulsar} = \vec{v}_1$, with Π the pulsar's velocity toward the Galactic center and Θ the Galactic rotation velocity at the pulsar's location and Z the vertical velocity (here it is 0). The SSB at the Sun's galactocentric radius R_0 has $(\Pi, \Theta, Z)_{\rm SSB} = (0, \Theta_0, 0) = \vec{v}_0$ as the Sun is to a good approximation moving in a circular galactic orbit in the galactic plane. The pulsar's space motion is then $\vec{v}_1 - \vec{v}_0 = (\mathrm{U}, \mathrm{V}, \mathrm{W}) = (\Pi, \Theta - \Theta_0, \mathrm{Z})$. For a flat Galactic rotation curve (Appendix A), $\Theta_{\rm pulsar} = \Theta_0$. The pulsar is at Galactic longitude l and distance d from the Sun. R denotes the pulsar's galactocentric radius.

A constant radial velocity introduces a constant offset on the period, but as D is small, for example, typically less than 0.1 for MSPs, this shift is negligible. However, a changing Doppler factor (non-constant radial velocity, i.e. radial acceleration) can lead to a significant shift on the spin-down rate $\dot{P}$. Differentiating Equation 4.10 results in the Doppler contribution $\dot{P}^{\rm D} \equiv \dot{P}^{\rm shk} + \dot{P}^{\rm gal}$ to the observed $\dot{P}$. The first item:

$$\dot{P}^{\rm shk} = \frac{1}{c}\mu^2 d P = k \left(\frac{\mu}{\mathrm{mas\,yr^{-1}}}\right)^2 \left(\frac{d}{\mathrm{kpc}}\right) \left(\frac{P}{\mathrm{s}}\right) \tag{4.12}$$

is known as the "Shklovskii effect" (Shklovskii 1970) due to the proper motion μ of the pulsar which modifies the vector $\vec{n}_{10}$ from the SSB to the pulsar ($\vec{r_{SP}}$ in Equation 4.4). $k = 2.43 \times 10^{-21}$, d is the distance of the pulsar to the SSB. The transverse velocity follows as:

$$V_{\rm T} = 4.74\,\mathrm{km\,s^{-1}} \left(\frac{\mu}{\mathrm{mas\,yr^{-1}}}\right) \left(\frac{d}{\mathrm{kpc}}\right) \tag{4.13}$$

The second item is the Galactic acceleration effect due to the gravitational field in the Galaxy:

$$\dot{P}^{\rm gal} = \frac{1}{c}\vec{n}_{10} \cdot (\vec{a}_1 - \vec{a}_0) P \tag{4.14}$$

with $\vec{a}_1$ and $\vec{a}_0$ the Galactic acceleration at the position of the pulsar and the SSB, respectively. The intrinsic value $\dot{P}^{\rm int}$ is then:

$$\dot{P}^{\rm int} = \dot{P} - \dot{P}^{\rm shk} - \dot{P}^{\rm gal} \tag{4.15}$$

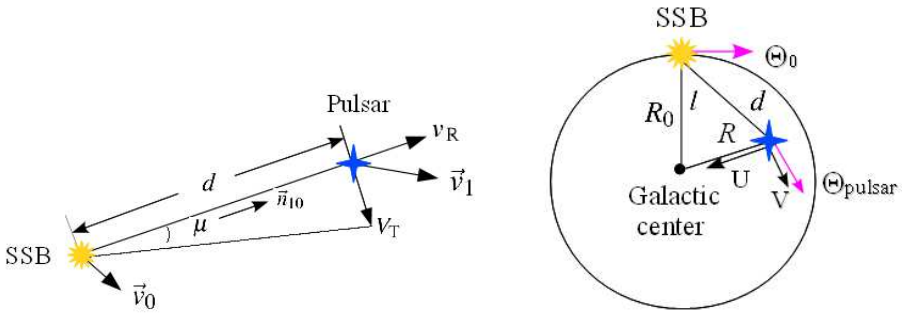

(A) Pulsar space motion (B) Galactic rotation model

Figure 4.3: (A): Illustration of the pulsar's space motion relative to the SSB. (B): Schema showing the pulsar's space motion in the galactocentric coordinate system in the absence of vertical velocity and for Galactic latitude $b = 0$. See text for details of the labels used.

The proper motion μ can be measured from the pulsar timing, e.g. in the equatorial coordinate system (right ascension α, declination δ), $\mu^2 = \mu_\alpha^2 + \mu_\delta^2$ with $\mu_\alpha = \dot{\alpha}\cos\delta$ and $\mu_\delta = \dot{\delta}$. Neglecting the pulsar's proper motion may lead to the gradually amplified sinusoidal curve in the timing residual (Figure 4.2).

For pulsars near the Galactic plane (small Galactic latitude b) and at small distance d, the Galactic acceleration contribution can be calculated using the approximate formula assuming a flat rotation curve as provided in Damour & Taylor (1991):

$$\left(\frac{\dot{P}}{P}\right)^{\rm gal} = -\frac{v_0^2}{cR_0}\left(\cos l + \frac{\beta}{\sin l^2 + \beta^2}\right) - \frac{a_z \sin b}{c} \tag{4.16}$$

where v_0 and R_0 represents the circular (tangential, rotation) velocity and the galactocentric radius of the Sun respectively. l, b are the pulsar's Galactic longitude and latitude, a_Z is the vertical Galactic acceleration, c is the speed of light and $\beta \equiv (d/R_0) - \cos l$. Lazaridis *et al.* (2009) extended this expression to high Galactic latitudes (always under the assumption of a flat rotation curve):

$$\left(\frac{\dot{P}}{P}\right)^{\rm gal} = -\frac{v_0^2}{cR_0}\left(\cos l + \frac{\beta}{\sin l^2 + \beta^2}\right)\cos b - \frac{a_z \sin b}{c} \tag{4.17}$$

In the general case, one can use the Galactic potential models (e.g. Carlberg & Innanen 1987; Kuijken & Gilmore 1989; Paczynski 1990) to calculate the acceleration effect (e.g. Arzoumanian *et al.* 1999; Wex *et al.* 2000). Usually $\dot{P}^{\rm shk}$ dominates, but the acceleration item in globular clusters may be large enough to compensate the Shklovskii term and even reverse the sign of $\dot{P}$ to have a negative value, showing that the pulsar is *spin-up*. This happens for some MSPs in binary systems in which the pulsar is accreting masses from the companion star.

The Doppler effect has similar influence on the orbital period derivative $\dot{P}_{\rm b}$ for pulsars in binary systems in the same way, along with other contributions. The observed $\dot{P}_{\rm b}$ can be expressed as:

$$\frac{\dot{P}_{\rm b}}{P_{\rm b}} = \left(\frac{\dot{P}_{\rm b}}{P_{\rm b}}\right)^{\rm D} + \left(\frac{\dot{P}_{\rm b}}{P_{\rm b}}\right)^{\rm GW} + \left(\frac{\dot{P}_{\rm b}}{P_{\rm b}}\right)^{\dot{m}} + \left(\frac{\dot{P}_{\rm b}}{P_{\rm b}}\right)^{\rm T} \tag{4.18}$$

The first item is the Doppler effect, the second one is the orbital decay due to the gravitational wave (GW)

[4] http://www.csiro.au/research/pulsar/tempo2/

emission[5], the third item is the effect of mass loss from the system and the last item represents the contribution from the tidal dispersion of the orbit. The measurement of $\dot{P}_b$ serves as a tool to test the General Relativity and provides a new way to constrain the Newtonian constant G. An example of such studies can be found in Damour & Taylor (1991) for J1913+16.

Comparison and validation of the method

The Doppler effect is applied to 2PC with the correction on $\dot{P}$ and $\dot{E}$ for MSPs listed in Appendix B. The routine to compute the Doppler correction is available as part of the software for the database used for 2PC (Appendix C). Before doing the correction, a comparison between the approximate formulas of Damour & Taylor (1991), Lazaridis *et al.* (2009) and Galactic potential models of Carlberg & Innanen (1987), Kuijken & Gilmore (1989), Paczynski (1990), as well as the comparison between these models were made.

4.2 γ-ray pulsar discovery

4.2.1 Searching techniques

- **Using known radio/X-ray ephemerides**: The *Fermi*-LAT photon rate is still low[6] even with a sensitivity more than 30 times greater than that of EGRET. Regular observations for known pulsars are important to obtain accurate rotation parameters (Section 4.1) which help to increase the LAT pulsed sensitivity. Since 2007, the *Fermi*-LAT collaboration has organized a pulsar timing campaign ("Pulsar Timing Consortium" (PTC), Smith *et al.* 2008) in cooperation with international radio telescopes, including Jodrell Bank observatory (England), Nançay radio telescope (France), Parkes radio telescope (Australia), Green Bank radio telescope (USA), Urumqi Observatory (China) and Arecibo radio telescope (Portugal). Pulsars not detected in radio but in X-rays were observed with the satellite RXTE[7] and XMM-Newton[8]. A list of 218 pulsar candidates with $\dot{E} \geq 10^{34}$ erg s^{-1} have been selected from the ATNF Pulsar Catalog as presented in Section 2.2. In reality, the engaged radio telescopes provide ephemerides for more than 700 pulsars regularly. This method has enabled more than 88 (Aug 2013) detections of γ-ray pulsars (see e.g. Abdo *et al.* 2010b, 2013), nearly half of the total LAT pulsars[9]. In particular, this method has permitted the first LAT detection of the MSP J1823−3021A in the globular cluster NGC 6624 (Freire *et al.* 2011a).

- **Blind search**: Long, sparse LAT data makes traditional Fast Fourier Transform (FFT) searches (used in radio timing) computationally expensive. The LAT collaboration has, prior to the launch of *Fermi*, developed a time-differencing technique to make the pulsar search faster by analysing the differences of photon arrival times rather than the time series itself (Atwood *et al.* 2006; Ziegler *et al.* 2008). Recently, the Max-Planck Hannover group joined the blind search work with LAT collaboration mem-

[5]Predicted by the theory of General Relativity in 1916, gravitational waves are the propagation, at the speed of light, of the spacetime curvature changes caused by accelerating objects moving in the specetime. The frequency of gravitational waves would be in the range of $10^{-7} - 10^{11}$ Hz (Hawking & Israel 1981). Sources expected to emit gravitational waves include γ-ray bursts, neutron-star and black-hole collisions, and rapidly rotating pulsars in our Galaxy. Although direct detections of gravitational waves have not been achieved yet due to the very small effect the waves would produce on the detector, indirect evidence of their existence was proposed by the discovery of the binary pulsar B1913+16 (Hulse & Taylor 1974) which showed an orbital period decay due to the energy loss from gravitational wave emission matching the prediction of the General Relativity.

[6]For example, the third brightest pulsar (the Crab), will trigger the LAT on average only once every 500 revolutions of the neutron star (15 s) and while it can be detected by LAT in a day, it takes years to detect weaker pulsars near the detection threshold.

[7]http : //heasarc.gsfc.nasa.gov/docs/xte/XTE.html

[8]http : //xmm.esac.esa.int/

[9]Public list at https://confluence.slac.stanford.edu/display/GLAMCOG/Public+List+of+LAT-Detected+Gamma-ray+Pulsars

bers, using a novel method adapted from a semi-coherent search method originally developed for gravitational wave detections from rapidly spinning neutron stars in Laser Interferometer Gravitational Wave Observatory (LIGO) data. Blind searching has been a great success for discoveries of young or middle aged pulsars (see e.g. Abdo *et al.* 2009b; Saz Parkinson *et al.* 2010; Pletsch *et al.* 2012). Their smaller radio beaming fractions make them be missed by radio surveys. They are therefore radio-quiet and constitute one third of the γ-ray pulsars to date. Only one MSP has been detected in the blind search of LAT data benefiting from its optical studies – radio detection followed (Romani & Shaw 2011; Kong *et al.* 2012; Romani 2012).

- **Radio pulsar search in LAT unassociated sources**: A complementary strategy is to perform radio searches for pulsars powering sources discovered in the LAT sky survey, given that there are about 30% unassociated *Fermi* sources in 2FGL (Nolan *et al.* 2012) and that most sources are localized with an accuracy $< 10'$ which is small enough to be covered by a single radio telescope beam. The *Fermi* Pulsar Search Consortium (PSC) has performed deep radio searches for LAT unassociated sources with pulsar-like spectra and low variability. This method has yielded more than 50 new radio MSPs and more than 25 now have LAT detections (see e.g. Ransom *et al.* 2011). These MSPs are distributed mostly away from the Galactic plane. Only four young pulsars are found in the Galactic plane, with only one being identified as γ-ray pulsar (J2030+3641, Camilo *et al.* 2012). This is probably because traditional radio surveys have been concentrated in the plane and that the young pulsars missed by radio surveys have been mostly discovered in LAT blind searches. More complete information is given by Ray *et al.* (2012).

The ephemerides used in *Fermi*-LAT publications are constructed using radio, γ-ray data or both, depending on the LAT pulsar detection methods used as described above. γ-ray light curves are then obtained by assigning rotational phases to LAT photons based on the parameters in the ephemeris using the **fermi** plug-in (Ray *et al.* 2011) in TEMPO2. The ephemerides are released to the pulsar science community through Fermi Science Support Center (FSSC)[10].

In this thesis, I have concentrated on the detection of γ-ray pulsars using radio ephemerides. After almost three years of *Fermi* observations at the beginning of my thesis, most bright ones had already been detected. The rest are rather weak and deserve "Tender Loving Care". We have therefore regularly followed the most promising candidates. Some of these new detections have been included in 2PC and others will be presented in Chapter 6.

4.2.2 Detection significance

For a given light curve, whether a pulsed periodic signal is present is determined by a statistical test. The periodicity test is actually a test for the absence of such periodic signal or a test for uniformity, i.e. the null hypothesis H_0. The standard process is: 1) calculate the test statistic from the phase; 2) calculate the p-value (probability that a result is obtained by chance given that the H_0 is true); 3) if p-value$< \alpha$, with α the predetermined significance level[11], indicating that the observed result would be highly unlikely under the null hypothesis, then H_0 is rejected at that level, i.e. the signal is periodic.

Weighted H-test

Let N_γ be the observed γ photons, the traditional H-test (de Jager *et al.* 1989; de Jager & Büsching 2010) based on the Z^2_m test (Buccheri *et al.* 1983) is:

$$H \equiv \max(Z^2_m - 4m + 4) \quad 1 \leq m \leq 20 \tag{4.19}$$

[10] http://fermi.gsfc.nasa.gov/ssc/data/access/lat/ephems/

[11] $\alpha = 0.05$ means that the result is obtained by chance with a probability of 5%, or the null hypothesis H_0 can be rejected at a 95% confidence level. *Fermi* uses 5σ detection criteria corresponding to $\alpha = 5.7 \times 10^{-7}$.

where

$$Z_m^2 \equiv \frac{2}{N_\gamma} \sum_{k=1}^{m} \alpha_k^2 + \beta_k^2 \tag{4.20}$$

with α_k and β_k the empirical trigonometric coefficients $\alpha_k \equiv \sum_{i=1}^{N_\gamma} \cos(2\pi k\phi_i)$ and $\beta_k \equiv \sum_{i=1}^{N_\gamma} \sin(2\pi k\phi_i)$. ϕ_i is the the ith phase. The Z_m^2 test has been mainly used for pulsation searches in COS-B and EGRET data (Nel *et al.* 1996). The H-test improves the Z_m^2 test by looking for an optimal m rather than pre-defining it which requires a knowledge of the pulse shape *a priori*. The H-test maintains thus the sensitivity to light curves with a large range of morphologies.

At an early stage of the *Fermi* mission, the standard H-test has been used by searching a grid of radius around the pulsar position and in certain energy bands to find the optimal radius and the minimum energy $E_{\rm min}$ which maximize the H-test. The light curves are then constructed by applying a ROI (region-of-interest) cut with the optimal radius above $E_{\rm min}$. The disadvantage of this method is the necessity to correct the trials. With the bright γ-ray pulsars already detected by the *Fermi*-LAT, the rest are rather faint due to different reasons: bigger distance, a lower spin-down power, a higher background... This requires to enhance the pulsation search sensitivity.

The weighted H-test (Kerr 2011) incorporating the probability that the photon originates from the candidate pulsar enables a higher signal-to-noise ratio and removes the trial penalty due to ROI and $E_{\rm min}$ cuts. Weights come from the measured spectrum convoluted with the energy dependent PSF. The weight, w_i, representing the probability that the ith event originates from the pulsar is:

$$w_i = \frac{dN/dE_{\rm psr}(E_i, \vec{x}_i)}{\sum_j dN/dE_j(E_i, \vec{x}_i)}, \tag{4.21}$$

where E_i and $\vec{x}_i$ are the observed energy and position on the sky of the ith event and dN/dE_j is the phase-averaged spectrum for the jth source in the ROI. The weighted H-test is therefore:

$$H_w \equiv \max(Z_{mw}^2 - 4m + 4) \quad 1 \leq m \leq 20 \tag{4.22}$$

with the weighted Z_{mw}^2 test:

$$Z_{mw}^2 \equiv \frac{2}{N_\gamma} \left(\frac{1}{N_\gamma} \sum_{i=1}^{N_\gamma} w_i^2 \right)^{-1} \sum_{k=1}^{m} \alpha_{kw}^2 + \beta_{kw}^2 \tag{4.23}$$

where $\alpha_{kw} = \sum_{i=1}^{N_\gamma} w_i \cos(2\pi k\phi_i)$ and $\beta_{kw} = \sum_{i=1}^{N_\gamma} w_i \sin(2\pi k\phi_i)$.

The p-value for a given H value is $e^{-0.4H}$ which can be then converted to σ via $p = 1 - \mathrm{erf}\left(\sigma/\sqrt{2}\right)$ assuming a Gaussian distribution where erf is the error function.

CHAPTER 5

Fermi-LAT data analysis

Contents

5.1 Data preparation

The *Fermi*-LAT data set for high level science analysis is publicly available to download from the FSSC server[1]. For all kinds of *Fermi*-LAT analysis (AGN, pulsar, GRB...), two basic Flexible Image Transport System (FITS) format files are needed prior to the analysis:

- Event file FT1: containing the information of every recorded photon having passed the reconstruction stage (Section 3.3): energy, time of arrival (in units of MET[2]), direction of arrival, etc.
- Spacecraft file FT2: containing the information related to the satellite position and orientation at e.g. 30 second intervals.

Depending on the type of analysis to be performed (point source, extended source, diffuse emission, spectral analysis, timing analysis, etc), different data selection criteria (cuts) are necessary. Such cuts are performed using the *Fermi Science Tools*[3] developed in the *Fermi* collaboration. Typical cuts on the FT1 file including time range, energy range, position (right ascension RA, declination DEC) of the source of interest, region-of-interest (ROI, e.g. 15° around the source of interest in the spectral analysis), maximum zenith angle (100°, to exclude the contamination from the γ-ray emission of the Earth's limb which lies at a zenith angle of 113°) and event class are done with *gtselect* in the *Science Tools*. The corresponding time intervals should therefore be removed using *gtmktime* by looking at the spacecraft information stored in the FT2 file. *gtmktime* also excludes time intervals based on data quality and LAT configuration, for example, when the LAT is passing the Southern Atlantic Anomaly (SAA), or when its rocking angle exceeds 52°. Such cuts are important for exposure calculation in the spectral analysis to obtain correct flux predicted by a source model. The resulting FT1 event file is now ready to use in the spectral and light curve analysis described in the following sections.

[1] http://fermi.gsfc.nasa.gov/ssc/data/access/

[2] MET: Mission Elapsed Time, seconds passed since the 1st Jan 2001 at UTC 00:00:00 which corresponds to the Modified Julian Date (MJD) 51910 in the UTC system.

[3] http://fermi.gsfc.nasa.gov/ssc/data/analysis/scitools/overview.html

5.2 Spectral analysis

5.2.1 Diffuse emission models

The diffuse emission constitutes 80% of the observed γ-rays and should be modelled with precision to extract the signals of the studied sources from the data. Two components of this diffuse emission have been established: Galactic diffuse emission and Extragalactic diffuse emission. The following paragraphs describe diffuse models constructed for the *Fermi*-LAT to account for these two diffuse sources, which are available on the FSSC server[4]. These models are subject to evolve as our understanding of the diffuse emission evolves (e.g. identification of large scale excess emissions).

Galactic diffuse emission

The interaction of energetic cosmic ray electrons and protons with nucleons and photons in the ISM creates the high-energy Galactic γ-ray emission. This results in two contributors: the decay of neutral pions π^0 produced in hadron collisions between the protons and the interstellar nucleons; the Inverse Compton scattering (ICS) of the interstellar radiation field by cosmic electrons and their bremsstrahlung emission[5] in the ISM.

Given that about 99% of the mass of the ISM is gas, of which about 90% is atomic (HI) or molecular hydrogen (H_2), and that energetic cosmic rays uniformly penetrate all gas phases in the ISM, the Galactic diffuse emission model in the LAT collaboration has been developed using spectral line surveys[6] of HI and CO to derive the distribution of interstellar gas in galactocentric rings. In addition, infrared tracers of the dark gas (e.g. dust) column density were used as a "correction" to the total gas density in the case of incomplete HI or CO surveys. Since there is no simple template for the ICS emission, the prediction from the GALPROP[7] code has been used to account for this contribution. The Galactic diffuse model was then constructed by fitting the γ-ray emissivities of the rings in several energy bands to the LAT observations (after removal of point sources). The up-to-date public model is a FITS file *gll_iem_v05.fits* for the P7REP dataset.

Isotropic diffuse emission

The isotropic diffuse model includes both extragalactic γ-ray background and remaining residual cosmic ray emission that is misclassified as γ rays. The model is constructed by fitting only the high latitude ($|b| > 30^\circ$) all-sky emission that is not represented in the Galactic diffuse model. Such a model is determined with a specified Galactic diffuse model and for one of the LAT event class selections, like SOURCE or CLEAN, so the resulting spectral template should be used with the same Galactic diffuse model and event class selection that were used to derive it. The up-to-date public model is a text file, e.g. for P7REP SOURCE class, *iso_source_v05.txt*, in which two columns of the central energy (in MeV) for the band and the differential flux in that band (in $\mathrm{ph\,cm^{-2}s^{-1}MeV^{-1}sr^{-1}}$) represent the spectral form of this isotropic diffuse emission which is approximately a power law with index $\Gamma = 2$. The origin of the extragalactic γ-ray background is still unclear and several sources have been proposed to account for this emission: unresolved AGNs, interactions of cosmic rays with the cosmological background photons and infrared photons, or dark matter annihilation, etc.

[4] http://fermi.gsfc.nasa.gov/ssc/data/access/lat/BackgroundModels.html

[5] Radiation produced by a decelerated charged particle when passing by another charged particle, for example, when an electron passes by an atomic nucleus.

[6] HI is traced by its radio 21 cm line, while H_2 can't be reliably observed directly in its cold phase, it's traced by the 2.6 mm line of CO when the latter collides with H_2 molecules.

[7] http://galprop.stanford.edu

Dedicated templates

During the development of new diffuse models for the P7V6 data set, large-scale regions of excess emission after applying the simple GAS (HI+CO+dust)+ICS model have been identified as unmodelled in earlier versions of the Galactic diffuse model. Examples are Loop 1 (characterised by synchrotron emission using the 408 MHz Haslam map[8]) and Fermi Bubbles (giant symmetric γ-ray bubbles extending $\sim 50^\circ$ ($\sim$ 10 kpc) in Galactic altitude above and below the Galactic center with sharp edges, Su *et al.* 2010). Dedicated templates have been constructed and included in the Galactic diffuse model to account for these emission regions. A template for the Earth limb's emission has also been made since the emission is in the broad tails of the PSF and so passes the 100° zenith angle cut and is not completely removed from the data at energies below 200 MeV. The limb template is used to construct the Galactic diffuse model, but is not in the model, like the point sources.

5.2.2 Spectral and spatial models

In the spectral analysis, two types of sources can be defined, PointSource and DiffuseSource (including the Galactic and isotropic diffuse emissions described in Section 5.2.1). Each type of source model consists of a spectral and a spatial model component with each one characterised by several parameters.

Spectral models

The spectral model describes the energy dependence of the photon numbers $\frac{dN}{dE}$ emitted by the source. The units are $\mathrm{MeV}^{-1}\,\mathrm{cm}^{-2}\,\mathrm{s}^{-1}$ for point source spectral models, and $\mathrm{MeV}^{-1}\,\mathrm{cm}^{-2}\,\mathrm{s}^{-1}\,\mathrm{sr}^{-1}$ for diffuse sources. Note that in γ-ray astronomy, the spectral property of the source is usually shown as the Spectral Energy Distribution (SED) expressed by the quantity $E^2\frac{dN}{dE}$. The spectral models involved in *Fermi* pulsar data analysis are:

– PLSuperExpCutoff (PLEC, Equation 2.4)

– PowerLaw (PL)

$$\frac{dN}{dE} = N_0 \left(\frac{E}{E_0}\right)^{-\Gamma} \tag{5.1}$$

with N_0 the prefactor or normalization of the spectrum, Γ the spectral index and E_0 the energy scale. This function is suitable for the study of various sources, like PWN, SNR. For pulsars, it is used to test the validity of the PLEC model (Section 5.2.4).

– PowerLaw (PL2)

$$\frac{dN}{dE} = \frac{N(1-\Gamma)E^{-\Gamma}}{E_{\mathrm{max}}^{1-\Gamma} - E_{\mathrm{min}}^{1-\Gamma}} \tag{5.2}$$

with N the integral flux in the energy band of $(E_{\mathrm{min}}, E_{\mathrm{max}})$. This model is used to obtain the spectral points in different energy bands when constructing the SED. Use of this model has the advantage of evaluating directly the uncertainties on the integrated flux by likelihood (Section 5.2.4), obviating the need to propagate the uncertainties when using the PL form.

Spatial models

The spatial model defines the spatial dependence of the observed photons. There are four spatial models:

– SkyDirFunction: specify a direction (RA, DEC) on the sky, used only for point sources.

– ConstantValue: uses a constant value in the case of isotropic diffuse emission.

[8] http://lambda.gsfc.nasa.gov/product/foreground/haslam_408.cfm

– SpatialMap: uses a 2-dimensional (two sky coordinates) FITS image file as a template to determine the photon distribution on the sky for extended sources.

– MapCubeFunction: uses a 3-dimensional FITS map (two sky coordinates plus energy) for diffuse sources as is the case for Galactic diffuse emission.

5.2.3 Source model creation

A source model in eXtensible Markup Language (XML) format needs to be created for the usage of the spectral analysis tool *gtlike*. In the XML file, all the point sources and diffuse sources (including the Galactic diffuse and Isotropic diffuse) in the selected ROI are specified by their spectral and spatial parameters described above. Such a source list is extracted from a *Fermi*-LAT source catalog, such as 2FGL. Due to the large PSF at lower energies and the large FoV of the LAT, many sources can be detected in the neighborhood of the source of interest. Along with the diffuse components, they will overlap significantly with the emission from the sources of interest. To fit the source of interest accurately, it is therefore required to free the spectral parameters not only for the source of interest but also for nearby sources (e.g. set free_ROI= 5°) and for the Galactic diffuse and isotropic components. The likelihood method that will be discussed in the following Section 5.2.4 can thus model all of them simultaneously.

5.2.4 Likelihood method

Likelihood model fitting

In statistics, a likelihood $\mathscr{L}$ is defined as the probability of obtaining the data x given an input model Θ. In our case, the input model is the distribution of γ-ray sources on the sky, including their intensity and spectra as specified in the XML source model for a given ROI. To obtain a model which best reproduces the observed data implies maximizing this probability, whence the name maximum likelihood method.

The LAT data being characterized by many variables (coordinates on the sky, energy, etc), they can be binned into multiple dimensional bins. The observed number of counts (photons) in each bin is characterized by the Poisson distribution, the likelihood $\mathscr{L}$ is then the product of the probabilities of observing n_i counts in the bin i with m_i photons predicted by the model (i.e. the expected counts):

$$\mathscr{L} = \prod_i \frac{m_i^{n_i} e^{-m_i}}{n_i!} \tag{5.3}$$

which can be expressed by two factors:

$$\mathscr{L} = \prod_i e^{-m_i} \prod_i \frac{m_i^{n_i}}{n_i!} = e^{-N_{\rm pred}} \prod_i \frac{m_i^{n_i}}{n_i!} \tag{5.4}$$

The first factor involving the total predicted counts by the model $N_{\rm pred}$ is purely a function of the source model, while the second depends on both the source model and the data.

Since binning destroys information of the individual counts and reflects rather the averaged properties of the counts in each bin, there is a trade-off between the number of bins (and thus the bin size) and the accuracy; smaller bins result in a more accurate likelihood. The binned likelihood with finite bin size and n_i that may be greater than 1 is appropriate to analyse large data sets which will otherwise make the calculation time prohibitive in the unbinned likelihood case. The *binned likelihood* will be used in this thesis.

In practice it is often more convenient to work with the logarithm of the likelihood function, called the log-likelihood:

$$\ln \mathscr{L} = \sum_i \ln M_i - N_{\rm pred} \tag{5.5}$$

with M_i the event density of the model. To calculate M_i and $N_{\rm pred}$, it is important to know the LAT exposure on the sky which is essentially the integral of the effective area over time. To generate the exposure map, it's first required to calculate the "livetime", i.e. the amount of time that the LAT observed a given position on the sky at a given direction, using the *gtltcube* tool. The exposure map is then generated by *gtexpcube2* for binned likelihood given the "livetime".

The likelihood fitting involves finding the set of parameters of the input model that maximizes the likelihood. Since the likelihood is a non-linear function of the parameters, different algorithms are provided in the *gtlike* tool for maximizing the likelihood. In this thesis, an alternate tool "*pointlike*" (Kerr 2010) has also been used to cross-check the fit result.

Test statistic

The Test Statistic is defined as:

$$\mathrm{TS} = 2\Delta \ln \mathscr{L} \tag{5.6}$$

where $\Delta ln\mathscr{L}$ is the difference of the maximum log-likelihood between two models. This can be used to quantify the existence of an additional source in a model by computing $\Delta ln\,\mathscr{L} = \ln \mathscr{L}_{\rm source} - \ln \mathscr{L}_{\rm null}$ where $\mathscr{L}_{\rm source}$ is the maximum likelihood value for a model with the additional source at a specified location, and $\mathscr{L}_{\rm null}$ is the value for a model without the additional source (the "null hypothesis"). It's clear that maximizing the TS is equivalent to maximizing the likelihood. A larger TS indicates that the null hypothesis is incorrect (i.e. an additional source is present). The detection significance for a given source is approximately $\mathrm{TS}^{1/2}$ in units of σ assuming a Gaussian distribution of the TS.

In the pulsar analysis, the TS is also used to quantify the cutoff significance. In this case, $\Delta ln\mathscr{L} = \ln \mathscr{L}_{\rm PLEC} - \ln \mathscr{L}_{\rm PL}$, with $\mathscr{L}_{\rm PLEC}$ the likelihood when modeling the pulsar spectrum by a PL with an exponential cutoff, and $\mathscr{L}_{\rm PL}$ the likelihood for a PL model.

In the spectral analysis, an upper limit on the observed source flux will be estimated if the significance of the source is $< 3\sigma$ (TS < 9).

5.2.5 Systematic uncertainties

In the spectral analysis, the systematic uncertainties, distinguished from the statistical uncertainties which come from the statistical model fitting, are mainly related to our imperfect understanding of the diffuse emissions (Section 5.2.1) and the uncertainties on the LAT IRFs (Section 3.3.2).

The effects on the spectral parameters due to the uncertainties on the PSF and the energy resolution are negligible compared to that induced by the uncertainty on the effective area $\mathrm{A_{eff}}$. For the P7SOURCE_V6 and P7CLEAN_V6 event classes, the uncertainties on the $\mathrm{A_{eff}}$ are roughly 10% at 100 MeV, decreasing to 5% at 560 MeV, and increasing to 10% at 10 GeV and above (Ackermann *et al.* 2012a). To propagate this uncertainty to the measured spectral quantities, like flux, index Γ and cutoff energy $E_{\rm cut}$ (for pulsars), bracketing IRFs have been generated in the LAT collaboration which replace the standard $\mathrm{A_{eff}}$ by:

$$A^{\rm B}_{\rm eff}(E) = A_{\rm eff}(E)[1 + err(E)B(E)] \tag{5.7}$$

where $err(E) = \dfrac{\delta A_{\rm eff}(E)}{A_{\rm eff}(E)}$ is the relative uncertainty on the $\mathrm{A_{eff}}$ and $B(E)$ is the bracketing function. To maximize the effect on the flux, $B(E) = \pm 1$; for Γ and $E_{\rm cut}$, $B(E) = \pm \tanh(\log(E/E_0)/\kappa)$, with E_0 the spectral pivot energy of the source of interest and κ a constant to control the smoothness of the function. In practice choosing $\kappa = 0.13$ smooths over twice the energy resolution. This results in four sets of IRFs as are shown in Table 5.1.

The uncertainty on the Galactic diffuse model is about 4% at the 1σ level with a mean of 1.01. To estimate the uncertainty on spectral parameters of the source of interest due to the uncertainty on the diffuse model, the diffuse model is conservatively modified to have a flux of $1 \pm 6\%$ of the best fit value from the standard analysis as demonstrated in Abdo *et al.* (2010c).

IRF	$B(E)$
flux_lo	$+1$
flux_hi	-1
index_soft	$+\tanh(\log(E/E_0)/\kappa)$
flux_hard	$-\tanh(\log(E/E_0)/\kappa)$

Table 5.1: LAT bracketing IRFs for the $A_{\rm eff}$ and the corresponding bracketing functions (Ackermann *et al.* 2012a).

The systematic uncertainties on the spectral parameters are estimated by repeating the spectral analysis with the bracketing IRFs and modified diffuse models separately and then comparing with the standard analysis. Total systematic uncertainties are set by adding in quadrature the uncertainties due to the Galactic diffuse model and the effective area.

5.3 Profile characteristics

5.3.1 γ-ray and radio light curves

As in 2PC, weighted γ-ray light curves are constructed using weights w_j from the spectral analysis as defined in Equation 4.21. The uncertainty on the ith bin of the histogram containing N_i photons is estimated as $\sigma_i^2 = 1 + \sum_{j=0}^{N_i} w_j^2$. The number of bins in the histogram is chosen based on the weighted H-test: 25 bins ($H < 100$); 50 bins ($100 < H < 1000$); and 100 bins ($H > 1000$). In the cases of weak pulsars, even less bins have been used to smooth the background structure (Chapter 6).

The background contribution from diffuse sources and nearby point sources is estimated by the expected value b of w under the assumption that the photon doesn't originate from the pulsar:

$$b \equiv \int_0^1 w \times [1 - f(w)] dw \approx \sum_{j=0}^{N_\gamma} w_j - \sum_{j=0}^{N_\gamma} w_j^2 \tag{5.8}$$

with $f(w)$ the probability distribution of the photon weights and N_γ the total γ photon number. The background level averaged over all bins is then $b/N_{\rm bins}$. The dominant uncertainty on this quantity comes from the estimate of the Galactic diffuse emission for which a $\pm 6\%$ error is applied as in the spectral analysis.

Since my thesis concentrates on radio-loud γ-ray pulsars, the radio profile is displayed along with the γ-ray light curves if available. The alignment of the radio and γ-ray light curves is performed by looking for the fiducial point defined by TZRMJD (the MJD time of arrival of the zero phase), TZRFRQ (the frequency for which this time is correct), and TZRSITE (encoding the radio telescope/site of arrival) in the radio ephemeris.

5.3.2 γ-ray light curve fitting

γ-ray light curves can be fit using statistical distributions (Abdo *et al.* 2013). To determine the best-fit parameters of the distribution, the maximum likelihood method is employed by defining the log-likelihood function as:

$$\log \mathscr{L} = \sum_{j=1}^{N_\gamma} \log [w_i f(\phi_i) + (1 - w_i)] \tag{5.9}$$

where w_i is the weight for photon i, $f(\phi_i)$ is the wrapped probability density function of $\phi \in [0,1)$:

$$f(\phi) = \sum_{i=1}^{N_\gamma} n_i\, g_i(\phi) + \left(1 - \sum_{i=1}^{N_\gamma} n_i\right) \tag{5.10}$$

$g(\phi)$ representing the pulsed component can be the Gaussian or Lorentzian distribution, while the unpulsed component is modelled by a uniform distribution $1 - \sum_{i=1}^{N_\gamma} n_i \leq 1$.

The likelihood fit gives the peaks number of γ-ray $N_{\rm peaks}$, the phase offset δ of the leading γ-ray peak from the radio peak and the phase separation Δ between the leading and trailing γ-ray peaks in the case of $N_{\rm peaks} > 1$.

The uncertainty on δ has contributions from the statistical uncertainty on the position of the relevant γ-ray peak, from that induced by the DM uncertainty, and that in the timing solution (the time residual incurs $\delta\phi \approx {\rm residual}/P$). We add in quadrature these contributions. The statistical uncertainty on Δ is determined by adding in quadrature the uncertainties on the relevant γ-ray peak positions. The systematic uncertainty of the fit stems from the different distributions chosen to model the light curves, which is ~ 0.01 in phase.

PART III

RESULTS

CHAPTER 6

Detections of seven faint γ-ray pulsars

Contents

6.1 Introduction

1PC (Abdo *et al.* 2010b) established pulsars as the dominant class of GeV sources in the Milky Way with 46 detections of energetic γ-ray pulsars amongst which all ten CGRO γ-ray pulsars have been confirmed. Using three years of data, 2PC (Abdo *et al.* 2013) largely extended the sample with 117 pulsars detected above the 5σ level. Nevertheless, candidates with $< 5\sigma$ significance deserve special follow-up and investigations from the point of view of either possible future detection or ultimately, a definitive non-detection. New discoveries are expected to be weaker but will be valuable since they will further enrich the 2PC population and help to probe and extend the parameter space of γ-ray pulsars. I have focused on γ-ray pulsation searches using radio ephemerides for radio-loud pulsars which are regularly observed under the pulsar timing campaign agreement (Section 4.2, Smith *et al.* 2008). Each half year, the engaged radio telescopes provide us up-to-date ephemerides for all the timed pulsars, the *Fermi*-LAT collaboration then performed a pulsation search to obtain new γ-ray pulsar candidates and finally confirms the detections. Based on our late 2011 pulsation search results, we made a list of pulsars with pulsed significance $> 3\sigma$.

This chapter presents seven new pulsars (four young radio-loud pulsars, three radio-loud MSPs. Table 6.1) finally detected at $> 5\sigma$ level during my thesis. After a brief description of their general properties, including radio observations used to phase-fold γ-ray photons, we report the γ-ray detections using the weighted H-test. Details of the γ-ray spectral analysis and light curve characterizations follow. Then, we discuss the spectral properties, geometry constraints and γ-ray detectability. We conclude our findings in the last Section.

Parameters	J0729−1448	J1055−6028	J1705−1906	J1913+0904
Galactic longitude, l (degree)	230.39	289.13	3.19	43.50
Galactic latitude, b (degree)	1.42	−0.75	13.03	−0.68
Spin period, P (ms)	251.7	99.7	299.0	163.2
Dispersion measure, DM ($\mathrm{pc\,cm^{-3}}$)	92.3 ± 0.3	633	22.91	97.27
Spin-down power $\dot{E}$ ($10^{33}\mathrm{erg\,s^{-1}}$)	282	1180	6.1	160
Characteristic age τ (kyr)	35.2	53.5	1.14×10^3	147
Magnetic field at light cylinder, $B_{\rm LC}$ (10^3 G)	3.18	16.4	0.4	3.7
Distance (kpc)	3.5 ± 0.4	$15.5^{+3.5}_{-6.3}$	0.9 ± 0.1	3.0 ± 0.4
Observatories	JBO, NAN, PKS	PKS	PKS	JBO
$N_{\rm TOA}$	177	102	73	195
Timing residual RMS (μs)	3322.56	980.659	247.957	1330.55
Ephemeris validity (MJD)	54220 − 55794	54505 − 56397	54221 − 56398	54589 − 56423

Parameters	J1640+2224	J1732−5049	J1843−1113
Galactic longitude, l (degree)	41.05	340.03	22.06
Galactic latitude, b (degree)	38.27	−9.45	−3.4
Spin period, P (ms)	3.16	5.31	1.85
Dispersion measure, DM ($\mathrm{pc\,cm^{-3}}$)	18.43	56.83	59.97
Proper motion in right ascension, μ_α ($\mathrm{mas\,yr^{-1}}$)	1.66 ± 0.12	...	-2.17 ± 0.07
Proper motion in declination, μ_δ ($\mathrm{mas\,yr^{-1}}$)	-11.3 ± 0.2	-9.77 ± 0.12	-2.74 ± 0.25
Spin-down power $\dot{E}$ ($10^{33}\mathrm{erg\,s^{-1}}$)	2.6 ± 0.2	3.2 ± 0.1	57.8 ± 0.2
Magnetic field at light cylinder, $B_{\rm LC}$ (10^3 G)	23.8 ± 1.0	15.8 ± 0.2	192.7 ± 0.3
Binary period, PB (days)	175.4607	5.2630	...
Distance (kpc)	1.2 ± 0.2	1.4 ± 0.2	1.7 ± 0.2
Observatories	NAN	PKS	NAN
$N_{\rm TOA}$	158	344	107
Timing residual RMS (μs)	1.386	3.311	0.952
Ephemeris validity range (MJD)	53313 − 56438	52647 − 55724	55041 − 56473
Proper motion reference	Löhmer *et al.* (2005)	July 2013 ephemeris	July 2013 ephemeris

Table 6.1: General properties and radio observations of seven new pulsars (Top four: young radio-loud pulsars; Bottom three: radio-loud MSPs). The Doppler correction is applied to $\dot{E}$ for pulsars with proper motion measurements. Uncertainties on $\dot{E}$ are from the proper motion and the distance. "..." means no measurements or not applicable. Notes: at the moment of finalizing this manuscript, we got new distance estimate of 8^{+5}_{-3} kpc for J1055−6028 by exploring the HI, CO, Hα maps and parallax distance of $0.45^{+0.66}_{-0.16}$ kpc for J1640+2224. The Doppler corrected $\dot{E}$ and $B_{\rm LC}$ for J1640+2224 are then $3.3^{+0.8}_{-0.2} \times 10^{33}\,\mathrm{erg\,s^{-1}}$ and $27.0^{+3.5}_{-0.8} \times 10^3\,\mathrm{G}$ respectively. The new results are reported in Hou *et al.* (2014).

6.2 General properties

6.2.1 Radio observations

The ephemerides used to phase-fold γ-ray data for the seven new pulsars are constructed using TOAs from the radio 1.4 GHz observations made by Parkes (PKS), Nançay (NAN) and Jodrell Bank (JBO). These ephemerides are valid till 2013 spring (April, May, June) except for J1732−5049, Jan 2011. Table 6.1 lists the general properties of the seven pulsars, along with the radio observations performed which allowed the construction of the ephemerides[1]. Except for the MSP J1732−5049, the validity ranges for the ephemerides completely cover the γ-ray data sample presented in Table 6.2.

The young pulsar J0729−1448 was discovered in the Parkes Multibeam Pulsar Survey II (Morris *et al.* 2002). It experienced two glitches: MJD 52149.6 (2001 Aug 28, Hobbs *et al.* 2004b) and MJD 54700 (from

[1]J1640+2224 is also observed by JBO, J1705−1906 is also observed by NAN and JBO, J1843−1113 is also observed by JBO. In this thesis, we didn't mix the TOAs from different observatories to obtain combined ephemerides for these three pulsars, while this has only been done for J0729−1448.

the adopted ephemeris).

The young pulsar J1055−6028 was discovered in a survey using new techniques for ranking candidates from a previous Parkes Multi-beam Pulsar Survey (Keith *et al.* 2009). It's cited only five times in the literature since then.

The young pulsar J1705−1906 was discovered in the second Molongo and Parkes survey of all the sky south of declination +20° (Manchester *et al.* 1978). It is called 'notorious' pulsar where the RVM fits can't distinguish between orthonogal and aligned rotators (Keith *et al.* 2010). We will discuss its geometry in detail in Section 6.4.2.

The young pulsar J1913+0904 was discovered in the Parkes Multibeam Pulsar Survey VI (Lorimer *et al.* 2006). Only three references exist after the discovery.

The MSP J1640+2224 is in a 175.46 day binary system with a low mass white dwarf companion of $m = 0.15\ \mathrm{M}_\odot$ (Löhmer *et al.* 2005). It was discovered in the High Latitude Millisecond Pulsar Survey with Arecibo Telescope (Foster & Wolszczan 1993). Owing to its very stable rotation and low noise timing properties, this pulsar is among the pulsars selected for gravitational wave searches through measurement of correlated disturbances in pulse arrival times (see e.g. Abbott *et al.* 2010; Burt *et al.* 2011).

The MSP J1732−5049 was discovered in a survey of intermediate Galactic latitudes at 1.4 GHz with the Parkes radio telescope (Edwards & Bailes 2001). It's in a 5.26 day binary system with a high mass white dwarf companion. Knight *et al.* (2005) searched giant radio pulses[2] with the telescope in Parkes for a sample of 18 MSPs, including this pulsar. Only upper limit was obtained.

The MSP J1843−1113 was discovered in The Parkes multibeam pulsar survey - IV (Hobbs *et al.* 2004a). Giant pulse searches have also been performed for this pulsar using data from the Parkes (Knight *et al.* 2005) and the Green Bank Telescope (Knight *et al.* 2006), but only upper limit was obtained. Nevertheless, the authors argued that the pulsar might emit giant pulses that are scatter-broadened beyond the sensitivity limits of the telescope, given that this pulsar is close to the Galactic plane with high diffuse emissions.

The distances we adopted for the seven new pulsars are all estimated using the NE2001 model from the DM measurement (Section 1.5.4). The uncertainties are obtained by varying the DM by ±20%, except for J1055−6028, the upper limit has been obtained at less than 1.2 DM since no more electrons are modelled after that value. J1055−6028 is the most distant pulsar in our sample and the third known γ-ray pulsar with a distance larger than 10 kpc.

In most cases, NE2001 is the only available pulsar distance estimate method and gives good estimates for the true distance within uncertainties. However, the NE2001 distance can be sometimes completely wrong due to unmodelled "clumps" along the line of sight as is the case of J0248+6021 (Theureau *et al.* 2011).

For J1055−6028, we observed, from the Galaxy map (Reid *et al.* 2009, Section 7.1), a dense region (including the massive stars AG Carinae and GG Carinae) at a distance of ~ 7.4 kpc which scratches the line of sight of the pulsar ($l = 289.13°$), while in the NE2001 model, there is no "clump" along this line of sight. I added therefore a sphere of cloud with a typical electron density of $5e^-/\mathrm{cm}^3$ and an angular width of 0.1° (which are already huge) for this line of sight to the model. The distance of J1055−6028 became 7.4 kpc, still large but greatly reduced.

A three-dimensional map of the Galactic electron distribution may be possible in the future to improve the NE2001 model, benefiting from deep sky surveys at radio and infrared wavelengths in support of the Planck[3] mission.

Other improvements and the most precise measurement on the distance come from the parallax. We have explored the parallax induced time delay (Equation 4.5) and compared it with the timing residual for the three MSPs (Figure 6.1). J1843−1113 has a timing residual of $\lesssim 1\,\mu$s and the amplitude of the parallax

[2]"Giant pulses" refer to individual pulses more than 10−20 times the mean pulse energy.

[3]http://www.esa.int/Our_Activities/Space_Science/Planck

induced time delay is right at the low end of its DM distance range, making the detection of timing parallax possible. The corresponding parallax distance would be > 1.2 kpc, making its DM distance more reliable than the other two MSPs. It may also be possible to have a parallax measurement for J1640+2224 if its DM distance is right, while less hope is expected for J1732−5049. For young pulsars, the parallax time delay is totally invisible facing their much bigger timing residuals than those of MSPs, so there is no hope to get a parallax distance from radio timing. They are not shown here. In this thesis, we use the DM distances.

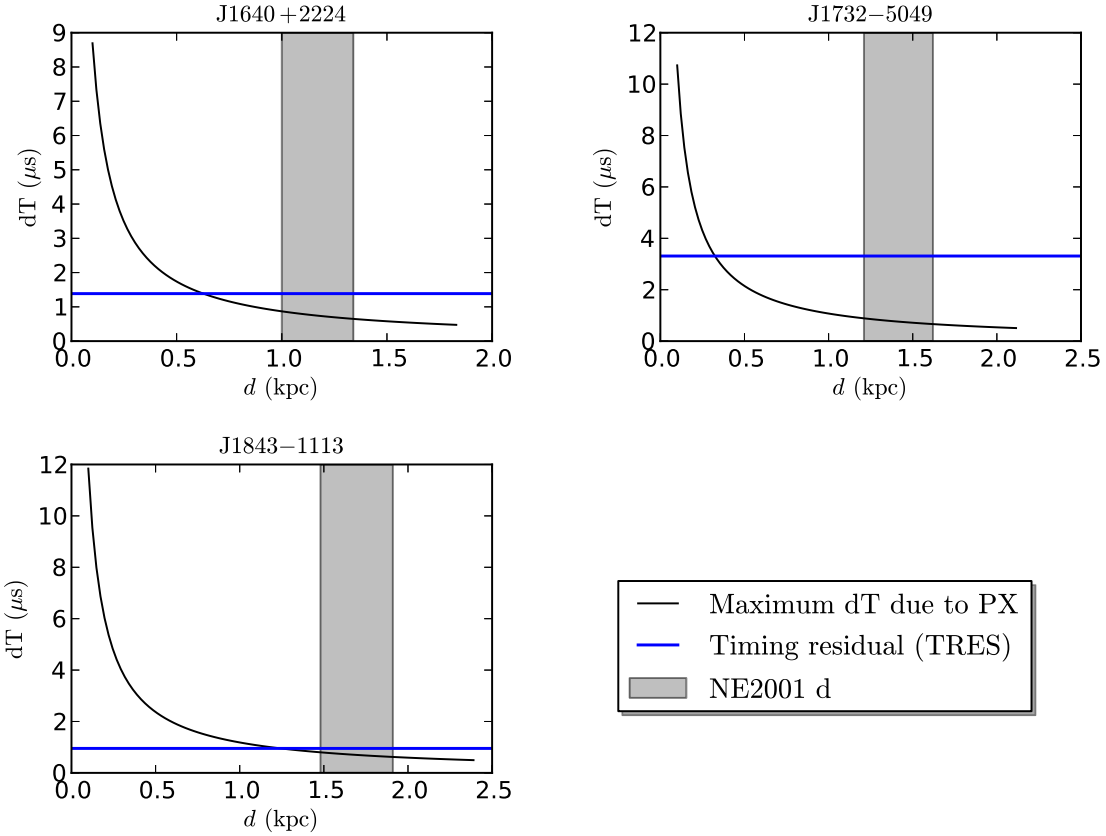

Figure 6.1: Comparison of parallax (PX) induced time delay with timing residual for three new MSPs.

6.2.2 X-ray/optical observations

None of our seven pulsars have been detected in X-ray or at optical wavelengths. However, Malov (2003) proposed J0729−1448 and J1705−1906 to be X-ray emitter candidates. Kargaltsev *et al.* (2012) reported a 4σ X-ray detection of J0729−1448 using data from the Chandra survey taken between 2001 and 2011. However, M. Marelli studied the X-ray properties for 2PC γ-ray pulsars, the detection significance for J0729−1448 is only 2.7σ and an upper limit of 0.37×10^{-13} erg cm^{-2} s^{-1} on the non-thermal X-ray emission from this pulsar has been derived. The pulsar is considered as a non-detection if taking 3σ as the criterion. No X-ray counterparts have been identified for the other six pulsars based on the analysis of XMM-Newton, Swift[4] and Chandra[5] data performed by M. Marelli.

[4]http://swift.gsfc.nasa.gov/index.html
[5]http://chandra.harvard.edu/

Parameters	J0729−1448	Other six new pulsars
Time interval	Aug 4 2008 – Aug 4 2011 (MJD 54682.6 – 55777.0)	Aug 4 2008 – Dec 12 2012 (MJD 54682.6 – 56273.0)
Dataset	*Pass 7*	*Reprocessed Pass 7*
IRFs	P7SOURCE_V6	P7REP_SOURCE_V15
Event class	Source	Source
Energy band	100 MeV−100 GeV	100 MeV−100 GeV
Zenith cut	100°	100°
Rocking angle	$< 52°$	$< 52°$
ROI (spectral analysis)	15°	10°
ROI (light curves)	2°	2°
ROI shifted?	NO	YES (except for J1640+2224)
Catalog	*gll_psc_v06.xml* (2FGL)	*P202_uw27.xml* (4 years)
Source list	TS $\geq$ 25	TS $\geq$ 16
Galactic diffuse model	*gal_2yearp7v6_v0.fits*	*gll_iem_v05.fit*
isotropic model	*iso_p7v6source.txt*	*iso_source_v05.txt*
ScienceTools version	v9r27p0	v9r32p04

Table 6.2: *Fermi*-LAT dataset for seven new pulsars for spectral and light curves analysis.

6.2.3 Environment

Existence of a dust disk around J0729−1448 is proposed by Wang *et al.* (2008) based on the Spitzer/IRAC[6] survey searching for debris disks around 7 relatively young, energetic radio pulsars. There are two massive stars near the pulsar J1055−6028. AG Carinae is a luminous blue variable of 50 $M_{\odot}$, 0.07° degrees away and has a ring nebula of angular size 0.01°. Hoekzema *et al.* (1992) placed AG Car at 6 ± 1 kpc from Earth. GG Carinae is a β Lyrae-type eclipsing binary which is 0.09° degrees away and with a distance of 5 ± 1 kpc (Marchiano *et al.* 2012). Galactic Plane Transient of the nearby pulsar J1057−6027[7] has been reported first in γ rays with the *Fermi*-LAT and then in X-ray with Swift/XRT. AG Carinae is suspected to be associated with the Swift source J105611.74−602714.1.

6.3 γ-ray observations

The dataset used in γ-ray analysis for the seven new pulsars is summarized in Table 6.2. The *Fermi*-LAT *Pass 7* dataset has been used for J0729−1448 covering the period of Aug 4 2008 − Aug 4 2011 while for the other six pulsars, we selected *reprocessed Pass 7* dataset between Aug 4 2008 and Dec 12 2012[8]. Photons of "Source" class with energies between 100 MeV and 100 GeV have been selected along with the corresponding IRFs (P7SOURCE_V6 for J0729−1448 and P7REP_SOURCE_V15 for the others). For all the seven pulsars, the standard zenith angle cut ($< 100°$) and ROI-based zenith cut have been applied. In addition, we only included events with good quality flags and collected when the LAT has a rocking angle smaller than 52°. γ rays from the Sun and the Moon have been excluded as well to remove possible contamination.

[6] http://www.spitzer.caltech.edu/

[7] http://www.astronomerstelegram.org/?read=2083

[8] The reprocessed Pass 7 dataset was not available at the time of the analysis for J0729−1448.

6.3.1 Detections

Among the seven pulsars, only J1913+0904 was detected at a $> 5\sigma$ level (trials corrected) if using energy dependant PSF cut and optimized radius cut by scanning the grid of radius to maximize the H-test, while the others were not detected. To improve the detection sensitivity, spectral analysis has been performed and the light curve was weighted by the probability that a given γ-ray event comes from the pulsar. All of the seven pulsars were detected at higher significance using the weighted H-test (Section 4.2.2). Figure 6.2 shows the unweighted light curves above 100 MeV for the seven pulsars, while weighted light curves in six energy bands are presented in Figure 6.10−6.16.

6.3.2 Spectral analysis

In the phase-averaged spectral analysis, originally, the standard ROI of 15° around the pulsar's radio position was adopted for all the seven pulsars. This worked for J0729−1448. In the case of the other six pulsars, due to strong background emission close to the Galactic plane and the complexity of the sky regions, ROIs for all but J1640+2224 have been shifted to be farther from the Galactic plane and to avoid very bright nearby sources. We also reduced the ROI to 10° which is a trade off between having a good diffuse emission fit and having a better fit for the pulsar.

We used the 2FGL catalog *gll_psc_v06.xml* for J0729−1448, along with the corresponding Galactic diffuse model *gal_2yearp7v6_v0.fits* and isotropic model *iso_p7v6source.txt* (Section 5.2.1). For the other six pulsars, we used the preliminary 4 year catalog *P202_uw27.xml* (hereafter *uw27*), along with the 4 years diffuse models *gll_iem_v05.fit* and *iso_source_v05.txt*. Sources with TS $\geq$ 16 (TS $\geq$ 25 for J0729−1448) were extracted from the catalog for each ROI. The seven pulsars were fixed at their radio positions. Note that J1640+2224 and J1705−1906 have no catalog associations, they were added by hand to the source models. Table 6.2 summarizes the different ROI definitions applied in the spectral analysis.

We used the standard *gtlike* tool integrated in the *Science Tools*. An alternate tool *pointlike* has also been used for J0729−1448 for cross checking. The best fit parameters are obtained using the maximum likelihood method described in Section 5.2.4 with the fitting optimizer MINUIT. The pulsar is modelled by a power law with a simple exponential cutoff (PLEC1, $b = 1$ in Equation 2.4). The integrated photon flux F_{100} and energy flux G_{100} in the band of 100 MeV−100 GeV are:

$$F_{100} = \int_{100\,\mathrm{MeV}}^{100\,\mathrm{GeV}} \frac{\mathrm{d}N}{\mathrm{d}E}\mathrm{d}E, \quad G_{100} = \int_{100\,\mathrm{MeV}}^{100\,\mathrm{GeV}} E\frac{\mathrm{d}N}{\mathrm{d}E}\mathrm{d}E. \tag{6.1}$$

To obtain the spectral energy distribution (SED, Figure 6.3), similar maximum likelihood analysis have been performed in logarithmically - spaced energy bands between 100 MeV and 100 GeV with the pulsar modelled by a simple power law (PL, $\Gamma = 2$ in Equation 5.1) in each band. Upper limits on the observed pulsar flux are computed if the pulsar has TS < 9 in a given band.

First we performed the ALL phase analysis, i.e. without selection on pulsar rotational phases. To benefit from a higher signal-to-noise ratio, which is important for our weak pulsars, we repeated the analysis by selecting only photons in the ON-peak interval for each pulsar (definitions in Table 6.3). We found that the energy flux G_{100} is compatible within statistical uncertainties whether cutting or not in phase, while the significance (TS) is improved by the cut.

The PLEC1 model may not always be significantly better than a PL. This could be due to different physics (ICS component instead of curvature radiation, cutoff feature invisible in the summed (phase-averaged) spectrum...), or simply because of statistics (diffuse emission dominates at low energy, there are not enough photons at higher energy to show the cutoff). In our case, we consider the latter be more reasonable given the weakness of our pulsars.

To test the significance of modeling the pulsar spectrum with a PLEC1 compared to a PL, I repeated the analysis using PL. As introduced in Section 5.2.4, this significance is obtained by computing $\mathrm{TS}_{\mathrm{cut}} =$

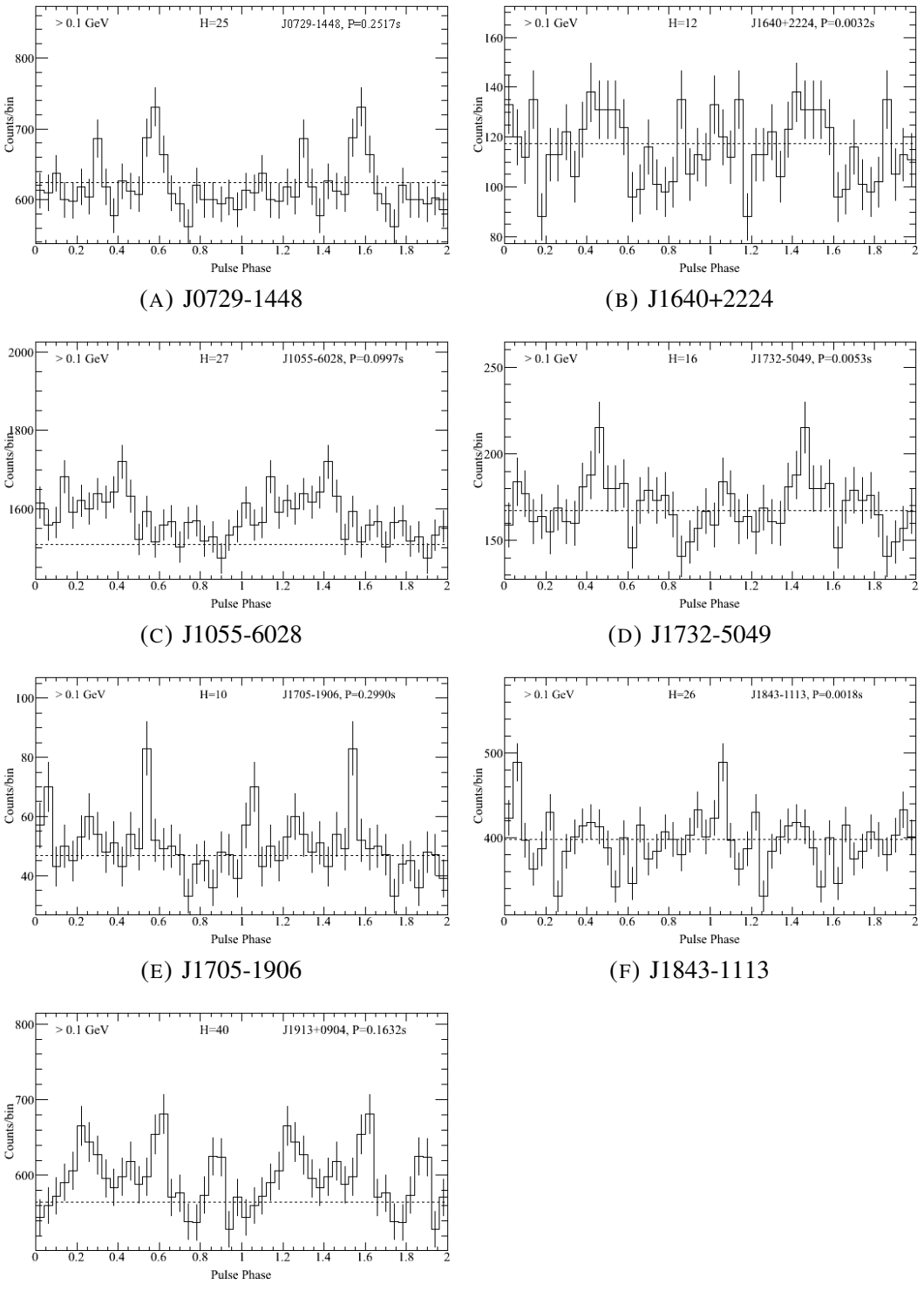

Figure 6.2: Unweighted light curves for seven new γ-ray pulsars. Left: young pulsars; Right: MSPs. Only PSR J1913+0904 has a trial corrected detection significance of $> 5\sigma$.

Parameters	J0729−1448	J1055−6028	J1705−1906	J1913+0904
TS	58	334	31	139
TS_{cut}	10	54	12	40
Spectral index, Γ	$1.5 \pm 0.2 \pm 0.1$	$1.6 \pm 0.1 \pm 0.2$	$0.00 \pm 0.01 \pm 1.3$	$1.5 \pm 0.3 \pm 0.1$
Cutoff energy, E_c (GeV)	$1.7 \pm 0.4 \pm 0.3$	$2.2 \pm 0.5 \pm 0.2$	$0.7 \pm 0.2 \pm 1.5$	$1.6 \pm 0.8 \pm 0.5$
Integral energy flux, G_{100} (10^{-12} erg cm^{-2} s^{-1})	$4.8 \pm 0.8 \pm 0.9$	$36.2 \pm 3.8 \pm 6.7$	$2.0 \pm 0.5 \pm 0.4$	$31.4 \pm 4.7 \pm 11.1$
Luminosity, L_γ (10^{33} erg s^{-1})	$7.1 \pm 1.2 \pm 2.0$	$1041 \pm 111^{+557}_{-700}$	$0.18 \pm 0.04 \pm 0.05$	$34 \pm 5 \pm 15$
Efficiency, η (%)	$2.5 \pm 0.4 \pm 1.0$	$88 \pm 9^{+47}_{-60}$	$3.0 \pm 0.7 \pm 0.9$	$21 \pm 3 \pm 9$
Weighted H–test	52	61	47	52
Significance (σ)	6.1	6.7	5.8	6.1
N_{peak}	1	2 (3)	1	2 (3)
Radio lag (δ)	0.58 ± 0.02	0.13 ± 0.05	0.57 ± 0.01	0.33 ± 0.04
γ peak separation (Δ)	...	0.31 ± 0.05	...	0.32 ± 0.04
ON-peak definition (ϕ)	$0.50 - 0.65$	$0.90 - 0.70$	$0.40 - 0.65$	$0.0 - 0.8$
Light curve bins	25	20	25	25
Light curve fit type	G2	G	L	G

Parameters	J1640+2224	J1732−5049	J1843−1113
TS	32	65	83
TS_{cut}	1.6	7	6
Spectral index, Γ	$2.1 \pm 0.2 \pm 0.2$	$2.2 \pm 0.1 \pm 0.3$	$2.8 \pm 0.1 \pm 0.1$
Cutoff energy, E_c (GeV)	...	...	...
Integral energy flux, G_{100} (10^{-12} erg cm^{-2} s^{-1})	$2.3 \pm 0.5 \pm 0.3$	$7.0 \pm 1.1 \pm 2.2$	$15.5 \pm 2.1 \pm 10.3$
Luminosity, L_γ (10^{33} erg s^{-1})	$0.4 \pm 0.1 \pm 0.1$	$1.7 \pm 0.3 \pm 0.7$	$5.4 \pm 0.7 \pm 3.8$
Efficiency, η (%)	$14 \pm 3 \pm 5$	$52 \pm 8 \pm 21$	$9.3 \pm 1.2 \pm 6.5$
Weighted H–test	45	36	49
Significance (σ)	5.7	5.0	5.9
N_{peak}	1	2	1
Radio lag (δ)	0.48 ± 0.03	0.39 ± 0.04	0.09 ± 0.01
γ peak separation (Δ)	...	0.27 ± 0.04	...
ON-peak definition (ϕ)	$0.21 - 0.61$	$0.25 - 0.80$	$0.80 - 0.20$
Light curve bins	25	25	16
Light curve fit type	G	G2	L2

Table 6.3: *Fermi*-LAT ON-peak spectral analysis results and light curve characterizations for seven new pulsars. The four young pulsars are fitted with a PLEC1 spectrum while the three MSPs are fitted with a simple PL due to low statistics. The first uncertainty is statistical, the second one is systematic. The luminosity has been calculated assuming a beaming factor $f_\Omega = 1$. See the text for details of the systematic uncertainty estimation method employed in this analysis. Light curve fit type definitions – G: Gaussian; G2: 2-sides Gaussian; L: Lorentzian; L2: 2-sides Lorentzian. Notes: with new distance estimates for J1055−6028 and J1640+2224 reported in Table 6.1, the luminosities decreased to $\sim 276 \times 10^{33}$erg s^{-1} and $\sim 0.056 \times 10^{33}$erg s^{-1} respectively, the efficiencies became ~ 23 and ~ 1.7 respectively. Refer to Hou *et al.* (2014) for details.

$2\Delta \ln\mathscr{L}$, with $\Delta ln\mathscr{L}$ the log-likelihood difference between PLEC1 and PL. We define the PLEC1 model to be significantly preferred over the PL model if $TS_{cut} \geq 9$ (3σ).

We take the ON-peak analysis as the final result and report it in Table 6.3. The ON-peak spectra are shown in Figure 6.3. The PLEC1 is preferred at the $> 3\sigma$ level only for the four young pulsars. Note that for the very faint pulsar J1705−1906, even though the PLEC1 is prefered by *gtlike*, with only one spectral point and index $\Gamma = 0$, we would say that a further analysis using more data is necessary to determine its actual spectrum. Individual pulsars and a study of systematic uncertainties are presented below.

J0729−1448

Included in 2PC, but flagged as having an unreliable spectral fit, J0729−1449 has undetermined spectral properties. My analysis was first performed with *pointlike* in the energy range of 100 MeV−100 GeV. The

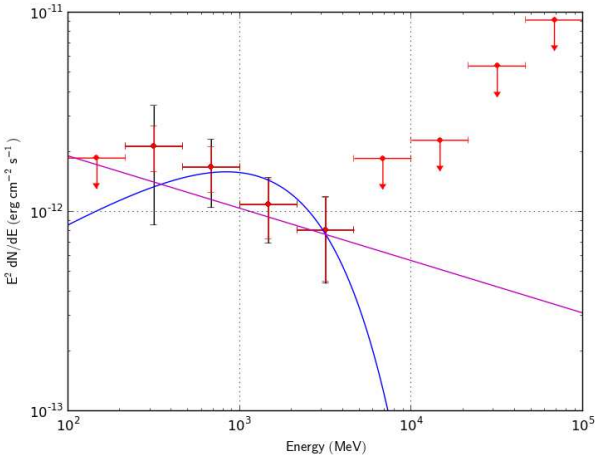

(A) J0729-1448

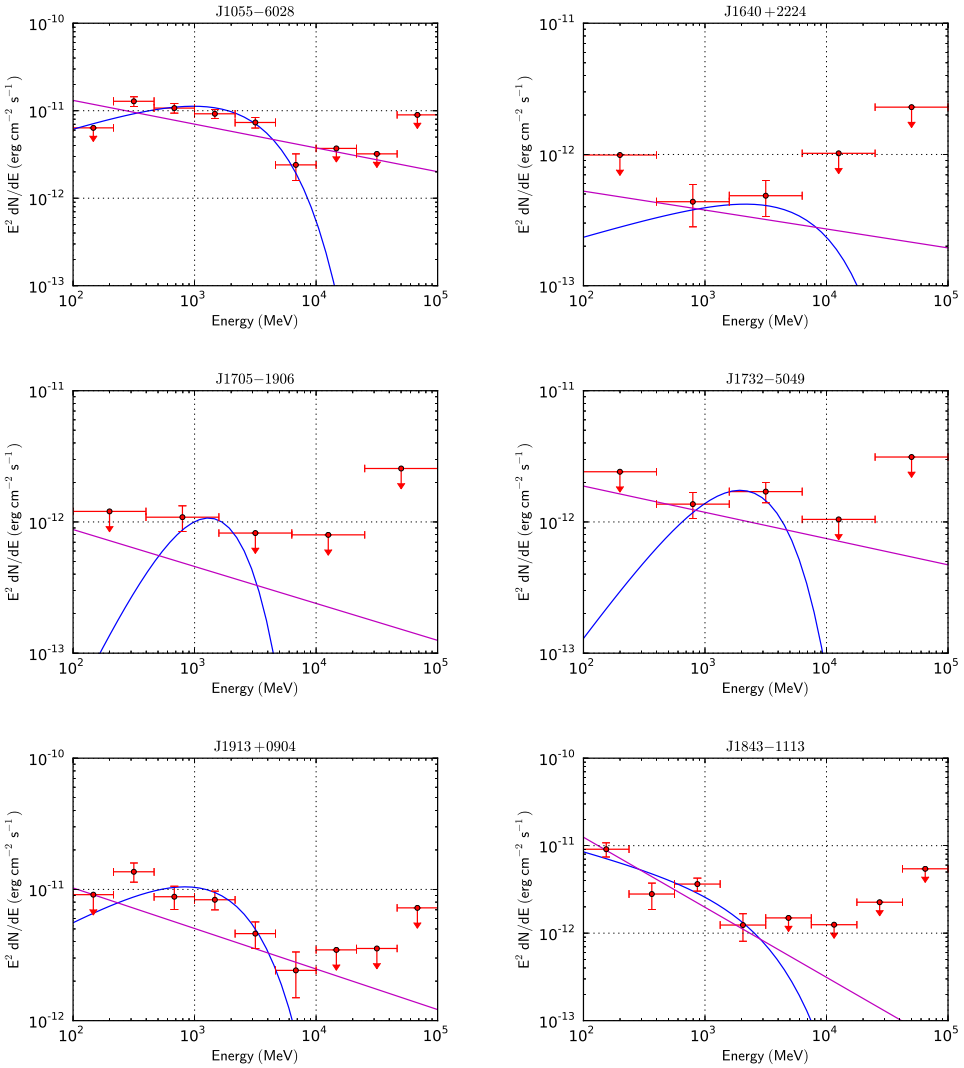

(B) Six other new pulsars

Figure 6.3: ON-peak spectral energy distribution (SED) for (A) J0729−1448 and (B) three young pulsars (left panels) and three MSPs (right panels) in the energy band of 100 MeV−100 GeV. The blue solid curve represents the global maximum likelihood fit with a PLEC1 spectrum, while the magenta solid line is the PL fit. Red points are obtained by performing similar maximum likelihood fits in logarithmically - spaced energy bands between 100 MeV and 100 GeV using a PL with index $\Gamma = 2$. Upper limits indicated by red arrows are calculated if TS < 9. Red solid vertical lines are the statistical uncertainties, and black solid vertical lines are the systematic uncertainties. The PLEC1 is preferred at the $> 3\sigma$ level only for the four young pulsars.

Model	Γ	E_c (GeV)	F_{100} (10^{-9} ph cm^{-2}s^{-1})	G_{100} (10^{-12} erg cm^{-2}s^{-1})
gtlike (nominal)	1.52 ± 0.46	1.74 ± 1.27	7.08 ± 2.21	4.78 ± 0.87
gtlike (add J0729−1836)	1.51 ± 0.20	1.68 ± 0.35	7.12 ± 1.94	4.81 ± 0.79
pointlike	1.65 ± 0.83	2.17 ± 1.85	6.85 ± 2.41	4.47 ± 0.91
pointlike (add J0729−1836)	1.55 ± 0.82	1.86 ± 1.56	6.54 ± 2.21	4.41 ± 0.88

Table 6.4: Comparison of ON-peak spectral fits in the energy band of 100 MeV−100 GeV for J0729−1448 between *gtlike* and *pointlike*, in the case of with/without J0729−1836 included in the source model.

best ON-peak model with *pointlike* was then given to *gtlike* to redo the fitting. The resulting fit with *gtlike* is compatible with that of *pointlike* within statistical uncertainties (Table 6.4).

One way to qualify the fit is to look at the TS map which is created by moving a putative point source (modelled with a PL with spectral index $\Gamma = 2$) through a grid of locations on the sky and maximizing the log-likelihood at each grid point. For an ideal fit, i.e. all sources accounting for the studied region have been well-modelled in the source model, the TS map should have no significant TS residuals (TS < 13), meaning that no supplementary sources are needed. In contrast, if a source responsible for the emission at a certain position is not included in the source model, it will appear in the TS map.

Following this approach, I found the radio pulsar J0729−1836 which is spatially coincident with the brightest spot in the TS map. At the time of this analysis, I performed a quick pulsation search for this pulsar and got a $\sim 3\sigma$ detection which was not enough to promote it to a γ-ray pulsar. Even though, to test the impact of this pulsar on J0729−1448, I took the previously obtained best ON-peak model and repeated the analysis by adding this pulsar into the source model with a PL. Table 6.4 summarizes the resulting spectral parameters in the case of without/with J0729−1836 in the source model using *gtlike* and *pointlike*. We can see that adding this extra pulsar in the source model gives results compatible with the standard analysis but with decreased error bars. This improvement can also be clearly inferred from the TS map (Figure 6.4).

From Table 6.4, we can see that my analysis is rather robust with typical spectral parameters compared to the 2PC sample. It's worth noting that at the moment of doing the analysis with J0729−1836 added, we had already finished the systematic analysis using the best ON-peak fit without J0729−1836 as the input spectral model. We take the best ON-peak fit with J0729−1836 in the source model as the final result, but with systematic uncertainties from analysis without J0729−1836. The corresponding spectrum is presented in Figure 6.3.

J1705−1906

J1705−1906 has no LAT association in the 4 year catalog *uw27*, while the closest source P7R42591[9] is 0.55° away from it. To clarify whether they are the same source or two different sources, we compare the counts map and TS map at > 100 MeV (Figure 6.5) and > 1 GeV (Figure 6.6) with both the pulsar and P7R42591 in the source model for the cases of ALL phase, ON-peak ($0.4 - 0.65$ in phase), and OFF-peak ($0.8 - 0.2$ in phase). Counts maps represent the counts excess for all sources in the region and are smoothed by a Gaussian with $\sigma = 0.5°$. TS maps are constructed by removing the pulsar and P7R42591 from the source model.

To assure that the LAT has correctly localized the detected γ-ray source, we have first re-localized P7R42591 at > 1 GeV (to benefit from a better PSF) for ALL phase, and we found the same position as that in *uw27*. Then, we fix the pulsar at its radio position and P7R42591 at its re-localized position. At

[9]Such funny names are only used in the development of the LAT source catalog. The formal public catalog names sources in a more comprehensible style, e.g. 2FGL J1705−1906.

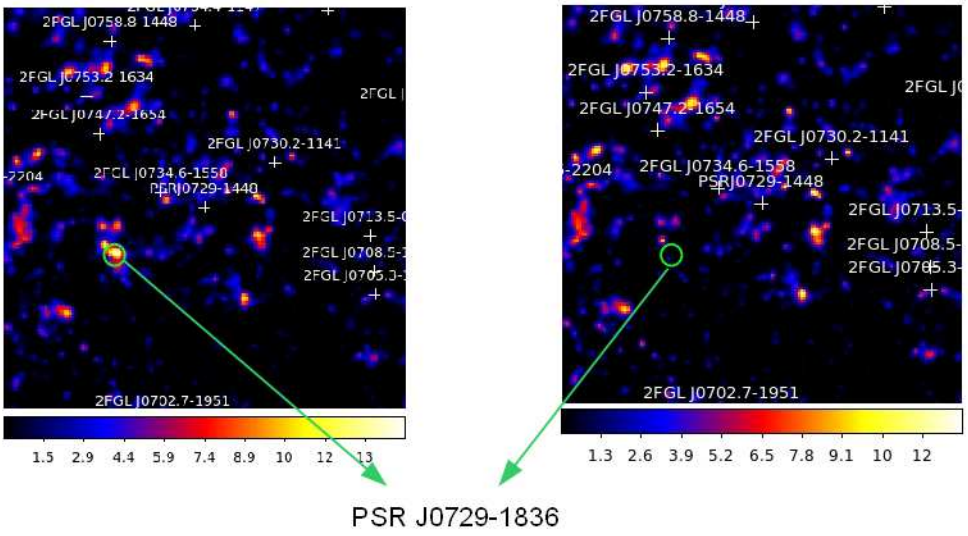

Figure 6.4: ON-peak residual TS map ($10^\circ \times 10^\circ$, 0.1°/pixel) in Galactic coordinates in the region centred at J0729−1448 without (left) and with (right) J0729−1836 in the source model, indicated by the green circle. Horizontal axis: Galactic longitude; Vertical axis: Galactic latitude.

$>$ 100 MeV, both J1705−1906 and P7R42591 are visible in ALL phase but the pulsar is less significant than P7R42591 as can be inferred from the TS map. However significant counts and TS excess are evident simultaneously at the pulsar's position when selecting ON-peak photons, benefiting from a higher signal-to-noise ratio. P7R42591 is also significant for ON-peak. In the case of OFF-peak, the pulsar disappears while P7R42591 is still visible. At $>$ 1 GeV, the pulsar is only significant for ON-peak, while P7R42591 persists for both ALL phase and ON-peak, implying a harder spectrum than J1705−1906. For OFF-peak, both sources disappear.

We conclude that J1705−1906 and P7R42591 are two different γ-ray sources. The phase-averaged spectrum of J1705−1906 has then been obtained by including both in the source model.

Systematic uncertainties

Systematic uncertainties on spectral parameters Γ, E_c and G_{100} are mostly due to the imperfect knowledge of the Galactic diffuse emission and the LAT effective area $A_{\rm eff}$. In this thesis, The standard procedure to estimate systematic uncertainties (Section 5.2.5) was followed for J0729−1448 and the result is presented in Table 6.5. The total uncertainty is obtained by adding in quadrature the maximum of the difference of each pair of variations with respect to the nominal value. For the other six pulsars, we estimate the systematics by comparing our ALL phase, ON-peak results and the PLEC1 results in the preliminary 4 year catalog 3FGL (*gll_psc4yearsource_v7_assoc_v6r1p0.fit*) for three young pulsars and the PL results in *uw27* for three MSPs (Table 6.6). Given that *uw27* models all pulsars with PLEC1, to be comparable with PL results obtained in our analysis, we have taken the PLEC1 SED in *uw27* and fit it with a PL by hand to get an estimate of the spectral index and the energy flux. Since J1640+2224 and J1705−1906 are included in neither catalog, we only compared their ALL phase and ON-peak results to estimate the systematic uncertainties. The total uncertainty is obtained by adding in quadrature the differences with respect to the nominal value.

Systematic uncertainties on L_γ are obtained by adding in quadrature those on distance and G_{100} and are propagated to the γ-ray efficiency η accordingly. The resulting total systematic uncertainties have been propagated to Table 6.3. We can see that systematic uncertainties dominate in most cases, especially for L_γ and η, where the distance steps in.

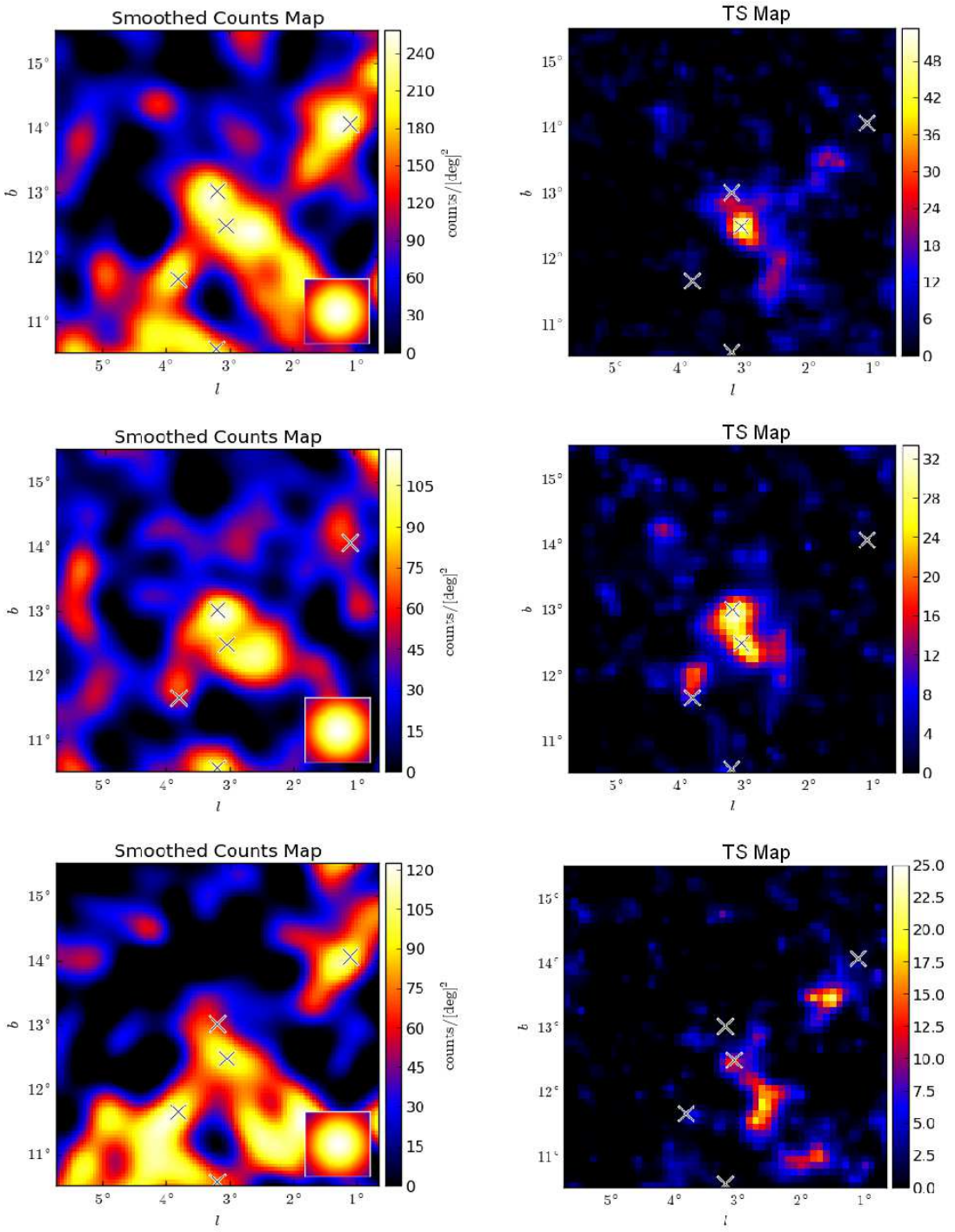

Figure 6.5: Smoothed counts maps (left column: $5^\circ \times 5^\circ$, 0.25°/pixel) and TS maps (right column: $5^\circ \times 5^\circ$, 0.1°/pixel) at > 100 MeV for J1705−1906 and P7R42591 in a region of 5° centred at J1705−1906 in Galactic coordinates for ALL phase (upper row), ON-peak ($0.4-0.65$ in phase, middle row) and OFF-peak ($0.8-0.2$ in phase, bottom row) analysis. Counts maps represent the counts excess for all sources in the region and are smoothed by a Gaussian with $\sigma = 0.5^\circ$. TS maps are constructed by removing the pulsar and P7R42591 from the source model. The pulsar is at its radio position and the LAT source P7R42591 (lower-right to the pulsar) is fixed at its re-localized position determined at > 1 GeV in ALL phase.

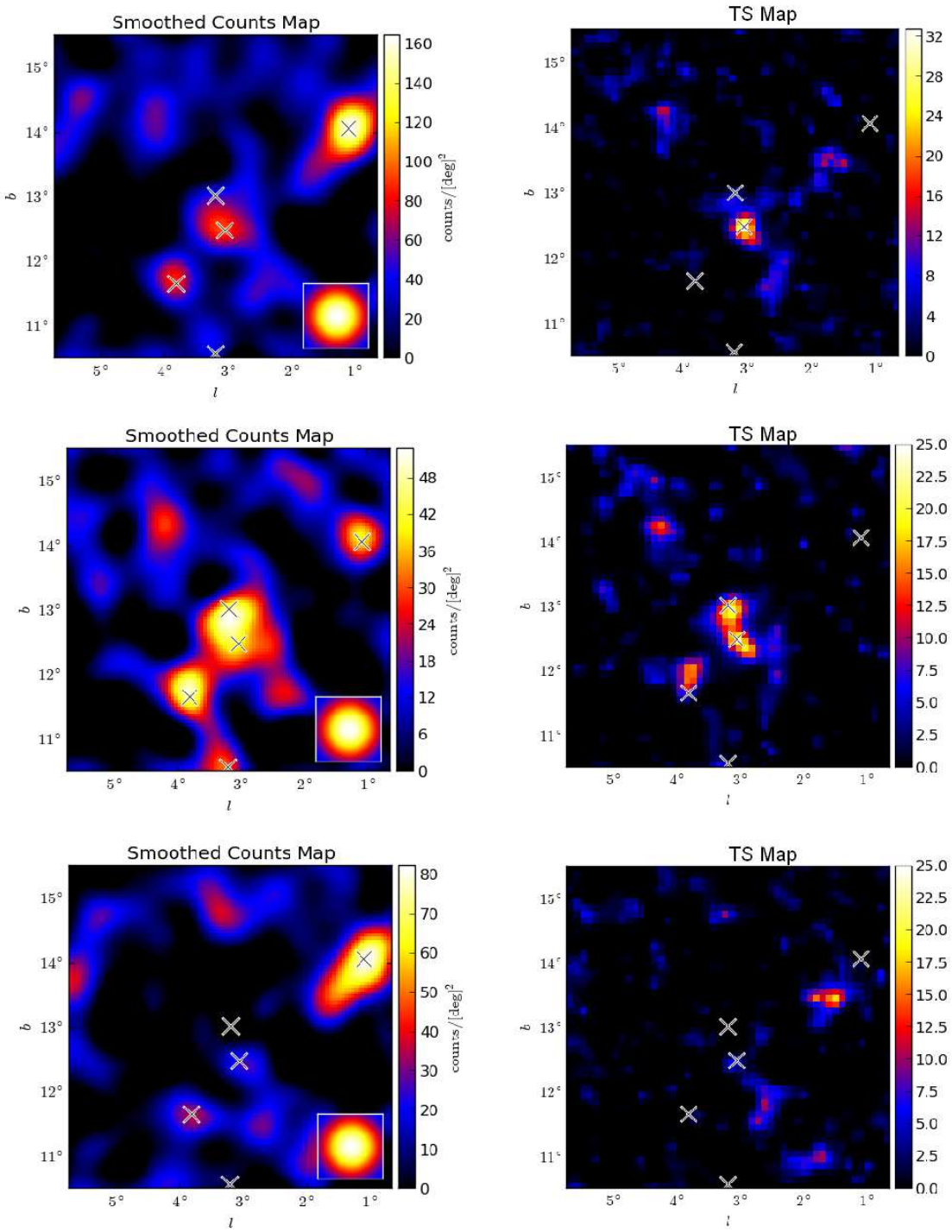

Figure 6.6: Labels are as for Figure 6.5 but for > 1 GeV.

Bracketing IRFs	Γ	E_c (GeV)	G_{100} (10^{-12} erg cm^{-2}s^{-1})
Nominal	1.52	1.74	4.78
flux_hi	1.56	1.88	5.11
flux_lo	1.50	1.71	4.42
index_hard	1.54	1.82	5.08
index_soft	1.52	1.75	4.44
$gal + 6\%$	1.50	1.89	4.09
$gal - 6\%$	1.50	1.54	5.45
Total	0.05	0.26	0.85

Table 6.5: ON-peak study of systematic uncertainties for J0729−1448 with Bracketing IRFs and by varying the Galactic diffuse emission by ±6%. The "Total" uncertainty is obtained by adding in quadrature the maximum of the difference of each pair of variations with respect to the nominal value.

6.3.3 Light curves

Light curves are constructed in a region of 2° around the pulsar's radio position using the weighted method described in Section 4.2.2. Weights come from the best ON-peak spectral fit described in Section 6.3.2 and reported in Table 6.3. We define the zero phase at the pulsar's radio peak. We use 25 bins per rotation for the light curves, except for J1055−6028 (20 bins) and J1843−1113 (16 bins) in order to smooth the background noise and thus to make the peak more pronounced. Figure 6.10−6.16 show the γ-ray light curves (histograms) for the seven new pulsars in six energy bands ($0.1-0.3$ GeV, $0.3-1.0$ GeV, $1.0-3.0$ GeV, >3.0 GeV, >10.0 GeV and >0.1 GeV) along with the best profile fit (blue solid line) at >0.1 GeV. Superposed (red solid line) is the phase-aligned ~ 1.4 GHz radio profile. Black dashed lines represent the estimated background level and its uncertainties (blue dashed lines) from the weighted method. Best light curve fit parameters are summarized in Table 6.3.

γ-ray profile characterization

To best characterize the observed profile at >0.1 GeV, therefore to obtain the radio lag δ and γ-ray peak separation Δ, different profile shapes were explored, including Gaussian, Lorentzian, 2-sides Gaussian, 2-sides Lorentzian[10], as in 2PC. Special care was taken for J1055−6028, J1732−5049 and J1913+0904 due to the wide ON-peak regions and the complexity of the pulse shapes (Figure 6.7). A variety of pulse shapes based on a Gaussian have been employed and the "fit quality" is qualified by the chi-squared (χ^2) statistical test. It's worth noting that for these three pulsars, no minimization was done, the pulse shape was adjusted by hand to find the one that best matches the observed profile.

Table 6.7 summarizes the light curve fits for these three pulsars with the best fits highlighted in bold. For 1055−6028, we fitted the first peak with three Gaussians: two narrow leading and trailing ones and the third broader one filling in the "bridge". For J1913+0904, the first peak is simply fitted with two Gaussians. For J1055−6028 and J1913+0904, a narrow peak just before the radio pulse is also detected at $\sim 3\sigma$ level. Note that this doesn't take into account the uncertainty on the background level (blue dashed lines in Figure 6.10−6.16). Given the high background uncertainties for these two pulsars, this peak may not be real. For J1732−5049, the profile is best described by a 2-sides Gaussian.

[10] 2-sides Gaussian or 2-sides Lorentzian refer to a Gaussian or Lorentzian curve the left and right part of which share the same center and amplitude but with different width.

Spectra	Γ	E_c (GeV)	G_{100} (10^{-12} erg cm^{-2} s^{-1})	$\mid \Delta\Gamma \mid$	$\mid \Delta E_c \mid$ (GeV)	$\mid \Delta G_{100} \mid$ (10^{-12} erg cm^{-2} s^{-1})
			J1055−6028			
ON (nominal)	1.6	2.24	36.16	...	...	...
ALL	1.5	2.04	40.35	0.1	0.20	4.19
Catalog (3FGL)	1.4	2.22	30.98	0.2	0.02	5.18
Total	...	...	...	0.2	0.20	6.66
			J1705−1906			
ON (nominal)	0.0	0.7	1.96	...	...	...
ALL	1.3	2.2	1.61	1.3	1.5	0.35
Catalog (3FGL)	...	...	...	...	...	...
Total	...	...	...	1.3	1.5	0.35
			J1913+0904			
ON (nominal)	1.49	1.64	31.39	...	...	...
ALL	1.53	1.61	37.04	0.04	0.03	5.65
Catalog (3FGL)	1.60	2.11	40.89	0.11	0.47	9.50
Total	...	...	...	0.12	0.47	11.05
			J1640+2224			
ON (nominal)	2.1	...	2.30	...	...	...
ALL	2.3	...	2.57	0.2	...	0.27
Catalog (uw27)	...	...	...	...	...	...
Total	...	...	...	0.2	...	0.27
			J1732−5049			
ON (nominal)	2.2	...	7.02	...	...	...
ALL	2.3	...	7.25	0.1	...	0.23
Catalog (uw27)	2.5	...	9.16	0.3	...	2.14
Total	...	...	...	0.3	...	2.15
			J1843−1113			
ON (nominal)	2.80	...	15.54	...	...	...
ALL	2.90	...	25.40	0.10	...	9.86
Catalog (uw27)	2.87	...	18.42	0.07	...	2.88
Total	...	...	...	0.12	...	10.27

Table 6.6: Study of systematic uncertainties for new young pulsars (top three) and new MSPs (bottom three). "..." means no data or not applicable. Γ, E_c and G_{100} are the spectral index, cutoff energy and integral energy flux respectively. $\mid \Delta\Gamma \mid$, $\mid \Delta E_c \mid$ and $\mid \Delta G_{100} \mid$ are the corresponding errors for different fits with respect to the nominal ON-peak value. The "Total" uncertainty is obtained by adding in quadrature the errors.

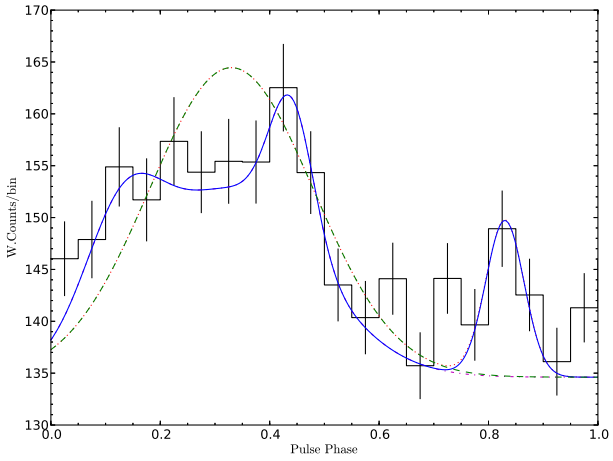

(A) J1055−6028

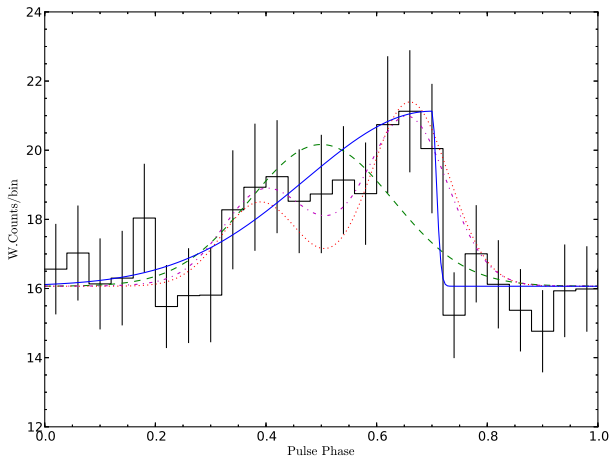

(B) J1732−5049

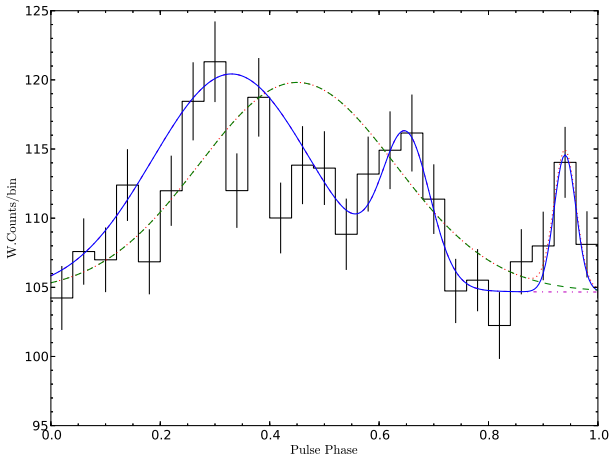

(C) J1913+0904

Figure 6.7: light curve fits for three pulsars with complicated pulses using different curves. For J1055−6028 and J1913+0904, Green dashed line: 1 broad peak fitted with a single Gaussian; Magenta dash-dotted line: 2 peaks fitted with 3 (2) Gaussians; Red dotted line: 1 broad peak plus 1 narrow peak fitted with 2 Gaussians; Blue solid line: 2 peaks plus 1 narrow peak fitted with 4 (3) Gaussians. For J1732−5049, Green dashed line: 1 broad peak fitted with a single Gaussian; Blue solid line: 1 peak fitted with a 2-sides Gaussian; Magenta dash-dotted line: 2 peaks fitted with 3 Gaussians. Red dotted line: 2 peaks fitted with 2 Gaussians. Fit qualities are reported in Table 6.7.

Pulse Shape	Parameter No.	dof.	χ^2	χ^2/dof.
J1055−6028				
1 broad peak (Gaussian)	3	16	62.28	3.89
2 peaks (3 Gaussians)	9	10	41.93	4.19
1 broad peak (Gaussian) + 1 narrow peak (Gaussian)	6	13	40.34	3.10
2 peaks (3 Gaussians) + 1 narrow peak (Gaussian)	12	7	19.74	2.82
J1732−5049				
1 broad peak (Gaussian)	3	21	16.38	0.78
2 peaks (2 Gaussians)	6	18	16.81	0.93
2 peaks (3 Gaussians)	9	15	13.68	0.91
1 broad peak (2-sides Gaussian)	4	20	9.57	0.48
J1913+0904				
1 broad peak (Gaussian)	3	21	77.60	3.70
2 peaks (2 Gaussians)	6	18	53.90	2.99
1 broad peak (Gaussian) + 1 narrow peak (Gaussian)	6	18	63.34	3.52
2 peaks (2 Gaussians) + 1 narrow peak (Gaussian)	9	15	38.14	2.54

Table 6.7: Comparison of γ-ray light curve "fits quality" for three pulsar with complicated pulses using different shapes. Best fits are highlighted in bold. dof: degree of freedom.

Figure 6.8 shows the Δ vs. δ for 2PC and our seven new γ-ray pulsars, highlighted by their names. 1PC observed an anti-correlation between δ and Δ, a general property of outer-magnetosphere models with caustic pulses, shown by Romani & Yadigaroglu (1995). However, 2PC shows that for MSPs, there is more dispersion around this trend and many young pulsars only have one γ-ray peak. In addition, Watters & Romani (2011) argued that most single-peak young pulsars have $\delta \approx 0.3 - 0.6$, while 2PC shows that disagreements exist for some young pulsars and especially MSPs. Within uncertainties, adding the six new pulsars (J0729−1448 is included in 2PC) seems to confirms these observations in 2PC.

Radio/γ-ray profile properties

J0729−1448 has one single sharp γ-ray peak. At $0.1 - 0.3$ GeV, the peak is invisible given the high background level. From $0.3 - 1.0$ GeV, the peak becomes evident and is stable with energy. In general, the peak is not very dependent on the energy. The pulsar's radio profile undergoes significant frequency evolution. At 1.4 GHz, there is one component, while at 3.1 GHz, there are two main components linked by a "bridge", each containing more components. The profile is highly polarized at both frequencies (Johnston & Weisberg 2006; Weltevrede & Johnston 2008b).

J1055−6028 has broad ON-peak region and complicated peaks. It's very close to the Galactic plane. At $0.1 - 0.3$ GeV, the peak is not convincing given the high background level uncertainties. One single peak becomes visible from $0.3 - 1.0$ GeV and gets broader with energy. The narrow peak just before the radio peak seems visible at $0.3 - 3.0$ GeV, but disappears at > 3.0 GeV. This peak may be just due to fluctuations at low energy. The radio profile has two (or three) components, and is very lowly polarized. Weltevrede & Johnston (2008a) studied the radio profile characterizations for a sample of energetic (high $\dot{E}$) pulsars and suggested that they are highly polarized compared to low $\dot{E}$ pulsars, with J1055−6028 the only exception.

J1705−1906 shows one single sharp γ-ray peak. It's invisible at $0.1 - 0.3$ GeV and becomes pronounced from $0.3 - 1.0$ GeV. It seems to get narrower with energy. Its radio profile at 1.4 GHz has a double peaked main pulse (MP), a weak interpulse (IP) and a modulation with the same periodicity at both longitudes

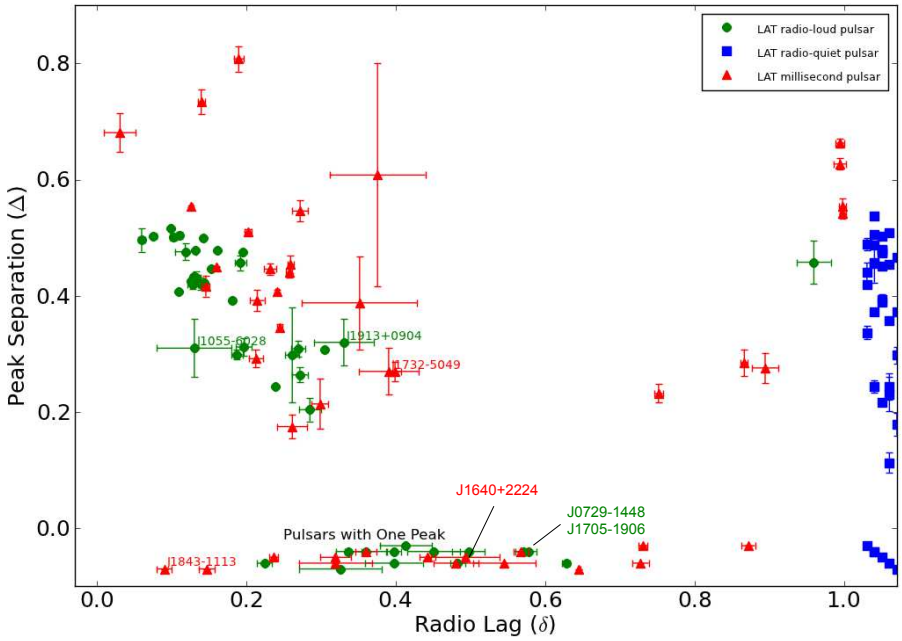

Figure 6.8: Radio lag δ vs. γ peak separation Δ. Single-peaked pulsars along the horizontal axis and radio-quiet pulsars along the right-hand vertical axis are plotted with artificial values of Δ and δ respectively to enhance readability. Seven new pulsars are highlighted with their names.

(phases) (Weltevrede *et al.* 2007). Components of the MP become complex at higher frequencies and the radio profile is marginally polarized (Figure 1.6).

As J1055−6028, J1913+0904 also has a broad ON-peak region and exhibits a narrow peak right before its radio peak. Given that it's also close to the Galactic plane, it's not surprising that the main peak becomes convincing only from $1.0-3.0$ GeV, as is the case of the narrow peak. Its narrow radio profile shows high linear polarization, but no circular polarization has been observed.

J1640+2224 has one single γ-ray peak. It's invisible at $0.1-0.3$ GeV but becomes more pronounced with energy. The position of the peak has a small offset in different energy bands, while the peak width at > 0.1 GeV appears to be due to summing of the energy sub-bands. Its not so narrow radio profile has three components. Xilouris *et al.* (1998) measured high linear and circular polarizations at 1.4 GHz, while at 774 MHz, the radio profile shows very weak linear and circular polarization, indicating a significant frequency evolution (Han *et al.* 2009).

Similar to J1055−6028 and J1913+0904, J1732−5049 has a broad ON-peak region. The pulse shape changes slightly with energy, but the ON-peak region is rather stable. We observe two photons with energy > 10.0 GeV at exactly the same bins as the leading and trailing peaks. Its radio profile[11] has one main component and three small components. The radio emission is slightly polarized for the whole phase (Ord *et al.* 2004).

J1843−1113's γ-ray peak is concentrated on a single same bin, but the whole profile shape evolves much with the energy. At > 3.0 GeV, the peak becomes invisible, indicating a small signal-to-noise ratio.

[11] It is obtained by hand using the profile presented in Ord *et al.* (2004)

Its radio profile exhibits one single component. No polarization information has been found in the literature.

Most of 2PC pulsars have two peaks (3/4 for young pulsars and 60% for MSPs). For my pulsar sample, the percentage is $\sim 2/3$ for young pulsars (ignoring the possible existence of a third peak and J0729−1448 which is included in 2PC) and $1/3$ for MSPs respectively, a little bit smaller than that in 2PC.

6.4 Discussion

6.4.1 Deathline, luminosity, efficiency

All γ-ray pulsars to date lie above an apparent "γ deathline" of $\dot{E} \approx 3 \times 10^{33}$ erg s^{-1}, a striking feature of the $P - \dot{P}$ plot (Figure 1.9). J1705−1906 has the lowest $\dot{E}$ among all the young radio-loud γ-ray pulsars, and is the third lowest one of any young γ-ray pulsars, the first two being radio-quiet. Two of the new MSPs, J1640+2224 and J1732−5049, are right at the limit of the deathline.

MSPs seem to have lower deathline than young pulsars, taking into account the Doppler correction which drives it even lower. Guillemot & Tauris (2014) studied the non-detection of nearby radio pulsars with helium white dwarf companions from the point of view of viewing angles ζ. Half of the MSPs in their sample with distance normalized spin-down power $\dot{E}/d^2 \gtrsim 10^{33}$ erg s^{-1} kpc^{-2} are detected in γ rays; all MSPs in their sample with such $\dot{E}/d^2$ have indeed $\dot{E} \gtrsim 10^{33}$ erg s^{-1} (this means their distances must be smaller than 1 kpc) and are therefore potential γ-ray emitters. This suggests that we could expect detections of radio-loud γ-ray MSPs with $\dot{E}$ less than 3×10^{33} erg s^{-1}, implying a lower "deathline".

Figure 6.9 shows the dependence of L_γ on $\dot{E}$ for 2PC and our seven γ-ray pulsars, highlighted by their names. The observation shows large dispersion around the "heuristic" relation $L_\gamma \propto \sqrt{\dot{E}}$ (Section 2.2.2) and suggests especially a "roll-off" at low $\dot{E}$. This depends strongly on the distance, which biases the interpretation of the dependence on $\dot{E}$ of L_γ. However, distances issue can't explain all the dispersion, e.g. J0659+1414 has a reliable parallax distance, but lies far out-of-family. In fact, it's one of the sub-luminous (low L_γ, or no γ-ray detection) pulsars discussed in Romani *et al.* (2011), which suggested that such cases could be due to the beaming effect, favoring an aligned pulsar geometry. J1705−1906 is also sub-luminous, though it was not included by the authors because of the selection criterion $\dot{E} > 10^{34}$ erg s^{-1}. Perera *et al.* (2013) investigated the luminosity trend in terms of P, $\dot{P}$ for 35 young γ-ray pulsars mostly from 1PC and found a best fit of $L_\gamma \propto P^{-a}\dot{P}^{b}$ with $a = 1.36 \pm 0.03$ and $b = 0.44 \pm 0.22$ provided by the OG model. This fit is consistent with, though not exactly identical to the "heuristic" relation $L_\gamma \propto \sqrt{\dot{E}} \propto P^{-1.5}\dot{P}^{0.5}$. Similar work on 2PC pulsars has not yet been done and we prefer to first remove the distance pollution before performing a robust modelling of the luminosity dependence on pulsar rotation parameters. Adding my six (J0729−1448 is in 2PC) new pulsars doesn't make the current trend (or dispersion) more or less strong.

J1055−6028 has the highest γ-ray efficiency in our sample, but also with large uncertainties. This results evidently from its very large distance. The pulsar should be at 12.7 kpc to get the efficiency down to 60%, 11.6 kpc to 50% and 9 kpc to 30%. With the reduced distance of 7.4 kpc discussed in Section 6.2.1, the efficiency would be pulled down to $\sim 20\%$, a typical value for the current γ-ray pulsar sample.

In Chapter 7, we will perform a detailed study for high efficiency pulsars in 2PC, with a method applicable to all the pulsars.

6.4.2 Geometry

Knowing pulsar geometry, i.e. the inclination α and the line of sight ζ, gives both the beaming factor f_Ω and γ peak widths which are important for the luminosity determination and pulsar detectability estimates. Pulsars with a radio interpulse (IP) separated by half a rotation from the main pulse (MP) are expected to have better geometric constraints from the RVM fit (Section 1.3.3) owing to additional polarisation

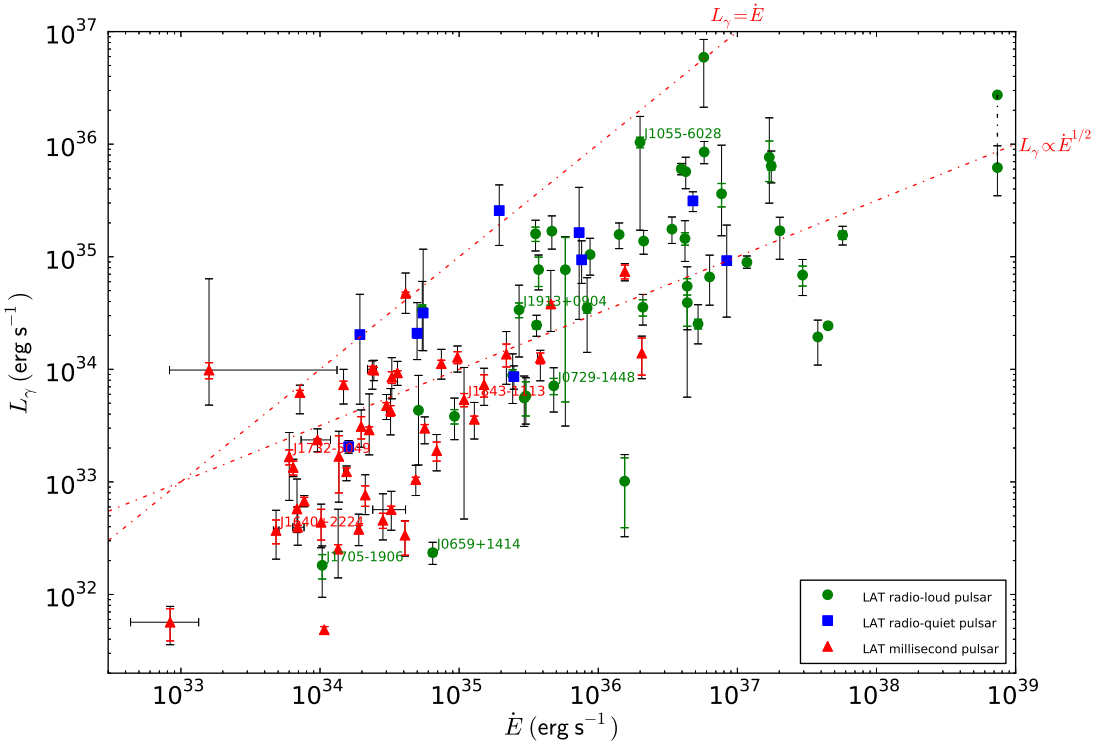

Figure 6.9: γ-ray luminosity L_γ vs. spin-down power $\dot{E}$ in the energy band of 100 MeV−100 GeV. The vertical error bars in color are from the statistical uncertainty on the energy flux G_{100}, while in black are due to the distance uncertainties. Horizontal error bars come from Doppler corrections (Section 4.1.2) applied to MSPs with known proper motions. The upper diagonal line indicates 100% conversion of $\dot{E}$ into γ rays, and the lower diagonal line indicates the heuristic relation $L_\gamma \propto \sqrt{\dot{E}}$. Seven new pulsars and J0659+1414 are highlighted with their names.

information in the IP, though only less than 5% of known pulsars have IP, making such cases rare. The geometry constraints for the seven pulsars are summarized in Table 6.8 and detailed below.

J1705−1906 is the third γ-ray pulsar with a radio IP, the other two being J0908−4913 and J1057−5226 (an EGRET pulsar) included in 2PC. A γ-ray IP is also detected for J0908−4913 and in addition follows the radio IP with same separation in phase, $\delta = 0.1$. We have $\delta = 0.57$ for J1705−1906 by defining the zero phase $\phi = 0$ at the radio maximum (main pulse). However taking the radio IP to be at $\phi = 0$ will give $\delta = 0.07$, slightly smaller than for J0908−4913. For J1057−5226, three overlapping peaks have been modelled to represent its wide ON region. Its radio IP consists of a strong leading component and a double-peaked trailing component, very similar to J1705−1906.

Weltevrede *et al.* (2007) studied J1705−1906 in detail (polarization, radio beam modulation, MP-IP interaction) and determined $\alpha \approx \xi \approx 90°$, corresponding to an orthogonal rotator. However, the authors couldn't distinguish between two possible emission theories to explain the observed profile and the MP-IP interaction (the modulations of MP and IP are precisely periodic and in phase): Two-pole model (Rickett & Lyne 1968) which proposed that the MP and IP originate from opposing magnetic poles, and Bidirectional model (Dyks *et al.* 2005) in which the IP is considered as part of the MP emission directed downward towards the neutron star. Similar geometry (α, ζ) was obtained for J0908−4913, but $\alpha \approx 75°$ and $\zeta \approx 70°$ for J1057−5226 (Keith *et al.* 2010).

The gap width w, i.e. the γ-ray efficiency, as defined by Romani & Watters (2010) is ~ 0.03 for

PSR	w	α		ζ		f_Ω	
		OG	TPC	OG	TPC	OG	TPC
J0729−1448	$\sim 0.03 \sim 0.1$	$\sim 55^\circ - 75^\circ$	...	$\sim 65^\circ - 90^\circ$	...	$\sim 0.5 - 0.95$	...
J1055−6028	~ 0.9	...	...	...	...	...	...
J1705−1906	~ 0.03	$\sim 90^\circ$		$\sim 90^\circ$		$0.75 - 0.95$	
J1913+0904	~ 0.2	...	$\sim 15^\circ - 35^\circ$	...	$\sim 35^\circ - 65^\circ$	...	$\sim 0.5 - 1.25$
J1640+2224	~ 0.1	$\sim 55^\circ - 90^\circ$	$\sim 35^\circ - 55^\circ$	$\sim 35^\circ - 65^\circ$	$\sim 35^\circ - 65^\circ$	$\sim 0.75 - 1.25$	$< 0.25, 0.25 - 1.25, > 1.25$
J1732−5049	$\sim 0.5 \sim 0.3$	$\sim 15^\circ$	$\sim 15^\circ$	$\sim 90^\circ$	$\sim 35^\circ - 80^\circ$	$\sim 0.5 - 0.75$	$\sim 0.75 - 1.25, > 1.25$
J1843−1113	same as J1640+2224						

Table 6.8: Geometry constraints for seven new pulsars with the OG and TPC model predictions from Romani & Watters (2010). For J1705−1906, α and ζ are from Weltevrede *et al.* (2007).

J1705−1906 and ~ 0.07 for J0908−4913. According to the Atlas (Romani & Watters 2010), only the OG model allows a single γ peak for small w in the case of J1705−1906. The second peak grows with the gap width and the separation of the first peak relative to the main radio pulse also increases. Both OG and TPC models predict two γ-ray peaks for J0908−4913, which is in great agreement with the observed profile. As for J1057−5226, only the OG model permits a single peak for all but the largest w, broadening as w decreases. With $w \sim 0.14$ in 2PC, the observed wide peak of J1057−5226 corresponds qualitatively with the prediction of the Atlas. Given the constrained angles, the Atlas predicts $0.75 < f_\Omega < 0.95$ for J1705−1906 and J0908−4913, and $f_\Omega \sim 1$ for J1057−5226. This implies the calculated γ-ray luminosity L_γ of the three pulsars represents almost their all-sky emission.

Two MSPs, J1640+2224 and J1843−1113 have a rather sharp single peak. With $w \sim 0.1$, the OG model predicts $\alpha \sim 55^\circ - 90^\circ$ and $\zeta \sim 35^\circ - 65^\circ$. This results in $f_\Omega \sim 0.75 - 1.25$. The TPC model predicts same range for ζ as the OG model, but $\alpha \sim 35^\circ - 55^\circ$, yielding a wide range values of f_Ω: from < 0.25, $0.25 - 1.25$ to > 1.25. The geometry of the OG model better constrains f_Ω.

Löhmer *et al.* (2005) measured the Shapiro delay and proper motion for J1640+2224, and obtained an orbital inclination $78^\circ < i < 88^\circ$. The recent study by Guillemot & Tauris (2014) proposed however $i \sim 50^\circ$ using the white dwarf mass-orbital period relation (TS99) established by Tauris & Savonije (1999). They used the inclination i as an estimate for the viewing angle ζ assuming that the rotation plane coincides with the orbital plane. This is the rare case where the Shapiro effect is not in agreement with the TS99. In addition, they couldn't reproduce the Shapiro effect using Nançay data, leaving a doubt on the measurement by Löhmer *et al.* (2005).

The young pulsar J0729−1448 has a single sharp peak and $w \sim 0.03 \sim 0.1$. Only the OG model allows such observations and predicts $\alpha \sim 55^\circ - 75^\circ$ and $\zeta \sim 65^\circ - 90^\circ$, corresponding to $f_\Omega \sim 0.5 - 0.95$.

For J1913+0904, the OG model has no light curve predictions corresponding to a $w \sim 0.2$, while the TPC model points to $\alpha \sim 15^\circ - 35^\circ$ and $\zeta \sim 35^\circ - 65^\circ$. This results in $f_\Omega \sim 0.5 - 1.25$.

J1055−6028 has $w \sim 0.9$, which is out of the Atlas work in Romani & Watters (2010). If taking into account the uncertainties, the lower value of w of ~ 0.2 will give similar α, ζ and f_Ω values as for J1913+0904.

For J1732−5049, $w \sim 0.5 \sim 0.3$. Both the OG and TPC models predict $\alpha \sim 15^\circ$, while $\zeta \sim 90^\circ$ for the OG model and $\zeta \sim 35^\circ - 80^\circ$ for the TPC model. f_Ω is then $0.5 - 0.75$ for the OG model and $0.75 - 1.25$ or > 1.25 for the TPC model. Guillemot & Tauris (2014) predict $\zeta > 45^\circ$ using the TS99 relation. This value is compatible with both the OG and TPC models.

6.4.3 Detectability

Whether a pulsar is detectable on Earth in γ rays depends on several parameters. The spin-down power $\dot{E}$, derived from the spin-down period P, the magnetic field B, and the inclination α, determines the intrinsic

energy power available. Higher $\dot{E}$ is preferred. However, since all the rotational energy is not converted to γ rays, it's logical to consider also the γ-ray luminosity, which depends on the distance d, the observed integral energy flux G_{100} and the beaming factor f_Ω. f_Ω compares the pulsar's averaged all-sky emission for a full rotation with that where the emission beam crosses the line of sight, but it doesn't give the γ-ray pulse sharpness: narrow peaks are easier to detect than broad ones given the same f_Ω.

So, given the magnetic field B, the rotation period P and the inclination α of a pulsar, whether and how well the pulsation would be seen depend on the distance, the local background level and the peak sharpness.

The approximate LAT threshold in terms of the effective flux $\sqrt{\dot{E}}/d^2$ is $\sim 10^{16}\,\mathrm{erg}^{1/2}\,\mathrm{s}^{-1/2}\,\mathrm{kpc}^{-2}$ despite the uncertainty on distances (Figure 15 in 2PC). All the pulsars in our sample have $\sqrt{\dot{E}}/d^2 > 3\times10^{16}\,\mathrm{erg}^{1/2}\,\mathrm{s}^{-1/2}\,\mathrm{kpc}^{-2}$, except J1055−6028, $4.5\times10^{15}\,\mathrm{erg}^{1/2}\,\mathrm{s}^{-1/2}\,\mathrm{kpc}^{-2}$ due to its large distance.

J1640+224 and J1705−1906 are nearby and off the Galactic plane. The reason why it took four years for them to be detected could be simply due to their faintness: $\dot{E}$ is near the deathline. Fortunately, they have rather sharp peaks which compensate the faintness and make the detection finally possible.

J1055−6028 has the highest $\dot{E}$ and is one of the rare undetected pulsars with $\dot{E} > 10^{36}$ erg s^{-1} in 2PC. Its large distance may account for this, while its single broad peak and low Galactic latitude also make the detection harder.

J1913+0904 is also close to the Galactic plane and some very bright sources are within 5° as is the case for J1055−6028. The closest bright source SNR W49B is $< 1^\circ$ away. Together with its wide ON region, this explains why it was necessary to accumulate four years of data to detect it.

The $\dot{E}$, b and d values, and the narrow γ peak for J1843−1113 are such that it is surprising that it took 4 years to have a 5σ detection. The reason may be that its flux G_{100} is right at the LAT's sensitivity limit (Figure 2.4).

Due to its high declination (-50°), J1732−5049 is only observable by Parkes. Since its $\dot{E}$ is below the threshold of the pulsar timing campaign and no radio ephemeris had been obtained, we had never previously looked at it. Pulsations from J1732−5049 were discovered in early 2013 when it appeared as a steady source in the preliminary 4 year catalog and after obtaining an updated ephemeris from Parkes.

J0729−1448 has the second highest $\dot{E}$ in our sample, but its flux is at the limit of the LAT's sensitivity. The possible reason for its detection using less than 4 years data is its very sharp peak.

6.5 Conclusion

We report seven new pulsars (four young radio-loud pulsars, three radio-loud MSPs) discovered during my thesis work, with J0729−1448 already included in 2PC. We performed detailed spectral analysis and characterized their light curves. The spectra of the four young pulsars can be fitted by a power law with a simple exponential energy cutoff, a spectrum shape generally employed for pulsars, while the three MSPs are fitted by a simple power law due to low statistics. Light curves are fitted by exploring different shapes, trying to find the one that best matches the observed profiles in order to derive different parameters which determine the pulsar geometry.

These pulsars are weak compared to the 2PC population, making the spectral and profile characterization difficult and less precise, but they show similar properties compared to the 2PC sample based on our analysis. We discussed the parameter space which affects the pulsar detectability, such as distance, sky location, energy flux vs LAT's sensitivity, deathline, and peak sharpness, etc. These new detections enriched the 2PC sample. In general, the OG model is preferred, but it can't explain all the observed properties.

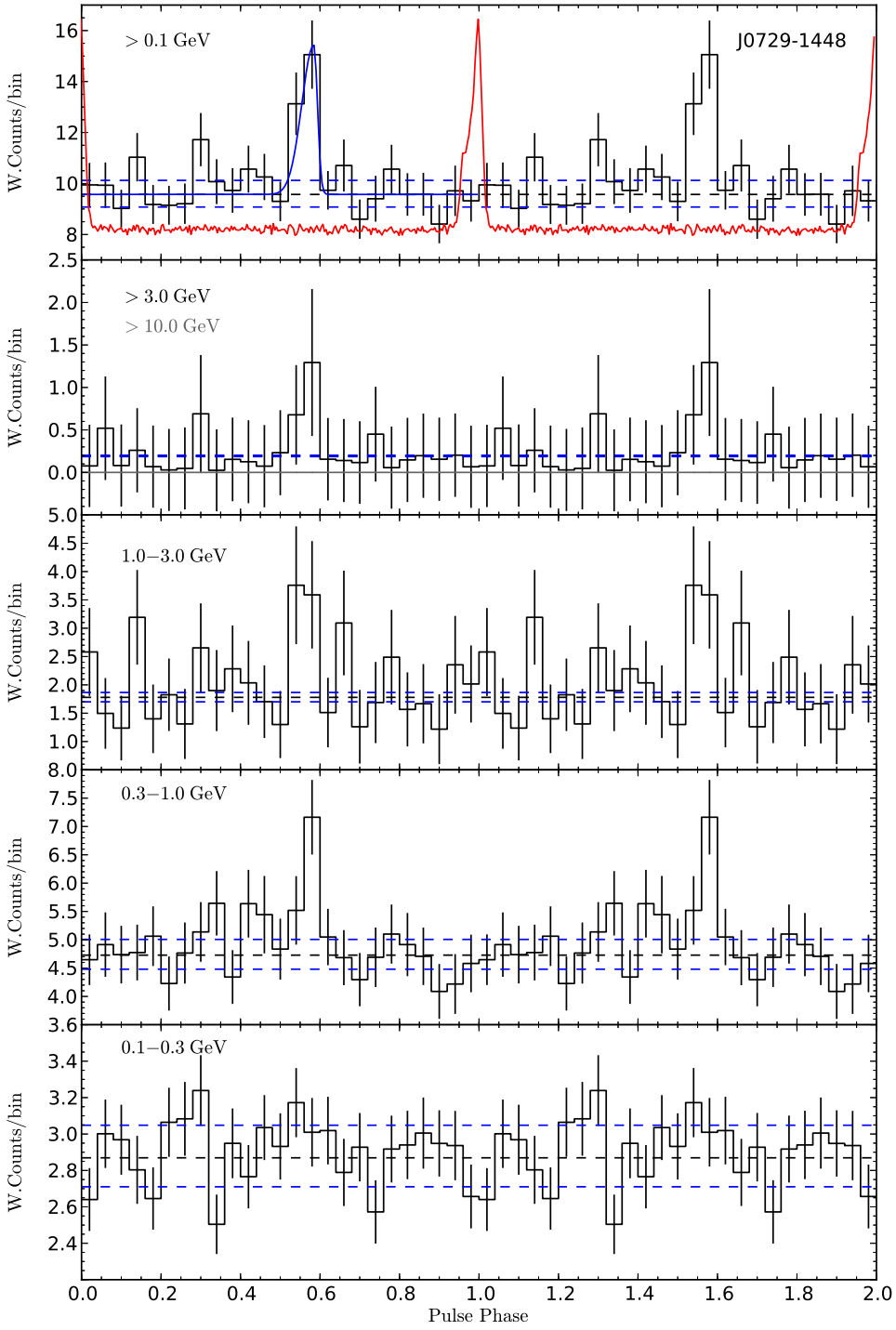

Figure 6.10: Weighted light curves of J0729−1448 in six energy bands (black histogram; gray histogram for > 10.0 GeV). Two rotations in phase are shown. The estimated background level (black dashed lines) and its uncertainties (blue dashed lines) are from the weighted method. The blue solid line is the best light curve fit, and the red solid line is the 1.4 GHz radio profile. From bottom to top: $0.1 - 0.3$ GeV, $0.3 - 1.0$ GeV, $1.0 - 3.0$ GeV, > 3.0 GeV (> 10.0 GeV in gray), > 0.1 GeV.

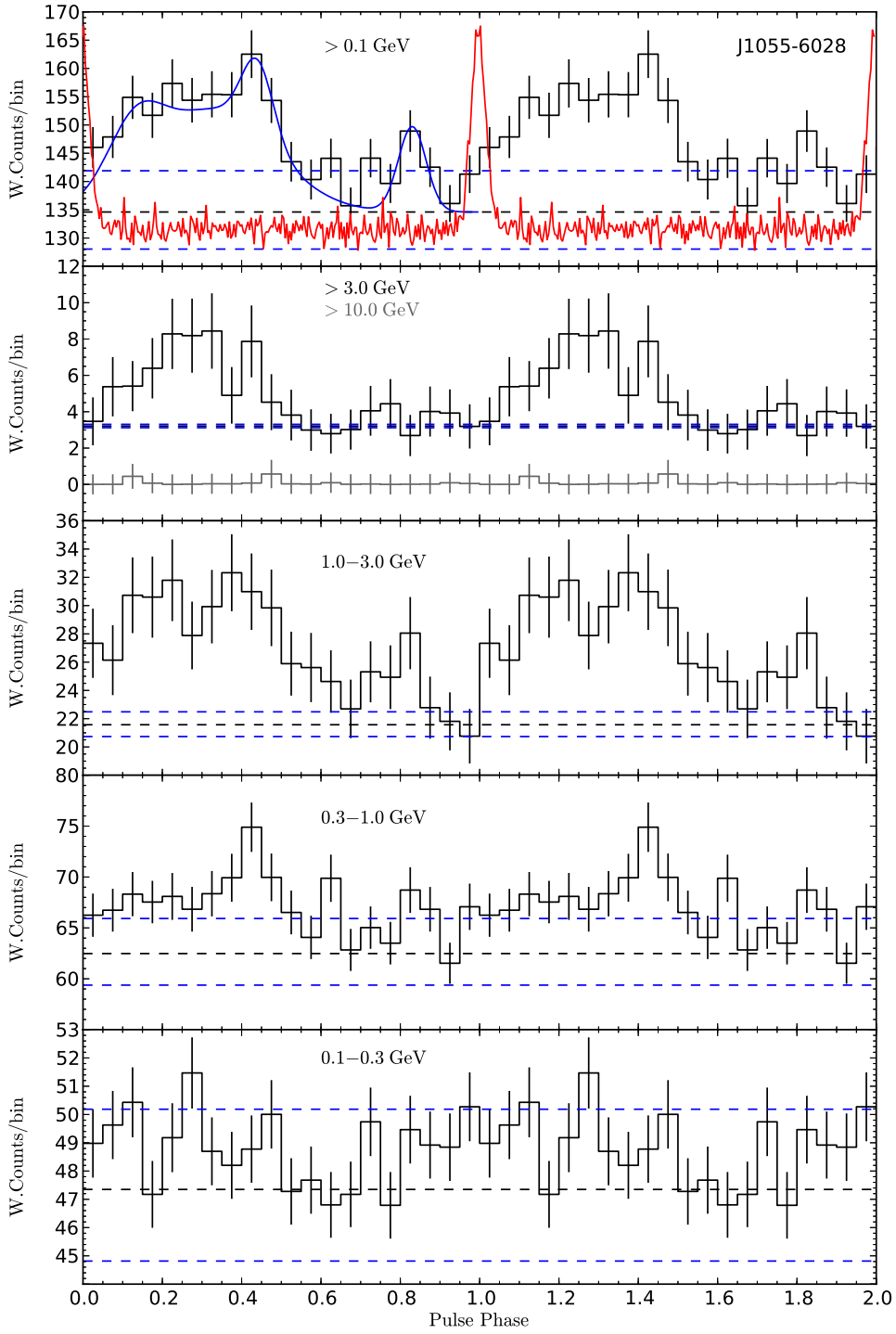

Figure 6.11: Weighted light curves of J1055−6028. Labels are as for Figure 6.10.

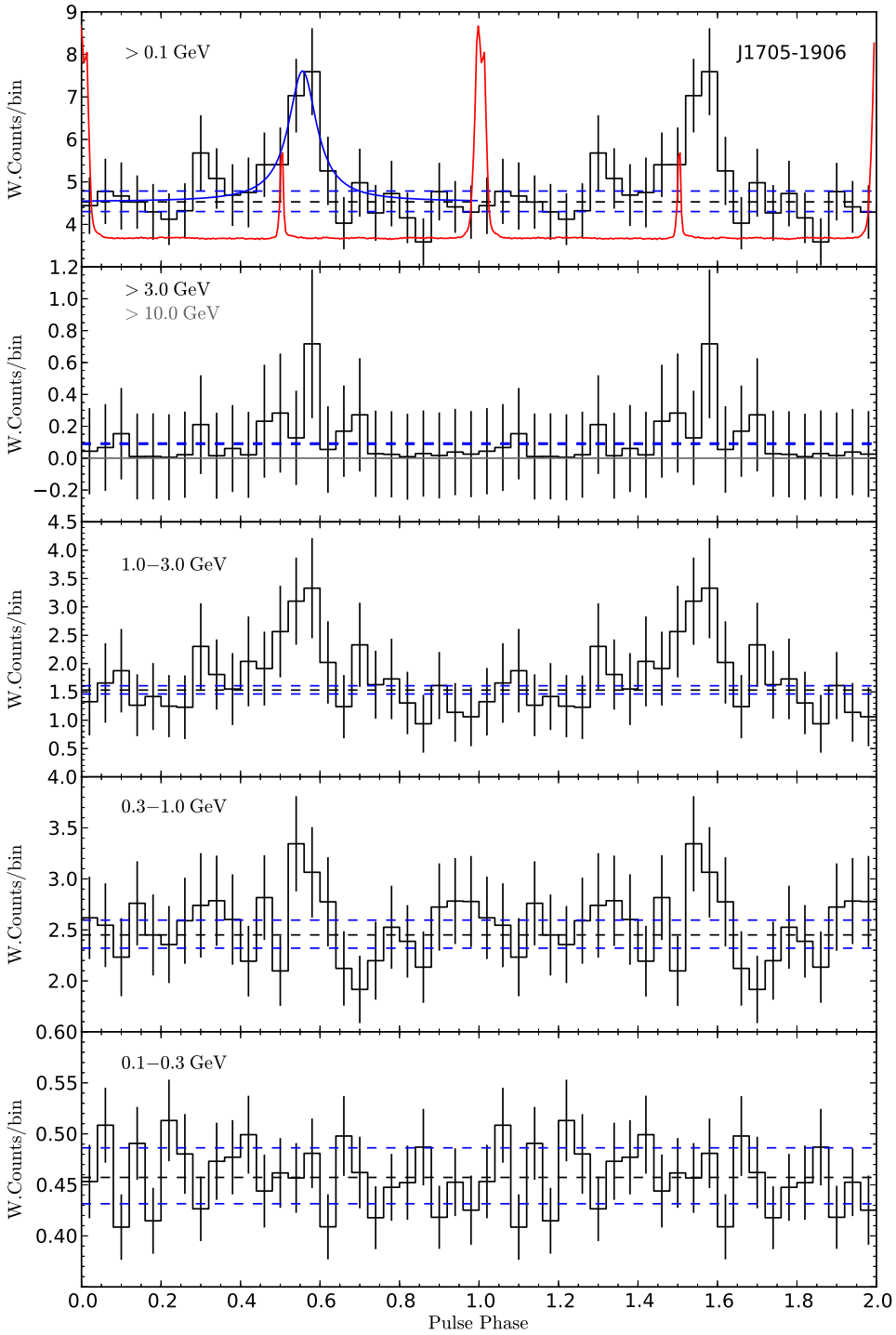

Figure 6.12: Weighted light curves of J1705−1906. Labels are as for Figure 6.10.

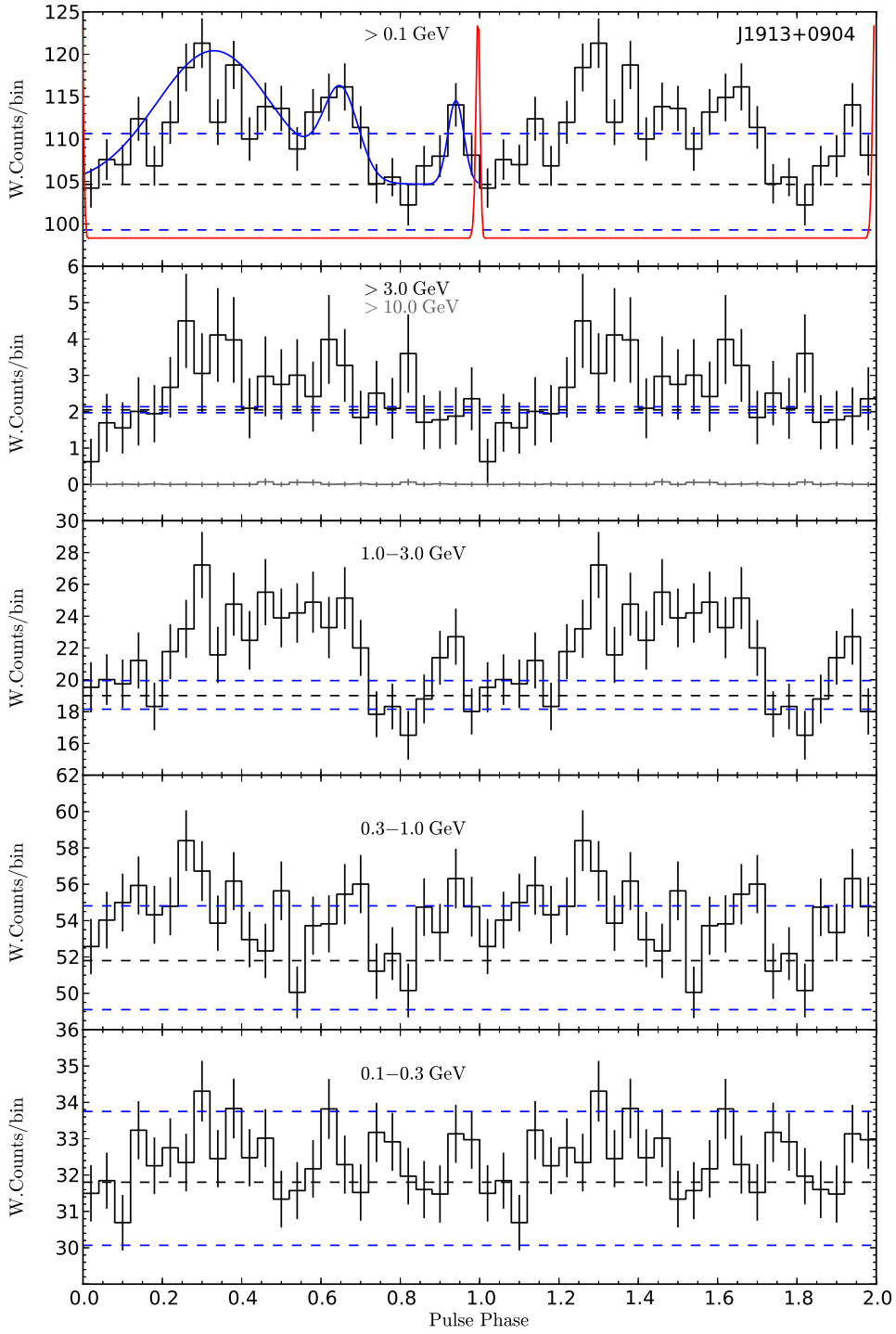

Figure 6.13: Weighted light curves of J1913+0904. Labels are as for Figure 6.10.

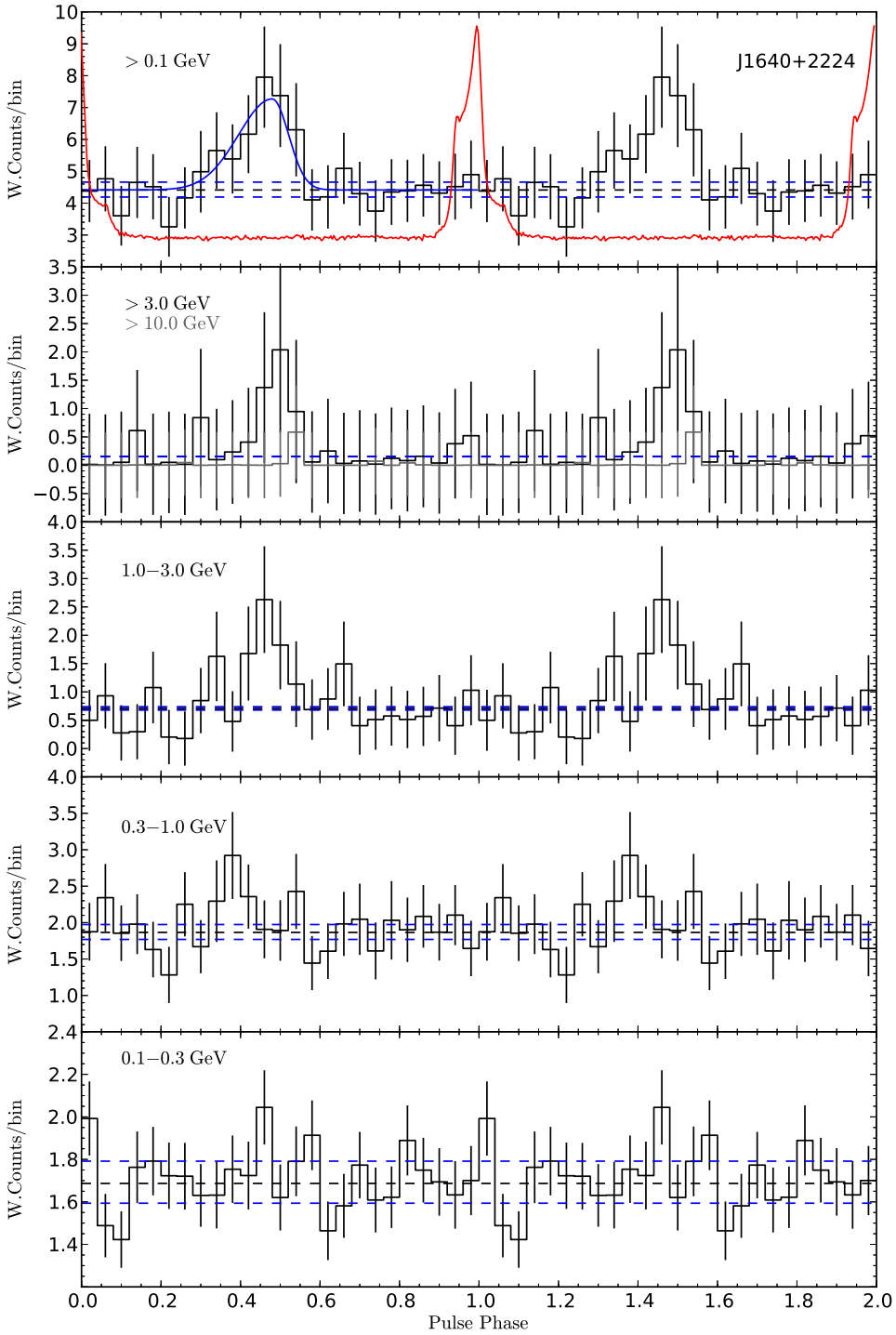

Figure 6.14: Weighted light curves of J1640+2224. Labels are as for Figure 6.10.

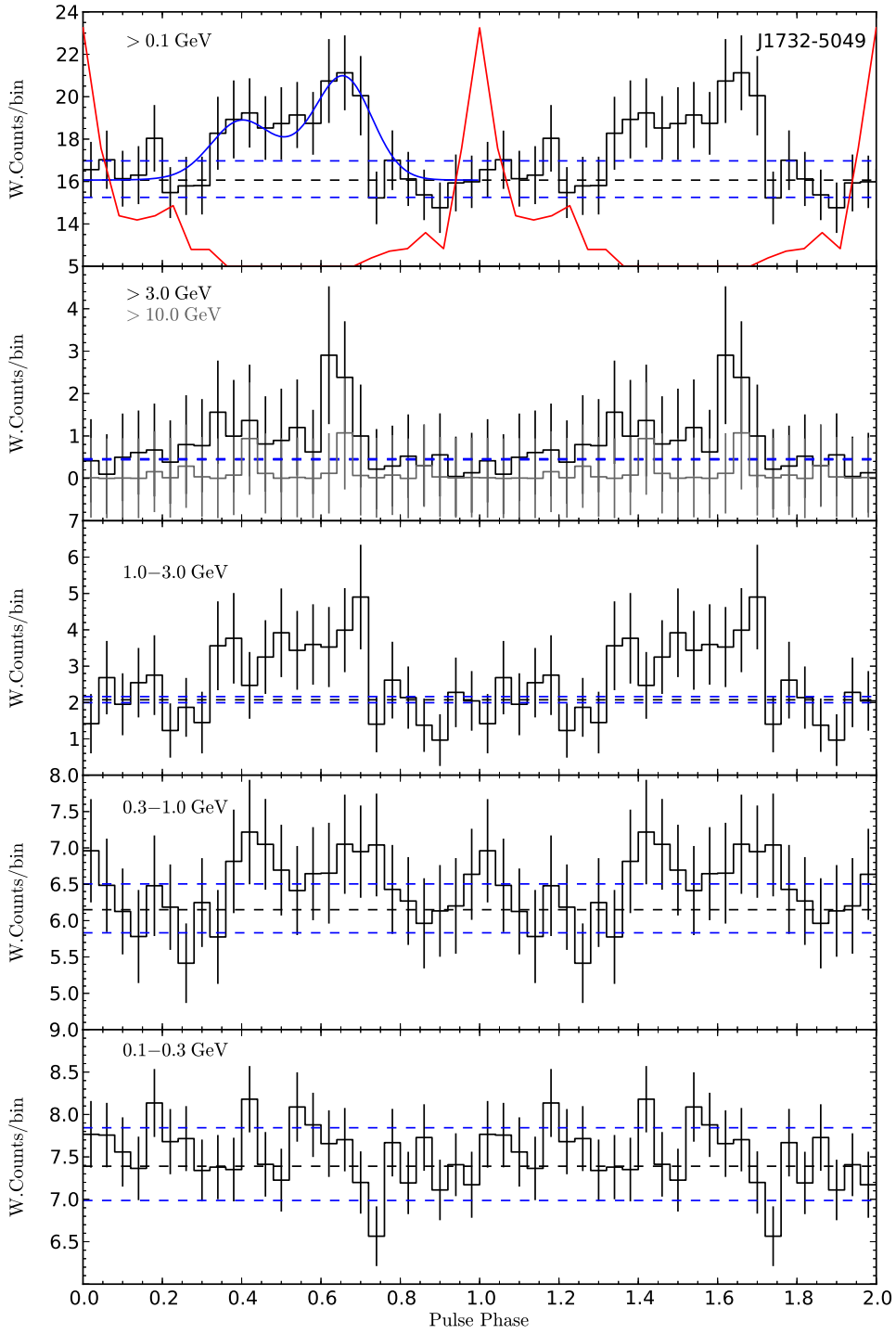

Figure 6.15: Weighted light curves of J1732−5049. Labels are as for Figure 6.10.

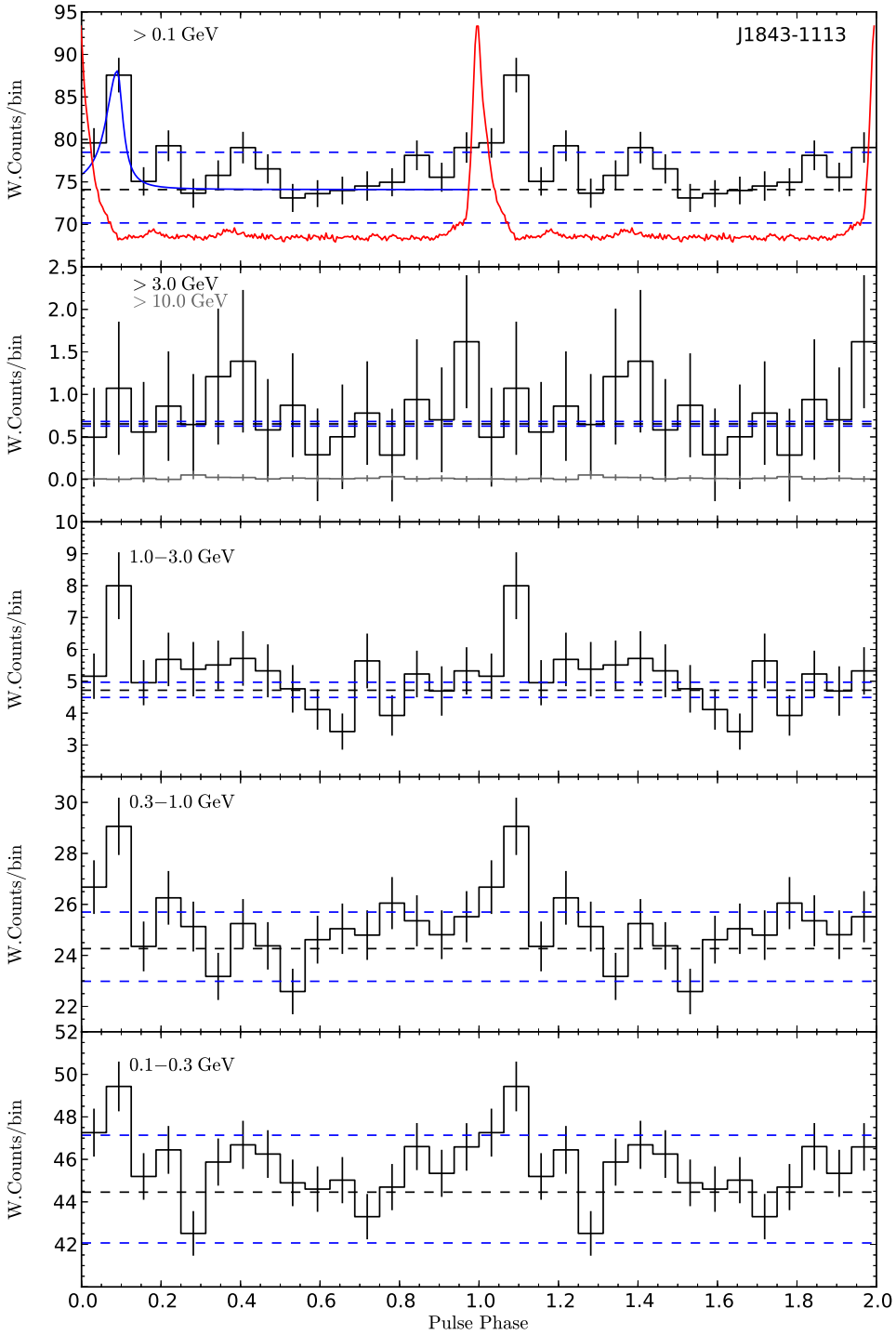

Figure 6.16: Weighted light curves of J1843−1113. Labels are as for Figure 6.10.

CHAPTER 7

High γ-ray efficiency pulsars

Contents

7.1 Introduction

The high γ-ray efficiency pulsar sample discussed in this chapter comes from 2PC (Abdo *et al.* 2013). As introduced in Section 2.2, the luminosity:

$$L_\gamma = 4\pi d^2 f_\Omega G_{100} \tag{7.1}$$

is one of the most important quantities in γ-ray pulsar astronomy. The γ-ray efficiency is:

$$\eta = \frac{L_\gamma}{\dot{E}} \tag{7.2}$$

However, as discussed in Section 4.1.2, the Doppler effect combining the Shklovskii effect due to the pulsar proper motion in the sky and the Galactic acceleration leads to a significant shift of the pulsar spin-down rate $\dot{P}$ (Equation 4.15), thus of $\dot{E}$, for MSPs. The intrinsic $\dot{E}$ is expressed as:

$$\dot{E}^{\rm int} = 4\pi^2 I(\dot{P} - k\mu^2 dP - \dot{P}^{\rm gal})P^{-3} \tag{7.3}$$

with I the pulsar moment of inertia, μ the pulsar proper motion, d the pulsar distance, P the spin period, $\dot{P}^{\rm gal}$ the Galactic acceleration effect, $\dot{P}$ the spin-down rate and $\dot{P} - k\mu^2 dP - \dot{P}^{\rm gal} = \dot{P}^{\rm int}$, the intrinsic value. In 2PC, I calculated $\dot{P}^{\rm int}$ and its uncertainties for a library of 242 pulsars with proper motion measurements, distance estimates (for LAT pulsars, distances are from Table B.1, B.2) and $\dot{P}$ measurements from the literature. Of these, 69 have $P < 30$ ms, and 20 are γ-ray MSPs, listed in Table B.2. We used $\dot{P}^{\rm int}$ from Table B.2 to replace $\dot{P}$ and the derived quantities ($\dot{E}$, characteristic age τ, etc) throughout 2PC. More discussions on the Doppler correction are in 2PC.

Table 7.1 lists the high efficiency pulsars in 2PC with an arbitrary criterion $\eta \geq 60\%$. $\dot{E}$ is Doppler corrected. The uncertainties on $\dot{E}$ come from those on distances and proper motions. The first uncertainty on η is statistical coming from G_{100}, the second is systematic coming from the distances. Note that the uncertainty on $\dot{E}$ has been ignored when calculating the uncertainty on η to avoid propagating twice the distance uncertainties. Taking into account the uncertainties on η, we reduce the sample by keeping only those with $\eta - \delta\eta \geq 60\%$ (highlighted in bold in Table 7.1) in the following discussions.

The distance d is the most uncertain while the integral energy flux above 100 MeV, G_{100}, from the spectral analysis, is better known in comparison. The beaming fraction f_Ω (Equation 2.5), is not the biggest

PSR	d (pc)	Method	μ (mas yr^{-1})	$10^{-33}\dot{E}$ (erg s^{-1})	$10^{11}G_{100}$ (erg cm^{-2} s^{-1})	η (%)	$\eta-\delta\eta$ (%)
			MSPs				
J0340+4130	1730 ± 300	DM		7.87	2.04 ± 0.15	$92.6\pm7.0^{+33.7}_{-29.3}$	56.3
J0610 − 2100	3540^{+5460}_{-1000}	DM	18.2 ± 0.2	$0.8^{+11.7}_{-0.8}$	0.66 ± 0.11	$1160\pm189^{+6337}_{-563}$	408
J0614 − 3329	1900^{+440}_{-350}	DM		22.00	10.94 ± 0.27	$214.7\pm5.3^{+111.0}_{-71.8}$	137.6
J2017+0603	1570 ± 150	DM		13.01	3.33 ± 0.21	$75.5\pm4.8^{+16.2}_{-13.7}$	57
J2043+1711	1760^{+150}_{-320}	DM	13.0 ± 2.0	$12.7^{+1.6}_{-1.8}$	2.70 ± 0.16	$79.0\pm4.7^{+14.0}_{-26.1}$	48.2
J2302 + 4442	1190^{+90}_{-230}	DM		3.82	3.67 ± 0.17	$162.6\pm7.5^{+25.5}_{-56.8}$	98.3
			Young pulsars				
J0106+4855	3010^{+1100}_{-690}	DM		29.38	1.93 ± 0.18	$71.2\pm6.7^{+61.6}_{-28.9}$	35.6
J0633+1746	250^{+230}_{-80}	P	169.0 ± 4.0	$32.49^{+0.011}_{-0.003}$	423.31 ± 1.23	$97.4\pm0.3^{+262}_{-52}$	45.1
J1648−4611	4960 ± 690	DM		208.76	5.44 ± 0.79	$76.7\pm11.2^{+21.8}_{-19.8}$	45.7
J1836+5925	530 ± 270	X		11.41	60.57 ± 0.41	$178.5\pm1.2^{+228.2}_{-135.5}$	41.8
J2021 + 3651	10000^{+2000}_{-4000}	O		3378.81	49.43 ± 0.75	$175.0\pm2.7^{+77.0}_{-112.0}$	60.3
J2021 + 4026	1500 ± 450	K		114.49	95.53 ± 0.88	$224.6\pm2.1^{+155.0}_{-114.6}$	108
J2030+3641	3000 ± 1000	O		32.02	3.14 ± 0.33	$105.7\pm11^{+82.2}_{-58.7}$	36
J2032+4127	3650 ± 600	DM		273.45	10.59 ± 0.62	$62\pm4^{+22}_{-19}$	39

Table 7.1: High γ-ray efficiency pulsars in 2PC. Distance measurement methods: P from parallax; DM from dispersion measure using the NE2001 model (Cordes & Lazio 2002). X from X-ray, O from other measurements. The uncertainty on DM distance is obtained by varying the DM by 20%. Pulsars with γ-ray efficiency $\eta-\delta\eta\geq60\%$ are in bold. PM and distance references can be found in 2PC.

obstacle if one favors the values calculated from current γ-ray emission models. A novelty in our approach is that the pulsar's proper motion μ, if known, provides further constraints, via the Doppler correction to $\dot{P}$ and the pulsar's space velocity. In the next sections, we first explore the distances of the reduced sample as best as we can. We then focus on the sub-sample with known μ to constrain the distance. Next, we use the f_Ω calculations to characterise the uncertainty on η due to beaming. In the end, we propose the candidates that require a large moment of inertia to account for their high efficiencies. We discuss the implication of large moments of inertia in the context of current Equations of State (EOS) models.

7.2 Parameter investigation

7.2.1 Distance

DM Distance

The large scale structure of our Galaxy, the Milky Way (Figure 7.1, Reid *et al.* 2009), is represented by a bar-shaped core region and a disk of gas, dust and stars roughly in the form of spiral arms. Small structures like "clumps" and "voids" exist in the arms. Free electrons, depending on the ionisation degree of the atoms, are easier to be found in HII regions ionized by the hot O and B stars residing in the arms. The whole galaxy rotates with a constant circular velocity over a large range of distances from the Galactic center (flat rotation curve, Appendix A).

In our sample, three pulsars have DM (free electron column density along a given line of sight, Section 1.5.4) distances estimated from the NE2001 model (Cordes & Lazio 2002). NE2001 has no systematic modelling for high and low density regions in our Galaxy, which results in a very smooth overall distribution of free electrons, but with locally sharp transitions from one region to another, compared to the Galaxy map

shown in Figure 7.1. Figure 7.5−7.9 (bottom two panels) show the NE2001 model for all the five pulsars in our sample in terms of electron number density n_e and DM as a function of distance d for each line of sight (i.e. Galactic longitude l and Galactic latitude b). Indeed, there are steep "jumps" for the modelled n_e, indicating possible missing "clumps" along the line of sight, e.g. Figure 7.5 shows an extreme n_e jump where the neutral hydrogen HI cloud surface temperature shows a more physical structure.

In the articles referenced, the authors all suspect overestimated distances. J0610−2100 has the highest and definitely non-physical efficiency among all the pulsars discussed here. Espinoza *et al.* (2013) discussed the possibility of a reduced DM distance taking into account the possible unmodelled clouds inferred from infra-red images. From the H_α map (Figure 7.2, Finkbeiner 2003) which traces HII regions, J0610−2100 seems to lie right at the edge of an extended HII region, consistent with the observation from the infra-red images. We suspect the pulsar couldn't be closer than the HI "bump" at $\sim$ 1 kpc as inferred from Figure 7.5.

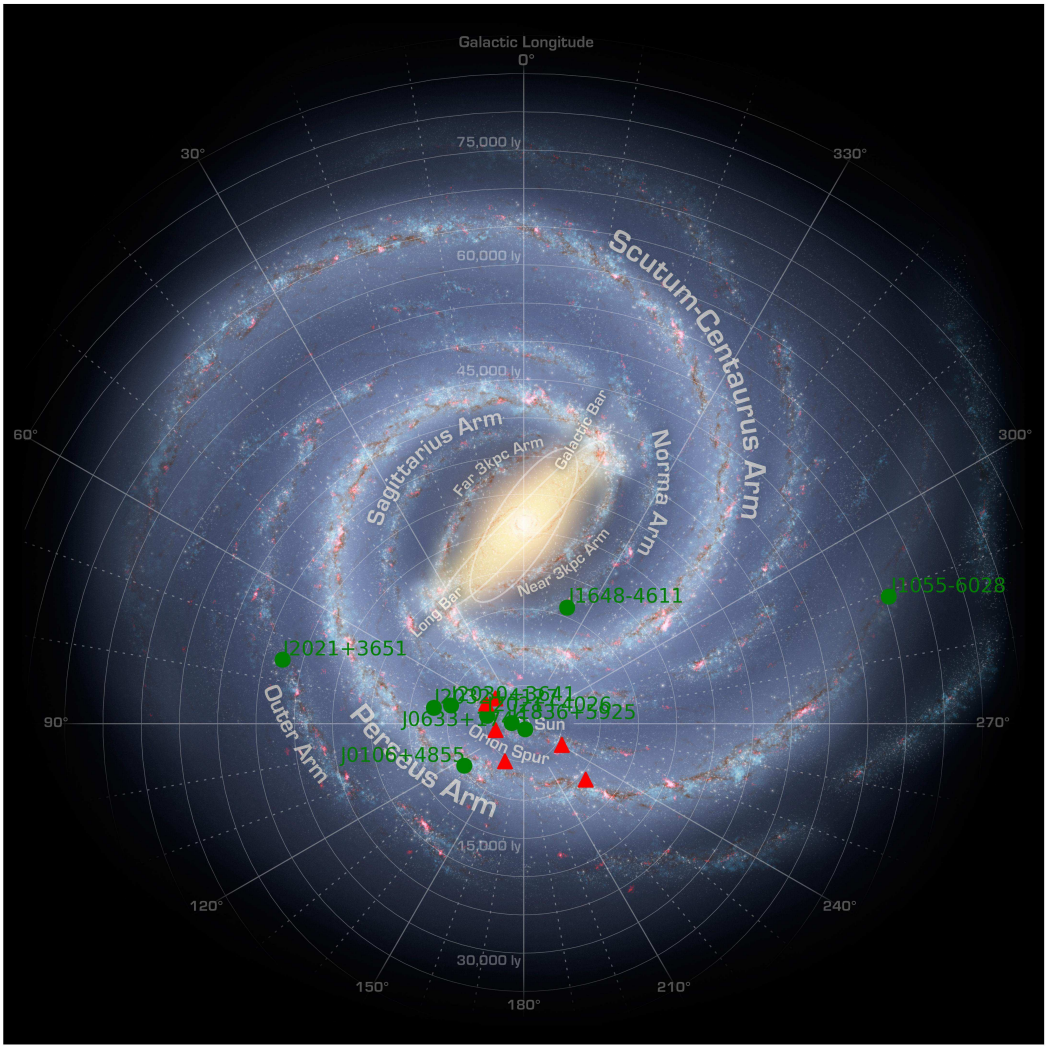

Figure 7.1: High γ-ray efficiency pulsars (color symbols) projected onto the Milky Way model of Reid *et al.* (2009). Labels for pulsars are as for Figure 1.9. Circles indicate the distances to the Sun in units of light year (ly). Almost all 2PC pulsars are within 15000 ly, i.e. 4.6 kpc (1 kpc = 3.26 kly). Radial lines are the Galactic longitudes. Only names for young radio-loud pulsars are shown for readability including the new pulsar J1055−6028 presented in Chapter 6.

J2021+4026 is radio-quiet without DM measurement. It has a kinematic distance estimated from a possible association with the SNR γ Cygni. However, its characteristic age is $\sim$ 10 times larger than that of the SNR making this association distance suspicious, as argued in Abdo *et al.* (2010b).

Also located toward the Cygnus region, the large DM distance from NE2001 put J2021+3651 ($\sim$ 12 kpc, Figure 7.8) on the far side of the outer Galactic spiral arm. Hessels *et al.* (2004) proposed a conservative DM distance of 10 kpc basing on hydrogen column density $N_{\rm H}$ from X-ray absorption and the total Galactic density from HI map of Dickey & Lockman (1990). From X-ray spectral analysis for the pulsar and its nebular (the "Dragonfly nebula") and the comparison of its γ-ray luminosity with other Vela-type pulsars/PWNe, Van Etten *et al.* (2008) suggested that J2021+3651 may be as close as $3-4$ kpc. However, no obvious source of ionized gas is seen that could account for its large DM value. Although the OB associations Cyg 1, 8 and 9 are located at 1.4 kpc in the direction of J2021+3651 (Yadigaroglu & Romani 1997; Mel'Nik & Efremov 1995), there is no evidence that this contributes to the amount of ionized gas along the line of sight or that the pulsar was born in this association.

The small DM distance of J2302+4442 seems true since the pulsar resides along a line of sight with almost lowest free electron density as can be inferred from Figure 7.2. This may also be the case for J0614$-$3329.

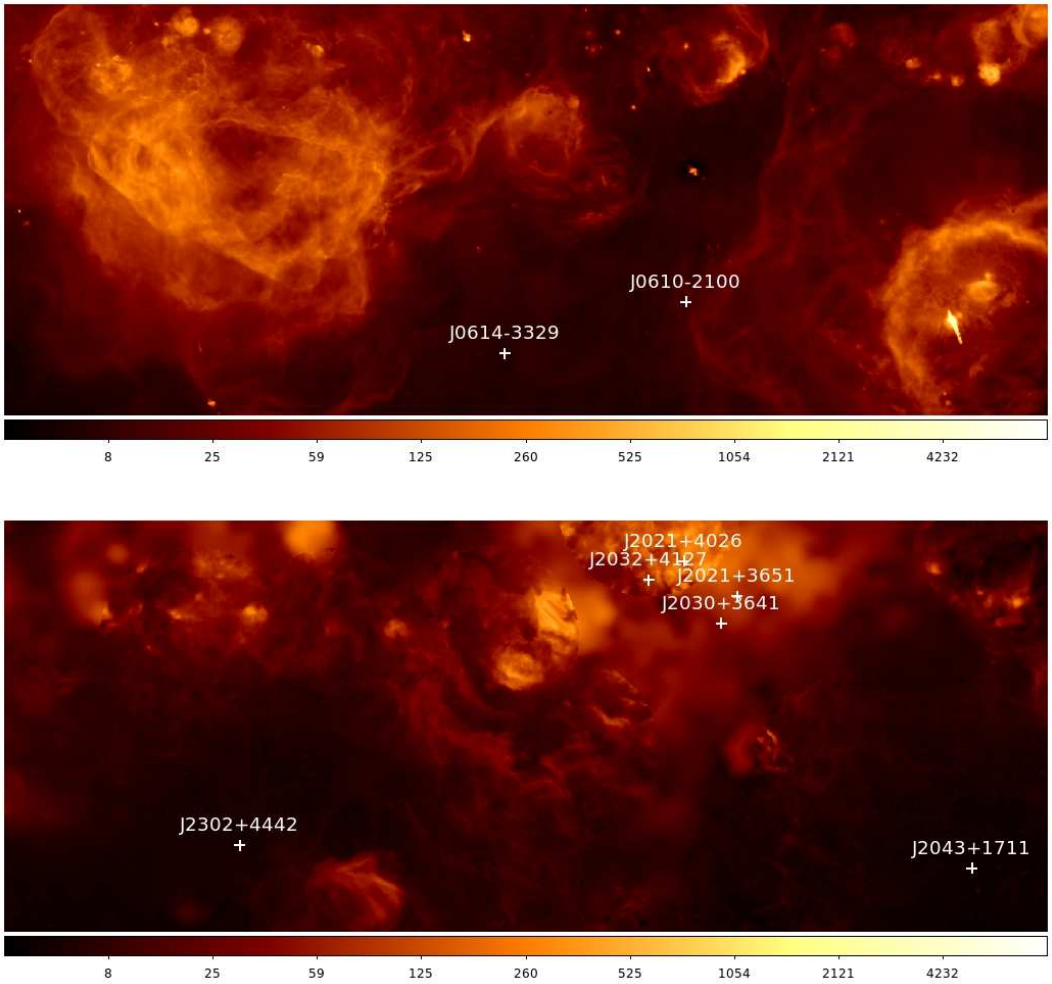

Figure 7.2: H_α map in Galactic coordinates (Finkbeiner 2003) with some 2PC high efficiency pulsars superposed. X-axis: Galactic longitude; Y-axis: Galactic latitude.

Constraints from $N_{\rm H}$

A relation between DM and the hydrogen column density $N_{\rm H}$ in the ISM commonly used in the literature to estimate one quantity from the other is one electron per 10 equivalent hydrogen atoms on average (see e.g. Seward & Wang 1988; Gil *et al.* 2008; Camilo *et al.* 2012), while without clear justification. He *et al.* (2013) performed a statistical study of this correlation using $N_{\rm H}$ from X-ray absorption for a sample of radio pulsars. They found $N_{\rm H}\,(10^{20}\,{\rm cm}^{-2}) = 0.30^{+0.13}_{-0.09}$ DM $({\rm pc\,cm}^{-3})$, corresponding to an average ionization of $10^{+4}_{-3}\%$ ($1\,{\rm pc} = 3.1\times10^{18}$ cm). This suggests that the assumed one electron per 10 hydrogen relation can be generally used with the uncertainties.

In our study, we will explore the DM and $N_{\rm H}$ for each pulsar (Table 7.2) using this empirical relation. DM is from the 2PC ephemerides. We also calculate the maximum DM using the NE2001 model assuming a large enough distance of 50 kpc for the line of sight of each pulsar. This is to make sure that the NE2001 model will compile DM till to the edge of our Galaxy, given that the diameter of our Galaxy is about 30 kpc.

We have two sources of $N_{\rm H}$ measurement. One is the total Galactic column density $N_{\rm H}^{\rm Survey}$ (column 6 of Table 7.2) along a line of sight obtained from the combination of the Galactic LAB HI survey[1] (Kalberla *et al.* 2005) and the CfA[2] CO survey[3] (Dame *et al.* 2001). The dataset of each survey is a 3D cube listing the HI or CO brightness T_b as a function of $(l, b, v_{\rm R})$. $v_{\rm R}$ is the radial velocity of the HI or CO clouds. For a given line of sight, we first extract the HI and CO profiles which are T_b versus $v_{\rm R}$. By using a flat Galactic rotation model along with the current IAU recommended values for the circular velocity and the galactocentric radius of the Sun (Appendix A), $v_{\rm R}$ can be converted to distances d (the third top panel in Figure 7.5−7.9). Then the cumulative integration of T_b over $v_{\rm R}$ gives the intensity $W_{\rm HI}$ and $W_{\rm CO}$ which are finally converted to $N_{\rm H}$. The conversion is $N_{\rm H}\,({\rm cm}^{-2}) = 1.823\times10^{18}\times{\rm W_{HI}\,(K.km/s)}$ under assumption of an optically thin ISM (Dickey & Lockman 1990), and $N_{\rm H_2}\,({\rm cm}^{-2}) = 1.8\times10^{20}\times{\rm W_{CO}\,(K.km/s)}$, with $N_{\rm H} = 2N_{\rm H_2}$ (Dame *et al.* 2001). Figures 7.5−7.9 (top two panels) illustrate T_b and the cumulative $N_{\rm H}$ as a function of d for the cases of HI, CO (if available) and HI+CO (if CO data is available).

The other one is the measured values $N_{\rm H}^{\rm X-ray}$ (column 5 of Table 7.2) from the X-ray analysis for 2PC pulsars (M. Marelli, Abdo *et al.* 2013) using Chandra, XMM-Newton, SWIFT and Suzaku[4] observations. In this analysis, three different types (column 4 of Table 7.2) are defined based on the analysis result: 1) Type 0: no confirmed X-ray counterpart; 2) Type 1: the X-ray counterpart may be a chance coincidence and the spectrum is poorly constrained; 3) Type 2: X-ray counterpart is identified and the spectral shape is determined (thermal + non-thermal components).

We first compare $N_{\rm H}^{\rm X-ray}$ with $N_{\rm H}^{\rm Survey}$. In principle, $N_{\rm H}^{\rm X-ray}$ should be $\lesssim N_{\rm H}^{\rm Survey}$ [5]. J0614−3329 has $N_{\rm H}^{\rm X-ray} > N_{\rm H}^{\rm Survey}$ which is not plausible at $\sim 2\sigma$ level. Since this pulsar is type 1, $N_{\rm H}^{\rm X-ray}$ is not reliable, no constraints could be obtained. The other four pulsars have $N_{\rm H}^{\rm X-ray} < N_{\rm H}^{\rm Survey}$, suggesting that they are not on the edge of the Galaxy. For the type 0 pulsar J0610−2100, $N_{\rm H}^{\rm X-ray}$ is obtained by scaling the Galactic $N_{\rm H}$ value obtained with webtools (http://heasarc.gsfc.nasa.gov/docs/tools.html) to its DM distance, so here $N_{\rm H}^{\rm X-ray}$ brings no constraints on the distance.

Then, we compare $N_{\rm H}^{\rm Survey}$ with ${\rm DM^{Max}}$ from the NE2001 model. Four pulsars have $N_{\rm H}^{\rm Survey}/{\rm DM^{Max}} < 10$, which means that modelled free electrons may be more than in reality, therefore the pulsars would actually be FARTHER. So the DM distance could be true. This method is not applicable to the radio-quiet

[1] http://www.astro.uni-bonn.de/hisurvey/profile/index.php

[2] Harvard-Smithsonian Center for Astrophysics

[3] Only available for low Galactic altitude regions.

[4] http://www.isas.jaxa.jp/e/enterp/missions/suzaku/

[5] In the case where there is no intrinsic absorption to the pulsar by the nebulae, supernova remnant and the magnetosphere. None of the pulsars in our sample has a nebulae or supernova remnant. The $N_{\rm H}$ in the magnetosphere is negligible, i.e. $\ll 10^{21}{\rm cm}^{-2}$, even if assuming a Goldreich-Julian density of neutral hydrogen which is indeed for protons and/or electrons (Section 1.3.2)

PSR	DM (pc cm^{-3})	DM$^{\rm Max}$ (pc cm^{-3})	Type	$N_{\rm H}^{\rm X-ray}$ (10^{21} cm^{-2})	$N_{\rm H}^{\rm Survey}$ (10^{21} cm^{-2})	$\frac{N_{\rm H}^{\rm X-ray}}{\rm DM}$	$\frac{N_{\rm H}^{\rm Survey}}{\rm DM^{Max}}$	$\cos\beta$	TRES (μs)
MSPs									
J0610−2100	60.68	73	0	0.8$^{\rm c}$	0.92	4.3	4.1	0.71	2.92
J0614−3329	37.05	65	1	$0.64^{+0.63}_{-0.20}$	0.29	$5.6^{+5.5}_{-1.8}$	1.4	0.55	4.06
J2302+4442	13.76	98	2	$1.3^{+0.9}_{-0.5}$	1.34	$30.5^{+21.1}_{-11.7}$	4.4	0.70	6.66
Young pulsars									
J2021+3651	367.50	420	2	$6.38^{+0.05}_{-0.04}$	9.22	$5.62^{+0.05}_{-0.03}$	7.1	0.59	936.85
J2021+4026	...	350	2	$6.5^{+3.1}_{-3.7}$	12.3	...	11.3	0.54	1705.5

Table 7.2: Measured or derived properties for high γ-ray efficiency pulsars in 2PC with $\eta - \delta\eta \geq 60\%$. Type 0: no confirmed X-ray counterpart; Type 1: the X-ray counterpart may be a chance coincidence and the spectrum is poorly constrained; Type 2: X-ray counterpart is identified and the spectral shape is determined (thermal + non-thermal components). "..." means radio quiet, no DM measurement is available. c: $N_{\rm H}^{\rm X-ray}$ is set to the Galactic $N_{\rm H}$ value for the pulsar line of sight obtained with webtools (http://heasarc.gsfc.nasa.gov/docs/tools.html), scaled for the DM distance. $1\,{\rm pc} = 3.1 \times 10^{18}$ cm.

pulsar J2021+4026.

Next, we compare $N_{\rm H}^{\rm X-ray}$ with DM. Three pulsars J0610−2100, J0614−3329, and J2021+3651 have $N_{\rm H}^{\rm X-ray}/{\rm DM} < 10$. Since DM is well determined from pulsar timing, to get a ratio of 10, a bigger $N_{\rm H}^{\rm X-ray}$ will be needed. Only J2021+3651 is a type 2 pulsar, which means its $N_{\rm H}^{\rm X-ray}$ is reliable, with tiny uncertainties. Another type 2 pulsar J2302+4442 has $N_{\rm H}^{\rm X-ray}/{\rm DM} > 10$, even using the lower value of $N_{\rm H}^{\rm X-ray}$. In this case, if we believe that both DM and $N_{\rm H}^{\rm X-ray}$ are reliable, then no real constraints could be obtained for these two Type 2 pulsars, as is the case for the type 0 pulsar J0610−2100 and the type 1 pulsar J0614−3329. Again, this method is not applicable to J2021+4026.

Finally, for three type 2 pulsars which have $N_{\rm H}^{\rm X-ray} < N_{\rm H}^{\rm Survey}$, we tried to get distance estimates from the above discussed $N_{\rm H}^{\rm X-ray}$ and $N_{\rm H}^{\rm Survey}$ along with the flat Galactic rotation model as shown in Figure 7.5−7.9 (top three panels).

We obtained, in approximation, $d \sim 2.2$ kpc for J2021+3651 (with invisibly small uncertainties as inferred from Figure 7.8), $d = 4.5^{+1.1}_{-1.3}$ kpc for J2021+4026 and $d > 4.5$ kpc for J2302+4442 (with the lower $N_{\rm H}^{\rm X-ray}$). The estimated distance for J2021+3651 is consistent with Van Etten *et al.* (2008) and with what we argued as in 1PC (Abdo *et al.* 2010b) and Abdo *et al.* (2009c). With this distance, the efficiency of J2021+3651 would be pulled down to 8.5%, a typical value compared to the 2PC sample. However, for J2021+4026 and J2302+4442, the estimated distances are larger than the adopted values in 2PC, yielding even higher efficiencies. This suggest that they may be FARTHER in reality and other factors may account for their high efficiencies.

Constraints from parallax

The best possible distance determination comes from parallax, when available. As introduced in Section 4.1, timing parallax can induce a pulse arrival time delay (Equation 4.5) which is only large for pulsars near the Ecliptic plane (Ecliptic latitude $\beta < 60^\circ$) and at close distances. Values of $\cos\beta$ and timing residuals (TRES, from 2PC ephemerides) for three MSPs are included in Table 7.2. Figure 7.3 shows the comparison of this time delay with TRES for all six high efficiency MSPs[6] listed in Table 7.1. Vertical lines represent the distances corresponding to $\eta = 60\%$ (magenta dashed) and $\eta = 30\%$ (green dot-dashed).

[6]Here we abandon the $\eta - \delta\eta \geq 60\%$ selection criterion in order to show how our methodology works.

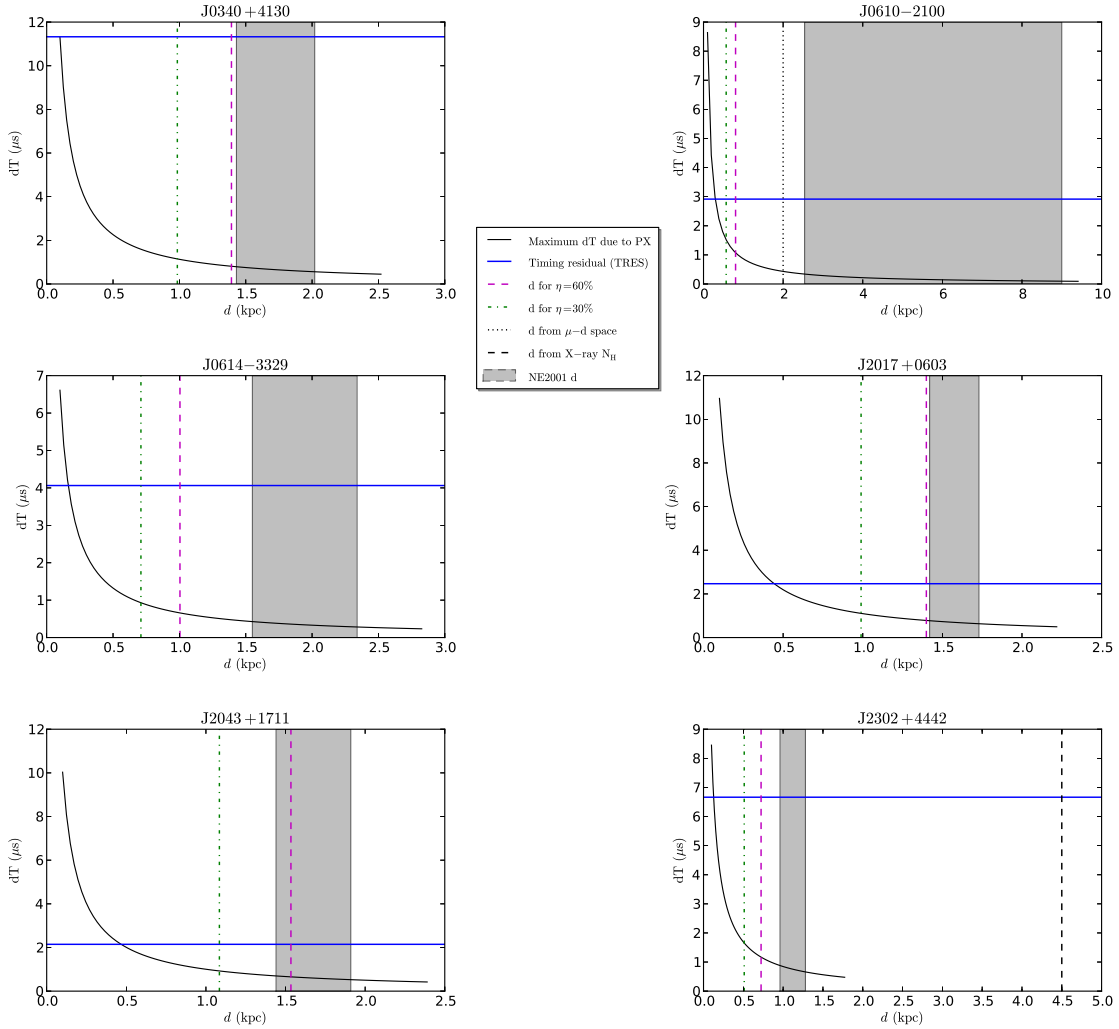

Figure 7.3: Comparison of parallax induced pulse time delay with timing residuals for high efficiency MSPs. The solid curve (black) represents the parallax induced time delay as a function of distance. The magenta dashed and green dot-dashed vertical lines correspond to the distances for $\eta = 60\%$ and $\eta = 30\%$ respectively. The blue solid horizontal line indicates the timing residual level. The DM distance with uncertainties from the NE2001 model is represented by the gray zone. The black dotted vertical line is the distance constraint from $\mu - d$ space for J0610−2100 (Section 7.2.2). The black dashed vertical line indicates the distance estimated from the X-ray hydrogen column density $N_{\rm H}^{\rm X-ray}$ for J2302+4442 (Section 7.2.1).

We see that, for all six MSPs, TRES is bigger than the parallax time delay for e.g. the DM distance range. For J0340+4130, J0614−3329 and J2302+4442, it's difficult to expect a parallax measurement given the large lag between TRES and the time delay. Nevertheless, for J2017+0603, J2043+1711, at the lower end of the DM distance, the amplitude of the parallax time delay is not very far from TRES, implying a possible parallax measurement.

A much more precise distance would then be obtained given the measured parallax. Lower limits on parallax distances would be ~ 0.2 kpc for J0340+4130, J0610−2100, J0614−3329 and J2302+4442, ~ 0.5 kpc for J2017+0603 and J2043+1711 by looking at the intersection of TRES with the parallax delay curve. DM distances within uncertainties are all compatibles with the lower limits.

Inversely, the non-detection of parallax for these pulsars suggests that their DM distances couldn't be so wrong, otherwise, parallax measurements should have been possible.

For young pulsars, the parallax time delay is totally invisible facing the much bigger TRES than MSPs, so there is no hope to get a parallax distance from radio timing. They are not shown here.

With less hope from the timing parallax, fortunately, three high efficiency pulsars, J0614−3329, J2021+3651 and J2302+4442, are in the VLBI parallax project for *Fermi* pulsars lead by S. Chatterjee[7]. Possible constraints from this project are expected in the next year.

7.2.2 Proper motion

For pulsars with proper motion measurement, the distance can be further constrained by exploring $\mu - d$ space using different physical constraints:
(1) spin-down, not spin-up: $\dot{P}^{\rm int} > 0 \Longleftrightarrow \dot{E}^{\rm int} > 0$. We have:

$$\mu < \sqrt{\frac{\dot{P}}{kPd}} \tag{7.4}$$

with $k = 2.43 \times 10^{-21}$ (Section 4.1.2).
(2) Conservation of energy: $L_\gamma \leq \eta \dot{E}^{\rm int}$. We have:

$$\mu \leq \sqrt{\frac{\dot{P}}{kPd} - \frac{9.4864 \times 10^{42} P^2 G_{100} f_\Omega}{k\pi I \eta} d} \tag{7.5}$$

(3) $\dot{E}^{\rm int} \geq \dot{E}^{\rm deathline} \approx 3 \times 10^{33}\,{\rm erg\,s^{-1}}$ (γ-ray deathline). We have:

$$\mu \leq \sqrt{\frac{\dot{P}}{kPd} - \frac{3 \times 10^{33} P^2}{4\pi^2 I k d}} \tag{7.6}$$

(4) Reasonable transverse velocity $V_{\rm T} \leq V_{\rm T}^{\rm max}$. We have:

$$\mu \leq \frac{V_{\rm T}^{\rm max}}{4.739\,d} \tag{7.7}$$

For our reduced pulsar sample with $\eta - \delta\eta \geq 60\%$, only J0610−2100 has a proper motion measurement. Figure 7.4 shows $\mu - d$ space for J0610−2100. We use P, $\dot{P}$, d, G_{100}, η, f_Ω and I as input to plot five curves corresponding to the above four cases. For case (2), we have chosen $\eta = 100\%$ and $\eta = 60\%$ with specific f_Ω values for the pulsar coming from the light curve model fits as shown in Table 7.3. We use the 3σ extremum of the MSP transverse velocity ($V_{\rm T} = 150$ km/s) distribution of Lyne *et al.* (1998) for case (4). The conventional moment of inertia $I_0 = 10^{45}\,{\rm g\,cm^2}$ (left panels) and a higher value $I = 2I_0$ (right panels) have been applied. Allowed (or favored) regions are to the left of the curves.

From the Figure, we see that the nominal (μ, d) point adopted in 2PC for this pulsar is to the right of most of the curves. In spite of the non-physical efficiency that exceeds 100%, the intrinsic spin-down power

[7] http://www.astro.cornell.edu/research/parallax/

$\dot{E}^{\rm int}$ is well below the empirical γ-ray deathline, and the space velocity is much higher than typical. This pulsar violates all but the $\dot{E} = 0$ curves.

Using modelled f_Ω values can't resolve the violation, which is evident since modelled $f_\Omega > 1$. It's apparent that a different proper motion measurement (moving the horizontal light blue zone up and down) will not help to resolve the high efficiency problem either, implying that the adopted μ is rather reliable. A typical larger moment of inertia of $2I_0$ (Section 1.2.3) by itself doesn't improve the situation either. It seems that these apparent paradoxes can only be resolved if the pulsar is closer than 1.5 kpc, or closer than 2 kpc but with a greater moment of inertia at the same time. This pulsar could be a high moment of inertia candidate.

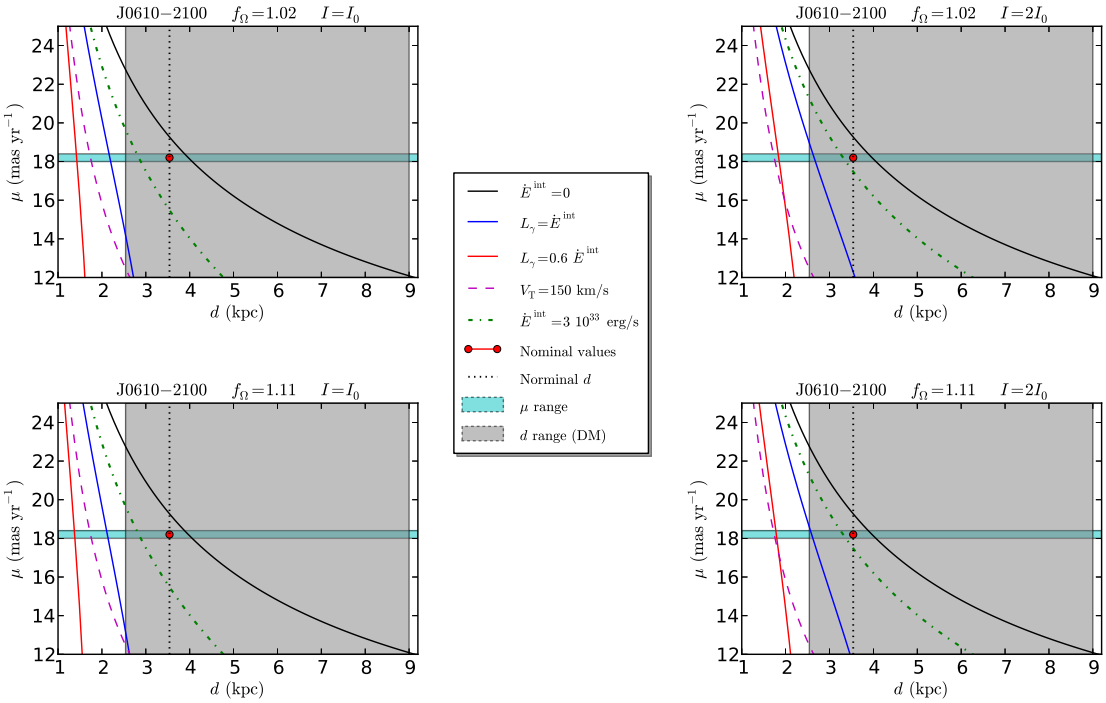

Figure 7.4: Constraints on the proper motion μ and the distance d for J0610−2100. The first solid curve (black) on right requires $\dot{E}^{\rm int} > 0$. The second solid curve (blue) requires $L_\gamma < \dot{E}^{\rm int}$. The most left solid curve (red) represents our efficiency criterion $\eta = 60$ %, that is, $L_\gamma < \eta \dot{E}^{\rm int}$. The violet dashed line corresponds to a pulsar transverse space velocity of 150 km s^{-1} and the green dot-dashed line traces the empirical γ-ray deathline value of $\dot{E}^{\rm int} \approx 3 \times 10^{33}$ erg s^{-1}. The red dot is at the adopted values of μ and d in 2PC. The DM distance with uncertainties is represented by the vertical gray zone. The horizontal light blue zone indicates the proper motion measurement with uncertainties.

7.2.3 Beaming factor

Assuming that the distances in 2PC are correct or not far from the true values, we now evaluate the effect of the beaming factor on the γ-ray efficiency. The problematic high efficiency is obtained with $f_\Omega = 1$ assuming that the observed γ-ray emission represents its averaged all-sky emission for a pulsar rotation. Table 7.3 shows the beaming factor estimates for our pulsars from light curve modellings (Johnson *et al.* 2013; Pierbattista *et al.* 2013). The authors use $-\ln Likelihood$ to quantify the modelling and choose the smaller value to be favored. We use their values directly in our study. For MSPs, the TPC and OG models

PSR	f_Ω			$-\ln Likelihood$		
	TPC	OG	PSPC	TPC	OG	PSPC
			MSPs			
J0610−2100	$1.11^{+0.74}_{-0.64}$	$1.02^{+0.21}_{-0.74}$		71	79.6	
J0614−3329	1.03 ± 0.01	0.98 ± 0.01		1312.5	1487.9	
J2302+4442	$0.93^{+0.06}_{-0.11}$	$0.98^{+0.16}_{-0.03}$		383.4	390	
			Young pulsars			
PSR	f_Ω			$-\ln Likelihood$		
	PC	SG	OG	OPC	PC	SG	OG	OPC
J2021+3651	0.02	0.98	0.65	0.87	2469	1809	2734	1699
J2021+4026		1.22	0.28	0.15	2534	350	1220	690

Table 7.3: Beaming factor f_Ω from light curve modelling for high γ-ray efficiency ($\eta - \delta\eta \geq 60\%$) MSPs (Johnson *et al.* 2013) and young pulsars (Pierbattista *et al.* 2013) with different emission models (OPC stands for One Pole Caustic, Romani & Watters 2010).

give very similar results (close to 1). Since a lower efficiency requires a smaller f_Ω, we have taken the lower values of f_Ω to derive the new efficiencies from the original ones $\eta - \delta\eta$. For young pulsars, we calculate the efficiency with each modelled f_Ω since no uncertainties were given in the articles referenced.

The new efficiencies are calculated by taking the original $\eta - \delta\eta$, multiplied with the modelled f_Ω (Table 7.4). We see that for three MSPs, since both models give $f_\Omega \sim 1$, they are not strongly skewed by the beaming effects, therefore stay as high efficiency pulsars. For J2021+3651, four models with $f_\Omega < 1$ all give a lower efficiency $\eta < 60\%$, thus it's no longer a high efficiency pulsar. For J2021+4026, the high efficiency is "cured" by the OG and OPC models, whereas the SG model gives an even higher efficiency with $f_\Omega > 1$. However, the SG model is favored with the smallest $-\ln Likelihood$. The pulsar stays therefore as a high efficiency pulsar.

PSR	TPC	OG	PC	SG	OPC
		MSPs			
J0610−2100	192%	114%			
J0614−3329	140%	133%			
J2302+4442	81%	93%			
		Young pulsars			
J2021+3651		39%	1.2%	59%	52%
J2021+4026		30%		132%	16%

Table 7.4: γ-ray efficiency calculated with f_Ω from light curve modelling for high efficiency ($\eta - \delta\eta \geq 60\%$) pulsars. The new values are calculated from the original $\eta - \delta\eta$ values. For MSPs, lower values of f_Ω are used.

Parameter	J0610−2100	J0614−3329	J2302+4442	J2021+3651	J2021+4026
Distance, d (kpc)	< 2 √	? √	> 4.5 √	2.2 √	4.5 √
Beaming factor, f_Ω	X	X	X	√	X
Moment of inertai, I (g cm^2)	√	√	√	√	√

Table 7.5: Parameter investigation results for 2PC pulsars with γ-ray efficiency $\eta - \delta\eta \geq 60\%$. Distances are estimated from the methods described in Section 7.2.1, 7.2.2. "?" means no distance constraints has been obtained. "√" and "X" denotes whether the parameter can or can't account for the pulsar's high efficiency.

7.3 Large moment of inertia candidates

Based on discussions in previous sections, we summarize the parameter investigation results in Table 7.5.

For J0610−2100, f_Ω or a larger moment of inertia by itself is not responsible for the high efficiency problem. It has rather a problematic distance, which should be less than 1.5 kpc if we stay with I_0 as inferred from $\mu - d$ space. Alternatively, its distance should be less than 2 kpc in combination with a higher moment of inertia. It may be a high I candidate.

For J0614−3329, no new distance estimate has been obtained from either $N_{\rm H}$ or the parallax. Its distance is still under question. On the other hand, f_Ω can't "cure" its high efficiency. It may be a large I candidate.

For J2302+4442, new distance estimate from $N_{\rm H}$ is even bigger than the 2PC value. Either the original one is correct, or the pulsar is more distant, implying an even higher efficiency than 60%. In addition, f_Ω seems reliable to be close to 1, thus can't account for its high efficiency even with its original small distance. It stays as high efficiency pulsar. It may be a candidate for large I.

For J2021+3651, the new distance estimate from $N_{\rm H}$ has already resolved the problem. Furthermore, the modelled f_Ω brings its efficiency to be below 60% even with the original big distance. In this case, it's hard to say whether a higher moment of inertia also contributes or not to its high efficiency. It may be a large I candidate.

J2021+4026 is similar to J2302+4442. It may be a large I candidate.

In summary, all the pulsars in our sample may be possible candidates for large moment of inertia.

As discussed in Section 1.2, neutron star mass measurements place strong constraints on different equations of state (EOS) families. The $\sim$2 $M_\odot$ mass measurements for J1614−2230 and J0348+0432 limit the neutron star radius to be $11 - 15$ km. We have deduced that the moment of inertia is $\sim 1.4 - 2.7 I_0$ by taking $M = 1.4$ $M_\odot$ (given the mean value of $\sim 1.2 - 1.5$ $M_\odot$ in the literature, Özel *et al.* 2012b). Owing to the high mass neutron star measurements, large moments of inertia exist and accordingly, the "rigid" EOS which are on the right part in the mass-radius diagram (Figure 1.3 (A)) are favored. Our investigation on high γ-ray efficiency pulsars in 2PC results in some large moment of inertia candidates. *Fermi* seems to confirm independently the existence of large moments of inertia, thus to favor the "rigid" EOS.

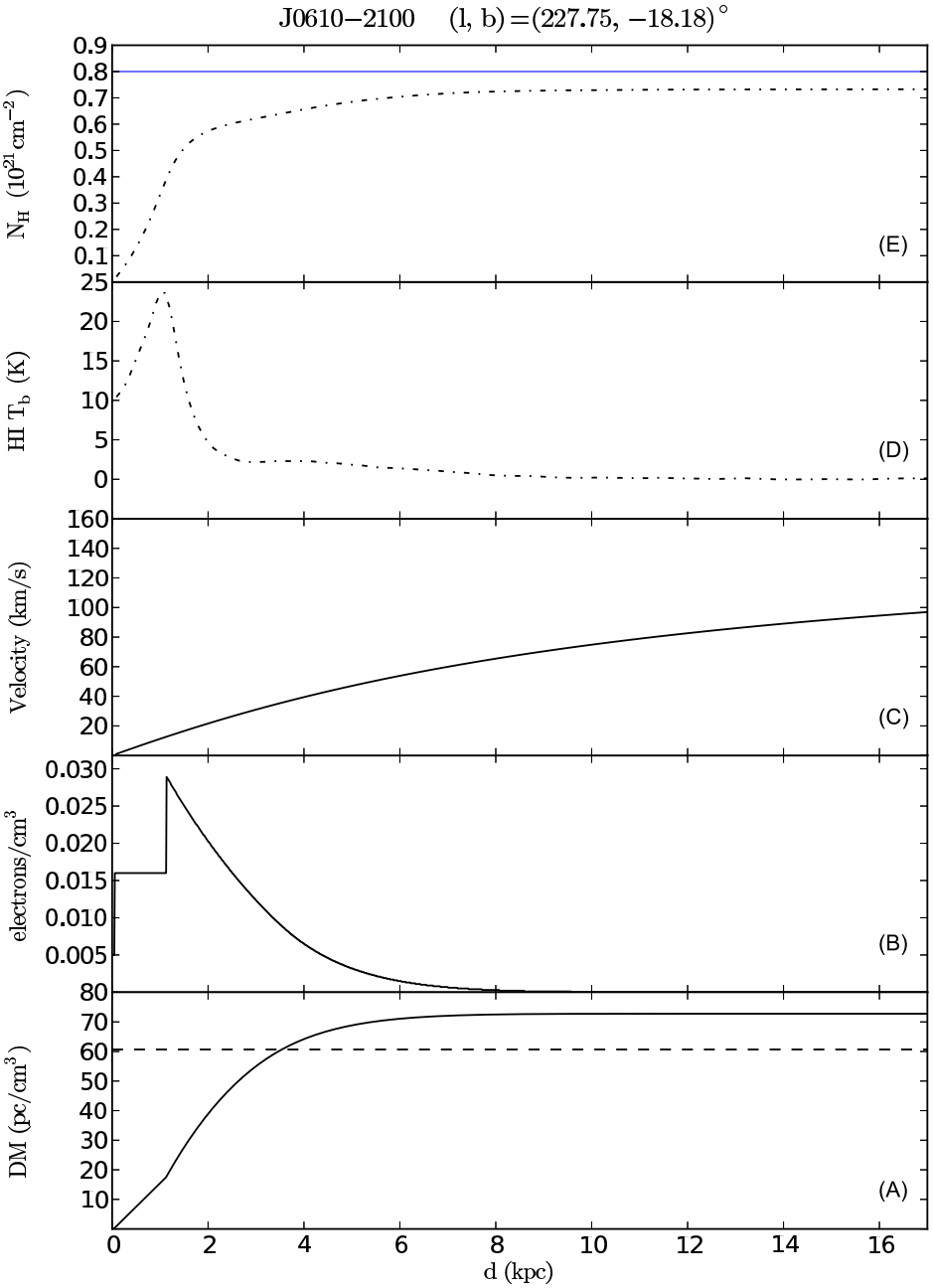

Figure 7.5: From bottom to top, (A): DM vs. distance from the NE2001 model for the line of sight of the pulsar. The black dashed horizontal line indicates the DM measurement for the pulsar; (B): Electron density n_e vs. distance from the NE2001 model for the line of sight of the pulsar; (C): Radial velocity vs. distance (flat Galactic rotation model with current IAU values: $R_0 = 8.5$ km, $\Theta_0 = 220$ km/s); (D): Brightness temperature of HI (black dot-dashed) clouds from the LAB HI survey vs. distance; (E): Cumulative hydrogen column density $N_{\rm H}$ from the LAB HI survey (black dot-dashed). The blue solid horizontal line represents the $N_{\rm H}$ from X-ray observations. For this pulsar, $N_{\rm H}^{\rm X-ray}$ is set to the Galactic $N_{\rm H}$ value obtained from webtools, scaled to its DM distance. No CfA CO survey data is available due to the pulsar's high Galactic latitude.

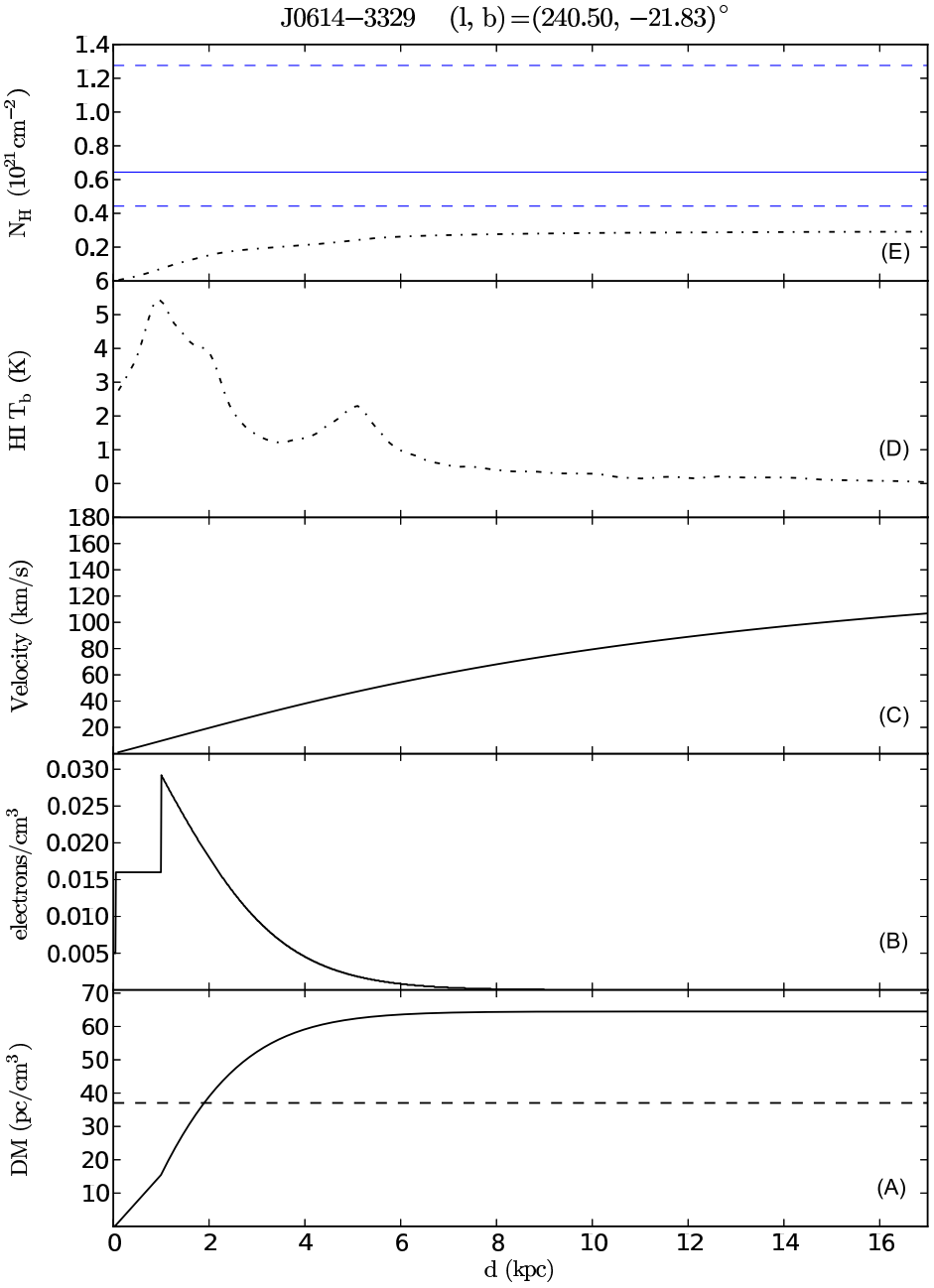

Figure 7.6: Labels are as for Figure 7.5, except that uncertainties on $N_{\rm H}^{\rm X-ray}$ are also shown (blue dashed horizontal lines on the top panel (E)). For this pulsar, $N_{\rm H}^{\rm X-ray}$ exceeds the total $N_{\rm H}$ obtained from the LAB HI survey. No CfA CO survey data is available due to the pulsar's high Galactic latitude.

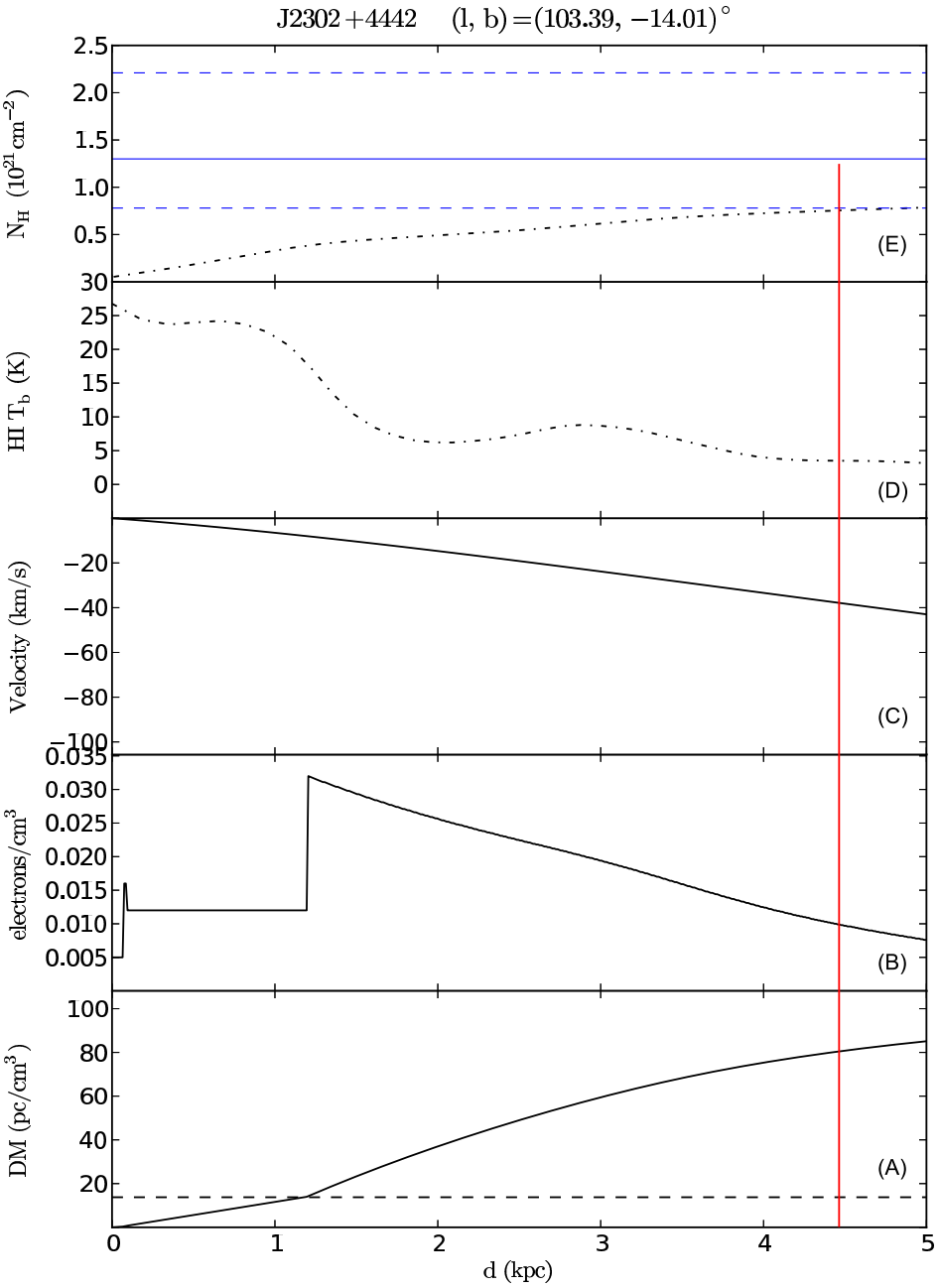

Figure 7.7: Labels are as for Figure 7.6, except that the red solid vertical line indicates the distance estimate (lower limit ~ 4.5 kpc) from the lower value of $N_{\rm H}^{\rm X-ray}$ along with the flat rotation model. For this pulsar, the central value of $N_{\rm H}^{\rm X-ray}$ exceeds the total $N_{\rm H}$ obtained from the LAB HI survey. No CfA CO survey data is available due to the pulsar's high Galactic latitude.

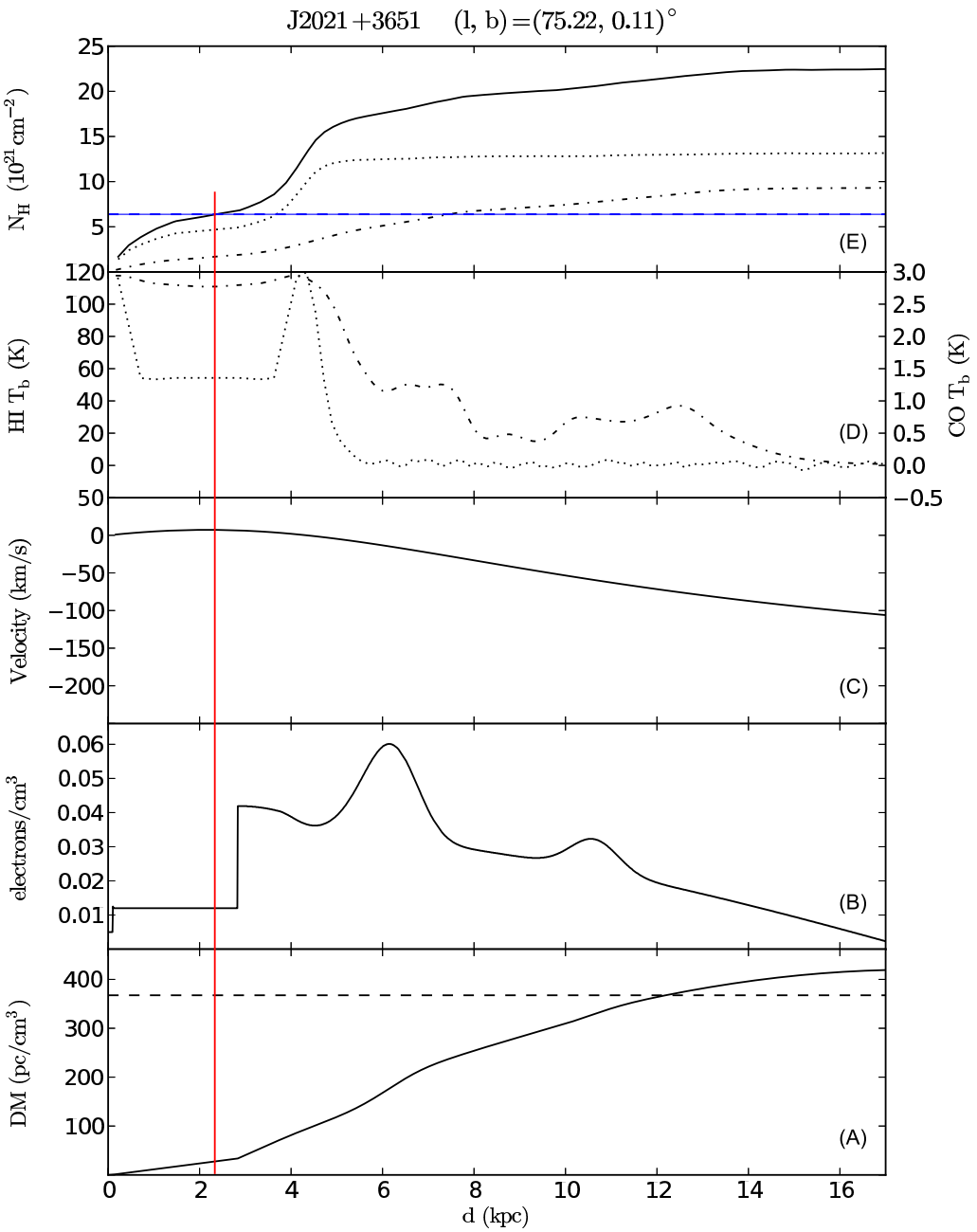

Figure 7.8: Labels are as for Figure 7.7, except that CO cloud observations from CfA survey (black dotted) are added on the top two panels (D) and (E). The black solid curve on the panel (E) represents the total $N_{\rm H}$ combining the LAB HI survey and the CfA CO survey. The distance estimate from $N_{\rm H}^{\rm X-ray}$ is ~ 2.2 kpc with invisible small uncertainties due to the tiny uncertainties on $N_{\rm H}^{\rm X-ray}$.

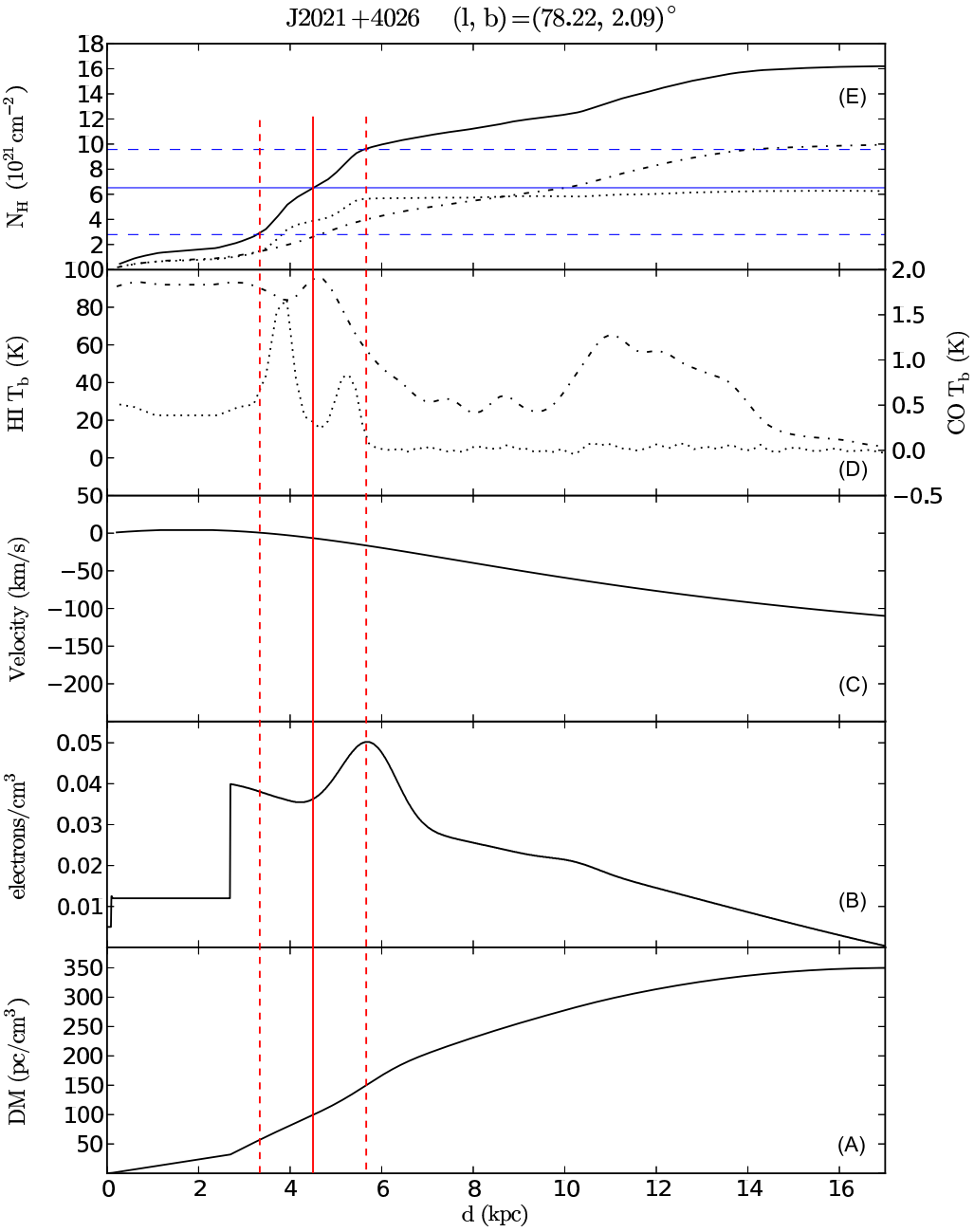

Figure 7.9: Labels are as for Figure 7.8, except that no DM measurement is available for this radio-quiet pulsar. The distance estimate from $N_{\rm H}^{\rm X-ray}$ is roughly $d = 4.5^{+1.1}_{-1.3}$ kpc.

CONCLUSION

After five years of on-orbit operation, the Large Area Telescope (LAT), main instrument on NASA's *Fermi* satellite, has enabled detections of 148 (December 2013) γ-ray pulsars, over fourteen times as many as seen by its predecessor EGRET aboard the Compton Gamma Ray Observatory. 117 of them were presented in the second *Fermi*-LAT catalog of γ-ray pulsars (2PC), more than doubling the tally of the first *Fermi*-LAT catalog of γ-ray pulsars (1PC). Pulsars are by far the largest GeV source-class in the Milky Way. The sample can be evenly divided into three categories: radio-loud young or middle aged pulsars, radio-quiet young or middle aged pulsars, and radio-loud millisecond pulsars (MSPs). For the first time, MSPs have been established as a sub-class of γ-ray emitters, settling the longstanding debate raised before *Fermi*. γ-ray pulsations from individual globular cluster pulsars have also been reported, confirming the interpretation that the observed γ-ray emission from clusters is a sum of the emission from MSPs in the cluster.

The growing number of γ-ray pulsars detected with *Fermi* has offered an excellent opportunity for population studies through spectral analysis and light curve (histogram of rotational phase or photon number vs. phase) modeling, the result of which has favoured γ-ray emission from the neutron star outer magnetosphere (OG, TPC models, etc) rather than being near the magnetic pole region (PC model), where radio and thermal X-ray emission originate.

The 1PC and 2PC pulsars have strong and clear signatures: high statistical test (H-test) significance, peaked light curves (Figure 2.5) and evident spectral cutoff at a few to several GeV (Figure 2.6). This leads to a bright but biased sample. Model discriminations by comparing observations to predictions are distorted by the bias.

Pulsar geometry represented by the inclination α (angle between the pulsar magnetic and rotation axes) and viewing angle ζ (angle between the observing line of sight and the rotation axis) affects the observed light curve shapes and thus the H-test performance – narrow peaks are easier to detect than broad ones. On the other hand, theoretical models (e.g. OG) predict little or no emission modulation for some rare parts of (α, ζ) space. More robust model tests would benefit from detections of pulsars with broader and maybe more complex pulses to explore the unsampled parts of (α, ζ) space.

If (α, ζ) is rare, and/or the "detection efficiency" is low for some (α, ζ), then one needs a bigger pulsar/neutron star sample to obtain γ-ray detections. This requires that one must probe a larger volume of space, meaning bigger distances. Bigger distances mean lower Galactic latitudes, on average, yielding lower signal-to-noise ratios, $\mathrm{S/N} = \mathrm{flux/background}$, given the strong diffuse emission in the Galactic plane. In this case, the spectral cutoff is impossible to measure or is unreliable due to the poor S/N. It is no longer a reliable signature for pulsar identification.

Distance is critical for our study of the γ-ray luminosity L_γ versus spin-down power $\dot{E}$, since $L_\gamma \propto G_{100}\, d^2$, with G_{100} the observed integral energy flux above 100 MeV, and d the distance. The open field-line voltage, above some threshold of which γ-ray emitting electron-positron pair (e^+e^-) cascade occurs, is $V \propto \sqrt{\dot{E}}$. Assuming a linear dependence of L_γ on V gives the "heuristic" relation $L_\gamma \propto \sqrt{\dot{E}}$. High $\dot{E}$ leads to high L_γ which translates to a measurable flux G_{100}, depending partly on the distance.

The *Fermi* pulsar timing campaign targeted the 10% of the over 2000 known pulsars in the ATNF pulsar catalog that have $\dot{E} > 10^{34}$ erg s^{-1}. This choice was based on the results from the Compton observatory, and theoretical considerations. In addition, the radio astronomers provided the LAT team with rotation ephemerides for another 600 pulsars covering a broad range of periods and $\dot{E}$ (the bulk coming from Jodrell Bank observatory). The pre-launch bias that bright γ-ray pulsars have high $\dot{E}$ is confirmed, but we discovered that detectable emission extends as low as $\dot{E} \approx 3 \times 10^{33}$ erg s^{-1}, an empirical "deathline". Weak emission from older non-recycled pulsars might still exist. It could then be an indication of a different

emission process, e.g. emissions from the same e^+e^- population which generates the radio beam.

In this thesis, I have studied an eclectic sample of new pulsars. These new detections enriched the 2PC population, confirming some trends observed in 2PC, e.g. roughly $L_\gamma \propto \sqrt{\dot{E}}$, and the anti-correlation between the radio-γ peak lag and γ-ray peak separation, etc. They mark the transition from the early part to the later part of the *Fermi* mission by illustrating the above problems through the fact that, e.g. one pulsar has the lowest $\dot{E}$ of all young radio-loud pulsars, not all of them have well identified spectral cutoffs, three of them have higher duty cycles (very wide pulses) than in the 2PC sample, filling the otherwise unsampled parts of (α, ζ) space.

Entering the second half of its nominal ten-year mission, the discovery rate of *Fermi* γ-ray pulsars is slowing as expected from a simple $\sqrt{T}$ improvement in sensitivity as the mission livetime T increases. Nevertheless, the whole five years of LAT data will soon be reprocessed with *pass 8*, with much better acceptance below 100 MeV, improving our ability to detect pulsars with low energy spectral cutoffs, as is already the case for the high-magnetic field pulsar B1509$-$58. In addition, the Pulsar Timing Consortium is adding more pulsars near the $\dot{E}$ deathline, and another few hundred old pulsars. Such breakthroughs will indeed not only maintain the discovery rate, but permit discoveries of more pulsars unlike those in 2PC.

Currently, the LAT collaboration insists on $> 5\sigma$ statistical pulsation significance using H-test, before declaring a γ-ray pulsar detection. This was critical in the early mission to unambiguously determine pulsar characteristics, as is done in 1PC and 2PC. Now, the detection criteria could be loosened given the weakness of new pulsar discoveries to come. This will effectively lower the minimum flux required to be detectable, towards the left in the pulsar logN-Log$G$ distribution, increasing the numbers that can be seen. An other approach may be to explore other statistical tests/strategies to compensate the shortcomings of the H-test. This implies that looking towards the longer term, we will have to accept, and quantify, some false detection rates in order to obtain the largest, most complete pulsar sample possible. Careful Monte Carlo simulations can calculate the false detection rate, that is, the fraction of spurious pulsar candidates. Such contamination is a reasonable price to pay for a complete census of the Galactic neutron star population. Additionally, unresolved pulsars contribute to the γ-ray diffuse background. A larger and more complete γ-ray pulsar sample will help to clarify the nature of the recent observed "GeV bump" in the Milky Way center: dark matter or pulsars?

I have also worked on a sample of 2PC γ-ray pulsars with implausible efficiency (e.g. $> 100\%$). Such a high efficiency may indicate that the pulsar distance and/or the beaming factor are overestimated. An alternate solution would be a large neutron star moment of inertia. By investigating parameters which influence the efficiency one by one, especially for distance constraints through different methods (radio/X-ray neutral hydrogen emission, parallax, etc.), I proposed some pulsars to be large moment of inertia candidates. The high mass neutron star measurements in the literature imply large moments of inertia and favor the "rigid" theoretical equations of state (EOS) of neutron stars. My study suggests that *Fermi* γ-ray observations may bring independent constraints on the moment of inertia and thus on the EOS of neutron stars.

APPENDIX

APPENDIX A

Galactic rotation curve and potential models

In the cylindrical coordinates system with the origin at the Galactic center (Figure A.1), a star's position is expressed as (R, φ, z). R is the galactocentric radius in the Galactic plane, φ is the azimuthal angle, and z is the height above the Galactic plane. $R_{\rm g}$ is the height-elongated galactocentric radius. In such a frame, the star's velocity is denoted as (Π, Θ, Z), with Π the velocity toward/from the Galactic center, Θ the tangential velocity and Z the vertical velocity. Note that in the Cartesian coordinates system with the Galactic center at its origin, the Sun has coordinates $(x, y, z)_\odot = (-8.5, 0, 0.015)$ kpc.

A.1 Galactic rotation curve

Many studies of the Milky Way rely on a model of the Galactic rotation curve which can be expressed as the tangential velocity Θ versus the galactocentric radius R projected on the Galactic plane. Such rotation curve can be used to construct the Galaxy mass distribution model, to estimate the kinematic distance of objects from radial velocity if available, or to study the non-circular motions in the Galaxy, etc. It can be determined by fitting the HI, CO and/or spectrophotometric observation data to different simple forms like linear or power law functions. The current observations favors a rather flat rotation curve (Fich *et al.* 1989) with the IAU (International Astronomical Union) recommended fundamental constants be (Kerr & Lynden-Bell 1986):

$$\Theta_0 = 220\,\mathrm{km\,s^{-1}}, \quad R_0 = 8.5\,\mathrm{kpc} \tag{A.1}$$

for the LSR (Local Standard of Rest) defined at the solar neighbourhood. We use this rotation model throughout this thesis if applicable. Examples of the rotation curve analysis can be found in e.g. Reid *et al.* (2009).

Following Lazaridis *et al.* (2009), the galactic acceleration of a star relative to the LSR projected on the line of sight assuming a flat rotation curve is (equivalent to Equation 4.17):

$$a = -\frac{v_0^2}{R_0}\left(\cos l + \frac{\beta}{\sin l^2 + \beta^2}\right)\cos b - a_z \sin b \tag{A.2}$$

with $v_0 = \Theta_0 = 220\,\mathrm{km\,s^{-1}}$. l, b are the star's Galactic longitude and latitude, a_Z is the vertical Galactic acceleration and $\beta \equiv (d/R_0) - \cos l$. d is the distance of the star to the LSR.

A.2 Galactic gravitational potential models

In general, the acceleration due to the Galactic potential Φ in the cylindrical coordinates system $\Phi(R, z)$ is:

$$a_{\rm R} = \frac{\partial \Phi}{\partial R}, \quad a_{\rm z} = \frac{\partial \Phi}{\partial z} \tag{A.3}$$

and in the Cartesian coordinates system (to avoid the singularity of cylindrical coordinates at $R = 0$) is:

$$a_{\rm x} = \frac{x}{R}\frac{\partial \Phi}{\partial R}, \quad a_{\rm y} = \frac{y}{R}\frac{\partial \Phi}{\partial R}, \quad a_{\rm z} = \frac{\partial \Phi}{\partial z}, \quad R^2 = x^2 + y^2 \tag{A.4}$$

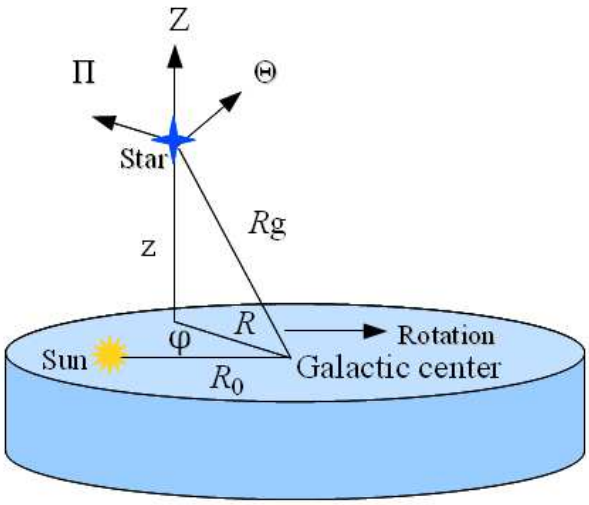

Figure A.1: Scheme of the cylindrical coordinates system of the Milky Way. A star's position is expressed as (R, φ, z), and its velocity is denoted as (Π, Θ, Z). φ is the azimuthal angle, z is the height above the Galactic plane, R represents a star's galactocentric radius and R_g is the height-elongated galactocentric radius. Π is the velocity toward/from the Galactic center, Θ is the tangential velocity and Z is the vertical velocity. The Sun is at a galactocentric radius of $R_0 = 8.5$ kpc.

The radial (along the line of sight) galactic acceleration of a star relative to the LSR is then:

$$a = (\vec{a_{\text{star}}} - \vec{a_{\text{LSR}}}) \cdot \vec{n} \tag{A.5}$$

with $\vec{a_{\text{star}}} = (a_x, a_y, a_z)_{\text{star}}$, $\vec{a_{\text{LSR}}} = (a_x, a_y, a_z)_{\text{LSR}}$, and $\vec{n}$ the unit vector pointing from the LSR to the star.

Table A.1 summarizes the different parameters involved in the below two Galactic potential models.

A.2.1 Model 1

This Galactic potential (Carlberg & Innanen 1987; Kuijken & Gilmore 1989) has three components: nucleus, bulge and disk-halo (3 contributions further more).

$$\Phi = \sum \Phi_i, \quad i = 1,2,3 \tag{A.6}$$

$$\Phi_i(R,z) = -\frac{GM_i}{\sqrt{\left(a_i + \sum_{j=1}^{3} \beta_j^i \sqrt{z^2 + h_j^i}\right)^2 + b_i + R^2}}, \quad j = 1,2,3 \tag{A.7}$$

$G = 6.67384 \times 10^{-11} \text{m}^3\text{kg}^{-1}\text{s}^{-1}$ is Newton's gravitational constant, M is the mass of the three components in units of 10^9 $M_\odot$, a is the scale length of the disk-halo, and b is the core radius of the three components. The three contributions of the disk-halo are the old disk, the young disk and a dark component respectively. h is the scale height of the three contributions. The fractional proportions of the three contributions are given by β.

Model 1									
Component	M (10^9 $M_\odot$)	a (kpc)	b (kpc)	β_1	β_2	β_3	h_1 (kpc)	h_2 (kpc)	h_3 (kpc)
Nucleus ($i=1$)	9.3	0	0.25	1	0	0	0	0	0
Bulge ($i=2$)	10	0	1.5	1	0	0	0	0	0
Disk-halo ($i=3$)	145	2.4	5.5	0.4	0.5	0.1	0.325	0.090	0.125

Model 2				
Component	M (10^9 $M_\odot$)	a (kpc)	b (kpc)	r_c (kpc)
Spheroid ($i=1$)	11.2	0	0.277	...
Disk ($i=2$)	80.7	3.7	0.20	...
halo	50	...	...	6.0

Table A.1: Galactic potential model parameters for the model 1 (Carlberg & Innanen 1987; Kuijken & Gilmore 1989) and the model 2 (Paczynski 1990). Refer to the text for definitions of the parameters.

A.2.2 Model 2

This Galactic potential (Paczynski 1990) consists of three components: spheroid, disk and halo. For the spheroid and the disk components:

$$\Phi_i(R,z) = -\frac{GM_i}{\sqrt{R^2+(a_i+(z^2+b_i^2)^{1/2})^2}}, \quad i=1,2 \tag{A.8}$$

The halo component is:

$$\Phi_h(R,z) = -\frac{GM_c}{r_c}\left[\frac{1}{2}\ln\left(1+\frac{r^2}{r_c^2}\right)+\frac{r_c}{r}\arctan\left(\frac{r}{r_c}\right)\right], \quad r^2=R^2+z^2 \tag{A.9}$$

The total potential is:

$$\Phi = \Phi_i + \Phi_h, \quad i=1,2 \tag{A.10}$$

G is Newton's gravitational constant, M is the mass of the three components in units of 10^9 $M_\odot$, a is the scale length of the disk, b is the scale height of the disk, r_c is the halo core radius and r is the height-elongated galactocentric radius (R_g in Figure A.1).

APPENDIX B

Distances and Doppler corrections for *Fermi*-LAT pulsars

Below two tables give the distances of γ-ray pulsars included in the Second *Fermi*-LAT Calatog of Gamma-ray Pulsars (2PC, Abdo *et al.* 2013). Doppler corrections are applied to 20 MSPs with proper motion measurements. For each MSP, the best proper motion is provided, followed by the intrinsic spin-down rate $\dot{P}^{\rm int}$, the contribution of the Shklovskii effect $\dot{P}^{\rm shk}$, that of the Galactic acceleration $\dot{P}^{\rm gal}$, the intrinsic spin-down power $\dot{E}^{\rm int}$, and the relative correction ξ defined from $\dot{E}^{\rm int} = \dot{E}\,(1-\xi)$. For $|\xi|$ greater than a few percent, $\dot{P}^{\rm shk} > |\dot{P}^{\rm gal}|$ and the corrected $\dot{E}^{\rm int}$ is *less* than the observed value. Hence flagging γ-ray pulsar candidates that have large $\dot{E}$ selects some with lower $\dot{E}^{\rm int}$, but candidates would not be missed if neglecting Doppler effect. For large Doppler corrections, $\dot{P}^{\rm shk} \gg \dot{P}^{\rm gal}$, the Galactic term is negligible and we calculate only the uncertainty due to $\dot{P}^{\rm shk}$. For the distance methods, P: parallax; K: kinematic; DM: dispersion measure with the NE2001 model (Cordes & Lazio 2002); DMM: distance to the Galaxy edge as upper limit from the NE2001 model; X: X-ray. O: other measurements (optical, association...). References for distances and proper motions can be found in 2PC.

PSRJ	Distance (kpc)	Method
J0007+7303	1.4 ± 0.3	K
J0106+4855	$3.0^{+1.1}_{-0.7}$	DM
J0205+6449	1.95 ± 0.04	KP
J0248+6021	2.0 ± 0.2	K
J0357+3205	< 8.2	DMM
J0534+2200	2.0 ± 0.5	O
J0622+3749	< 8.3	DMM
J0631+1036	1.0 ± 0.2	O
J0633+0632	< 8.7	DMM
J0633+1746	$0.2^{+0.2}_{-0.1}$	P
J0659+1414	0.28 ± 0.03	P
J0729−1448	3.5 ± 0.4	DM
J0734−1559	< 10.3	DMM
J0742−2822	2.1 ± 0.5	DM
J0835−4510	$0.29^{+0.02}_{-0.02}$	P
J0908−4913	2.6 ± 0.9	DM
J0940−5428	3.0 ± 0.5	DM
J1016−5857	$8.0^{+3.5}_{-2.1}$	DM
J1019−5749	$6.8^{+13.2}_{-2.5}$	DM
J1023−5746	< 16.8	DMM
J1028−5819	2.3 ± 0.3	DM
J1044−5737	< 17.2	DMM
J1048−5832	2.7 ± 0.4	DM
J1057−5226	0.3 ± 0.2	O
J1105−6107	5.0 ± 1.0	DM
J1112−6103	$12.2^{+7.8}_{-3.8}$	DM
J1119−6127	8.4 ± 0.4	K

PSRJ	Distance (kpc)	Method
J1124−5916	$4.8^{+0.7}_{-1.2}$	X
J1135−6056	< 18.4	DMM
J1357−6429	$2.5^{+0.5}_{-0.4}$	DM
J1410−6132	$15.6^{+7.4}_{-4.2}$	DM
J1413−6205	< 21.4	DMM
J1418−6058	1.6 ± 0.7	O
J1420−6048	5.6 ± 0.9	DM
J1429−5911	< 21.8	DMM
J1459−6053	< 22.2	DMM
J1509−5850	2.6 ± 0.5	DM
J1513−5908	4.2 ± 0.6	DM
J1531−5610	$2.1^{+0.4}_{-0.3}$	DM
J1620−4927	< 24.1	DMM
J1648−4611	5.0 ± 0.7	DM
J1702−4128	4.8 ± 0.6	DM
J1709−4429	2.3 ± 0.3	DM
J1718−3825	3.6 ± 0.4	DM
J1730−3350	$3.5^{+0.4}_{-0.5}$	DM
J1732−3131	0.6 ± 0.1	DM
J1741−2054	0.38 ± 0.02	DM
J1746−3239	< 25.3	DMM
J1747−2958	4.8 ± 0.8	X
J1801−2451	$5.2^{+0.6}_{-0.5}$	DM
J1803−2149	< 25.2	DMM
J1809−2332	1.7 ± 1.0	K
J1813−1246	< 24.7	DMM
J1826−1256	< 24.7	DMM
J1833−1034	4.7 ± 0.4	K
J1835−1106	2.8 ± 0.4	DM
J1836+5925	0.5 ± 0.3	X
J1838−0537	< 24.1	DMM
J1846+0919	< 22.0	DMM
J1907+0602	3.2 ± 0.3	DM
J1952+3252	2.0 ± 0.5	K
J1954+2836	< 18.6	DMM
J1957+5033	< 14.5	DMM
J1958+2846	< 18.5	DMM
J2021+3651	$10.0^{+2.0}_{-4.0}$	O
J2021+4026	1.5 ± 0.4	K
J2028+3332	< 17.2	DMM
J2030+3641	3.0 ± 1.0	O
J2030+4415	< 15.7	DMM
J2032+4127	3.7 ± 0.6	DM
J2043+2740	1.8 ± 0.3	DM
J2055+2539	< 15.3	DMM
J2111+4606	< 14.8	DMM
J2139+4716	< 14.1	DMM

PSRJ	Distance (kpc)	Method
J2229+6114	$0.80^{+0.15}_{-0.20}$	K
J2238+5903	< 12.4	DMM
J2240+5832	7.7 ± 0.7	O

Table B.1: Distances for the 77 young pulsars detected with the *Fermi*-LAT in 2PC.

PSRJ	Distance (pc)	Method	μ (mas yr^{-1})	$\dot{P}^{\rm int}$ (10^{-21})	$\dot{P}^{\rm shk}$ (10^{-21})	$\dot{P}^{\rm gal}$ (10^{-21})	$\dot{E}^{\rm int}$ (10^{33} erg s^{-1})	ξ (%)
J0023+0923	690^{+210}_{-110}	DM						
J0030+0451	280^{+100}_{-60}	P	5.7 ± 1.1	10.7 ± 0.1	0.11	-0.60	3.64 ± 0.02	-5
J0034−0534	540 ± 100	DM	31.0 ± 9.0	2.9 ± 1.4	2.37	-0.31	17.3 ± 8.6	41
J0101−6422	550^{+90}_{-80}	DM	15.6 ± 1.7	4.4 ± 0.2	0.84	-0.39	10.1 ± 0.5	9
J0102+4839	2320^{+500}_{-430}	DM						
J0218+4232	2640^{+1080}_{-640}	DM	5.0 ± 6.0	76.9 ± 0.9	0.37	0.09	243.2 ± 2.8	0.6
J0340+4130	1730 ± 300	DM						
J0437−4715	156 ± 1	P	141.3 ± 0.1	14.1 ± 0.3	43.59	-0.40	2.9 ± 0.1	75
J0610−2100	3540^{+5460}_{-1000}	DM	18.2 ± 0.2	$1.2^{+17.0}_{-1.1}$	11.00	0.10	$0.8^{+11.7}_{-0.8}$	90
J0613−0200	900^{+400}_{-200}	P	10.8 ± 0.2	$8.7^{+0.3}_{-0.2}$	0.77	0.08	$12.0^{+0.5}_{-0.2}$	9
J0614−3329	1900^{+440}_{-350}	DM						
J0751+1807	400^{+200}_{-100}	P	6.0 ± 2.0	7.7 ± 0.1	0.12	-0.02	7.2 ± 0.1	1
J1024−0719	386 ± 38	DM	59.9 ± 0.2	$1.6^{+1.8}_{-1.4}$	17.37	-0.44	$0.4^{+0.5}_{-0.4}$	92
J1124−3653	1720^{+430}_{-360}	DM						
J1125−5825	2620 ± 370	DM						
J1231−1411	438 ± 50	DM	62.2 ± 4.7	6.5 ± 2.9	15.15	-0.41	5.1 ± 2.3	70
J1446−4701	1460 ± 220	DM						
J1514−4946	940 ± 120	DM						
J1600−3053	1630^{+310}_{-270}	DM	7.2 ± 0.3	$8.6^{+0.2}_{-0.1}$	0.74	0.15	7.3 ± 0.1	9
J1614−2230	650 ± 50	P	36.5 ± 0.2	3.0 ± 0.5	6.65	-0.003	3.8 ± 0.6	69
J1658−5324	930^{+110}_{-130}	DM						
J1713+0747	1050^{+60}_{-50}	P	6.30 ± 0.01	$8.28^{+0.03}_{-0.02}$	0.46	-0.21	3.42 ± 0.01	3
J1741+1351	1080^{+40}_{-50}	P	11.71 ± 0.01	29.1 ± 0.1	1.35	-0.20	$21.76^{+0.04}_{-0.05}$	4
J1744−1134	417 ± 17	P	21.02 ± 0.03	7.0 ± 0.1	1.82	0.08	4.11 ± 0.04	21
J1747−4036	3390 ± 760	DM						
J1810+1744	2000^{+310}_{-280}	DM						
J1823−3021A	7600 ± 400	O						
J1858−2216	940^{+200}_{-130}	DM						
J1902−5105	1180 ± 210	DM						
J1939+2134	3560 ± 350	DM	0.80 ± 0.02	105.5 ± 0.1	0.01	-0.36	1096.6 ± 0.5	-0.3
J1959+2048	2490^{+160}_{-490}	DM	30.4 ± 0.6	$8.1^{+0.7}_{-1.8}$	9.00	-0.25	$76.3^{+6.4}_{-17.1}$	52

PSRJ	Distance (pc)	Method	μ (mas yr^{-1})	$\dot{P}^{\rm int}$ (10^{-21})	$\dot{P}^{\rm shk}$ (10^{-21})	$\dot{P}^{\rm gal}$ (10^{-21})	$\dot{E}^{\rm int}$ (10^{33} erg s^{-1})	ξ (%)
J2017+0603	1570 ± 150	DM						
J2043+1711	1760^{+150}_{-320}	DM	13.0 ± 2.0	4.3 ± 0.6	1.72	-0.35	$12.7^{+1.6}_{-1.8}$	24
J2047+1053	2050^{+320}_{-290}	DM						
J2051$-$0827	1040 ± 150	DM	7.3 ± 0.4	12.6 ± 0.1	0.61	-0.47	5.43 ± 0.05	1
J2124$-$3358	300^{+70}_{-50}	P	52.3 ± 0.3	$11.2^{+2.3}_{-1.6}$	9.83	-0.46	$3.7^{+0.8}_{-0.5}$	46
J2214+3000	1540 ± 180	DM						
J2215+5135	3010^{+330}_{-370}	DM						
J2241$-$5236	513 ± 76	DM						
J2302+4442	1190^{+90}_{-230}	DM						

Table B.2: Distances and Doppler corrections for the 40 MSPs detected with the *Fermi*-LAT in 2PC.

APPENDIX C

BigFile database

The *BigFile* database is created to simplify the manipulation and the follow up of an increasing number of γ-ray pulsars. It's constructed in a "scalable" manner that is easy to share with people working on pulsars and to add info to the database. The goal is to maintain it as a standard "tool" for γ-ray pulsars on the long term. The *BigFile* has been the base for the content of 2PC and its on line material. The *BigFile* is based on a series of python code which reads in different pulsar information from:

- The online ATNF pulsar catalog, with pre-defined interested variables, e.g. JName, RaJ, DecJ, P, $\dot{P}$, $\dot{E}$, etc.
- *Fermi* internal list of detected γ-ray pulsars with flags of "radio-loud", "radio-quiet" or "MSP", etc.
- All $>$ 700 ephemerides provided by the PTC.
- List of radio MSPs found in *Fermi* unidentified sources.
- Lists of 3σ, 4σ, 5σ candidates based on the pulsation search using radio/X-ray ephemeris.
- Pulsar proper motions mostly from ATNF.
- γ-ray pulsar distances maintained by *Fermi*.
- γ-ray pulsar spectral parameters if available.
- γ-ray pulsar light curve parameters if available.
- X-ray analysis results for γ-ray pulsars if available.
- Optical analysis results for γ-ray pulsars if available.
- More to come if necessary.

The output of the python code is an EXCEL file and a FITS file containing all the information described above. From the EXCEL or the FITS file, publication-quality plots with different colors, symbols for different pulsar types and LaTeX tables along with bibliographic references can be made with simple python code after setting up the library path where the *BigFile* python code is constructed.

Bibliography

Abbott, B. P., Abbott, R., Acernese, F., *et al.* 2010, *Searches for Gravitational Waves from Known Pulsars with Science Run 5 LIGO Data*, ApJ, 713, 671

Abdo, A. A., Ackermann, M., Ajello, M., *et al.* 2010a, *Fermi Large Area Telescope First Source Catalog*, ApJ Suppl., 188, 405

Abdo, A. A., Ackermann, M., Ajello, M., *et al.* 2009a, *The on-orbit calibration of the Fermi Large Area Telescope*, Astroparticle Physics, 32, 193

Abdo, A. A., Ackermann, M., Ajello, M., *et al.* 2009b, *Detection of 16 Gamma-Ray Pulsars Through Blind Frequency Searches Using the Fermi LAT*, Science, 325, 840

Abdo, A. A., Ackermann, M., Ajello, M., *et al.* 2010b, *The First Fermi Large Area Telescope Catalog of Gamma-ray Pulsars*, ApJ Suppl., 187, 460

Abdo, A. A., Ackermann, M., Ajello, M., *et al.* 2009c, *Pulsed Gamma-rays from PSR J2021+3651 with the Fermi Large Area Telescope*, ApJ, 700, 1059

Abdo, A. A., Ackermann, M., Ajello, M., *et al.* 2010c, *Fermi-LAT Study of Gamma-ray Emission in the Direction of Supernova Remnant W49B*, ApJ, 722, 1303

Abdo, A. A., Ackermann, M., Ajello, M., & Guillemot, L. 2009d, *A Population of Gamma-Ray Millisecond Pulsars Seen with the Fermi Large Area Telescope*, Science, 325, 848

Abdo, A. A., Ajello, M., Allafort, A., *et al.* 2013, *The Second Fermi Large Area Telescope Catalog of Gamma-Ray Pulsars*, ApJ Suppl., 208, 17

Ackermann, M., Ajello, M., Albert, A., *et al.* 2012a, *The Fermi Large Area Telescope on Orbit: Event Classification, Instrument Response Functions, and Calibration*, ApJ Suppl., 203, 4

Ackermann, M., Ajello, M., Atwood, W. B., *et al.* 2012b, *Fermi-LAT Observations of the Diffuse γ-Ray Emission: Implications for Cosmic Rays and the Interstellar Medium*, ApJ, 750, 3

Alcock, C. & Olinto, A. 1988, *Exotic phases of hadronic matter and their astrophysical application*, Annual Review of Nuclear and Particle Science, 38, 161

Allafort, A., Baldini, L., Ballet, J., *et al.* 2013, *PSR J2021+4026 in the Gamma Cygni Region: The First Variable γ-Ray Pulsar Seen by the Fermi LAT*, ApJ Lett., 777, L2

Alpar, M. A. 1977, *Pinning and Threading of Quantized Vortices in the Pulsar Crust Superfluid*, ApJ, 213, 527

Anderson, P. W. & Itoh, N. 1975, *Pulsar glitches and restlessness as a hard superfluidity phenomenon*, Nature, 256, 25

Antoniadis, J., Freire, P. C. C., Wex, N., *et al.* 2013, *A Massive Pulsar in a Compact Relativistic Binary*, Science, 340, 448

Archibald, A. M., Stairs, I. H., Ransom, S. M., *et al.* 2009, *A Radio Pulsar/X-ray Binary Link*, Science, 324, 1411

Archibald, R. F., Kaspi, V. M., Ng, C.-Y., *et al.* 2013, *An anti-glitch in a magnetar*, Nature, 497, 591

Arons, J. 1983, *Pair creation above pulsar polar caps - Geometrical structure and energetics of slot gaps*, ApJ, 266, 215

Arons, J. 1996, *Pulsars as gamma ray sources.*, A&AS, 120, C49

Arzoumanian, Z., Cordes, J. M., & Wasserman, I. 1999, *Pulsar Spin Evolution, Kinematics, and the Birthrate of Neutron Star Binaries*, ApJ, 520, 696

Atwood, W. B., Abdo, A. A., Ackermann, M., *et al.* 2009, *The Large Area Telescope on the Fermi Gamma-Ray Space Telescope Mission*, ApJ, 697, 1071

Atwood, W. B., Ziegler, M., Johnson, R. P., & Baughman, B. M. 2006, *A Time-differencing Technique for Detecting Radio-quiet Gamma-Ray Pulsars*, ApJ Lett., 652, L49

Baade, W. & Zwicky, F. 1934, *Cosmic Rays from Super-novae*, Contributions from the Mount Wilson Observatory, vol. 3, pp.79-83, 3, 79

Backer, D. C. & Hellings, R. W. 1986, *Pulsar timing and general relativity*, ARA&A, 24, 537

Bednarek, I., Haensel, P., Zdunik, J. L., Bejger, M., & Mańka, R. 2012, *Hyperons in neutron-star cores and a 2 M pulsar*, A&A, 543, A157

Bhattacharya, D. & van den Heuvel, E. P. J. 1991, *Formation and evolution of binary and millisecond radio pulsars*, Phys. Rep., 203, 1

Bisnovatyi-Kogan, G. S. & Komberg, B. V. 1974, *Pulsars and close binary systems*, Soviet Ast., 18, 217

Bisnovatyi-Kogan, G. S. & Seidov, Z. F. 1970, *Nonequilibrium β Processes as a Sources of Thermal Energy of White Dwarf Stars.*, Soviet Ast., 14, 113

Blgnami, G. F. & Caraveo, P. A. 1992, *Geminga: new period, old γ-rays*, Nature, 357, 287

Bogdanov, S. 2013, *The Nearest Millisecond Pulsar Revisited with XMM-Newton: Improved Mass-radius Constraints for PSR J0437-4715*, ApJ, 762, 96

Bogdanov, S. & Grindlay, J. E. 2009, *Deep XMM-Newton Spectroscopic and Timing Observations of the Isolated Radio Millisecond Pulsar PSR J0030+0451*, ApJ, 703, 1557

Bregeon, J., Charles, E., & M. Wood for the Fermi-LAT collaboration. 2013, *Fermi-LAT data reprocessed with updated calibration constants*, ArXiv e-prints

Buccheri, R., Bennett, K., Bignami, G. F., *et al.* 1983, *Search for pulsed gamma-ray emission from radio pulsars in the COS-B data*, A&A, 128, 245

Burbidge, E. M., Burbidge, G. R., Fowler, W. A., & Hoyle, F. 1957, *Synthesis of the Elements in Stars*, Reviews of Modern Physics, 29, 547

Burt, B. J., Lommen, A. N., & Finn, L. S. 2011, *Optimizing Pulsar Timing Arrays to Maximize Gravitational Wave Single-source Detection: A First Cut*, ApJ, 730, 17

Burton, W. B. 1988, The structure of our Galaxy derived from observations of neutral hydrogen, 295–358

Camilo, F., Kerr, M., Ray, P. S., *et al.* 2012, *PSR J2030+3641: Radio Discovery and Gamma-Ray Study of a Middle-aged Pulsar in the Now Identified Fermi-LAT Source 1FGL J2030.0+3641*, ApJ, 746, 39

Cappellaro, E., Evans, R., & Turatto, M. 1999, *A new determination of supernova rates and a comparison with indicators for galactic star formation*, A&A, 351, 459

Cappellaro, E. & Turatto, M. 2001, in Astrophysics and Space Science Library, Vol. 264, The Influence of Binaries on Stellar Population Studies, ed. D. Vanbeveren, 199

Carlberg, R. G. & Innanen, K. A. 1987, *Galactic chaos and the circular velocity at the sun*, AJ, 94, 666

Chandrasekhar, S. 1935, *The highly collapsed configurations of a stellar mass (Second paper)*, MNRAS, 95, 207

Cheng, K. S., Ho, C., & Ruderman, M. 1986, *Energetic radiation from rapidly spinning pulsars. I - Outer magnetosphere gaps. II - VELA and Crab*, ApJ, 300, 500

Cheng, K. S., Ruderman, M., & Zhang, L. 2000, *A Three-dimensional Outer Magnetospheric Gap Model for Gamma-Ray Pulsars: Geometry, Pair Production, Emission Morphologies, and Phase-resolved Spectra*, ApJ, 537, 964

Cordes, J. M. & Lazio, T. J. W. 2002, *NE2001.I. A New Model for the Galactic Distribution of Free Electrons and its Fluctuations*, ArXiv Astrophysics e-prints

Dame, T. M., Hartmann, D., & Thaddeus, P. 2001, *The Milky Way in Molecular Clouds: A New Complete CO Survey*, ApJ, 547, 792

Damour, T. & Taylor, J. H. 1991, *On the orbital period change of the binary pulsar PSR 1913 + 16*, ApJ, 366, 501

Daugherty, J. K. & Harding, A. K. 1982, *Electromagnetic cascades in pulsars*, ApJ, 252, 337

Daugherty, J. K. & Harding, A. K. 1994, *Polar CAP models of gamma-ray pulsars: Emision from single poles of nearly aligned rotators*, ApJ, 429, 325

Daugherty, J. K. & Harding, A. K. 1996, *Gamma-Ray Pulsars: Emission from Extended Polar CAP Cascades*, ApJ, 458, 278

de Jager, O. C. & Büsching, I. 2010, *The H-test probability distribution revisited: improved sensitivity*, A&A, 517, L9

de Jager, O. C., Raubenheimer, B. C., & Swanepoel, J. W. H. 1989, *A poweful test for weak periodic signals with unknown light curve shape in sparse data*, A&A, 221, 180

Deller, A. T., Verbiest, J. P. W., Tingay, S. J., & Bailes, M. 2008, *Extremely High Precision VLBI Astrometry of PSR J0437-4715 and Implications for Theories of Gravity*, ApJ Lett., 685, L67

Demorest, P. B., Pennucci, T., Ransom, S. M., Roberts, M. S. E., & Hessels, J. W. T. 2010, *A two-solar-mass neutron star measured using Shapiro delay*, Nature, 467, 1081

Deutsch, A. J. 1955, *The electromagnetic field of an idealized star in rigid rotation in vacuo*, Annales d'Astrophysique, 18, 1

Dickey, J. M. & Lockman, F. J. 1990, *H I in the Galaxy*, ARA&A, 28, 215

Du, Y. J., Han, J. L., Qiao, G. J., & Chou, C. K. 2011, *Gamma-ray Emission from the Vela Pulsar Modeled with the Annular Gap and the Core Gap*, ApJ, 731, 2

Du, Y. J., Qiao, G. J., & Chen, D. 2013, *Radio and Gamma-Ray Pulsed Emission from Millisecond Pulsars*, ApJ, 763, 29

Du, Y. J., Qiao, G. J., Han, J. L., Lee, K. J., & Xu, R. X. 2010, *The annular gap model for γ-ray emission from young and millisecond pulsars*, MNRAS, 406, 2671

Du, Y. J., Qiao, G. J., & Wang, W. 2012, *Radio-to-TeV Phase-resolved Emission from the Crab Pulsar: The Annular Gap Model*, ApJ, 748, 84

Dyks, J. & Rudak, B. 2003, *Two-Pole Caustic Model for High-Energy Light Curves of Pulsars*, ApJ, 598, 1201

Dyks, J., Zhang, B., & Gil, J. 2005, *Reversals of Radio Emission Direction in PSR B1822-09*, ApJ Lett., 626, L45

Edwards, R. T. & Bailes, M. 2001, *Recycled Pulsars Discovered at High Radio Frequency*, ApJ, 553, 801

Edwards, R. T., Hobbs, G. B., & Manchester, R. N. 2006, *TEMPO2, a new pulsar timing package - II. The timing model and precision estimates*, MNRAS, 372, 1549

Espinoza, C. M., Guillemot, L., Çelik, Ö., *et al.* 2013, *Six millisecond pulsars detected by the Fermi Large Area Telescope and the radio/gamma-ray connection of millisecond pulsars*, MNRAS, 430, 571

Fich, M., Blitz, L., & Stark, A. A. 1989, *The rotation curve of the Milky Way to 2 R(0)*, ApJ, 342, 272

Fichtel, C. E., Hartman, R. C., Kniffen, D. A., *et al.* 1975, *High-energy gamma-ray results from the second small astronomy satellite*, ApJ, 198, 163

Finkbeiner, D. P. 2003, *A Full-Sky Hα Template for Microwave Foreground Prediction*, ApJ Suppl., 146, 407

Foster, R. S. & Wolszczan, A. 1993, in Bulletin of the American Astronomical Society, Vol. 25, American Astronomical Society Meeting Abstracts, 1346

Freire, P. C. C., Abdo, A. A., Ajello, M., *et al.* 2011a, *Fermi Detection of a Luminous γ-Ray Pulsar in a Globular Cluster*, Science, 334, 1107

Freire, P. C. C., Bassa, C. G., Wex, N., *et al.* 2011b, *On the nature and evolution of the unique binary pulsar J1903+0327*, MNRAS, 412, 2763

Gangadhara, R. T. & Gupta, Y. 2001, *Understanding the Radio Emission Geometry of PSR B0329+54*, ApJ, 555, 31

Giacobbe, F. W. 2003, *Maximum stellar iron core mass*, Pramana, 60, 415

Gil, J., Gronkowski, P., & Rudnicki, W. 1984, *Geometry of the emission region of PSR 0950+08*, A&A, 132, 312

Gil, J., Haberl, F., Melikidze, G., *et al.* 2008, *XMM-Newton Observations of Radio Pulsars B0834+06 and B0826-34 and Implications for the Pulsar Inner Accelerator*, ApJ, 686, 497

Glendenning, N. K. 1992, *First-order phase transitions with more than one conserved charge: Consequences for neutron stars*, Phys. Rev. D, 46, 1274

Gold, T. 1968, *Rotating Neutron Stars as the Origin of the Pulsating Radio Sources*, Nature, 218, 731

Goldreich, P. & Julian, W. H. 1969, *Pulsar Electrodynamics*, ApJ, 157, 869

Green, D. A. 1984, *Statistical studies of supernova remnants*, MNRAS, 209, 449

Guillemot, L. 2009, *Detections of millisecond pulsars with the Fermi Large Area Telescope*, ArXiv e-prints

Guillemot, L., Kramer, M., Johnson, T. J., *et al.* 2013, *Fermi LAT Pulsed Detection of PSR J0737-3039A in the Double Pulsar System*, ApJ, 768, 169

Guillemot, L. & Tauris, T. M. 2014, *On the non-detection of gamma-rays from energetic millisecond pulsars – dependence on viewing geometry*, MNRAS, submitted, arXiv:1401.2773

Guillot, S., Rutledge, R. E., & Brown, E. F. 2011, *Neutron Star Radius Measurement with the Quiescent Low-mass X-ray Binary U24 in NGC 6397*, ApJ, 732, 88

Guillot, S., Servillat, M., Webb, N. A., & Rutledge, R. E. 2013, *Measurement of the Radius of Neutron Stars with High Signal-to-noise Quiescent Low-mass X-Ray Binaries in Globular Clusters*, ApJ, 772, 7

Güver, T. & Özel, F. 2013, *The Mass and the Radius of the Neutron Star in the Transient Low-mass X-Ray Binary SAX J1748.9-2021*, ApJ Lett., 765, L1

Güver, T., Özel, F., & Psaltis, D. 2012a, *Systematic Uncertainties in the Spectroscopic Measurements of Neutron-star Masses and Radii from Thermonuclear X-Ray Bursts. II. Eddington Limit*, ApJ, 747, 77

Güver, T., Psaltis, D., & Özel, F. 2012b, *Systematic Uncertainties in the Spectroscopic Measurements of Neutron-star Masses and Radii from Thermonuclear X-Ray Bursts. I. Apparent Radii*, ApJ, 747, 76

Han, J. L., Demorest, P. B., van Straten, W., & Lyne, A. G. 2009, *Polarization Observations of 100 Pulsars at 774 MHz by the Green Bank Telescope*, ApJ Suppl., 181, 557

Han, J. L., Manchester, R. N., Lyne, A. G., Qiao, G. J., & van Straten, W. 2006, *Pulsar Rotation Measures and the Large-Scale Structure of the Galactic Magnetic Field*, ApJ, 642, 868

Harding, A. K. 1981, *Pulsar gamma-rays - Spectra, luminosities, and efficiencies*, ApJ, 245, 267

Harding, A. K. 2007, in American Institute of Physics Conference Series, Vol. 921, The First GLAST Symposium, ed. S. Ritz, P. Michelson, & C. A. Meegan, 49–53

Harding, A. K. 2009, in Astrophysics and Space Science Library, Vol. 357, Astrophysics and Space Science Library, ed. W. Becker, 521

Harding, A. K. & Muslimov, A. G. 2002, *Pulsar Polar Cap Heating and Surface Thermal X-Ray Emission. II. Inverse Compton Radiation Pair Fronts*, ApJ, 568, 862

Haskell, B., Pizzochero, P. M., & Sidery, T. 2012, *Modelling pulsar glitches with realistic pinning forces: a hydrodynamical approach*, MNRAS, 420, 658

Hawking, S. W. & Israel, W. 1981, *Book-Review - General Relativity - an Einstein Centenary Survey*, The Observatory, 101, 62

He, C., Ng, C.-Y., & Kaspi, V. M. 2013, *The Correlation between Dispersion Measure and X-Ray Column Density from Radio Pulsars*, ApJ, 768, 64

Heinke, C. O., Rybicki, G. B., Narayan, R., & Grindlay, J. E. 2006, *A Hydrogen Atmosphere Spectral Model Applied to the Neutron Star X7 in the Globular Cluster 47 Tucanae*, ApJ, 644, 1090

Hessels, J. W. T., Ransom, S. M., Stairs, I. H., *et al.* 2006, in American Astronomical Society Meeting Abstracts, Vol. 207, American Astronomical Society Meeting Abstracts #207, 209.07

Hessels, J. W. T., Roberts, M. S. E., Ransom, S. M., *et al.* 2004, *Observations of PSR J2021+3651 and its X-Ray Pulsar Wind Nebula G75.2+0.1*, ApJ, 612, 389

Hewish, A., Bell, S. J., Pilkington, J. D. H., Scott, P. F., & Collins, R. A. 1968, *Observation of a Rapidly Pulsating Radio Source*, Nature, 217, 709

Hirotani, K. 2011, *Pulsar Outer-gap Electrodynamics: Hardening of Spectral Shape in the Trailing Peak in the Gamma-Ray Light Curve*, ApJ Lett., 733, L49

Hobbs, G., Faulkner, A., Stairs, I. H., *et al.* 2004a, *The Parkes multibeam pulsar survey - IV. Discovery of 180 pulsars and parameters for 281 previously known pulsars*, MNRAS, 352, 1439

Hobbs, G., Lyne, A. G., Kramer, M., Martin, C. E., & Jordan, C. 2004b, *Long-term timing observations of 374 pulsars*, MNRAS, 353, 1311

Hobbs, G. B., Edwards, R. T., & Manchester, R. N. 2006, *TEMPO2, a new pulsar-timing package - I. An overview*, MNRAS, 369, 655

Hoekzema, N. M., Lamers, H. J. G. L. M., & van Genderen, A. M. 1992, *The distance and reddening of stars near the Luminous Blue Variable AG Carinae*, A&A, 257, 118

Hotan, A. W., Bailes, M., & Ord, S. M. 2006, *High-precision baseband timing of 15 millisecond pulsars*, MNRAS, 369, 1502

Hou, X., Smith, D. A., Guillemot, L., *et al.* 2014, *Six Faint Gamma-ray Pulsars Seen with the Fermi Large Area Telescope: Towards a Sample Blending into the Background*, A&A, submitted

Hu, Y.-M., Pitkin, M., Heng, I. S., & Hendry, M. A. 2013, *Glitch or Anti-Glitch: a Bayesian View*, ArXiv e-prints

Huang, Y. F. & Geng, J. J. 2013, *Anti-glitch induced by collision of a solid body with the magnetar 1E 2259+586*, ArXiv e-prints

Hulse, R. A. & Taylor, H. J. 1974, in Bulletin of the American Astronomical Society, Vol. 6, Bulletin of the American Astronomical Society, 453

Jackson, J. D. 1999, Classical Electrodynamics

Johnson, T. J., Venter, C., Harding, A. K., *et al.* 2013, *Light Curve Modeling of Gamma-ray Millisecond Pulsars from the Second LAT Pulsar Catalog*, ApJ, in prep

Johnston, S., Manchester, R. N., Lyne, A. G., *et al.* 1992, *PSR 1259-63 - A binary radio pulsar with a Be star companion*, ApJ Lett., 387, L37

Johnston, S. & Weisberg, J. M. 2006, *Profile morphology and polarization of young pulsars*, MNRAS, 368, 1856

Kalberla, P. M. W., Burton, W. B., Hartmann, D., *et al.* 2005, *The Leiden/Argentine/Bonn (LAB) Survey of Galactic HI. Final data release of the combined LDS and IAR surveys with improved stray-radiation corrections*, A&A, 440, 775

Kargaltsev, O., Durant, M., Pavlov, G. G., & Garmire, G. 2012, *Chandra Pulsar Survey (ChaPS)*, ApJ Suppl., 201, 37

Kaspi, V. M. & Helfand, D. J. 2002, in Astronomical Society of the Pacific Conference Series, Vol. 271, Neutron Stars in Supernova Remnants, ed. P. O. Slane & B. M. Gaensler, 3

Katz, J. I. 2013, *Implications of an anti-glitch in AXP/SGR*, Ap&SS

Keith, M. J., Eatough, R. P., Lyne, A. G., *et al.* 2009, *Discovery of 28 pulsars using new techniques for sorting pulsar candidates*, MNRAS, 395, 837

Keith, M. J., Johnston, S., Weltevrede, P., & Kramer, M. 2010, *Polarization measurements of five pulsars with interpulses*, MNRAS, 402, 745

Kerr, F. J. & Lynden-Bell, D. 1986, *Review of galactic constants*, MNRAS, 221, 1023

Kerr, M. 2010, PhD thesis, University of Washington

Kerr, M. 2011, *Improving Sensitivity to Weak Pulsations with Photon Probability Weighting*, ApJ, 732, 38

Knight, H. S., Bailes, M., Manchester, R. N., & Ord, S. M. 2005, *A Search for Giant Pulses from Millisecond Pulsars*, ApJ, 625, 951

Knight, H. S., Bailes, M., Manchester, R. N., Ord, S. M., & Jacoby, B. A. 2006, *Green Bank Telescope Studies of Giant Pulses from Millisecond Pulsars*, ApJ, 640, 941

Kong, A. K. H., Huang, R. H. H., Cheng, K. S., *et al.* 2012, *Discovery of an Unidentified Fermi Object as a Black Widow-like Millisecond Pulsar*, ApJ Lett., 747, L3

Koribalski, B., Johnston, S., Weisberg, J. M., & Wilson, W. 1995, *H I line measurements of eight southern pulsars*, ApJ, 441, 756

Kothari, D. S. & Singh, B. N. 1938, *The Relation of Electron Gas Pressure to Radiation Pressure in Degeneracy and Non-Degeneracy. Mit 3 Abbildungen.*, ZAp, 15, 143

Kramer, M., Wielebinski, R., Jessner, A., Gil, J. A., & Seiradakis, J. H. 1994, *Geometrical analysis of average pulsar profiles using multi-component Gaussian FITS at several frequencies. I. Method and analysis.*, A&AS, 107, 515

Kuijken, K. & Gilmore, G. 1989, *The Mass Distribution in the Galactic Disc - II - Determination of the Surface Mass Density of the Galactic Disc Near the Sun*, MNRAS, 239, 605

Lai, X.-Y. & Xu, R.-X. 2011, *A note on the discovery of a $2M_{odot}$ pulsar*, Research in Astronomy and Astrophysics, 11, 687

Large, M. I., Vaughan, A. E., & Mills, B. Y. 1968, *A Pulsar Supernova Association?*, Nature, 220, 340

Lasota, J.-P. 2001, *The disc instability model of dwarf novae and low-mass X-ray binary transients*, New Astron.Rev., 45, 449

Lattimer, J. M. & Prakash, M. 2001, *Neutron Star Structure and the Equation of State*, ApJ, 550, 426

Lattimer, J. M. & Prakash, M. 2004, *The Physics of Neutron Stars*, Science, 304, 536

Lattimer, J. M. & Prakash, M. 2007, *Neutron star observations: Prognosis for equation of state constraints*, Phys. Rep., 442, 109

Lattimer, J. M., Prakash, M., Masak, D., & Yahil, A. 1990, *Rapidly rotating pulsars and the equation of state*, ApJ, 355, 241

Lazaridis, K., Wex, N., Jessner, A., *et al.* 2009, *Generic tests of the existence of the gravitational dipole radiation and the variation of the gravitational constant*, MNRAS, 400, 805

Leahy, D. & Tian, W. 2010, in Astronomical Society of the Pacific Conference Series, Vol. 438, Astronomical Society of the Pacific Conference Series, ed. R. Kothes, T. L. Landecker, & A. G. Willis, 365

Lewin, W. H. G., van Paradijs, J., & Taam, R. E. 1993, *X-Ray Bursts*, Space Sci. Rev., 62, 223

Lindblom, L. 1992, *Determining the nuclear equation of state from neutron-star masses and radii*, ApJ, 398, 569

Link, B. 2003, *Constraining Hadronic Superfluidity with Neutron Star Precession*, Physical Review Letters, 91, 101101

Löhmer, O., Lewandowski, W., Wolszczan, A., & Wielebinski, R. 2005, *Shapiro Delay in the PSR J1640+2224 Binary System*, ApJ, 621, 388

Lorimer, D. R., Faulkner, A. J., Lyne, A. G., *et al.* 2006, *The Parkes Multibeam Pulsar Survey - VI. Discovery and timing of 142 pulsars and a Galactic population analysis*, MNRAS, 372, 777

Lorimer, D. R. & Kramer, M. 2004, Handbook of Pulsar Astronomy

Lutz, T. E. & Kelker, D. H. 1973, *On the Use of Trigonometric Parallaxes for the Calibration of Luminosity Systems: Theory*, PASP, 85, 573

Lyne, A. G., Burgay, M., Kramer, M., *et al.* 2004, *A Double-Pulsar System: A Rare Laboratory for Relativistic Gravity and Plasma Physics*, Science, 303, 1153

Lyne, A. G. & Lorimer, D. R. 1994, *High birth velocities of radio pulsars*, Nature, 369, 127

Lyne, A. G., Manchester, R. N., Lorimer, D. R., *et al.* 1998, *The Parkes Southern Pulsar Survey - II. Final results and population analysis*, MNRAS, 295, 743

Malov, I. F. 2003, *On the Mechanism of X-ray Emission from Radio Pulsars*, Astronomy Letters, 29, 502

Manchester, R. N., Hobbs, G. B., Teoh, A., & Hobbs, M. 2005, *ATNF Pulsar Catalog (Manchester+, 2005)*, VizieR Online Data Catalog, 7245, 0

Manchester, R. N., Lyne, A. G., Taylor, J. H., *et al.* 1978, *The second Molonglo pulsar survey - discovery of 155 pulsars.*, MNRAS, 185, 409

Manchester, R. N. & Taylor, J. H. 1977, Pulsars, 36

Marchiano, P., Brandi, E., Muratore, M. F., *et al.* 2012, *The spectroscopic orbits and physical parameters of GG Carinae*, A&A, 540, A91

Meegan, C., Lichti, G., Bhat, P. N., *et al.* 2009, *The Fermi Gamma-ray Burst Monitor*, ApJ, 702, 791

Melatos, A., Peralta, C., & Wyithe, J. S. B. 2008, *Avalanche Dynamics of Radio Pulsar Glitches*, ApJ, 672, 1103

Melatos, A. & Warszawski, L. 2009, *Superfluid Vortex Unpinning as a Coherent Noise Process, and the Scale Invariance of Pulsar Glitches*, ApJ, 700, 1524

Mel'Nik, A. M. & Efremov, Y. N. 1995, *A new list of OB associations in our galaxy*, Astronomy Letters, 21, 10

Meltzer, D. W. & Thorne, K. S. 1966, *Normal Modes of Radial Pulsation of Stars at the End Point of Thermonuclear Evolution*, ApJ, 145, 514

Morris, D. J., Hobbs, G., Lyne, A. G., *et al.* 2002, *The Parkes Multibeam Pulsar Survey - II. Discovery and timing of 120 pulsars*, MNRAS, 335, 275

Muslimov, A. G. & Harding, A. K. 2003, *Extended Acceleration in Slot Gaps and Pulsar High-Energy Emission*, ApJ, 588, 430

Muslimov, A. G. & Harding, A. K. 2004a, *High-Altitude Particle Acceleration and Radiation in Pulsar Slot Gaps*, ApJ, 606, 1143

Muslimov, A. G. & Harding, A. K. 2004b, *Particle Acceleration in Pair-starved Pulsars*, ApJ, 617, 471

Nel, H. I., Arzoumanian, Z., Bailes, M., *et al.* 1996, *EGRET High-Energy Gamma-Ray Pulsar Studies. III. A Survey*, ApJ, 465, 898

Nice, D. J., Splaver, E. M., Stairs, I. H., *et al.* 2005, *A 2.1 M_{solar} Pulsar Measured by Relativistic Orbital Decay*, ApJ, 634, 1242

Nolan, P. L., Abdo, A. A., Ackermann, M., *et al.* 2012, *Fermi Large Area Telescope Second Source Catalog*, ApJ Suppl., 199, 31

Oppenheimer, J. R. & Volkoff, G. M. 1939, *On Massive Neutron Cores*, Physical Review, 55, 374

Ord, S. M., van Straten, W., Hotan, A. W., & Bailes, M. 2004, *Polarimetric profiles of 27 millisecond pulsars*, MNRAS, 352, 804

Özel, F., Gould, A., & Güver, T. 2012a, *The Mass and Radius of the Neutron Star in the Bulge Low-mass X-Ray Binary KS 1731-260*, ApJ, 748, 5

Özel, F., Güver, T., & Psaltis, D. 2009, *The Mass and Radius of the Neutron Star in EXO 1745-248*, ApJ, 693, 1775

Özel, F., Psaltis, D., Narayan, R., & Santos Villarreal, A. 2012b, *On the Mass Distribution and Birth Masses of Neutron Stars*, ApJ, 757, 55

Pacini, F. 1967, *Energy Emission from a Neutron Star*, Nature, 216, 567

Paczynski, B. 1990, *A test of the galactic origin of gamma-ray bursts*, ApJ, 348, 485

Perera, B. B. P., McLaughlin, M. A., Cordes, J. M., *et al.* 2013, *Modeling the Non-recycled Fermi Gamma-Ray Pulsar Population*, ApJ, 776, 61

Pethick, C. J., Ravenhall, D. G., & Lorenz, C. P. 1995, *The inner boundary of a neutron-star crust*, Nuclear Physics A, 584, 675

Pétri, J. 2012, *High-energy emission from the pulsar striped wind: a synchrotron model for gamma-ray pulsars*, MNRAS, 424, 2023

Pétri, J. & Kirk, J. G. 2005, *The Polarization of High-Energy Pulsar Radiation in the Striped Wind Model*, ApJ Lett., 627, L37

Pierbattista, M., Harding, A. K., Grenier, I. A., *et al.* 2013, *Light-curve modelling constraints on the obliquities and aspect angles of the Fermi pulsars*, A&A, in prep

Pizzochero, P. M. 2011, *Angular Momentum Transfer in Vela-like Pulsar Glitches*, ApJ Lett., 743, L20

Pletsch, H. J., Guillemot, L., Allen, B., *et al.* 2012, *Discovery of Nine Gamma-Ray Pulsars in Fermi Large Area Telescope Data Using a New Blind Search Method*, ApJ, 744, 105

Qiao, G. J., Lee, K. J., Wang, H. G., Xu, R. X., & Han, J. L. 2004, *The Inner Annular Gap for Pulsar Radiation: γ-Ray and Radio Emission*, ApJ Lett., 606, L49

Qiao, G.-J., Lee, K.-J., Zhang, B., Wang, H.-G., & Xu, R.-X. 2007, *An Annular Gap Acceleration Model for γ-ray Emission of Pulsars*, Chin.J.Astron.Astrophys., 7, 496

Radhakrishnan, V. & Cooke, D. J. 1969, *Magnetic Poles and the Polarization Structure of Pulsar Radiation*, Astrophys. Lett., 3, 225

Radhakrishnan, V. & Shukre, C. S. 1985, in Supernovae, their Progenitors and Remnants, ed. G. Srinivasan & V. Radhakrishnan, 155

Rando, R. & for the Fermi LAT Collaboration. 2009, *Post-launch performance of the Fermi Large Area Telescope*, ArXiv e-prints

Ransom, S. M., Ray, P. S., Camilo, F., *et al.* 2011, *Three Millisecond Pulsars in Fermi LAT Unassociated Bright Sources*, ApJ Lett., 727, L16

Ray, P. S., Abdo, A. A., Parent, D., *et al.* 2012, *Radio Searches of Fermi LAT Sources and Blind Search Pulsars: The Fermi Pulsar Search Consortium*, ArXiv e-prints

Ray, P. S., Kerr, M., Parent, D., *et al.* 2011, *Precise γ-ray Timing and Radio Observations of 17 Fermi γ-ray Pulsars*, ApJ Suppl., 194, 17

Reid, M. J., Menten, K. M., Zheng, X. W., *et al.* 2009, *Trigonometric Parallaxes of Massive Star-Forming Regions. VI. Galactic Structure, Fundamental Parameters, and Noncircular Motions*, ApJ, 700, 137

Rhoades, C. E. & Ruffini, R. 1974, *Maximum Mass of a Neutron Star*, Physical Review Letters, 32, 324

Rickett, B. J. & Lyne, A. G. 1968, *Further Impulsive Emission from CP 0950*, Nature, 218, 934

Romani, R. W. 1996, *Gamma-Ray Pulsars: Radiation Processes in the Outer Magnetosphere*, ApJ, 470, 469

Romani, R. W. 2012, *2FGL J1311.7-3429 Joins the Black Widow Club*, ApJ Lett., 754, L25

Romani, R. W., Filippenko, A. V., Silverman, J. M., *et al.* 2012, *PSR J1311-3430: A Heavyweight Neutron Star with a Flyweight Helium Companion*, ApJ Lett., 760, L36

Romani, R. W., Kerr, M., Craig, H. A., *et al.* 2011, *Sub-luminous γ-ray Pulsars*, ApJ, 738, 114

Romani, R. W. & Shaw, M. S. 2011, *The Orbit and Companion of Probable γ-Ray Pulsar J2339-0533*, ApJ Lett., 743, L26

Romani, R. W. & Watters, K. P. 2010, *Constraining Pulsar Magnetosphere Geometry with γ-ray Light Curves*, ApJ, 714, 810

Romani, R. W. & Yadigaroglu, I.-A. 1995, *Gamma-ray pulsars: Emission zones and viewing geometries*, ApJ, 438, 314

Ruderman, M., Shaham, J., & Tavani, M. 1989, *Accretion turnoff and rapid evaporation of very light secondaries in low-mass X-ray binaries*, ApJ, 336, 507

Ruderman, M. A. & Sutherland, P. G. 1975, *Theory of pulsars - Polar caps, sparks, and coherent microwave radiation*, ApJ, 196, 51

Russell, H. N. 1921, *Stellar Evolution*, Popular Astronomy, 29, 541

Rutledge, R. E., Bildsten, L., Brown, E. F., Pavlov, G. G., & Zavlin, V. E. 2001, *Quiescent Thermal Emission from the Neutron Star in Aquila X-1*, ApJ, 559, 1054

Rybicki, G. B. & Lightman, A. P. 1979, Radiative processes in astrophysics

Saz Parkinson, P. M., Dormody, M., Ziegler, M., *et al.* 2010, *Eight γ-ray Pulsars Discovered in Blind Frequency Searches of Fermi LAT Data*, ApJ, 725, 571

Seveso, S., Pizzochero, P. M., & Haskell, B. 2012, *The effect of realistic equations of state and general relativity on the 'snowplough' model for pulsar glitches*, MNRAS, 427, 1089

Seward, F. D. & Wang, Z.-R. 1988, *Pulsars, X-ray synchrotron nebulae, and guest stars*, ApJ, 332, 199

Shapiro, I. I. 1964, *Fourth Test of General Relativity*, Physical Review Letters, 13, 789

Shibazaki, N., Murakami, T., Shaham, J., & Nomoto, K. 1989, *Does mass accretion lead to field decay in neutron stars?*, Nature, 342, 656

Shklovskii, I. S. 1970, *Possible Causes of the Secular Increase in Pulsar Periods.*, Soviet Ast., 13, 562

Smith, D. A., Guillemot, L., Camilo, F., *et al.* 2008, *Pulsar timing for the Fermi gamma-ray space telescope*, A&A, 492, 923

Spitkovsky, A. 2006, *Time-dependent Force-free Pulsar Magnetospheres: Axisymmetric and Oblique Rotators*, ApJ Lett., 648, L51

Splaver, E. M., Nice, D. J., Arzoumanian, Z., *et al.* 2002, *Probing the Masses of the PSR J0621+1002 Binary System through Relativistic Apsidal Motion*, ApJ, 581, 509

Staelin, D. H. & Reifenstein, III, E. C. 1968, *Pulsating Radio Sources near the Crab Nebula*, Science, 162, 1481

Standish, E. M. 1998, in Bulletin of the American Astronomical Society, Vol. 30, AAS/Division of Dynamical Astronomy Meeting #30, 1146

Standish, Jr., E. M. 1990, *The observational basis for JPL's DE 200, the planetary ephemerides of the Astronomical Almanac*, A&A, 233, 252

Strom, R. G. 1994, *'Guest stars', sample completeness and the local supernova rate*, A&A, 288, L1

Sturrock, P. A. 1971, *A Model of Pulsars*, ApJ, 164, 529

Su, M., Slatyer, T. R., & Finkbeiner, D. P. 2010, *Giant Gamma-ray Bubbles from Fermi-LAT: Active Galactic Nucleus Activity or Bipolar Galactic Wind?*, ApJ, 724, 1044

Swanenburg, B. N., Bennett, K., Bignami, G. F., *et al.* 1981, *Second COS B catalog of high-energy gamma-ray sources*, ApJ Lett., 243, L69

Takata, J., Chang, H.-K., & Shibata, S. 2008, *Particle acceleration and non-thermal emission in the pulsar outer magnetospheric gap*, MNRAS, 386, 748

Tauris, T. M. & Savonije, G. J. 1999, *Formation of millisecond pulsars. I. Evolution of low-mass X-ray binaries with P_orb> 2 days*, A&A, 350, 928

Tavani, M., Barbiellini, G., Argan, A., *et al.* 2009, *The AGILE Mission*, A&A, 502, 995

Taylor, J. H. 1992, *Pulsar Timing and Relativistic Gravity*, Royal Society of London Philosophical Transactions Series A, 341, 117

Taylor, J. H. & Cordes, J. M. 1993, *Pulsar distances and the galactic distribution of free electrons*, ApJ, 411, 674

Theureau, G., Parent, D., Cognard, I., *et al.* 2011, *PSRs J0248+6021 and J2240+5832: young pulsars in the northern Galactic plane. Discovery, timing, and gamma-ray observations*, A&A, 525, A94

Thompson, D. J. 2008, *Gamma ray astrophysics: the EGRET results*, Reports on Progress in Physics, 71, 116901

Thompson, D. J., Bailes, M., Bertsch, D. L., *et al.* 1999, *Gamma Radiation from PSR B1055-52*, ApJ, 516, 297

Thompson, D. J., Bertsch, D. L., Fichtel, C. E., *et al.* 1993, *Calibration of the Energetic Gamma-Ray Experiment Telescope (EGRET) for the Compton Gamma-Ray Observatory*, ApJ Suppl., 86, 629

Tolman, R. C. 1934, *Effect of Inhomogeneity on Cosmological Models*, Proceedings of the National Academy of Science, 20, 169

Tong, H. 2013, *Anti-glitch of magnetar 1E 2259+586 in the wind braking scenario*, ArXiv e-prints

van den Bergh, S. & Tammann, G. A. 1991, *Galactic and extragalactic supernova rates*, ARA&A, 29, 363

van den Heuvel, E. P. J. 2011, *Compact stars and the evolution of binary systems*, Bulletin of the Astronomical Society of India, 39, 1

van den Heuvel, E. P. J., Bhattacharya, D., Nomoto, K., & Rappaport, S. A. 1992, *Accreting white dwarf models for CAL 83, CAL 87 and other ultrasoft X-ray sources in the LMC*, A&A, 262, 97

Van Etten, A., Romani, R. W., & Ng, C.-Y. 2008, *Rings and Jets around PSR J2021+3651: The "Dragonfly Nebula"*, ApJ, 680, 1417

van Kerkwijk, M. H., Breton, R. P., & Kulkarni, S. R. 2011, *Evidence for a Massive Neutron Star from a Radial-velocity Study of the Companion to the Black-widow Pulsar PSR B1957+20*, ApJ, 728, 95

Venter, C. & De Jager, O. C. 2010, *Accelerating High-energy Pulsar Radiation Codes*, ApJ, 725, 1903

Venter, C., Harding, A. K., & Guillemot, L. 2009, *Probing Millisecond Pulsar Emission Geometry Using Light Curves from the Fermi/Large Area Telescope*, ApJ, 707, 800

Verbiest, J. P. W., Bailes, M., van Straten, W., *et al.* 2008, *Precision Timing of PSR J0437-4715: An Accurate Pulsar Distance, a High Pulsar Mass, and a Limit on the Variation of Newton's Gravitational Constant*, ApJ, 679, 675

Verbiest, J. P. W., Lorimer, D. R., & McLaughlin, M. A. 2010, *Lutz-Kelker bias in pulsar parallax measurements*, MNRAS, 405, 564

Verbiest, J. P. W., Weisberg, J. M., Chael, A. A., Lee, K. J., & Lorimer, D. R. 2012, *On Pulsar Distance Measurements and Their Uncertainties*, ApJ, 755, 39

Wang, R.-B. & Hirotani, K. 2011, *Death Line of Gamma-Ray Pulsars with Outer Gaps*, ApJ, 736, 127

Wang, Y., Takata, J., & Cheng, K. S. 2011, *Three-dimensional two-layer outer gap model: Fermi energy-dependent light curves of the Vela pulsar*, MNRAS, 414, 2664

Wang, Z., Kaplan, D., & Kaspi, V. 2008, *Possible Detection of A Dust Disk Around A Radio Pulsar*, Spitzer Proposal, 490

Watters, K. P. & Romani, R. W. 2011, *The Galactic Population of Young γ-ray Pulsars*, ApJ, 727, 123

Watters, K. P., Romani, R. W., Weltevrede, P., & Johnston, S. 2009, *An Atlas for Interpreting γ-Ray Pulsar Light Curves*, ApJ, 695, 1289

Webb, N. A. & Barret, D. 2007, *Constraining the Equation of State of Supranuclear Dense Matter from XMM-Newton Observations of Neutron Stars in Globular Clusters*, ApJ, 671, 727

Weissenborn, S., Chatterjee, D., & Schaffner-Bielich, J. 2012, *Hyperons and massive neutron stars: The role of hyperon potentials*, Nuclear Physics A, 881, 62

Weltevrede, P. & Johnston, S. 2008a, *Profile and polarization characteristics of energetic pulsars*, MNRAS, 391, 1210

Weltevrede, P. & Johnston, S. 2008b, *The population of pulsars with interpulses and the implications for beam evolution*, MNRAS, 387, 1755

Weltevrede, P., Wright, G. A. E., & Stappers, B. W. 2007, *The main-interpulse interaction of PSR B1702-19*, A&A, 467, 1163

Wex, N., Kalogera, V., & Kramer, M. 2000, *Constraints on Supernova Kicks from the Double Neutron Star System PSR B1913+16*, ApJ, 528, 401

Woosley, S. E., Heger, A., & Weaver, T. A. 2002, *The evolution and explosion of massive stars*, Reviews of Modern Physics, 74, 1015

Xilouris, K. M., Kramer, M., Jessner, A., *et al.* 1998, *The Characteristics of Millisecond Pulsar Emission. II. Polarimetry*, ApJ, 501, 286

Yadigaroglu, I.-A. & Romani, R. W. 1997, *Gamma-Ray Pulsars and Massive Stars in the Solar Neighborhood*, ApJ, 476, 347

Zamfir, M., Cumming, A., & Galloway, D. K. 2012, *Constraints on Neutron Star Mass and Radius in GS 1826-24 from Sub-Eddington X-Ray Bursts*, ApJ, 749, 69

Zhang, L. & Cheng, K. S. 1997, *High-Energy Radiation from Rapidly Spinning Pulsars with Thick Outer Gaps*, ApJ, 487, 370

Zhang, L., Fang, J., & Chen, S. B. 2007, *High-Energy Properties of Pulsed Emission from Millisecond Pulsars*, ApJ, 666, 1165

Ziegler, M., Baughman, B. M., Johnson, R. P., & Atwood, W. B. 2008, *A Search for Radio-Quiet Gamma-Ray Pulsars in EGRET Data Using a Time-Differencing Technique*, ApJ, 680, 620

List of Figures

List of Tables

Acronyms and abbreviations

2FGL	*Fermi-LAT Second Source Catalog*
2PC	*Second Fermi-LAT gamma-ray Pulsar Catalog*
ACD	*Anti Coincidence Detector*
AGN	*Active Galactic Nuclei*
ATNF	*Australia Telescope National Facility*
CAL	*Calorimeter*
CGRO	*Compton Gamma Ray Observatory*
DM	*Dispersion Measure*
EGRET	*Energetic Gamma Ray Experiment Telescope*
EOS	*Equations of State*
FOV	*Field of View*
FSSC	*Fermi Science Support Center*
GBM	*Gamma-ray Burst Monitor*
GRB	*Gamma-ray Burst*
IRF	*Instrument Response Function*
ISM	*Interstellar medium*
LAT	*Large Area Telescope*
LSR	*Local Standard of Rest*
MET	*Mission Elapsed Time*
MJD	*Modified Julian Date*
MSP	*Millisecond Pulsar*
NCS	*Null Charge Surface*
OG	*Outer Gap*
PC	*Polar Cap*
PSF	*Point Spread Function*
PSR	*Pulsating Source of Radio*
PTC	*Pulsar Timing Consortium*
PWN	*Pulsar Wind Nebula*
ROI	*Region of Interest*
RVM	*Rotating-Vector Model*
SED	*Spectral Energy Distribution*
SG	*Slot Gap*
SNR	*Supernova Remnant*
SSB	*Solar System Barycenter*
TAI	*Temps Atomique International*
TDB	*Temps Dynamique Barycentrique*
TKR	*Tracker*
TOA	*Time of Arrival*
TPC	*Two-Pole Caustic*
TS	*Test Statistic*
TT	*Temps Terrestre*
UTC	*Coordinated Universal Time*

Résumé

Le Large Area Telescope (LAT) à bord du satellite *Fermi*, lancé le 11 Juin 2008, est sensible au rayonnement γ de 20 MeV à plus de 300 GeV. 148 pulsars γ à ce jour ont été détectés avec le *Fermi*-LAT, dont 117 sont détaillés dans le Deuxième Catalogue de Pulsars γ de *Fermi* (2PC). Les pulsars forment la plus grande classe de sources au GeV dans la Voie Lactée. Les études de pulsars γ apportent des contraintes importantes sur les modèles d'émission γ et permettent des percées dans notre compréhension des pulsars.

Cette thèse présente des détections de sept pulsars γ faibles déjà connus en radio, dont quatre jeunes ou d'âges moyens et trois millisecondes (MSP). L'analyse spectrale et la caractérisation des courbes de lumiére sont décrites et comparées à la population de 2PC. Ces détections ont l'intérêt particulier de sonder et d'étendre l'espace des paramètres de la population actuelle. Elles illustrent la distorsion inhérente dans 2PC et marquent la transition de la première phase (pulsars brillants) à la seconde phase (pulsars faibles) d'opération de *Fermi*. Le développement des modèles théoriques et un recensement complet de la population galactique des étoiles à neutrons bénéficieront de plus de détections de pulsars faibles dans les années à venir.

Certains pulsars γ dans 2PC manifestant de grande efficacité γ sont étudiés dans cette thèse. L'examen des différents paramètres qui influencent l'efficacité conduit à quelques candidats pour lesquels un plus grand moment d'inertie est nécessaire afin de résoudre le paradoxe de grande efficacité. Les observations de *Fermi* en rayons γ ont l'air à apporter des contraintes indépendantes sur le moment d'inertie et les équations d'état des étoiles à neutrons.

Mots-clés: *Astronomie gamma, Fermi, Large Area Telescope (LAT), pulsars, étoiles à neutrons, moment d'inertie*

Abstract

The Large Area Telescope (LAT) on board the *Fermi* satellite, launched on June 11 2008, is sensitive to γ rays from 20 MeV to over 300 GeV. γ-ray pulsations from 148 pulsars to date have been detected with the *Fermi*-LAT, 117 are detailed in the Second *Fermi*-LAT Gamma-ray Pulsar Catalog (2PC). Pulsars are by far the largest GeV source-class in the Milky Way. Studies of the increasing γ-ray pulsar sample bring important constraints on theoretical γ-ray emission models and enable breakthroughs in our understanding of pulsars.

This thesis presents detections of seven faint γ-ray pulsars that are already known at radio wavelengths, including four young or middle aged pulsars and three millisecond pulsars (MSPs). Spectral analysis and light curve characterizations are detailed and compared to the 2PC sample. These detections have the special interest of allowing us to probe and extend the parameter space of the current population. They illustrate the inherent bias in 2PC and mark the transition from the early part (bright pulsars) to the later part (faint pulsars) of the *Fermi* mission. Theoretical model developments and a complete census of Galactic neutron star populations will benefit from more detections of weak pulsars in the years to come.

Some high γ-ray efficiency pulsars in 2PC are studied in this thesis. Investigations on different parameters which influence the efficiency result in a few candidates for which a large moment of inertia is necessary to cure the high efficiency paradox. *Fermi* γ-ray observations seem to bring independent constraints on the moment of inertia and equations of state of neutron stars.

Keywords: *Gamma-ray astronomy, Fermi, Large Area Telescope (LAT), pulsars, neutron stars, moment of inertia.*